
Wayne State University Dissertations


January 2014

Design Of Functional Dendrimer Nanocarriers And Their Formulations In Propellant-Based Inhalers For Pulmonary Drug Delivery

Lin Yang

Wayne State University, ed2837@wayne.edu

Follow this and additional works at: https://digitalcommons.wayne.edu/oa_dissertations

 Part of the [Chemical Engineering Commons](#), and the [Medicinal Chemistry and Pharmaceutics Commons](#)

Recommended Citation

Yang, Lin, "Design Of Functional Dendrimer Nanocarriers And Their Formulations In Propellant-Based Inhalers For Pulmonary Drug Delivery" (2014). *Wayne State University Dissertations*. 1001.
https://digitalcommons.wayne.edu/oa_dissertations/1001

This Open Access Dissertation is brought to you for free and open access by DigitalCommons@WayneState. It has been accepted for inclusion in Wayne State University Dissertations by an authorized administrator of DigitalCommons@WayneState.

**DESIGN OF FUNCTIONAL DENDRIMER NANOCARRIERS
AND THEIR FORMULATIONS IN PROPELLANT-BASED
INHALERS FOR PULMONARY DRUG DELIVERY**

by

LIN YANG

DISSERTATION

Submitted to the Graduate School

of Wayne State University,

Detroit, Michigan

in partial fulfillment of the requirements

for the degree of

DOCTOR OF PHILOSOPHY

2014

MAJOR: MATERIAL SCIENCE

Approved by:

Advisor Date

© COPYRIGHT BY

LIN YANG

2014

All Rights Reserved

ACKNOWLEDGEMENTS

The 5 years at Wayne State University Department of Chemical Engineering and Material Science is a rich and meaningful experience in every way. I have grown a lot thanks to the people around me – my friends, my labmates, and faculties in the department.

I would like to express my sincere thanks to my advisor, Prof. Sandro R.P. da Rocha for guiding me through possibly the most meaningful 5 years of my life so far. He is nice in personality but tough in science, he is open with discussions and determined with goals, he is a great mentor as well as a good friend. I am very lucky to have him as my advisor.

My gratitude also goes to my committee members, Prof. Guangzhao Mao, Jeffery Potoff, Zhiqiang Cao and Olivia Merkel for their continuous guidance and meaningful discussions. Special thanks goes to Prof. Charles W. Manke, for being supportive from many aspects. Special thanks also goes to Prof. H. Bernhard Schlegel, Joshua Reineke for helping me with their expertise. My thanks also goes to my labmates, for their encouragement and friendship. I thank the department of Chemical Engineering and Material Science for offering me this great Ph.D experience. Finally, I would like to thank my parents for doing such an incredible job of raising, loving, caring and supporting me through my life, while giving me all the freedom to make choices.

To graduate sounds like to finish. But in reality, it is the new beginning, to the next chapter in life. And I am so grateful to those who I worked with during my Ph.D study, to get me ready for the new chapter.

TABLE OF CONTENTS

Acknowledgements	ii
List of Tables	ix
List of Figures	xi
CHAPTER 1: INTRODUCTION	1
1.1. Pulmonary drug delivery	1
1.2. Challenges in the development of aerosol formulations for the delivery of therapeutics to and through the lungs.....	2
1.3. Challenges in designing nanocarriers for the delivery of therapeutics to and through the lungs.	4
1.4. Goals and approaches.....	6
1.5. Background relevance to this study	8
1.5.1. Lung Diseases.....	8
1.5.2. Pressurized Metered-dose Inhalers (pMDIs).....	8
1.5.3. Challenges of Formulating Active Ingredients in pMDIs.	9
1.5.4. Semi-fluorinated alkanes (HFAs) and olefins (HFOs).....	10
1.5.5. HFOs.....	10
1.5.6. Potential of functional nanocarriers for pulmonary drug delivery	12
1.5.7. Nanocarriers for siRNA Delivery to the Lungs	13
1.5.8. PAMAM Dendrimer Nanocarriers (DNCs)	13
1.5.9. PEG as Ligand for PAMAM dendrimers.....	14
1.5.10. Ab initio calculations.....	14
1.5.11. MD of the HFO Water Interface	15
1.6. Innovation and relevance.....	15
1.6.1. Aim #1	16
1.6.2. Aim# 2	16
CHAPTER 2: UNDERSTANDING IN THE LOW GLOBAL WARMING HYDROFLUOROOLEFIN HFO-1234ZE PROPELLANT.....	18
2.1. Introduction	18
2.2. Computational details.....	21

2.2.1.	Pair interaction (binding) energy of propellant-tail fragment (E_b^{st}).....	21
2.2.2.	Chemistry of propellants and tail fragments.	22
2.2.3.	Enhancement Factor (E_{enh}) incorporates tail-tail self-interaction binding energies (E_b^{tt})	23
2.2.4.	Cluster studies: (HFO-1234ze) _n -Tail Fragment.....	23
2.3.	Results and Discussions	24
2.3.1.	Tail chemistry and its effect on the binding energy (E_b^{st})	24
2.3.2.	Effect of Tail Polarity	25
2.3.3.	Optimized structure and strong interactions.....	27
2.3.4.	Effect of Tail Branching.....	38
2.3.5.	Electrostatic Potential and Strong Interaction Sites	40
2.3.6.	Tail-tail Self-interaction Binding Energy (E_b^{tt}) and Enhancement Factor (E_{enh}).....	41
2.3.7.	Effect of Tail Polarity	42
2.3.8.	Effect of Tail Branching.....	45
2.3.9.	Interactions in cluster of solvents.....	47
2.4.	Conclusions	49
CHAPTER 3: THE MICROSTRUCTURE AND INTERFACIAL TENSION OF THE BARE AND SURFACTANT-MODIFIED HFO-1234ZE WATER INTERFACE.....		51
3.1.	Introduction	51
3.2.	Models and Methods.....	53
3.2.1.	Force Field and Simulation Details	53
3.2.2.	Surfactant Molecules Investigated in the MD Simulation Studies.....	58
3.2.3.	In situ (high-pressure) Tensiometry.....	59
3.3.	Results and Discussions.....	61
3.3.1.	Surface Tension of HFO-1234ze and the Effect of Temperature.....	61
3.3.2.	The Binary HFO-1234ze H ₂ O Interface: Interfacial Tension and Microstructure.....	62
3.3.3.	The Surfactant-modified HFO-1234ze H ₂ O Interface: Microstructure, Interfacial Tension, and Surfactant Balance.	64
3.3.3.	Surfactant Balance at the HFO-1234ze H ₂ O Interface.....	71
3.4.	Conclusions	74
CHAPTER 4: PEGYLATED, NH₂-TERMINATED PAMAM DENDRIMERS: A MICROSCOPIC VIEW FROM ATOMISTIC COMPUTER SIMULATION		76
4.1.	Introduction	76

4.2.	Methods and Models	79
4.3.	Results and discussions.....	80
4.3.1.	Effect of generation on the size and shape of GXNH ₂ dendrimers.....	80
4.3.2.	Distribution and solvation of primary and branching amines.....	88
4.3.3.	Effect of PEGylation on PAMAM dendrimer microstructure	93
4.4.	Conclusions	103
CHAPTER 5: THE CHEMISTRY OF THE TERMINAL SURFACE GROUPS OF PAMAM DENDRIMERS DETERMINE THE MICROSTRUCTURE OF THE GRAFTED PEG LAYER		105
5.1.	Introduction	105
5.2.	Methods and Models	108
5.3.	Results and discussions.....	109
5.3.1.	Effect of terminal chemistry on size and shape of generation 3 PAMAM dendrimers.....	109
5.3.2.	Different terminal groups will lead to different microstructure of PEGylated DNCs.....	113
5.3.3.	Effect of PEGylation on microstructures of PAMAM dendrimers with different terminal chemistry	116
5.4.	Conclusionsions	125
Appendix A: Supplemental Information for Chapter 2.....		130
Appendix B: Supplemental Information for Chapter 3.....		137
Appendix C: Supplemental Information for Chapter 4.....		149
Appendix D: Supplemental Information for Chapter 5.....		160
References	174
Abstract	209
Autobiographical Statement.....		211

LIST OF TABLES

Table 1 Physical properties of semi-fluorinated alkanes (HFAs) and olefins (HFOs), and of chlorofluorocarbons (CFCs).....	11
Table 2 Some relevant physicochemical properties of the fourth generation propellant HFO-1234ze compared to the hydrofluoroalkanes HFA-134a and HFA227.....	19
Table 3 Summary of the binding energies (E_b).....	25
Table 4 Summary of “strong interactions” between the propellants and the different tail fragments.	37
Table 5 Summary of the “Enhancement Factors” (E_{enh}) for the different chemistries and propellants..	44
Table 6 Summary of “strong interactions” between the tail-tail fragment pairs.....	46
Table 7 Intramolecular and Lennard-Jones force field parameters for HFO-1234ze.	54
Table 8 Partial charge distribution for HFO-1234ze from ab initio calculations using Gaussian 09..	56
Table 9 Commercial name, molecular weight (MW), molecular structure, wt.%EO and experimental tension of the various surfactants studied in this work at the HFO-1234ze H ₂ O interface.....	59
Table 10 Computer simulation results for the surface tension of HFO-1234ze as a function of temperature (T).	62
Table 11 Computer simulation results for the interfacial tension (γ) of the bare and surfactant-modified HFO-1234ze H ₂ O interface.	63
Table 12 Radius of gyration (R_g) as a function of the generation of the NH ₂ -terminated PAMAM dendrimers (GXNH ₂).	81
Table 13 Radius of gyration (R_g) of equilibrated DNCs.	122

LIST OF FIGURES

Figure 1 Schematic diagram of our goals for the design of nanocarriers and formulations for pulmonary drug delivery.	6
Figure 2. Schematic diagram of main components of pMDI.	9
Figure 3 Schematic diagram of the calculation of the non-bonded interaction energy E_b^{st} between HFO and tail fragment.....	15
Figure 4 Effect of tail polarity on the binding energy between the different propellants (solvent = s) and tail fragments (tail = t) - E_b^{st} (kJ/mol).	26
Figure 5 Structure of optimized HFA-134a and the ester-based pairs.	30
Figure 6 Structure of optimized HFA-227 and the ester-based pairs.....	32
Figure 7 Structure of optimized pairs.....	36
Figure 8 Effect of the degree of branching	39
Figure 9 Effect of tail chemistry on the self-interaction binding energies of the different tail fragments (E_b^{tt}) (kJ/mol)	42
Figure 10 Optimized geometries of the self-interacting tail-tail fragments at the MP2/6-31g+(d,p) level of theory and basis set.	43
Figure 11 Effect of tail chemistry on their “Enhancement Factor” (E_{enh}).	43
Figure 12 Effect of the degree of branching (CH3) on the self-interaction binding energies between the ester-based tail (t) fragments (E_b^{tt}) (kJ/mol).....	45
Figure 13 Effect of the degree of branching (CH3) of the ester-based tail chemistries on their “Enhancement Factor” (E_{enh}).....	47
Figure 14 Study of the interactions between a cluster of HFO-1234ze molecules (n=6) surrounding a single tail fragment.	48
Figure 15 Optimized structure and atom assignment for HFO-1234ze from ab initio calculations using Gaussian 09.	55
Figure 16 Schematic diagram of the high-pressure tensiometer.	61
Figure 17 Z-density profile for the HFO-1234ze H ₂ O interface at 298K and 1.01MPa.	64

Figure 18 Z-density profile for the HFO-1234ze H ₂ O interface modified with (a) EO ₄ -CH ₄ surfactant; (b) EO ₄ -PO ₄ surfactant; (c) EO ₄ -LA ₄ surfactant	67
Figure 19 RDF of oxygen (O) atoms from H ₂ O to fluorine (F) atoms from HFO-1234ze.	70
Figure 20 Radial distribution function (RDF) of fluorine atoms (F) from HFO-1234ze and the backbone carbon (C) atoms of the tail group.	71
Figure 21 Interfacial tension of the surfactant-modified HFO-1234ze H ₂ O interface a function of EO % (weight) of the surfactant.	72
Figure 22 Time course of the radius of gyration (R _g) of the NH ₂ -terminated PAMAM dendrimers generation 2-5 – GXNH ₂	81
Figure 23 Autocorrelation function of the radius of gyration (R _g) as a function of time (C _{Rg} (t)) for NH ₂ -terminated PAMAM dendrimers generation 2-5 - GXNH ₂	83
Figure 24 Snapshots of equilibrium conformations of the NH ₂ -terminated PAMAM dendrimers generation 2-5 – GXNH ₂	85
Figure 25 Radial atom distribution (RAD) of the NH ₂ -terminated PAMAM dendrimers as a function of their generation - GXNH ₂	87
Figure 26 Radial pair distribution function (g _{N_i-N_j}) of branching amines (N _i) to different generation branching amines (N _j) for the G ₄ NH ₂ dendrimer.	89
Figure 27 Radial pair distribution function (solvation profiles) between the oxygen of H ₂ O (O _w) and the branching amines of G ₄ NH ₂ (N _i) (g _{O_w-N_i}).....	90
Figure 28 (a) Screen shots of GXNH ₂ dendrimers after equilibration. (b) Radial pair distribution functions of the primary amines of G ₂ -G ₅ NH ₂ (N _p) to the oxygen of H ₂ O (O _w) (g _{N_p-O_w}).....	92
Figure 29 Evolution of the radius of gyration (R _g) of PEGylated G ₃ NH ₂ conjugates as a function of graft density of PEG 500 Mw – G ₃ NH ₂ -XPEG500	94
Figure 30 Radial atom distribution (RAD) of PEGylated G ₃ NH ₂ conjugates (G ₃ NH ₂ -NPEG500) as a function of number of PEG 500 Mw grafts (N).	96
Figure 31 Radial pair distribution function of H ₂ O oxygen (O _w) to (a) primary amines (N _p) (g _{N_p-O_w}) and (b) inner amines (N _i) (g _{N_i-O_w}) of PEGylated G ₃ NH ₂ conjugates as a function of graft density of PEG 500 Mw – G ₃ NH ₂ -NPEG500.	97
Figure 32 Evolution of the radius of gyration (R _g) of G ₃ NH ₂ conjugates as a function of PEG length... ..	98

Figure 33 Radial atom distribution (RAD) of PEGylated G3NH ₂ conjugates as a function of the PEG length.....	100
Figure 34 Screenshots of the equilibrium configurations of PEGylated G3NH ₂ conjugates as a function of PEG density (N in G3NH ₂ -NPEG) and PEG length (500 or 1000Mw).....	101
Figure 35 Radial pair distribution function between the oxygen from PEG (O _{PEG}) and primary amines (N _p) (g _{N_p-O_{PEG}}) of dendrimers with generation 2-5 - GXNH ₂	102
Figure 36. Time course of the radius of gyration (R _g) of generation 3 PAMAM dendrimers as a function of the chemistry of the terminal surface group.....	111
Figure 37. Snapshots of equilibrium conformations of generation 3 PAMAM dendrimer as a function of the chemistry of the terminal surface group.....	112
Figure 38. Snapshots of equilibrium conformations of generation 3 PAMAM dendrimer as a function of the chemistry of the terminal surface group after 27ns simulation time.	114
Figure 39. RDF of heavy atoms of terminal groups (terminal N for G3NH ₃ ⁺ , terminal O for G3OH, terminal ether O for G2.5COO ⁻) to O atom of H ₂ O.	115
Figure 40. Snapshots of the equilibrium configurations of PEGylated G3 PAMAM dendrimers as a function of the chemistry of the terminal surface group.	117
Figure 41. Solvation profile of primary functional of G3 PAMAM dendrimers by water. Solvation profile before and after PEGylation.	118
Figure 42. Integral of the radial pair distribution function (RDF) of the terminal heavy atoms (N for NH ₃ ⁺ , O for OH, O for COO ⁻) of G3 PAMAM dendrimers to oxygen (O) atoms of the PEG chain.	120

CHAPTER 1

INTRODUCTION

1.1. Pulmonary drug delivery

Pulmonary drug has been long accepted as the preferred route for the *local* delivery of therapeutics *to the lungs* for the treatment of a range of prevailing lungs ailments including chronic obstructive pulmonary disease (COPD), asthma and cystic fibrosis [1, 2]. More recently, however, the lungs have been also recognized as a viable route for the *systemic* administration of therapeutics *through the lungs* [3]. The interest in using the lungs as an alternative pathway for the delivery of drugs to the blood stream is due in part to the reduced enzymatic activity in the lung tissue, avoidance of first pass metabolism, and the lungs large surface area [4, 5], characteristics that enhance drug bioavailability and pharmacokinetics [6, 7].

There are three main devices that are used for the delivery of therapeutics to the lungs: nebulizers, dry powder inhalers (DPIs) and pressurized metered-dose inhalers (pMDIs) [8, 9]. pMDIs are of great relevance in the context of pulmonary drug delivery as they are the least expensive and most widely used aerosol devices. pMDIs are portable, have long shelf life, and are highly compliant [10, 11]. pMDIs self-propelling mechanism also helps to improve lung deposition efficiency in patients with compromised lung airflow, such as those suffering from COPD and other lung disorders [12].

It may be surprising at first to note, therefore, that there is no pMDIs formulation in the US that has been approved for the delivery of therapeutics to the systemic circulation. Moreover, there are no OI formulations available for treatment or to aid in the treatment of many prevailing lung

diseases such as lung cancer and pulmonary tuberculosis, even when conventional delivery routes are known to be associated with high toxicity and poor patient compliance. Currently available pMDI formulations consist mostly of a small class of therapeutics (steroids and beta-agonist) [7, 13, 14].

However, a closer look into the literature reveals that our ability to develop pMDI-based OI formulations for local or systemic delivery of drugs to and through the lungs remains basic at best. Moreover, the breakthroughs seen in conventional delivery routes as nanotechnology is applied to the controlled and targeted delivery of therapeutics, have not been explored nor materialized to the same extent to the pulmonary route. A closer look into the literature reveals that our ability to develop pMDI-based OI formulations for local or systemic delivery of drugs to and through the lungs remains basic at best. Moreover, the breakthroughs seen in conventional delivery routes as nanotechnology is applied to the controlled and targeted delivery of therapeutics have not been explored nor materialized to the same extent to the pulmonary route.

It is our *main goal* in this work to address some key but focused issues on both fronts, in terms of nanocarrier design for pulmonary delivery, with a focus on dendrimers as nanocarriers, and to the formulation of such nanocarriers in pMDI formulations, with a focus on searching for pharmaceutically acceptable moieties to enhance stabilities of HFA/HFO suspension.

1.2. Challenges in the development of aerosol formulations for the delivery of therapeutics to and through the lungs.

In order to efficiently deliver therapeutics to the lung tissue, there are several important considerations. Because the propellants used in pMDIs are halocarbons that possess a dual hydrophobic and lipophobic character [15, 16], most therapeutics of interest, including small polar and hydrophobic drugs and biomacromolecules, have very limited solubility in these propellants.

Drugs are thus usually formulated in pMDIs in the form of suspensions – solutions can be formed, but with the help of co-solvents that negatively impact the chemical and physical stability of the formulation and their aerosol performance[17]. Another important consideration is that the optimum aerosol size for deep lung deposition is between 0.5 and 5.0 μm [18]. Particles smaller than 0.5 μm may be exhaled back – which brings the issue of the formulation of our nanocarriers, which are of the order of a few nm. This can be addressed by engineering particles of micron-size range containing such nanocarriers (core-shell particles). On the other hand, particles larger than 5.0 μm will be retained in mouth and throat and will end up in the digestive track, which suggests that the micron-sized engineered particles containing the nanocarriers need to be stabilized in the propellant so as to prevent coagulation that would in turn lead to large aerosol sizes of poor lung deposition [17, 19, 20]. Steric stabilization in low dielectric propellants is thus a key issue and will be addressed in this work at a fundamental level, combining *ab initio* calculations, molecular dynamics (MD) simulations and high pressure tensiometry.

In addressing formulation issues, another key consideration is the investment in and further development of new propellant-based formulations. Although HFA propellants are currently approved by the FDA for use in medical aerosols, and are non-ozone depleting, they are greenhouse gases with high global warming potential (GWP) [21]. Following similar trends that led to the replacement of chlorofluorocarbons with HFAs, the HFAs are also expected to be phased out once such medical aerosols can be formulated with more environmentally acceptable propellants. Hydrofluoro-olefins have emerged as the non-ozone depleting and low GWP alternatives to HFAs. With $\text{GWP} < 150$, HFOs satisfy (and have been approved by) European regulatory agencies mandating that all new model vehicles should use refrigerants with such GWP starting 2011 [22]. This criteria makes HFA's phase out in the automobile refrigerant market a

must. Based on historic grounds, such transition will also condition the transition in propellants used in other applications including medical aerosols, and HFO are the natural choice [23, 24].

We thus focus our *ab initio* and MD results and tensiometry studies on these novel propellants. We also employ molecular dynamics (MD) simulations as a tool for the design of surfactants for the stabilization of aqueous dispersions in HFOs in the form of microemulsions, which represents a potential strategy for the formulation of dendrimers in pMDIs.

1.3. Challenges in designing nanocarriers for the delivery of therapeutics to and through the lungs.

Once the therapeutic has reached the lung tissue; i.e., issues related to drug formulation have been addressed, there are several barriers it needs to overcome before reaching its site of action. For therapeutics that are aimed at the lung tissue (local delivery), enzymatic degradation, the presence of the mucus layer and mucociliary clearance in the airways, and macrophages and lung surfactants in the alveolar tissue represent important extracellular barriers. Meanwhile, the cellular membrane and endocytic vesicles are some of the potential intracellular barriers [25, 26]. For systemic delivery of drugs through the lungs, the lung epithelium will also represent significant barrier for the transport into the systemic circulation. Once in the systemic circulation, the ability to reach the target tissue, cell population within that tissue, and desired intracellular organelle represent other major challenges – which are similar to those seen for therapeutics delivered via oral delivery (once in systemic circulation) and i.v. [27].

There are many therapeutics of relevance for local or systemic pulmonary delivery. These include small molecules, peptides, proteins, and nucleotides [27-29]. There are many ongoing clinical trials studying the formulation of therapeutics in OI formulation for systemic delivery, suggesting the promise of this non-invasive route [30]. Silencing RNA (siRNA) has emerged as

a therapeutic with great promise in the treatment of a number of diseases, including cancer, COPD, asthma and others [31, 32]. Because siRNA can be easily degraded extracellularly (and intracellularly as well) [33], and has poor cellular internalization as it is large and negatively charged [34, 35], siRNA delivery agents can represent a strategy for improving its delivery and action [36]. An ideal delivery agent should protect siRNA from enzymatic degradation, facilitate cellular uptake and promote endosomal escape inside the cells, while possessing low toxicity. Polymeric nanocarriers (PNCs) have great potential to improve pulmonary delivery of nucleic acids. PNCs can be used to condensate, encapsulate, or conjugate nucleic acids into nano-sized particles that can be efficiently internalized by cells [37, 38]. PNCs can function to protect nucleic acids from degradation, promote sustainable release, help overcome extra- and intra-cellular barriers and offer versatility in terms of cellular internalization and targeting through conjugation of various ligands in order to improve delivery efficiency of therapeutics to and through the lungs [37, 39-41].

Dendrimers are particularly relevant nanocarriers. They are branched 3D structures, highly monodispersed, and contain a large number of functional end groups [42, 43] that can be used to conjugate with ligands to promote extracellular transport, to provide sustained release and also extra- and intracellular targeting capabilities. Poly(amido amine) (PAMAM) dendrimers are one of the most studied dendrimer nanocarriers (DNCs) [44-46]. PAMAM DNCs with NH_2 terminal groups are cationic polymers that can be used to complex siRNA, and have been shown to enhance gene knockdown of target tissues upon i.v. administration [45, 47-49].

In this work we first studied the microstructures of functionalized PEGylated NH_2 -terminated PAMAM DNCs, and their ability to condense and controllably release siRNA to lung epithelial cells. We use atomistic MD simulations to determine the microstructure of the ligand-modified

nanocarrier and their complexation to siRNA. Following the observation that PEG can interact quite favorably with NH₂-terminated PAMAM dendrimer, we expand the study further to see the interaction between PEG and PAMAM dendrimers with different terminal functional group.

1.4. Goals and approaches.

The strategy proposed to achieve our goals is schematically represented in Figure 1, and discussed in the following *two goals*:

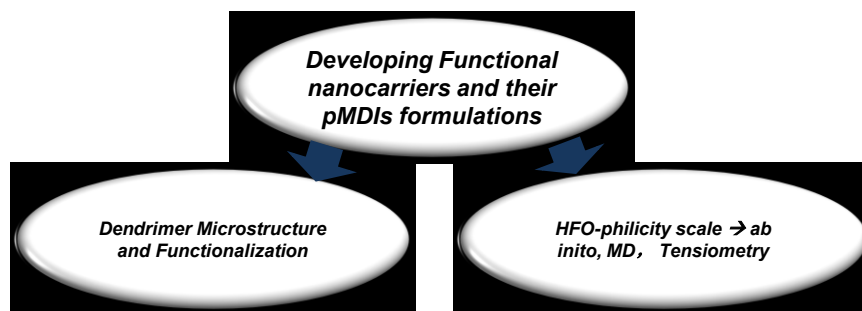


Figure 1 Schematic diagram of our goals for the design of nanocarriers and formulations for pulmonary drug delivery.

Goal #1: Design Biocompatible Moieties for the Steric Stabilization of Suspension Formulations in HFO-based Propellants.

HFA/HFO-philic moieties are required in order to impart stability to dispersions in HFO propellants [50], and are thus central to the development of novel HFA/HFO-based pMDI formulations for the delivery of drugs in general and nanocarriers – of particular interest in this work. In order to systematically address the issue of HFA/HFO philicity, we took a combined experimental and computational approach. Our strategy can be divided in three steps. **i)** search for tail chemistries that can be well solvated by HFA/HFO. Here we use *ab initio* calculations to investigate the interaction between HFA/HFO and three tail chemistries: alkane, ether and ester. The HFO-philicity scale was determined. The HFO propellant of choice was HFO-1234ze; **ii)**

with an HFO-philicity scale at hand, we studied the interface between HFO|H₂O in the presence of various non-ionic surfactants containing those HFO-philic tails groups. **iii)** The surfactant balance (minimum tension) was optimized. With the surfactant of choice – EO-PO, we altered the head to tail ratio and studied its effect on interfacial tension of HFO|H₂O interface, and the results from MD and high pressure tensiometry were compared to validate. This is the first step in the development of a feasible dispersion-based system for the delivery of water-soluble or water-dispersible therapeutics, as for example dendrimer-conjugated drugs, using HFO-based pMDIs.

Goal #2: Design PAMAM Functional Dendrimer Nanocarriers for the Delivery of Therapeutics to and through the Lungs.

Polymeric nanocarriers such as PAMAM DNCs can be employed to overcome the extra- and intracellular barriers discussed earlier for the delivery of therapeutics locally to the lungs or systemically through the lungs. Understanding the microstructure of such nanocarriers is the key for their design in drug delivery applications. The microstructure has an impact starting at the first design steps which is related to the ability to chemically functionalize the polymer with therapeutics, imaging agents and ligands; i.e., the chemistry with the DNCs will depend on the localization / availability of the functional end groups – are the end groups exposed to solvent environment or buried (hard to modify). The microstructure of the ligand-modified nanocarrier is also of great relevance, as the conformation of these ligands, which will depend on the interaction with the aqueous environment and the dendrimer itself, will dictate its interaction with the physiological environment, and thus its extra-cellular transport, its tissue and cellular targeting ability, release rate, etc. It can also impact the degree of complexation with siRNA, and thus its ability to improve gene knock down efficiency. Our approach to design DNCs for drug delivery applications to the lungs can be divided into 2 steps: **i)** Atomistic MD simulation studies of the

microstructure of ligand-modified PAMAM dendrimers. We studied the effect of the dendrimer size or generation (G), and of poly(ethylene glycol) (PEG) grafts – size and density, on their microstructure. These studies are relevant to a variety of drug delivery applications to the lungs, as PEG can be used to enhance transport across the mucus barrier, protect therapeutic cargo, as linkers to functional targeting groups (at the end of PEG) and others. The focus of this work is on how PEG can affect the complexation with siRNA. **ii)** Following the observation that O from PEG interact strongly with NH_2 terminal group of PAMAM, we expand the study further to see how PEG interact with PAMAM dendrimers with different terminal groups, and how the different interactions will affect the conformation of PEG and microstructures of PAMAM dendrimer. The interactions between PEG and different charged functional groups will have broad implication in different drug delivery systems as PEG is such a widely used ligand in drug nanocarriers.

1.5. Background relevance to this study

1.5.1. Lung Diseases

Lung Diseases, not including lung cancer, cause an estimated 225,000 deaths in the US yearly [51]. Lung cancer is a leading cause of cancer death in both man and women, with 226,000 new cases in 2012 [52]. COPD, a term used to describe chronic lung diseases that cause limitation in airflow, is the fourth cause of death in the US, and is estimated to become the third cause of death worldwide by 2030 [53]. The development of new technologies for the efficient delivery of therapeutics to treat lung diseases is, therefore, of great relevance today, and even greater significance in the future, as risk factors associated with many lung diseases, such as air pollution [54], represent an ever increasing health challenge in both developed economies and in the developing world alike.

1.5.2. Pressurized Metered-dose Inhalers (pMDIs)

Pressurized Metered-dose Inhalers (pMDIs) consist of a canister (pressure vessel) lodged upside down in a support, a metering valve, and an actuator, as schematically depicted in Figure 2.

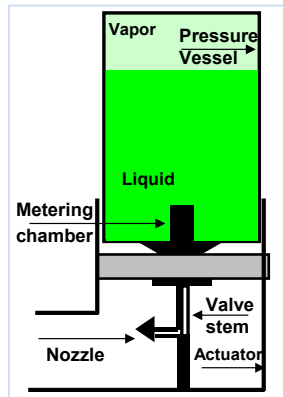


Figure 2. Schematic diagram of main components of pMDI.

pMDIs contain a drug in solution or in suspension in compressed liquid propellant, which is in equilibrium with its vapor. Because most drugs of interest, including small molecular weight or biomacromolecules, polar or hydrophobic, all have extremely low solubility in the semifluorinated propellants used in medical aerosols [55], solution formulations will require the use of large quantities of a co-solvent (ethanol), which negatively impacts both the chemical stability of the formulation and the quality of the resulting aerosol [55-59]. Dispersions (suspensions) are thus common for pMDIs formulation.

1.5.3. Challenges of Formulating Active Ingredients in pMDIs.

Challenges of Formulating Active Ingredients in pMDIs. While solution formulations in pMDIs can in general only be prepared with the help of co-solvents, the alternative strategy, which involves the dispersions of drug crystals, is also a challenge due to strong cohesive forces between the drug particles that lead to the agglomeration / coagulation, and thus decrease in aerosol quality [60, 61]. A natural strategy to overcome instability in low dielectric solvents such as halocarbon

propellants is to stabilize the dispersions with the help of amphiphilic species via steric barriers. However, surfactants approved by the FDA for use as dispersing agents in pMDIs today were developed during the time that CFCs was in use, which has a significantly lower μ and ϵ than halocarbons – Table1, and thus are no good stabilizers for existing pMDIs. Consequently, a systematic study leading to the design of moieties that are well solvated by the propellants is of great relevance in the formulation of dispersions in pMDIs.

1.5.4. Semi-fluorinated alkanes (HFAs) and olefins (HFOs)

Semi-fluorinated alkanes (HFAs) and olefins (HFOs) are employed in a variety of industrial applications, including as energy efficient refrigerants for heating, in ventilation and air conditioning (HVAC) systems [24, 62-64], in mobile air-conditioning systems [63-65], as blowing agents [64, 66, 67], in fire extinguishers [67, 68], as solvents [64, 69], foam forming agents [64, 70], and in medical aerosols [71], including topical[72, 73] and nasal sprays[74, 75], and pMDIs [55, 76, 77]. The design of chemistries highly compatible with the low dielectric (**Table 1**) semifluorinated propellants used in these industries is key to enable traditional and advanced propellant-based technologies. For example, in order to achieve high efficiency in HVAC systems, deposits of lubricants on the walls of heat exchange coils need to be prevented. This can only be achieved by either using highly soluble oils or dispersing such oils in the refrigerants/propellants. In the case of medical sprays, the formulation of active ingredients may require either aqueous or solid dispersions in the propellants.[55, 76] Dispersing agents with moieties that strongly interact with the propellant can be employed in the development of these and other suspensions of commercial/industrial interest.

1.5.5. HFOs

HFOs represent the fourth generation propellants/refrigerants [78, 79]. Different from CFCs, they have zero ozone depleting potential (ODP) - **Table 1**. Because of the presence of a chemically active double bond, which reacts with hydroxyl radicals in the atmosphere, HFOs have reduced lifetime and low GWP – **Table 1**. They represent, therefore, a significant advancement compared to HFAs. There are two major HFO propellants being produced in large scale: 1,3,3,3-tetrafluoropropene (HFO-1234ze) and 2,3,3,3-tetrafluoropropene (HFO-1234yf) [80, 81]. HFOs are classified as non-polar (hydrophobic), but they have a significant dipole moment (μ) and dielectric constant (ϵ). At the same time, the presence of the larger F atoms in the molecule decreases dispersive interactions with hydrophobic compounds (lipophobic). These molecules have, therefore, a simultaneous dual hydrophobic and lipophobic character, which causes significant challenges in the development of pharmaceutical formulations as discussed earlier. It is also important to note that a comparison between HFO-1234ze and HFA-134a – one of the propellants currently approved by the FDA for use in medical sprays, it has been shown that HFOs have similar toxicity profiles compared to HFAs [66, 82], thus paving the way for the consideration of HFOs in medical propellants [83].

Table 1 Physical properties of semi-fluorinated alkanes (HFAs) and olefins (HFOs), and of chlorofluorocarbons (CFCs)

	$P^{sat*}(bar)$	$\rho_l^*(g\cdot ml^{-1})$	$\mu(D)$	ϵ	ODP	GWP
<i>CFC 11 (CCl₃F) [84-89]</i>	0.87	1.49	0.46	2.3	HIGH	HIGH
<i>CFC 12 (CF₂Cl₂) [84-89]</i>	5.60	1.33	0.51	2.1	HIGH	8100

<i>CFC 114 (CF₂Cl₂) [84-89]</i>	1.81	1.47	0.50	2.3	HIGH	HIGH
<i>HFA 134a (CF₃CH₂F)[90]</i>	5.72	1.23	2.06	9.5	None	1430
<i>HFA 227 (CF₃CFHCF₃)[91]</i>	3.90	1.42	0.93	4.1	None	3200
<i>HFO-1234ze (CH(F)=CHCF₃)[92, 93]</i>	4.81 [@]	1.12	1.44	/	None	6
<i>HFO-1234yf (CH₂=CFCF₃)[93, 94]</i>	5.96 ^{&}	1.09	2.54	/	None	4

ρ = density; μ = dipole moment; ε = dielectric constant; ODP = ozone depleting potential; GWP = global warming potential, relative to that of CO₂. * at 20°C; @ at 25°C; & at 21.1°C

1.5.6. Potential of functional nanocarriers for pulmonary drug delivery

There are many barriers for the therapeutic molecules to reach their site of action. In OI formulations, the first challenge is to reach the lung tissue. The optimum aerodynamic diameter of the aerosol particles for deep lung deposition is between 0.5-5.0 μ m. Once drug particles are successfully deposited into lungs, they face extracellular barriers that may be a healthy or diseased mucus (in case the target is the airways) or macrophages and lung surfactants (in case the target is the alveolar cells) – note that macrophages may be the target themselves [95]. The therapeutic molecules will also have to transverse the plasma membrane. Once inside the cell, the drug has to be carried across several other barriers in order to reach desired target and exert their therapeutic effect. For siRNA, its site of action is in the cytosol. Therefore, after internalized, they need to escape the endolysosomal compartments. If the therapeutic is intended for systemic delivery, it also has the lung epithelium as extracellular barrier even before it reaches the systemic circulation. Functional nanocarriers may serve in all steps of the way to improve delivery efficiency. In the case of siRNA as the therapeutic molecule, PEGylation of NH₂ terminated PAMAM DNCs may help decrease the interaction with the mucus layer and/or macrophage uptake [96]. It can also decrease interaction between nanoparticles that may lead to aggregation. PEGylation may also

help to modulate the interactions between siRNA and the dendrimers, and thus to modulate the rate of release, and how pH (such as the low pH in endolysosomes) affect the release.

1.5.7. Nanocarriers for siRNA Delivery to the Lungs

Nanocarriers for siRNA Delivery to the Lungs. Gene therapy is a broad term that involves any approach to treat diseases using intracellular transfer of nucleic acids (DNA or RNA) to modulate cellular functions by activation or inhibiting induction of specific genes [97-99]. Gene down-regulation is a critical research area in life science, and it can be achieved either at transcriptional level or at the post-transcriptional level [100-103]. Small interfering RNA (siRNA) and antisense oligodeoxynucleotides (ODN) are two effectors acting on the post-transcriptional level small nucleic acids [104, 105]. Cancers are very good candidates for siRNA based treatment for several reasons. Abnormal gene pattern is usually observed in cancer cells, thus gene down-regulation strategy can be either used to mute gene expression of mutated genes or to down-regulate genes that controls proliferation [106-109]. There are many nanocarriers for delivery of siRNA being evaluated for their efficiency and toxicity [110-114]. Different poly-cations can electrostatically complex with siRNA (negatively charged), including chitosan, PEI, PLL, PAMAM and others [39, 40, 115-117]. Block copolymers can be used to prepare micelles as siRNA nanocarriers [118]. siRNA can also be conjugated directly to PEG and other polymers via chemical bonds [119]. Nanoparticles made of biocompatible polymers like chitosan or PLGA can be used to incorporate siRNA [110, 120]. The ability to evaluate the capabilities of such nanocarriers with respect to their protection against siRNA degradation, delivery efficiency, functions in specific targeting or controlled release and toxicity are relevant to the design of the nanocarrier, and will be carried out in this work.

1.5.8. PAMAM Dendrimer Nanocarriers (DNCs)

PAMAM Dendrimer Nanocarriers (DNCs) are very promising in a wide range of biomedical applications including gene and drug delivery and as imaging agents due to their unique structure, which is characterized by high size uniformity, low polydispersity and a large number of modifiable surface functional groups. There are several strategies for drugs to be loaded onto PAMAM dendrimers, including complexation, which is driven by electrostatic interactions, conjugation through the formation of covalent bonds, and encapsulation, which is driven by hydrophobic forces. The cationic nature of NH_2 -terminated PAMAM dendrimers enables their complexation with siRNA. The multivalent surface functional groups in DNCs can be engineered to covalently conjugate drugs and/or ligands to the carriers as well.

1.5.9. PEG as Ligand for PAMAM dendrimers

PEG as Ligand for PAMAM dendrimers. Drug-dendrimer conjugates/complexes are usually further modified by the conjugation of ligands in order to confer the carriers specific characteristics designed to enhance their efficacy as a drug delivery agents. Among the many choices of ligands, PEG is widely used to modify the surface of PAMAM dendrimers. PEG can be used to provide extra protection to the payload, to modulate the transport across extracellular barriers and reduce the cytotoxicity of cationic PAMAM dendrimers by neutralizing and/or shielding surface charges, and also to improve system circulation, and to provide a mechanism to controlled the release of the therapeutic cargo [121-126].

1.5.10. Ab initio calculations

Ab initio calculations (Figure 3) was employed to determine the HFO-philicity of candidate chemistries [127]. The pair interaction (binding) energy between the propellant and tail fragment (E_b^{st}) was computed using the supramolecular approach [128]:

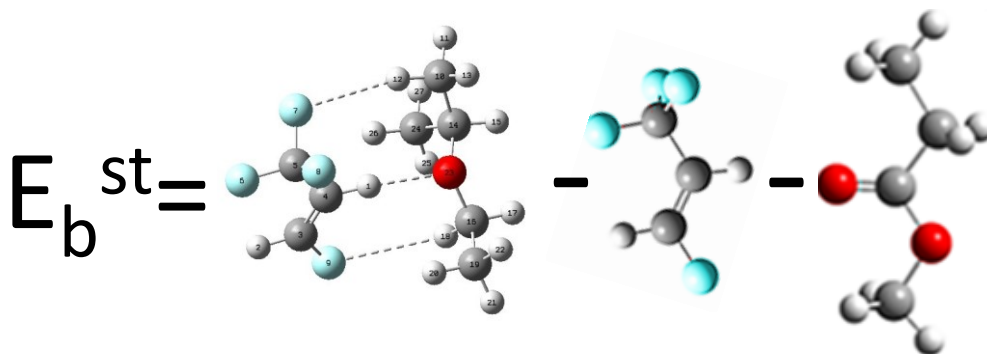


Figure 3 Schematic diagram of the calculation of the non-bonded interaction energy E_b^{st} between HFO and tail fragment.

$$E_b^{st} = E^{st} - E^s - E^t \quad \text{Equation 1}$$

where E_b^{st} is the binding energy between the propellant and tail fragment, E^{st} is the total energy of the pair, E^s and E^t are the energies of isolated propellant and tail fragment, respectively. The more negative E_b^{st} , the more favorable the interaction between the pair, and thus the better the solvation of that HFO-phile. As the tail chemistry is varied, and HFO-philicity scale can be then constructed.

1.5.11. MD of the HFO|Water Interface

MD of the HFO|Water Interface. MD can be used to gain microscopic insight into interfacial systems such as that of the HFO|Water (HFO|W) interface, and that of the surfactant-modified HFO|W interface. It can also be used to quantitatively assess the tension reduction upon surfactant adsorption at the interface, and thus be used to guide the design of amphiphiles that can be employed to form stable water-in-HFO dispersions, which may be potentially employed in the formulation and delivery of dendrimer nanocarriers to the lung tissue.

1.6. Innovation and relevance

This work is relevant for the design of functional dendrimer nanocarriers and their pMDI formulation for the local and systemic delivery of therapeutics, including small drugs and nucleic

acids *to and through the lungs*. Given the advancement of nanocarrier technologies in drug delivery, there is great promise in using nanocarriers for pulmonary delivery. The challenges come from 1) formulating nanocarriers in a form of high efficiency and efficacy, 2) designing nanocarriers that is tailored to overcome barriers / challenges encountered in pulmonary environment. Thus we focus our efforts on 1) design biocompatible moieties for the steric stabilization of suspension pMDI formulations, and 2) design functional PAMAM dendrimer nanocarriers for the delivery of therapeutics to and through the lungs.

1.6.1. Aim #1

For Aim #1. In the design for suitable moieties for pMDI formulation, we started by 1) screening the fluorocarbon philicity of candidate tail chemistry, then 2) with the philicity scale at hand, we further our studied the propellant|H₂O interface in the presence of various non-ionic surfactants containing those HFO-philic tail groups, and 3) the surfactant balance was optimized (minimum tension) with selected surfactants.

This work is innovative as it represents the first study that the properties of the bare and surfactant modified HFO-1234ze|H₂O interface has been reported – either experimental or computational results. All prior studies published on HFOs were related to their thermophysical and toxicological properties [129, 130]. A basic understanding about interfacial/solvation behavior in HFOs is *relevant* as it will allow us to expand the applicability of medical aerosols for the delivery of therapeutics to and through the lungs. These results will also be of *relevance* to many other industries that currently employ/are preparing for switch to HFO refrigerant/propellants.

1.6.2. Aim# 2

For Aim# 2. This work is *innovative* in many ways. It represents the first work where the effect of PEG size and grafting density on the microstructures of solvated PAMAM DNCs is investigated with atomic resolution. This systematic computational study of PEGylated NH₂-terminated PAMAM dendrimers is *relevant* as it will help us understand how conformational changes, charge shielding/neutralization, and solvation forces may impact the microstructure of the nanocarrier, and thus its function under conditions relevant to the physiological environment. Moreover, we extend our study to include PAMAM dendrimers of different terminal chemistry, and the effect of PAMAM dendrimer chemistry on microstructures of PEG chains that are conjugated to them. The conclusions are not only meaningful for PAMAM dendrimers as nanocarriers, but also broadly applicable to other polymeric nanocarriers where PEGylation is used. This work is also *innovative* as there has been no systematic study on the effect of PEG length and graft density on the PAMAM dendrimer-siRNA complexation. The methodology used here can be broadly applicable to other field of study where microscopic structures is of interest yet hard to approach from experimental tools.

CHAPTER 2

UNDERSTANDING IN THE LOW GLOBAL WARMING HYDROFLUOROOLEFIN HFO-1234ZE PROPELLANT

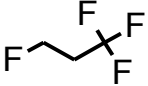
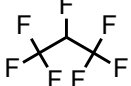
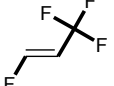
2.1. Introduction

Halocarbons find applications as refrigerants, foam-forming agents, blowing agents, solvents and are also of great relevance in medical aerosols.[131-134] There are two major considerations in choosing a working fluid as refrigerant/propellant: (i) the physicochemical properties that determine their performance, and (ii) their environmental impact that can be quantified by attributes such as their ozone depleting effect (ODE) and global warming potential (GWP). A major shift in propellant/refrigerant working fluids started in the late 80's when a mandate was put in place requiring the replacement of chlorofluorocarbons (CFCs) by hydrofluoroalkanes (HFAs).[135, 136] The switch was motivated by the highly negative environmental impact of CFCs, especially due to their high ODE. HFAs were acceptable candidates because they are non-ozone depleting, and their physicochemical properties were somewhat compatible with those of CFCs.[137, 138]

Past forward ca. 20 years, and there are still major challenges to be overcome in using HFAs as working fluids, especially in the pharmaceutical industry. These challenges can be to a large extent attributed to the unique solvation properties of HFAs.[139, 140] Another major working fluid switch is happening now, and is being largely driven by the EU regulations on fluorinated gases that were put forth in 2011. The mandate by the European regulatory agencies dictates that all new model vehicles should use refrigerants with $GWP < 150$. [140] This criterion makes HFAs' phase out in the automobile refrigerant market a must, due to the HFAs large GWP – relevant

properties of selected halocarbons are shown in **Table 2**. [141] Since then, car companies in the USA and Japan have also announced the switch to low GWP working fluids. Based on historic grounds, the shift in refrigerant is expected to drive the industry to seek for alternative propellants/solvents for the all the other major markets as well. [142, 143]

Table 2 Some relevant physicochemical properties of the fourth generation propellant HFO-1234ze compared to the hydrofluoroalkanes HFA-134a and HFA227.

properties reported @ 20°C and 1atm *Liquid properties measured at saturation pressure	HFA-134a 	HFA-227 	HFO-1234ze 
Molecular weight (g/mol)	102	170	114
Liquid density (g/mL)^{*bc}	1.21	1.46	1.12
Heat of vaporization (kJ/kg) @ NBP^{*a}	217.0	131.4	197.4
Surface tension (mN/m)^{*a}	8.11	10.24	8.55
Dipole moment (Debye)^{*bc}	2.058	0.94	1.443
Boiling point (°C)^{bc}	-26	-16	-19
Global warming potential (GWP)^{bc}	1430	3220	6
Solubility of water in propellant (ppm)^{bc}	1300	610	225
Solubility of propellant in water (ppm)^{bc}	193	58	373

^aHigashi et al. [144]

^bSolvay [145]

^cHoneywell [146]

*NBP = normal boiling point

Within this context, hydrofluoroolefins (HFOs) have emerged as the fourth generation propellants. HFOs have no ODE and very low GWP. [147] HFO-1234ze (1,1,1,3,3-tetrafluoropropene), one of the HFO candidates, has been shown to be non-flammable, [148] to have low toxicity - similar to that of HFAs, [145, 149, 150] and to possess physicochemical properties similar to HFAs. On one hand, these characteristics are expected to somewhat facilitate the transition process from HFAs to HFOs. However, in spite of all the potential benefits of this new generation of environmentally acceptable working fluids (HFOs), the transition process is still expected to bring tremendous challenges to the industry, just as it has happened during the

transition from CFCs to HFAs, as the industry will have to adapt the various processes to these new working fluids.[151-153]

One major issue to be expected is the solubility and solvation of additives that are used in all the above-mentioned industries. For example, in order to achieve high efficiency in HVAC systems, deposits of lubricants on the walls of heat exchange coils need to be prevented. This can be achieved by either using highly soluble oils or dispersing the oils in the refrigerants.[154] In the case of medical sprays, the formulation of active ingredients may require either aqueous or solid dispersions in the propellants.[155, 156] Dispersing agents with moieties that strongly interact with the propellant can be employed in the development of these and other suspensions of commercial/industrial interest. A key aspect in transition to the new propellants is thus the development of a fundamental understanding on the solvation behavior in HFO propellants. HFOs are interesting fluids as they have a dual hydrophobic and oleophobic character. The presence of bulky *F* atoms is expected to decrease their interaction with hydrophobic moieties thus imparting their oleophobic character. At the same time, they have non-negligible but small dipole moment. They can be thus also considered hydrophobic – refer to their very low mutual with water shown in **Table 2**. While there has been several studies in the literature discussing the physicochemical properties of HFOs,[144, 157-160] there is currently no work on their solvation capacity.

In light of the challenges and opportunities discussed above, our overall goal is to develop an understanding of the solvation forces in HFO propellants. A more specific goal, and the objective of this work, was to develop a scale of solvation in a selected HFO - HFO-1234ze. We investigate the solvation of relevant tail fragments that are (i) representative of the chemistries of the additives of interest to the various industries discussed above, and (ii) yet that have functionalities that are selected in a way to systematically probe the effect of both polarity and structure (degree of

branching) of the tail fragments on their solvation by HFOs. We employ *ab initio* calculations to determine the pair interaction (binding) energy between the HFO-1234ze and the tail fragments, and use that information to develop the scale of solvation in HFOs. We also determine the solvation of the same fragments in the HFA propellants most widely used in the industry (HFA-134a and HFA-227) to compare and contrast with the next generation HFO propellant HFO-1234ze.

2.2. Computational details

2.2.1. Pair interaction (binding) energy of propellant-tail fragment (E_b^{st})

Binding energies of the propellant-tail fragment (E_b^{st}) were computed using the supermolecule approach:[161]

$$E_b^{st} = E^{st} - E^s - E^t \quad \text{Equation 2}$$

where E_b^{st} is the binding energy of propellant (*solvent - s*) and tail fragment (*tail - t*), E^{st} is the total energy of the pair, and E^s and E^t are the energies of isolated propellant and tail fragments, respectively. More negative (bigger in magnitude) E_b^{st} 's indicate more favorable pair interactions, and thus enhanced HFO-philicity of the tail fragment.[162] Good solvation is a required attribute in the steric stabilization of colloidal dispersions in low dielectric solvents such as HFO propellants.[163] Calculations were carried out using Gaussian 09.[164] The structures were first optimized using second order Møller-Plesset perturbation theory (MP2) and 6-31g+(d,p) basis set. Single point energy calculations of the optimized structures were carried out at MP2 level of theory with the dunning basis set aug-cc-pVDZ.[165] Basis set superposition error (BSSE) was corrected by the counterpoise method of Boys and Bernadi.[166, 167] Partial charge distributions were calculated by fitting electrostatic potential using CHELPG subroutine of Gaussian 09.[168] Gas phase dipole moments were calculated at MP2/aug-cc-pVDZ with structures optimized at MP2/6-

31g+(d,p). A group of optimizations (no less than 4) were done for each solvent-tail or tail-tail pairs starting from different configurations to improve the chances of reaching a global minimum. An error of ± 0.42 kJ/mol is assumed based on the calculated difference in E_b 's for the CF_4 dimer calculated with the aug-cc-pVDZ basis set and the basis set limit at MP2 level of theory.[169]

2.2.2. Chemistry of propellants and tail fragments.

Setting up *ab initio* computational studies relevant to the behavior of polymer/oligomer systems representative of moieties required for the stabilization of colloidal dispersions in low dielectrics inevitably requires some tradeoffs between the level of detail in the model (size of the fragments) and the computational power available. Once we defined the chemistries of interest, we set the number of backbone atoms in the fragments to 5, which is the minimum number of atoms possible to accommodate all chemistries / represent all chemical features of interest, while the featuring functional group is represented once and only once. Fixing the number of atoms in the backbone to a common number of atoms also facilitates the comparison among tail fragments. It is worth mentioning, however, that by truncating the number of repeat units studied for each tail fragment, we are to some extent artificially (and inevitably) impacting the polarizability and dipole moment of the system, when compared to the full polymer chain,[170] and this is one of the necessary tradeoffs. We study three distinct chemistries, namely: alkanes, ethers and esters. Alkanes were chosen as negative control (we expect them not to interact well with the propellants). Ethers are relevant as they find many applications in the industry in the form of non-ionic surfactants (head-groups), and *EO* is present as an excipient in an FDA-approved portable inhalers (Symbicort HFA). Ester is a relevant chemistry given their biodegradable nature and wide use in medical and drug delivery applications.[171, 172] For each chemistry of interest, we also investigate fragments that have one or more pendant methyl groups (branching) attached to the backbone, as a potential

strategy to impact the self (fragment-fragment) interaction. Tail-tail self-interactions are also of great relevance in the stabilization of colloidal systems in low dielectric media such as the propellants discussed here – the lower the self tail-tail interaction, the more capable the tail is to help avoid colloidal aggregation.[173] The chemistries investigated in this work were: (i) alkanes: pentane (**C5**) - $(CH_3(CH_2)_3CH_3)$ and isohexane (**ISO**) $(CH_3CH(CH_3)CH_2CH_2CH_3)$, (ii) ethers: ethylene oxide (**EO**) - $(CH_3CH_2OCH_2CH_3)$ and propyleneoxide (**PO**) - $(CH_3CH(CH_3)OCH_2CH_3)$, and (iii) esters: glycolide (**GA**) $(CH_3CH_2C(O)OCH_3)$, lactide (**LA**) $(CH_3CH(CH_3)C(O)OCH_3)$, and tetramethyl-glycolide (**TMGA**) $(CH_3C(CH_3)_2C(O)OCH_3)$. Note that *ISO* has a pendant CH_3 group compared to *C5*, the same for *PO* (represent the hydrophobic group of many non-ionic surfactants) when compared to *EO*. In the case of the esters, we were able to further study the effect of branching, with the addition of one pendant CH_3 on going from *GA* to *LA*, and two CH_3 pendant groups on going from *GA* to *TMGA* based on practical availability of these chemical entities.

2.2.3. Enhancement Factor (E_{enh}) incorporates tail-tail self-interaction binding energies (E_b^{tt})

Another important component in understanding the ability of tail chemistries to provide stability to colloidal dispersions in HFOs besides solvent-tail interactions accounted for in the E_b^{ts} , is the fragment-fragment self-interaction.[173] It is important to maximize the solvent-fragment interaction, and at the same time minimize the tail-tail self-interactions. In order to account for both factors in our screening of tail chemistries with potential in the stabilization of colloidal dispersions in HFOs, we define the E_{enh} , which is the ratio between the binding energy between propellant and tail fragment (E_b^{st}) to that of tail fragments' self-interaction (E_b^{tt}) [173]:

$$E_{enh} = \frac{E_b^{st}}{E_b^{tt}} \quad \text{Equation 3}$$

2.2.4. Cluster studies: (HFO-1234ze)_n-Tail Fragment.

In order to gain more insight into the microscopic interactions between the propellant and fragment that will happen in a bulk-like environment, we also included in our investigations cluster studies in which one tail fragment is allowed to interact with multiple propellant molecules that closely resemble the first solvation shell of the fragment: (HFO-1234ze) $_n$ -tail fragment, where $n=6$. However, because such cluster systems include a large number of heavy atoms, calculations needed to be conducted at a lower level of theory and basis set - HF-6-31g(d). Because of the complexity of the energy surface in such systems and the relatively low level of theory and basis set, we limit our analysis to the cluster studies to understanding the accessibility of the local dipoles of the fragments by the propellant molecules. We focus our study on three tail chemistries - *EO*, *GA* and *TMGA* to understand the effect of both fragment polarity and branching on their interactions with the new generation propellant HFO-1234ze, as it is central to our work.

2.3. Results and Discussions

In this work we systematically investigate the effect of the chemistry and structure of tail fragments on their solvation by the hydrofluoroolefin HFO-1234ze using *ab initio* calculations. We also perform calculations with the hydrofluoroalkanes HFA-134a and HFA-227, which are the most common propellants currently being used by the industry. The binding energy (E_b^{st}), strong interaction sites of optimized pairs, and atomic charge distributions before and after interacting in a dimer system, together with other quantitative and qualitative results help us to quantify the philicity of fragment candidates of relevance to the various industries where such semi-fluorinated propellants are employed. The comparison/contrast between solvation in HFOs and HFAs can also help us understand and anticipate the challenges and opportunities that lie ahead in the expected transition from HFAs to HFOs, the next generation working fluids.

2.3.1. Tail chemistry and its effect on the binding energy (E_b^{st})

A summary of the E_b^{st} between all tail chemistries and the three propellants investigated in this work are presented in **Table 3**. Dipole moments of the propellants and tail fragments are from *ab initio* calculations and are shown in parentheses, next to the corresponding molecules.

Table 3 Summary of the binding energies (E_b) between the different propellants (*solvent = s*) and tail fragments (*tail = t*) - E_b^{st} (kJ/mol), calculated at the MP2/aug-cc-pVDZ//MP2/6-31g+(d,p) level of theory and basis set, with BSSE corrected by the counterpoise method. The dipole moments (in Debye, D) for the propellants and tail fragments are shown in parenthesis. Tail fragments are: pentane (*C5*), iso-pentane (*ISO*), ethylene oxide (*EO*), propylene oxide (*PO*), glycolic acid (*GA*), lactic acid (*LA*), and tetramethyl glycolic acid (*TMGA*). The dipole moment was calculated in this work using partial charges from *ab initio* calculations. The error in E_b^{st} is estimated to be ± 0.42 kJ/mol.

Tail fragment	E_b^{st} (kJ·mol ⁻¹)		
	HFA-134a (2.12)	HFA-227 (1.46)	HFO-1234ze (1.14)
C5 (0.09)	-6.8	-10.3	-8.4
ISO (0.15)	-6.3*	-10.0*	-9.1
EO (1.30)	-18.8*	-25.1*	-19.5
PO (1.23)	-19.2*	-26.4*	-19.0
GA (1.65)	-20.0	-24.1	-19.2
LA (1.69)	-19.7	-24.2	-18.9
TMGA (1.76)	-20.5	-25.3	-20.3

*Results by Pegiun *et al.* at the same basis set and level of theory.[31]

2.3.2. Effect of Tail Polarity

In order to isolate the effect of single parameters, the effect of the polarity of the tail fragments on E_b^{st} is investigated first. The results for those selected fragments are summarized in **Figure 4**, for all propellants investigated.

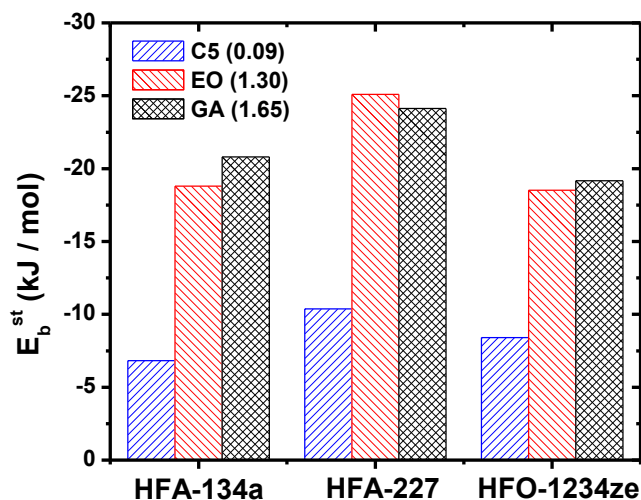


Figure 4 Effect of tail polarity on the binding energy between the different propellants (*solvent* = *s*) and tail fragments (*tail* = *t*) - E_b^{st} (kJ/mol), calculated at the MP2/aug-cc-pVDZ//MP2/6-31g+(d,p) level of theory and basis set, with BSSE corrected by the counterpoise method. Tail fragments are: pentane (*C5*), ethylene oxide (*EO*) and glycolic acid (*GA*), which are representatives of the alkane, ether and ester chemistries, respectively. The dipole moments (in Debye, *D*) for the tail fragments are shown in parenthesis. The dipole moment was calculated in this work using partial charges from *ab initio* calculations.

These three fragments, *C5*, *EO* and *GA*, are linear (do not have pendant methyl groups), and are representative of alkanes, ethers and esters, respectively. From **Figure 4**, it can be observed that the magnitude of the binding energy for all propellants dramatically increases as the fragment polarity increases on going from *C5* (0.09D) to *EO* (1.30D). This is in agreement with solubility data measurements in HFAs.[174] Dispersibility studies have also shown that alkane-based surfactant tail groups are poor stabilizers, whereas *EO*-moieties can be successfully employed to stabilize particle dispersions in propellant HFAs.[174, 175]

However, upon further increasing the polarity of the fragment upon the addition of a carbonyl oxygen besides the ether oxygen (compare *EO* with 1.30D and *GA* with 1.65D), no large gain in solvation is achieved, or the binding energy can even decrease in magnitude, as is the case for HFA-227. This can be attributed to the fact that the overall E_b^{st} is also impacted by two other

contributions, one being the polarity of the propellant and the other the overall dispersive interactions of the pair. HFA-227 shows the strongest solvation (E_b^{st}) of all propellants, even though its dipole moment is much smaller than that of HFA-134a, clearly demonstrating the impact of the dispersive energy of the system. HFA-227 has more heavy atoms (10 heavy atoms) than HFA-134a (6 heavy atoms) and HFO-1234ze (7 heavy atoms). These results are in agreement with our experimental observations that show that microparticles in general can be better dispersed in HFA-227 compared to HFA134a.

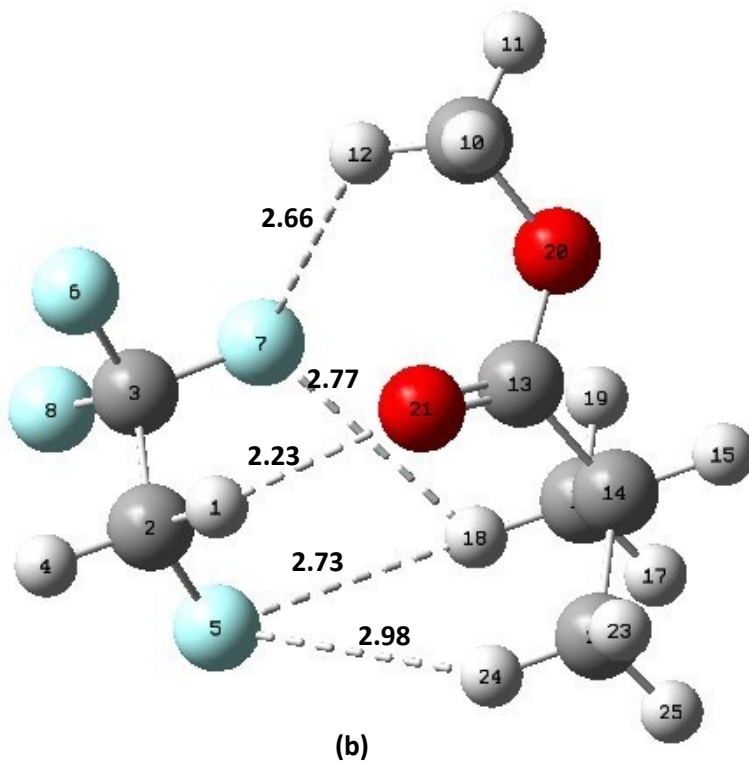
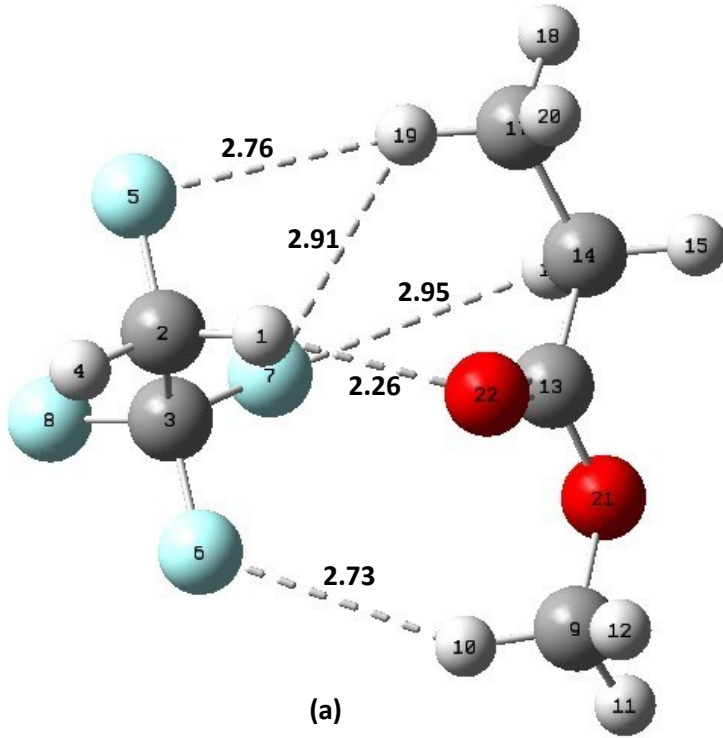
We can also observe from **Figure 4** that the magnitude of E_b^{st} for HFO-1234ze is similar to that of HFA-134a for the more polar fragments. This happens in spite of the lower dipole moment of HFO-1234ze (1.14D) compared to HFA-134a (2.12D). This behavior is attributed to a balancing/stronger dispersive interaction between HFO-1234ze and the fragments compared to those of HFA-134a, due to the greater number of heavy atoms in HFO-1234ze. This observation is supported by the larger E_b^{st} between HFO-1234ze and the non-polar fragment *C5*, when compared to that between HFA-134a and *C5*. The similar solvating behavior of HFO-1234ze and HFA134a propellants can be seen as a good indicator for the industry that depends on that solvent strength, such as in foam forming and topical foams. It suggests that HFO-1234ze may be a good alternative propellant in technologies that currently employ HFA-134a.

It is also worth noting that while differences in interaction energies (E_b^{st}) between two propellants towards a fragment may be small in term of KJ/mol – e.g. the difference in interaction energy between HFA-134a and HFA-1234ze towards *GA* is only 0.8 KJ/mol, these differences are expected to be amplified in experimental systems dealing with polymers made of many fragments, and many solvent-fragment interactions.

2.3.3. Optimized structure and strong interactions

As observed above, a general trend in solvation of the tail fragments by the propellants does not emerge based simply on the polarity of the tail fragments. To fully understand the nature of the propellant-tail fragment interactions it is necessary to look in more detail into the optimized geometries of these pairs to find microscopic evidence behind their E_b^{st} . Besides the dispersive interactions expected in these “non-polar” solvents/propellants, we do expect dipole interactions to arise due to the small but non-negligible dipole of the propellant molecules, and likely further polarization of the propellant upon interaction with the polar fragments. Here we single out those fluorine··hydrogen (F··H) and oxygen··hydrogen (O··H) non-bonded interactions with separation distance 3 Å or shorter, as they are expected to be the dominating contributors to E_b^{st} . [156, 175]

Optimized structures of the HFO-1234ze-, HFA-134a-, and HFA-227-tail fragments pairs are shown in **Figure 5**, **6**, and **7**, respectively. Strong interaction sites that have an O··H or F··H distance within 3Å are labeled with dashed lines in the optimized structures. These strong interaction sites are summarized in **Table 4**. As our control, pentane (C5) and ISO have no O··H strong interaction bonds, and the influence of this effect is clearly shown by the magnitude of their binding energies with propellants (see **Table 3**).



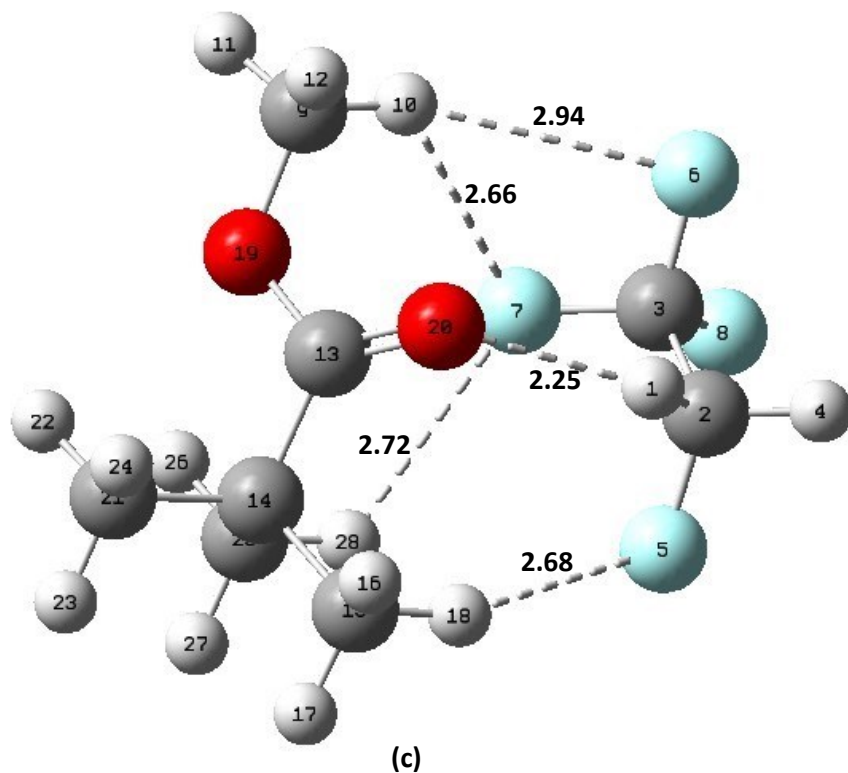
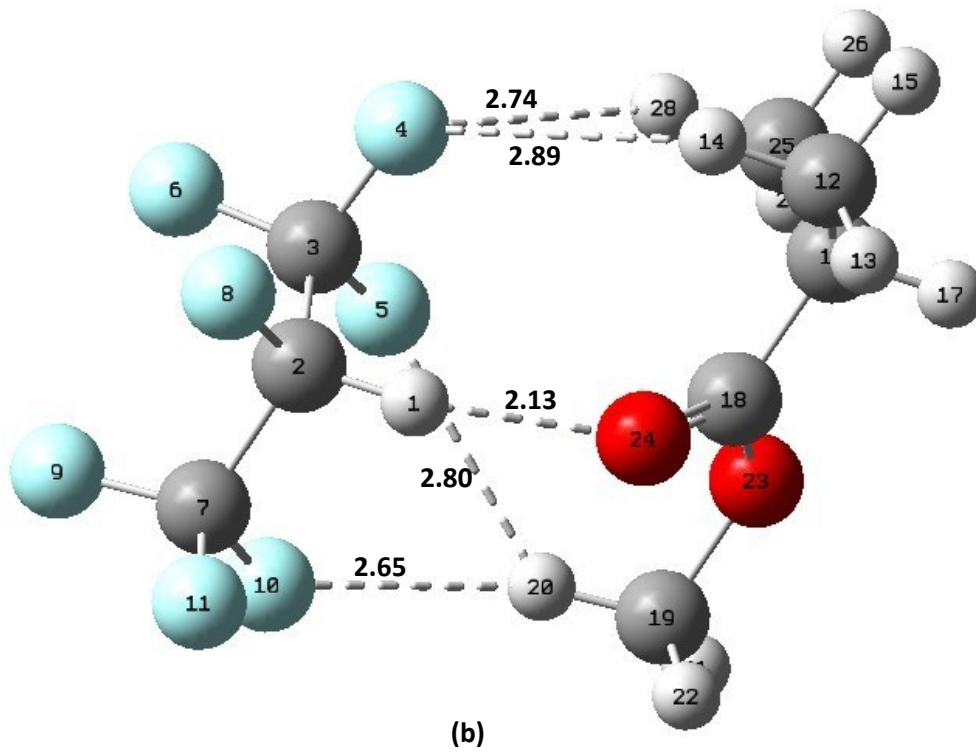
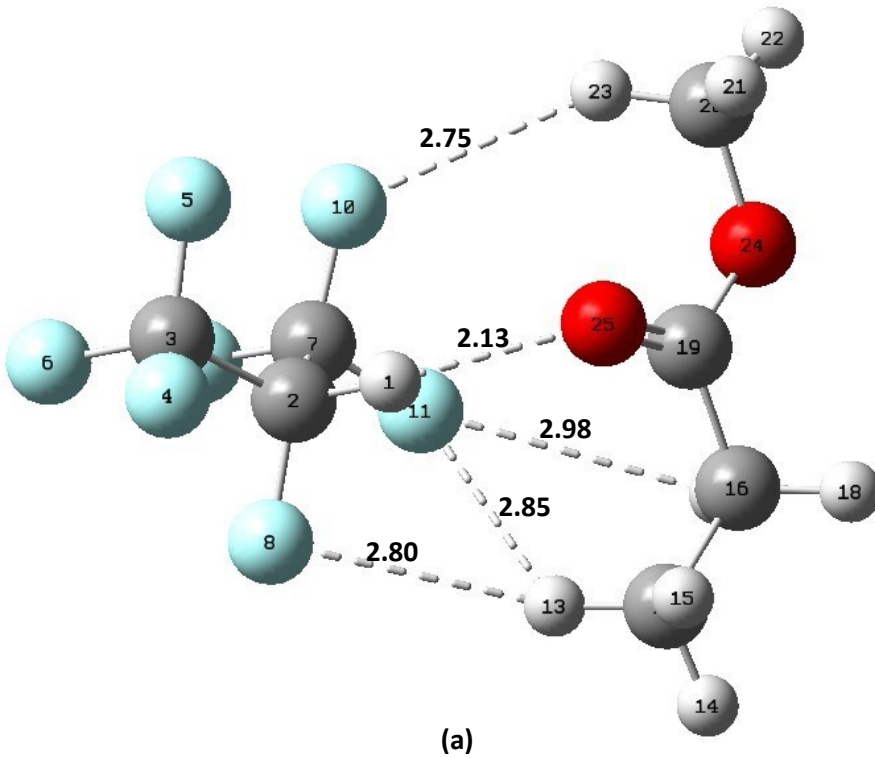


Figure 5 Structure of optimized HFA-134a and the ester-based pairs: (a) HFA-134a-GA; (b) HFA-134a-LA; and (c) HFA-134a-TMGA. Tail fragments are: glycolic acid (*GA*), lactic acid (*LA*), and tetramethyl glycolic acid (*TMGA*). All geometries shown were optimized at the MP2/6-31g+(d,p) level of theory and basis set. “Strong interactions” are labeled if O··H or F··H distances are within 3 Å. Distances are labeled next to each strong interaction, in Å.



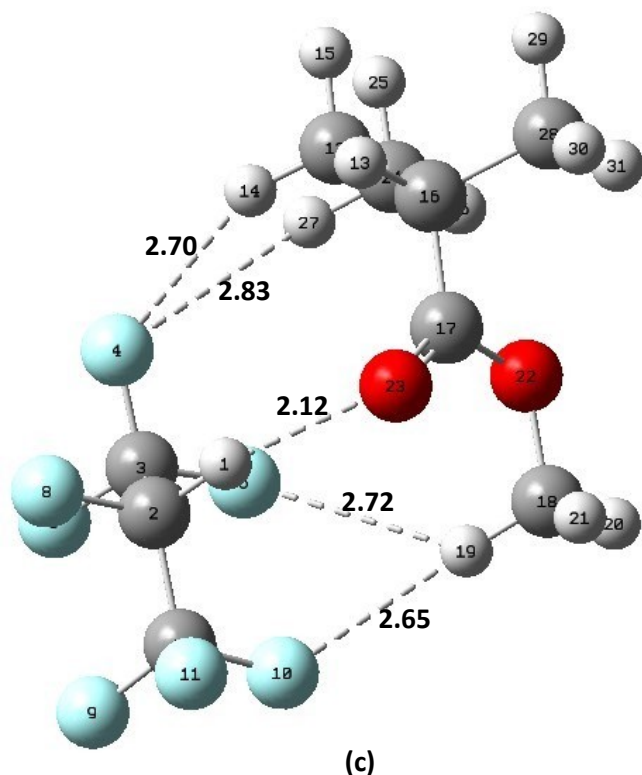
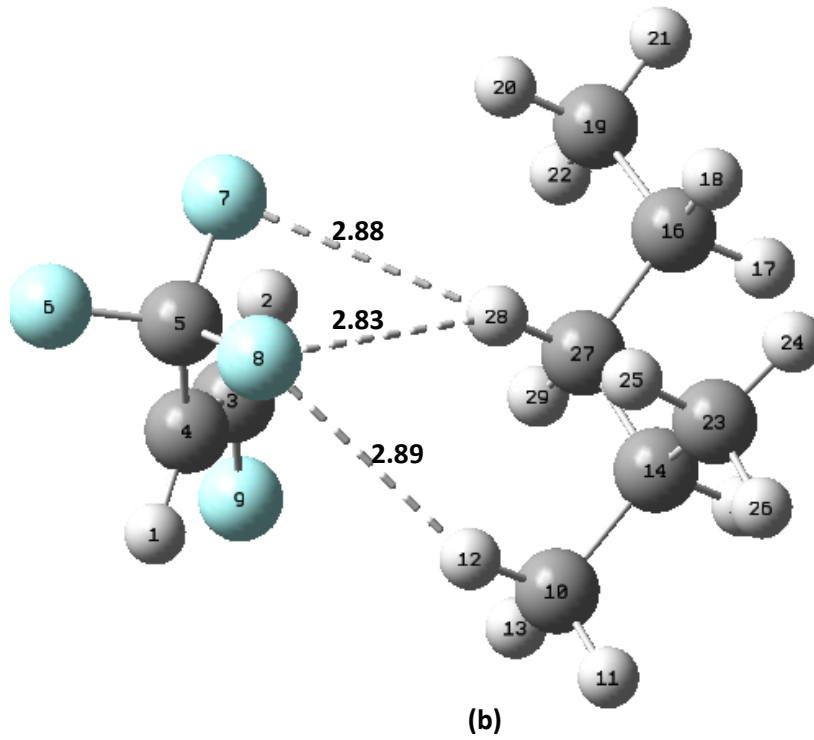
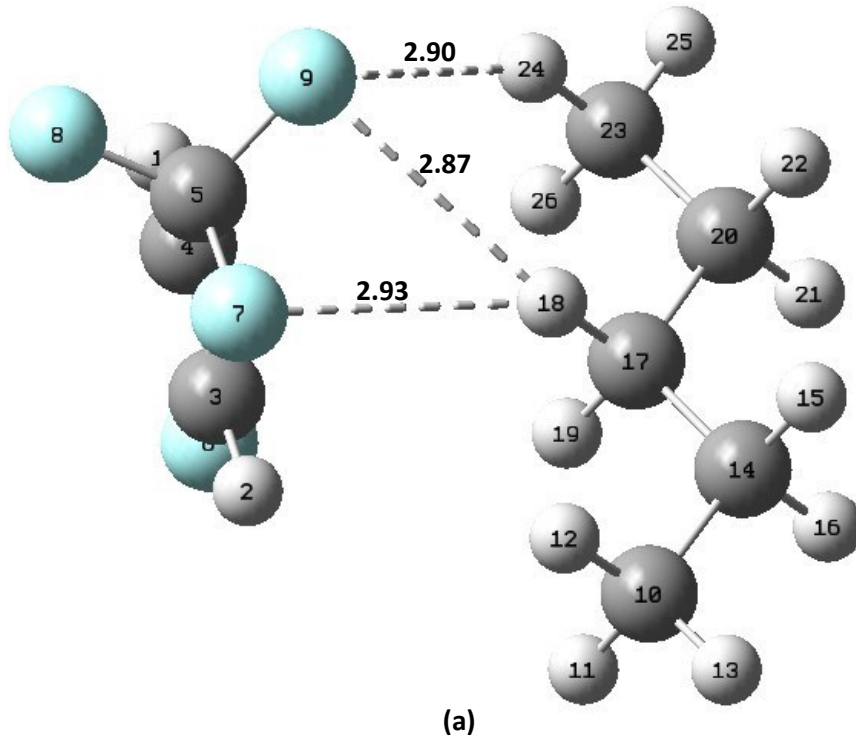
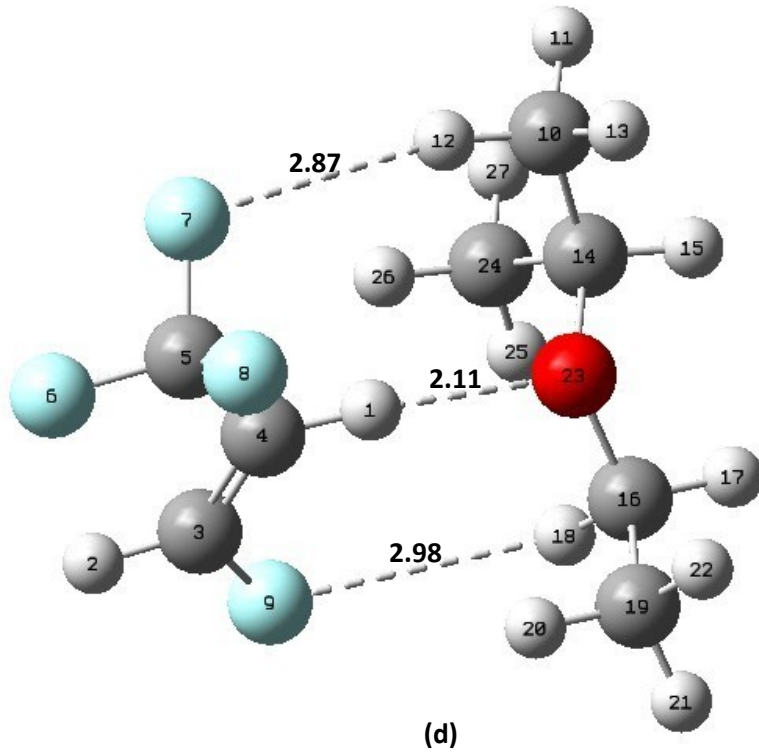
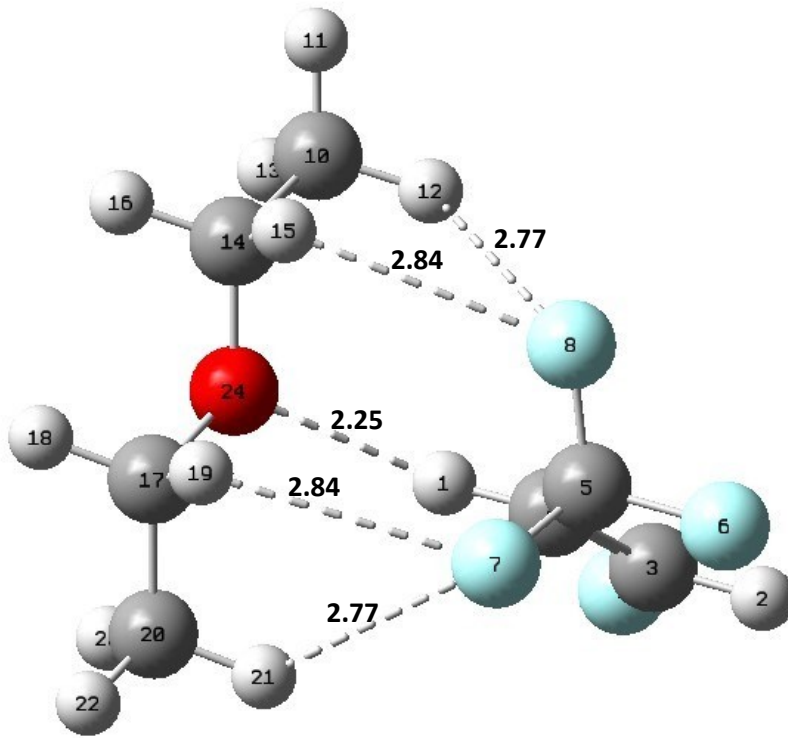
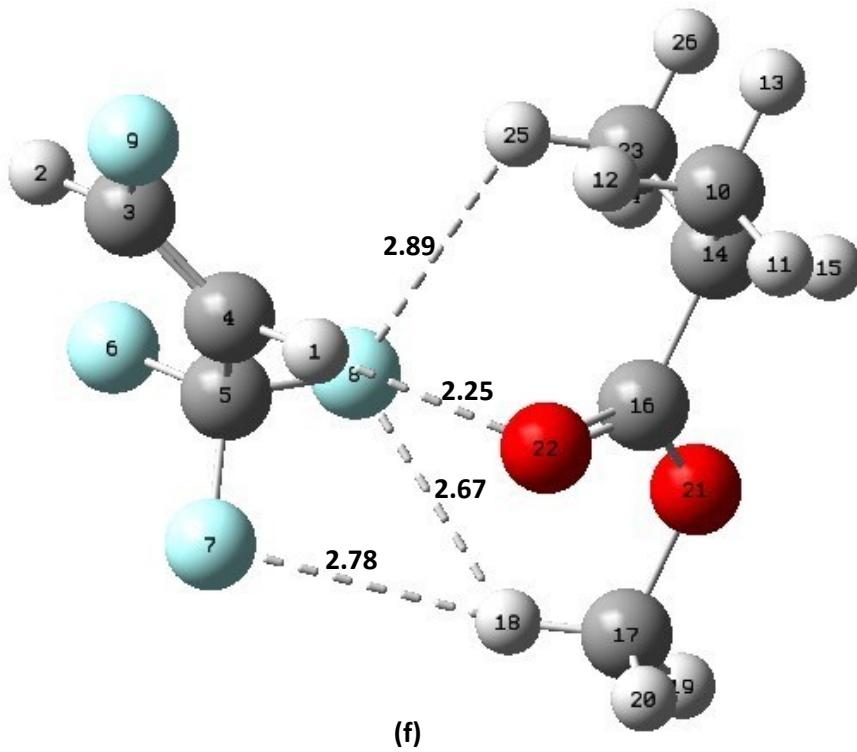
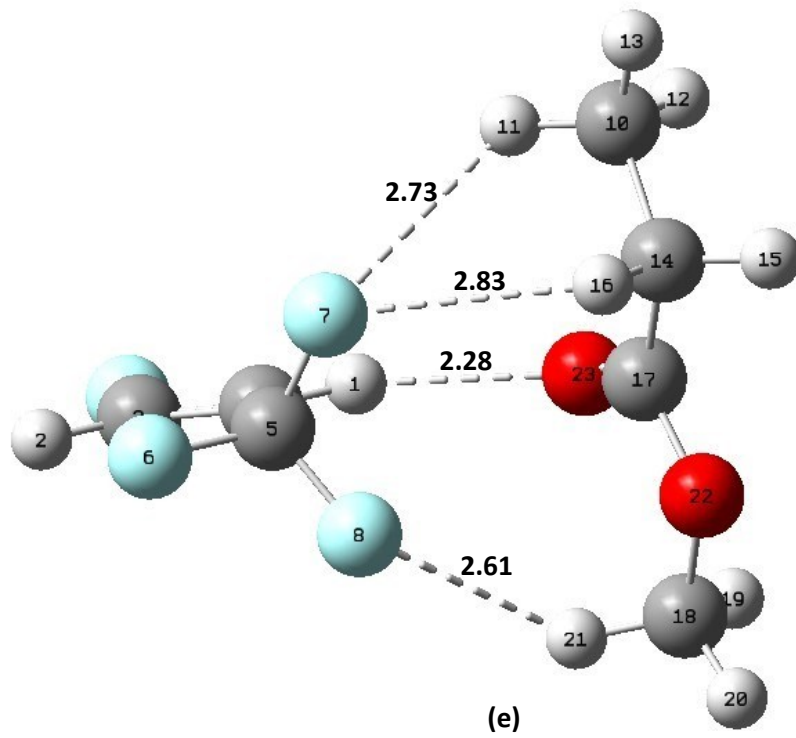


Figure 6 Structure of optimized HFA-227 and the ester-based pairs: (a) HFA-227-*GA*; (b) HFA-227-*LA*; and (c) HFA-227-*TMGA*. Tail fragments are: glycolic acid (*GA*), lactic acid (*LA*), and tetramethyl glycolic acid (*TMGA*). All geometries shown were optimized at the MP2/6-31g+(d,p) level of theory and basis set. “Strong interactions” are labeled if O··H or F··H distances are within 3 Å. Distances are labeled next to each strong interaction, in Å.







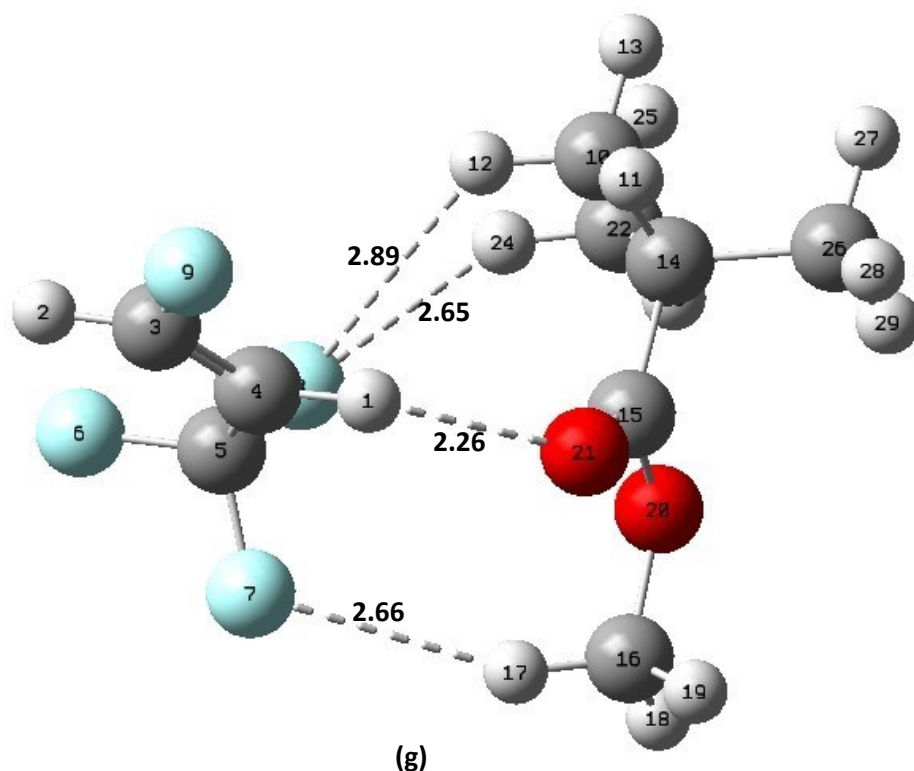


Figure 7 Structure of optimized pairs of (a) HFO-1234ze-C5, (b) HFO-1234ze-ISO, (c) HFO-1234ze-EO, (d) HFO-1234ze-PO, (e) HFO-1234ze-GA, (f) HFO-1234ze-LA, (g) HFO-1234ze-TMGA. Tail fragments are: pentane (C5), iso-hexane (ISO), ethylene oxide (EO), propylene oxide (PO), glycolic acid (GA), lactic acid (LA), and tetramethyl glycolic acid (TMGA). All geometries shown were optimized at the MP2/6-31g+(d,p) level of theory and basis set. “Strong interaction” is defined as those between O··H, and with a separation distance < 3Å.[31] Distances are labeled next to each strong interactions, in Å.

Table 4 Summary of “strong interactions” between the propellants and the different tail fragments - pentane (C5), iso-pentane (ISO), ethylene oxide (EO), propylene oxide (PO), glycolic acid (GA), lactic acid (LA), and tetramethyl glycolic acid (TMGA). Refer to **Figure 5, 6, and 7** for atom number identification. “Strong interaction” is defined as those between O··H or F··H, and with a separation distance < 3Å.[31] Partial charge of H₁ (hydrogen atom involved in strong O··H interactions) are shown in brackets.

HFA-134a		“Bond” length (Å)					
Bonds	C5	ISO*	EO*	PO*	GA	LA	TMGA
C-H ₁ ··O			2.21 (+0.046e)	2.21 (+0.055e)	2.26 (+0.103e)	2.23 (+0.089e)	2.25 (+0.095e)
C-H··F ₅	2.96 2.83	2.70 2.87 2.92	2.72		2.76	2.73 2.98	2.68
C-H··F ₇	2.78 2.90	2.71		2.68 2.82	2.95 2.91	2.66 2.77	2.66 2.72
C-H··F ₆		2.72	2.74	2.75	2.73		2.94
HFA-227		“Bond” length (Å)					
Bonds	C5	ISO*	EO*	PO*	GA	LA	TMGA
C-H ₁ ··O			2.04 (+0.118e)	2.06 (+0.130e)	2.13 (+0.180e)	2.13 (+0.160e)	2.12 (+0.176e)
C-H··F ₁₁	2.86 2.93		2.82	2.86 2.87	2.85 2.98		
C-H··F ₁₀				2.84	2.75	2.65	2.65
C-H··F ₅		2.89	2.82	2.81		2.8	2.72
C-H··F ₄	2.94 2.86					2.89 2.74	2.70 2.83
C-H··F ₈				2.81	2.8		
HFO-1234ze		“Bond” length (Å)					
Bonds	C5	ISO	EO	PO	GA	LA	TMGA
C-H ₁ ··O			2.25 (+0.188e)	2.11 (+0.279e)	2.28 (+0.213e)	2.25 (+0.222e)	2.26 (+0.230e)
C-H··F ₇	2.93	2.88	2.84 2.77	2.87	2.83 2.73	2.78	2.66
C-H··F ₈			2.84 2.77		2.61	2.67 2.89	2.65 2.89
C-H··F ₉	2.87 2.90	2.83 2.89		2.98			

*Reported by Penguin et al.[31]

It is proposed that oxygen atoms are crucial because they can provide strong interaction ($O \cdots H$) sites as they are solvated by the propellant molecules.[169, 173] Here we confirm this observation and also note that oxygen atoms can form strong interactions with sites in the HFO-1234ze propellant, in a similar fashion as to HFAs. We can also see from **Figure 5, 6, and 7** (and summary in **Table 4**) that although ester group has two oxygen atoms, only one oxygen atom is capable of forming strong interactions with the propellants given the conformational restrictions. Because ester and ether groups have the same number of strong interactions (involving oxygen atoms) with the propellants, the ester chemistry has no significant difference in E_b^{st} compared to the ether group, in spite of having more oxygen atoms and higher dipole.

It is also interesting to observe that whenever the ester moiety is interacting with propellant molecules, they always form strong $O \cdots H$ bond with carbonyl oxygen ($C=O$) instead of ether oxygen ($C-O-C$) (both within the ester functional group). This preference in interaction comes in part from the fact that the carbonyl oxygen ($C=O$) is geometrically more favorably oriented to interact with hydrogen atoms of the propellants. This is clearly shown in any one of the **Figures 5, 6 or 7**. The preference is also attributed to the more negative charge of the carbonyl oxygen compared to the ether oxygen, a fact that will be discussed below.

2.3.4. Effect of Tail Branching

The optimized structures of the tail-solvent fragments can also help us understand the effect of branching (methylation) on the solvation of the tail fragments. Branching is a strategy that may be employed to reduce fragment-fragment interactions as will be discussed in more detail below, and as a consequence, to improve the ability of such fragments to provide steric stabilization to particles and other dispersions in low dielectric propellants.[174] However, branching may also

adversely (negatively) affect the solvation of the fragments by the propellants, which would be undesirable, and is thus investigated here.

We have selected the following groups for our study of the effect of tail branching: *GA*, *LA*, *TMGA*. These fragments all contain ester-based groups, and differ only in the degree of branching. While *GA* has no pendant group, *LA* has one pendant *CH3* group and *TMGA* has two pendant *CH3* groups. Because these three chemicals all share the same functional group, we can isolate the effect of branching. The summary of the E_b^{st} between the various propellants and those tail fragments is shown in **Figure 8**:

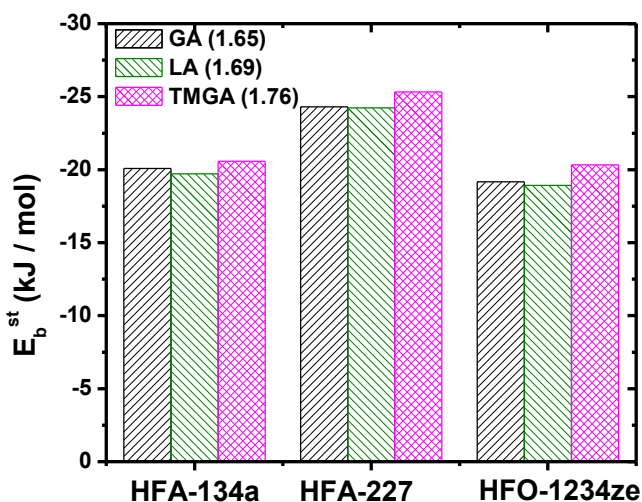


Figure 8 Effect of the degree of branching (number of *CH3* pendant groups) on the binding energy between the different propellants (*solvent* = *s*) and the ester-based tail fragments (*tail* = *t*) - E_b^{st} (kJ/mol), calculated at the MP2/aug-cc-pVDZ//MP2/6-31g+(d,p) level of theory and basis set, with BSSE corrected by the counterpoise method. Ester-based tail fragments are: glycolic acid (*GA*), lactic acid (*LA*), and tetramethyl glycolic acid (*TMGA*). The dipole moments (in Debye, *D*) for the tail fragments are shown in parenthesis. The dipole moment was calculated in this work using partial charges from *ab initio* calculations.

The results from **Figure 5** indicate that, to a large extent, branching does not affect the E_b^{st} between propellant and the fragments. The results also show that the performance of HFO-1234ze in terms of solvation is similar to HFA-134a, while HFA-227 has stronger solvation power than

both. Because of the stronger dipole of HFA-134a, the distance of the dominant C-H₁··O bond is shorter than that for HFO-1234ze (**Table 4**), and thus the slightly larger E_b^{st} 's (**Figure 8 and Table 3**). The overall number of F··H bonds in HFA-134a is also greater than that for HFO-1234ze, but this effect is less clear cut as the distances of those bonds are smaller on average for HFO-1234ze.

2.3.5. Electrostatic Potential and Strong Interaction Sites

Besides the dipole moments of the molecules, local dipoles (involving two atoms with large charge separation such as C=O or C-F) will also contribute to the magnitude of the pair interaction energies (E_b^{st}). The electrostatic potential (ESP) charge distribution of the propellant and tail fragment dimers are also examined here to better understand the differences between different solvation behaviors of propellants between ethers and esters as well as the nature of strong interaction sites. The ESP charge distribution was obtained at MP2/aug-cc-pVDZ level of theory using CHELPG, and is shown in *Supplementary Material*, in **Tables S1, S2, and S3**. The ESP is determined for the propellants and fragments alone and then again for the optimized pair, so that the effect of polarization is also captured – and it is indicated as the change in the atomic partial charge before (alone) and after the optimization of the solvent-fragment pair = Δ in **Tables S1, S2 and S3**. The bond distance and partial charges for *H* participating in the strong C-H··O bonds between propellants and fragments are summarized in **Table 4**.

It is believed that it is the acidity of the C-H group, and to a less extent the basicity of the oxygen that is expected to dictate the strength of the H-bonds.[176, 177] Since we have C-H₁··O strong interactions that are similar to the typical H-bonds, we focus our attention on the partial charge assumed by H₁'s of the propellants, as they interact with the oxygen of the various fragments. From **Table 4** we can see that in HFO-1234ze-tail fragment pairs, the H_1 's involved in strong interaction sites are more positive than those for HFA-134a and HFA-227-tail fragment

pairs, thus helping to enhance the E_b^{st} . The most positive H_I in HFO-1234ze can be attributed to the C=C bond, which increases the level to which electrons delocalize. The positive H_I hydrogen atoms in HFO-1234ze help compensate for the longer C-H \cdots O bond distances compared to that found with the HFA-134a and HFA-227 propellants.

2.3.6. Tail-tail Self-interaction Binding Energy (E_b^{tt}) and Enhancement Factor (E_{enh})

In colloidal dispersion systems, as for example particle suspensions, when the external medium is a low dielectric, such as the propellants being discussed here, the usual dominant mechanism of stabilization is steric.[178] In that case, the dispersibility of those particles may be imparted by the presence of a polymer layer adsorbed or grafted to the particle. This layer needs to represent a thick enough barrier so as to keep the attractive interaction (distance) between the particles of the order of thermal energy - kT . In this way permanent aggregation may be avoided, and any weakly flocculated aggregates can be broken up by thermal energy alone.[179] In order to prevent coagulation, therefore, not only the solvation forces (E_b^{st}) need to be strong – a topic addressed in our earlier discussions, but the self-interaction between the polymer fragments (E_b^{tt}) need to be minimized, so as to achieve that thick solvation layer. In order to capture both effects, we employ here a quantity termed Enhancement Factor (E_{enh}), which is defined as the ratio between the solvent-tail interaction (binding) energy to tail-tail self-interaction (binding) energy; i.e., $E_{enh} = E_b^{st} / E_b^{tt}$. Based on this definition, the E_{enh} is expected to be a better predictor of the ability of a given polymer to be able to sterically stabilize a dispersion in the low dielectric propellant HFO and HFAs. Clearly, this definition misses a very important contribution in the steric stabilization process which is of entropic nature.[179] Nonetheless, E_{enh} is expected to be a better predictor of the fragment's ability to stabilize colloidal dispersions that E_b^{st} alone. In order to be able to calculate E_{enh} , we thus determine E_b^{tt} for the fragments discussed earlier. We separate our

discussion in terms of the effect of the chemistry of the fragments and their structure (branching), as done in the discussion related to the solvation forces.

2.3.7. Effect of Tail Polarity

For different chemistries, tail-tail self-interaction energies are expected to depend to a large extent on their polarity. This general trend is confirmed in our results, as shown in **Figure 9**.

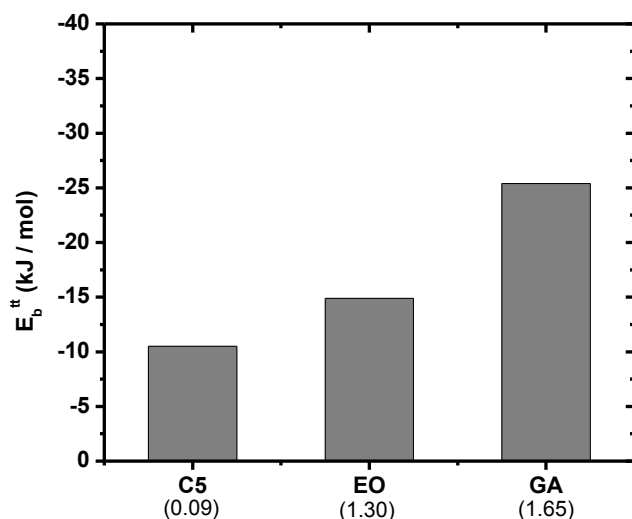


Figure 9 Effect of tail chemistry on the self-interaction binding energies of the different tail fragments (E_b^{tt}) (kJ/mol), calculated at the MP2/aug-cc-pVDZ//MP2/6-31g+(d,p) level of theory and basis set, with BSSE corrected by the counterpoise method. Tail fragments are: pentane (*C5*), ethylene oxide (*EO*) and glycolic acid (*GA*), which are representatives of the alkane, ether and ester chemistries, respectively. The dipole moments (in Debye, *D*) for the fragments are shown in parenthesis. The dipole moment was calculated in this work using partial charges from *ab initio* calculations.

The order of magnitude of E_b^{tt} is: *GA* (1.65*D*) > *EO* (1.30*D*) > *C5* (0.09*D*), which correlates well with their dipole moments. Self-interaction will magnify the importance of C-H··O strong interactions. From **Figure 10** we can see that *C5-C5* pair has (obviously) no C-H··O interactions, while the *EO-EO* pair has 3 and the *GA-GA* pair has 6 C-H··O strong interactions. Because the carbonyl oxygen is geometrically more available and is more negatively charged than the esters', the self-interaction energy of *GA* is significantly larger than that of *EO*.

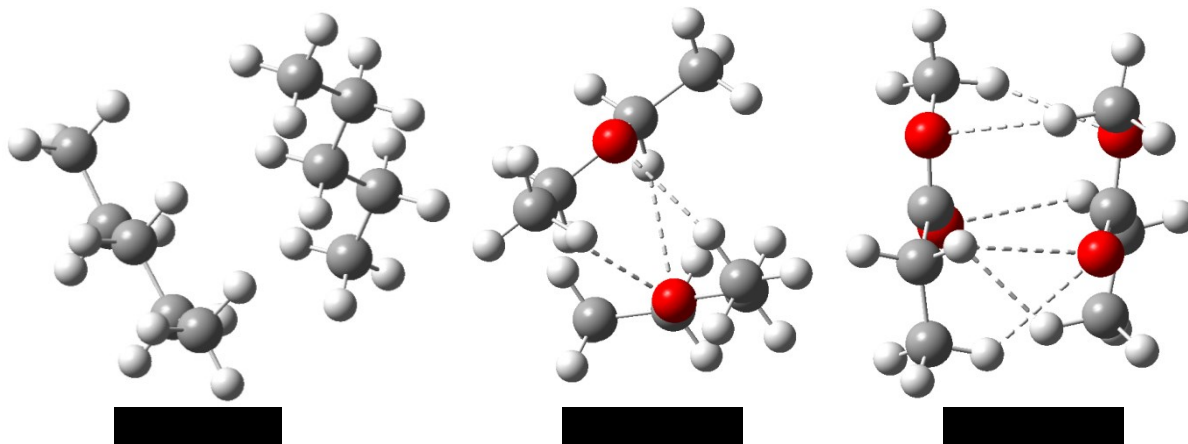


Figure 10 Optimized geometries of the self-interacting tail-tail fragments at the MP2/6-31g+(d,p) level of theory and basis set. Tail fragments are: pentane (C5), ethylene oxide (EO) and glycolic acid (GA), which are representatives of the alkane, ether and ester chemistries, respectively. Dashed lines and numbers in parenthesis represent the “strong interaction” sites and the number of “strong interactions”, respectively. “Strong interaction” is defined as those between $O \cdots H$, and with a separation distance $< 3 \text{ \AA}$. [31] Results are summarized in **Table 5**.

With the values for the tail-tail self interaction, the E_{enh} was determined, and the values are shown in **Figure 11**, and summarized (for all fragments) in **Table 5**.

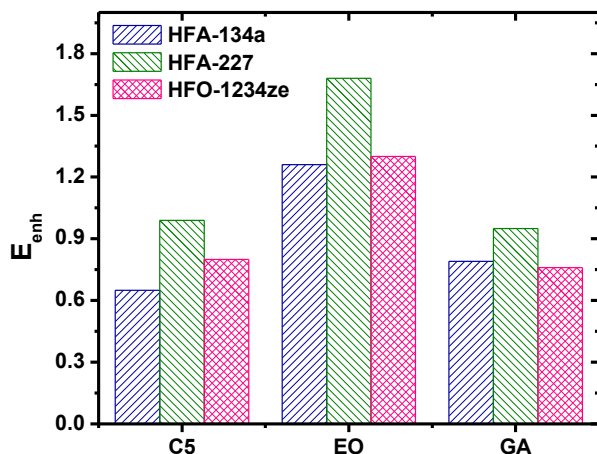


Figure 11 Effect of tail chemistry on their “Enhancement Factor” (E_{enh}). E_{enh} is defined as the ratio of the interaction energy between propellant ($solvent = s$) and tail fragment ($tail = t$) (E_b^{st})

over that of tail-tail self-interaction (E_b^{tt}): $E = E_b^{st} / E_b^{tt}$. A summary of E_{enh} for all chemistries and propellants is provided in **Table 5**.

Table 5 Summary of the “Enhancement Factors” (E_{enh}) for the different chemistries and propellants. E_{enh} is defined as the ratio of the interaction energy between propellant (*solvent* = *s*) and tail fragment (*tail* = *t*) (E_b^{st}) over that of tail-tail self-interaction (E_b^{tt}): $E_{enh} = E_b^{st} / E_b^{tt}$. All calculations at the MP2/aug-cc-pVDZ//MP2/6-31g+(d,p) level of theory and basis set, with BSSE corrected by counterpoise method. The dipole moments (in Debye, *D*) for the fragments and propellants are shown in parenthesis. The dipole moment was calculated in this work using partial charges from *ab initio* calculations. The values for E_{enh} above one are highlighted in the table.

<i>Tail fragments</i>	<i>Enhancement Factor (E_{enh})</i>		
	<i>HFA134a</i> (2.12)	<i>HFA227</i> (1.46)	<i>HFO1234ze</i> (1.14)
<i>C5 (0.09)</i>	0.58	0.99	0.80
<i>ISO (0.15)</i>	0.49	0.78	0.64
<i>EO (1.30)</i>	1.26	1.68	1.30
<i>PO (1.23)</i>	1.13	1.55	1.12
<i>GA (1.65)</i>	0.79	0.95	0.76
<i>LA (1.69)</i>	0.61	0.75	0.59
<i>TMGA (1.76)</i>	1.28	1.58	1.27

The results show that the largest E_{enh} , and the only above 1 ($E_b^{st} > E_b^{tt}$), is observed for the *EO* moiety. The E_{enh} thus serve to further discriminate the *EO* and *GA* tail solvation, which could not be singled out solely based on E_b^{st} , as they were similar for both moieties. Surprisingly, the magnitude of E_{enh} for *GA* is very similar to that of *C5*, our negative control. This value was not anticipated, given the strong interaction between the propellants and *GA*. However, the strong fragment-fragment interaction dominates the magnitude of E_{enh} for that system, so that $E_{enh} < 1$. It is also interesting to observe that this predictor of particle stability suggests that dispersions in HFO-1234ze may be expected to be of similar quality to those observed in HFA-134a - or better, as their E_{enh} is similar.

2.3.8. Effect of Tail Branching

Because the selected group of ether tail fragments have similar dipole moments - *GA* (1.65D), *LA* (1.69D) and *TMGA* (1.76D), it is particularly suitable to investigate the effect of tail branching on E_b^{tt} . The results are summarized in **Figure 12**.

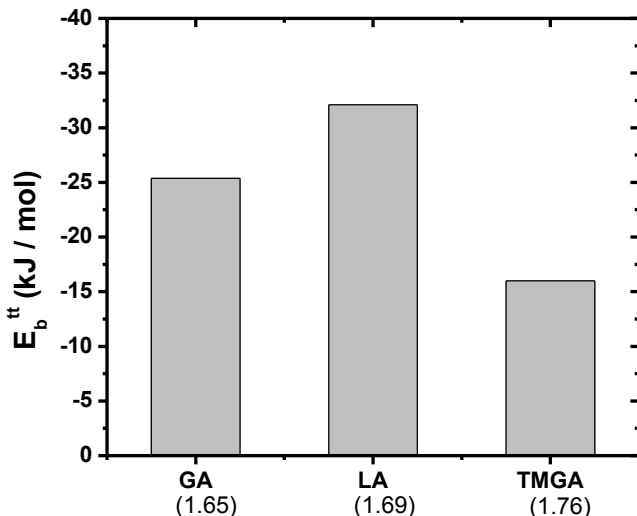


Figure 12 Effect of the degree of branching (*CH*3) on the self-interaction binding energies between the ester-based tail (*t*) fragments (E_b^{tt}) (kJ/mol) calculated at the MP2/aug-cc-pVDZ//MP2/6-31g+(d,p) level of theory and basis set, with BSSE corrected by the counterpoise method. Tail fragments are: glycolic acid (*GA*), lactic acid (*LA*), and tetramethyl glycolic acid (*TMGA*). The dipole moments (in Debye, *D*) for the fragments are shown in parenthesis. The dipole moment was calculated in this work using partial charges from ab initio calculations.

It is worth noticing in **Figure 12** is that the tail-tail interaction energy actually increases upon adding a methyl branching group, which may be unexpected at first. The results from **Table 5** indeed support the idea that the presence of the extra *CH*3 group in *LA* causes a decrease in the total number of strong interactions compared to *GA*, suggesting that the *CH*3 group indeed works as a steric barrier to tail-tail interaction.

Table 6 Summary of “strong interactions” between the tail-tail fragment pairs - glycolid acid (*GA*), lactic acid (*LA*), and tetramethyl glycolic acid (*TMGA*). “Strong interaction” is defined as those between O··H, and with a separation distance < 3Å.[31]

Bond	Length (Å)
GA+GA	
C=O··H	2.81
C=O··H	2.69
C=O··H	2.69
C=O··H	2.81
C-O··H	2.61
C-O··H	2.61
LA+LA	
C=O··H	2.65
C=O··H	2.54
C=O··H	2.80
C-O··H	2.58
TMGA+TMGA	
C=O··H	2.52
C=O··H	2.52
C-O··H	2.80
C-O··H	2.80

However, it can be seen that at the same time that the number of strong interactions decreases on going from *GA* to *LA*, the strength of the interactions increases (shorter bond distances). The tail-tail binding energy for *TMGA*, which represents an addition of two *CH3* groups compared to *GA* or one *CH3* compared to *LA*, is seen to decrease not only relative to *LA* but also to *GA* – **Figure 12**. The results suggest that the extra degree of branching is capable of providing enough steric hindrance to reduce the number and strength of the contacts enough to reduce tail-tail interaction – **Table 6**.

With the values for the tail-tail self-interaction at hand, the E_{enh} for the ether fragments as a function of branching was determined. The results are shown in **Figure 13**, and summarized in **Table 5**.

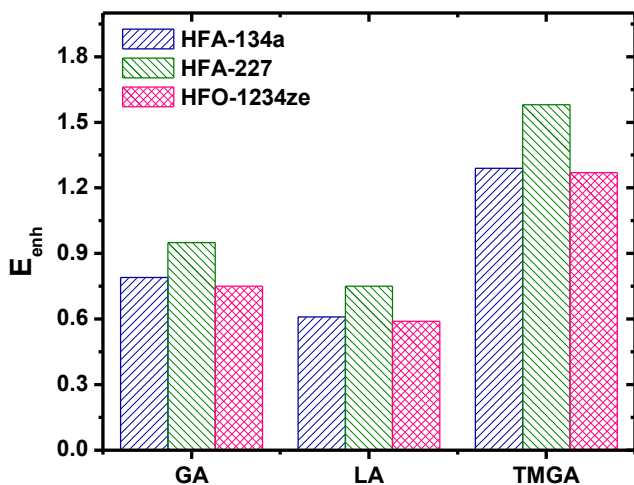


Figure 13 Effect of the degree of branching (CH_3) of the ester-based tail chemistries on their “Enhancement Factor” (E_{enh}). E_{enh} is defined as the ratio of the interaction energy between propellant (solvent = s) and tail fragment (tail = t) (E_b^{st}) over that of tail-tail self-interaction (E_b^{tt}): $E = E_b^{st} / E_b^{tt}$. A summary of E_{enh} for all chemistries and propellants is provided in **Table 5**.

The results show that, out of the ether fragments, the only chemistry with $E_{enh} > 1$ is that for TMGA, that has two CH_3 branching units. TMGA has the lowest self-fragment interaction, and at the same time the strongest interaction with the propellants. It is important to note that the steric hindrance effect should be amplified for all systems when going from a single fragment to a polymer system - every functional group will experience steric hindrances from CH_3 on both side of the chain in a polymer and many fragment-propellant interactions will be present. The expected effect here is to further decrease E_b^{tt} , and thus to further increase E_{enh} . Also this effect will be more pronounced as the polarity of the fragments increases, as a decrease in number of strong bonds and the distance between strong bonds will cause a much greater decrease in E_b^{tt} .

2.3.9. Interactions in cluster of solvents

It is important to note that, similar to limitations of the calculations of E_b^{tt} and thus E_{enh} , which focus on tail fragments vs. polymer chains, we focused on single solvent-tail fragment pairs in the

calculation of E_b^{st} instead of fully solvated fragments. In order to better understand the effect of fully solvated fragments, we performed a series of simulations where the geometry of multiple propellant molecules were minimized in the presence of a tail fragment. We focused on the new generation propellant HFO-1234ze, and three tail fragments: *EO*, *GA* and *TMGA*. The results for *EO* and *GA* will allow us to determine the effect of polarity, while the results for *GA* and *TMGA* will provide us with information regarding the effect of branching.

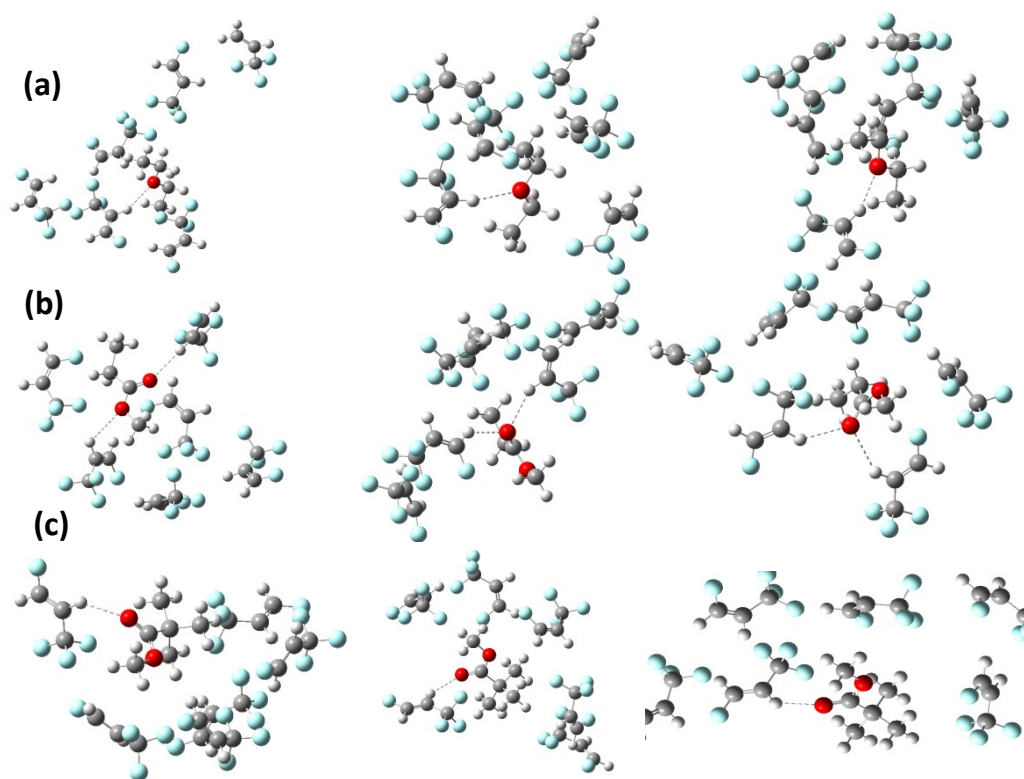


Figure 14 Study of the interactions between a cluster of HFO-1234ze molecules ($n=6$) surrounding a single tail fragment: (a) ethylene oxide (*EO*), (b) glycolic acid (*GA*), and (c) tetramethyl glycolic acid (*TMGA*). “Strong interactions” with oxygen atoms are labeled with dashed line. “Strong interaction” is defined as those between $O \cdots H$, and with a separation distance $< 3 \text{ \AA}$. [31] Structure optimized HF-6-31g(d) basis set/level of theory.

We can see from **Figure 14a** that for three possible configurations of 6 HFO propellants solvating the *EO*, only 1 strong interaction is formed – per possible configuration. However, for *GA* tail (**Figure 14b**) in all 3 possible configurations containing the same number of propellant

molecules in the solvation shell, 2 strong interactions were formed – per possible configuration. It is also worth noting that the *GA* system, the 2 strong interactions are formed either with one ether and one carboxyl oxygen (stronger interaction compared to *EO*) or both with the carbonyl oxygen (even stronger interaction compared to *EO*). These results thus suggest that when the fragments are fully solvated, E_b^{st} for *GA* fragments should be significantly enhanced, and thus their E_{enh} should also increase. Similar effect is expected for *LA*, but to a reduced extent as an extra *CH3* groups is present in that moiety. The results from **Figure 14c** show that upon adding two branching *CH3* groups to the ester group - leading from the *GA* to the *TMGA* fragment, the number of possible strong interactions in a fully solvated environment is just one – similar to a the solvent-fragment pair discussed earlier. In this case we should still expect the solvation forces to increase due to cohesive interactions between the fragment and other solvents, but no further strong bonds are expected to be formed.

2.4. Conclusions

In this work we studied the solvation of relevant tail fragments in HFO-1234ze using *ab initio* calculations. The chemistries investigated are representative of additives of interest to the various industries where HFOs may find use as working fluids. The tail fragments were selected to allow us to systematically probe the effect of both polarity and structure (degree of branching) on their solvation by HFOs. Binding energies between the HFO-1234ze solvent (*s*) and the tail fragment (*t*) (E_b^{st}) indicate that the more polar ether- (*EO* and *PO*) and ester-based fragments (*GA*, *LA* and *TMGA*) are well-solvated by HFO-1234ze with E_b^{st} 's of ca. -20 kJ.mol⁻¹. The non-polar alkane-based fragments (*C5* and *ISO*) are not solvated to the same extent, with E_b^{st} 's of ca. -9 kJ.mol⁻¹. However, polarity alone cannot be used to predict or discriminate which of the polar groups are best solvated. The self-interaction between the tail fragments (E_b^{tt}) is used to determine a quantity

termed the Enhancement Factor (E_{enh}), which is defined as the ratio between E_b^{st} / E_b^{tt} . Based on this definition, the E_{enh} is expected to be a better predictor of the solvation of a particular fragment compared to E_b^{st} alone, and can be used to further discriminate the effect of fragment chemistry/structure on their solvation. Because the interaction between $GA-GA$ is much stronger than that between $EO-EO$, the E_{enh} for the EO is much greater – the largest from all investigated fragment at $E_{enh} = 1.30$. This quantity, E_{enh} , thus allow us to further discriminate solvation in HFO. Different from polarity, the branching of the tail chemistry is seen to have little effect on E_b^{st} . However, at high enough branching densities, it can significantly impact tail-tail interaction. While E_b^{tt} for $GA-GA$ (no CH_3 pendant group) is $> -25 \text{ kJ.mol}^{-1}$, that for $TMGA-TMGA$ (two CH_3 pendant groups) is ca. -15 kJ.mol^{-1} . Branching can serve to reverse the trend in E_{enh} . While for GA (no branching) and LA (one methyl pendant group) E_{enh} is less than one; that for $TMGA$ (two methyl pendant groups) E_{enh} is greater than one (1.27), and very close to that for EO . These results suggest that the structure of the tail fragment will also have a significant impact in its solvation, along with the polarity. We also determined that the solvation in HFO-1234ze is similar to that of a working fluid currently being used in the industry, the HFA-134a. In summary, the results shown here provide information that can be utilized to further evaluate the potential of this new generation of greener working fluids, the HFOs, in replacing the HFAs

CHAPTER 3

THE MICROSTRUCTURE AND INTERFACIAL TENSION OF THE BARE AND SURFACTANT-MODIFIED HFO-1234ZE|WATER INTERFACE

3.1. Introduction

The consumption of hydrofluoroalkane (HFA) working fluids in 2010 totaled over 1,000 million metric tons CO₂ equivalent, with the refrigeration industry using the biggest share (79%), followed by foams (11%), aerosols (5%), fire extinguishing systems (4%) followed by the solvent industry (1%).[180] The large usage of HFAs is of concern given that they are green house gases. Hydrofluoroolefins (HFOs) have thermophysical properties similar to HFAs,[181] but much lower global warming potential (GWP). HFOs have thus emerged as the next generation high-pressure working fluids. HFOs have been recently approved by European regulatory agencies that mandate that, starting in 2011, all new model vehicles should use refrigerants with a GWP < 150.[182, 183] This criterion makes HFAs' phase out in the European automobile refrigerant market a must. HFOs are also making their way into the US market after receiving approval from the Environmental Protection Agency (EPA) for use as refrigerants in motor vehicles.[184]

The reduced environmental impact of HFOs come from their shorter atmospheric half-lives that arises due to the introduction of a C=C bond into their semi-fluorinated back-bone.[185] The GWP for 2,3,3,3-tetrafluoropropene (HFO-1234yf) and 1,3,3,3-tetrafluoropropene (HFO-1234ze) is only 4 and 6, respectively, compared to 1430 and 3220 for 1,1,1,2-tetrafluoroethane (HFA-134a) and 1,1,1,2,3,3,3- heptafluoropropane (HFA-227), respectively, which are the two most widely used working fluids.[186, 187] HFO-1234ze not only has a low GWP, but also low toxicity profile, which is similar to HFAs, and is practically non-flammable, being, therefore, a viable candidate

substitute to HFAs.[145, 188] While major environmental concerns in the use of such working fluids come understandably from use in the refrigeration industry, based on historic grounds, the transition of HFAs to new propellant systems in the refrigeration industry will eventually drive the transition in other industries as well.[189, 190] This has been observed in the past as we transitioned from chlorofluorocarbons (CFCs) to HFAs, and is also clearly indicated once again by patenting trends, with HFOs being proposed as working fluids in different applications such as blowing agents,[191, 192] foam forming agents,[193] and medical aerosols.[194]

With respect to the use of HFOs in medical aerosols, an interfacial system that is of relevance is the propellant-water interface. HFOs are hydrophobic, and have, therefore, low mutual solubility with water.[147] The propellant-water interface arises when water droplets are dispersed in the propellant in the form of emulsions or microemulsions, which may find use as topical foams and inhalers.[195] The ability to understand the behavior of the bare- and surfactant-modified-HFO|H₂O interface is of relevance in the design of surfactants for such medical sprays. Surfactants serve to decrease the tension of the interface, thus facilitating the formation of the dispersions, and once formed, to stabilize the interface from aggregation and coalescence.[179] While many studies have addressed the thermophysical properties of HFOs, including HFO-1234ze, no previous work has discussed the properties of the bare- or surfactant-modified- HFO|H₂O interface, which is the focus of this work. It is worth mentioning that this is a non-conventional interface in that HFOs are not only hydrophobic but are also lipophobic, and also because these propellants are under pressure at the conditions at interest.

Based on the challenges and opportunities described earlier, the goal of this work was to rationally design surfactants for the HFO-1234ze|H₂O interface using a combined computational and experimental approach. Molecular dynamics (MD) simulations and high-pressure tensiometry

were used to determine the tension (γ) and microstructure of the bare HFO-1234ze|H₂O interface using the SPC/E force field (FF) for water and a recently published 12-6 LJ FF for HFO-1234ze.[196] MD simulations were also used to systematically investigate the effect of surfactant tail chemistry on the HFO-1234ze|H₂O interface, using a series of non-ionic (ethylene oxide, EO)-based surfactants with the alkyl (*CH*), propylene oxide (*PO*) and lactide (*LA*) moieties as the HFO-philic (tail chemistries). Both the tension and microstructural properties of the interface were determined to probe the behavior of the surfactants. Once the optimum surfactant tail chemistry had been identified, a series of copolymer surfactants, with varying hydrophilic-to-HFO-philic balance (HFB), or *wt.* ratio between *EO* and the HFO-philic were studied using MD simulations to determine the optimum surfactant balance. Experimental tension results were also obtained with a series of non-ionic copolymer surfactants, and the results compared and contrasted with the MD simulations.

3.2. Models and Methods

3.2.1. Force Field and Simulation Details

All Molecular Dynamics (MD) simulations were performed on the computer cluster at the Center for Scientific Computing at Wayne State University using NAMD 2.8, and VMD 2.9 for visualization.[197, 198] The Force Field (FF) for HFO-1234ze has been recently published,[199] and the parameters are shown in **Table 7**.

Table 7 Intramolecular and Lennard-Jones force field parameters for HFO-1234ze.

Bond	Force Constant: K_b (kcal·mol ⁻¹ ·Å ⁻²)	r_0 (Å)	
CM=CM	676.8	1.331	
CM-CT	317.6	1.511	
CT-FT	369.2	1.353	
CM-HC	388.9	1.086	
CM-FM	445.7	1.330	
CM-HM	388.9	1.086	
Angle	Force Constant: K_θ (kcal·mol ⁻¹ ·rad ⁻²)	θ_0 (deg)	
HM-CM=CM	36.35	120.6	
FT-CT-FT	87.86	107.5	
CM-CT-FT	74.85	111.3	
HM-CM-HM	29.31	118.7	
CM=CM-FM	50.52	122.6	
FM-CM-FM	85.38	112.6	
FM-CM-CT	76.38	112.5	
CM=CM-CT	50.12	124.1	
CM=CM-HC	36.35	120.6	
CT-CM-HC	32.33	115.1	
FM-CM-HM	30.00	113.0	
Dihedral	Force constant: K_{dih} (kcal·mol ⁻¹)	N	δ (deg)
X-CM=CM-X	6.654	2	180
HC-CM-CT-FT	0.178	3	0
FM-CM-CT-FT	0.250	3	0
CM=CM-CT-FT	0.142	3	180
Atom	ϵ (kcal·mol ⁻¹)	$R_{min}/2$ (Å)	
CM	-0.09899235	1.908185	
CT	-0.07430927	1.908185	
FM	-0.05644599	1.62757	
FT	-0.05644599	1.650019	
HC	-0.01570268	1.038277	
HM	-0.01570268	1.487262	

Force field from Rabee et al.[198]

The FF for HFO-1234ze has been shown to be in quantitative agreement with the experimental VLE, liquid density and saturation properties of the propellant.[196] Charges for the model, which had not been initially reported with the FF, were calculated in our work. First, the

geometry of HFO-1234ze was optimized at B3LYP/DGDZVP level of theory and basis set, using Gaussian 03 (see **Figure 15**).[200]

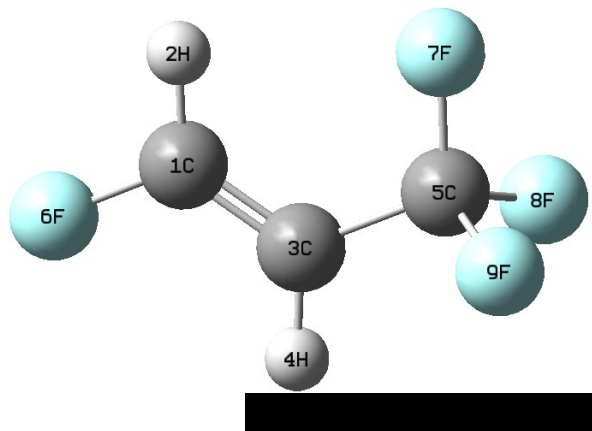


Figure 15 Optimized structure and atom assignment for HFO-1234ze from *ab initio* calculations using Gaussian 09.

The partial charge distribution was then computed at HF/6-31G* level of theory and basis set, as described in the initial publication with the FF. The charges are shown in **Table 8**. More recently, the authors of the FF have published the charge distribution for HFO-1234ze.[201] The two set of charges (from this work and the authors of the FF) are practically identical (deviation < 1%), thus validating both works.

Table 8 Partial charge distribution for HFO-1234ze from *ab initio* calculations using Gaussian 09. Geometry optimized at B3LYP/DGDZVP level of theory using Gaussian 03 and the partial charge distribution determined at the HF/6-31G* level of theory. Atom numbers are the same as those shown in Figure 15.

HFO-1234ze ¹		
Atom #	Type	q(e)
1	CM	0.25300
2	HM	0.13300
3	CM	-0.48500
4	HC	0.24500
5	CT	0.77700
6	FM	-0.19200
7	FT	-0.24500
8	FT	-0.24300
9	FT	-0.24300

The surfactant's FFs were derived from the CHARMM 35 FF, with slight modifications to achieve overall charge neutrality of the molecules – see the FF parameters on **Table S1** in *Supplementary Material*. [202, 203] The SPC/E FF was employed for water as it has been shown to reproduce not only the experimental surface tension of water, [204] but also the interfacial tension of several water binary systems, and of those interfaces in the presence of a variety of surfactants. [205, 206]

For the calculation of the HFO-1234ze surface tension, 127 HFO-1234ze molecules were placed in the center of a rectangular box (28*28*100 Å), giving rise to two HFO-1234ze|air interfaces. The constant temperature and constant volume ensemble (NVT) was used to make sure a stable liquid-vapor binary system develops at 298 K, as well as for the production runs for this interface. For HFO-1234ze|H₂O simulations, 1470 H₂O molecules were placed in one half of a simulation box (30*30*112 Å), and 254 HFO-1234ze molecules were placed in the other half, giving rise to two HFO-1234ze|H₂O interfaces that are separated at a distance of 56 Å, so that the two interfaces will not interact with one another. For the simulations of the surfactant-modified

HFO-1234ze|H₂O interface, equal number of surfactants were placed on each interface (12 each). A coverage of 75Å²/surfactant was thus established.

All simulations were performed with a time step of 1 fs and at 298 K. Except for the HFO-1234ze|Air interfacial systems that were run in the NVT ensemble, all other simulations were performed at 10 atm (1.01MPa) of normal pressure (P_N - pressure in the Z direction). Traditional constant pressure MD algorithms (NPT) are isotropic and vary all cell vectors in an attempt to fix the average of the tangential and normal pressures. With an interface, this results in a normal pressure that differs from the target pressure.[207] In order to address this issue, the constant normal pressure and surface area ensemble (NP_NAT) was used for all simulations of the HFO-1234ze|H₂O interface. The cell dimensions in X and Y directions are fixed while the dimension in Z direction (perpendicular to the interface) is allowed to fluctuate. Equilibration was monitored through the configurational energy as well as the periodic boundary size changes in the Z direction. The Langevin piston and Langevin thermostat were used to achieve the desired temperature and pressure.[208] Periodic boundary conditions (PBC) were applied to all directions. A cutoff of 14 Å was applied to both vdW and electrostatic interactions. VdW interactions were smoothly shifted to zero from 10-14 Å, while electrostatic interactions were smoothly shifted to zero from 0-14 Å. Particle Mesh Ewald (PME) was used to compensate for long range electrostatic interactions.[209, 210]

The interfacial tension was calculated using the following expression:[211, 212]

$$\gamma = \int_{-l}^l [P_N - P_t(z)] dz \quad \text{Equation 4}$$

where γ is interfacial tension, P_N is pressure tensor in the normal direction where constant pressure is applied, $P_t(z)$ is tangential pressure tensor and it is a function of the Z coordinate. A similar equation is used for the calculation of the surface tension. According to this equation, only

the changes in the pressure component in the vicinity of the interface can contribute to the integral.[213] Because we used PBC in our simulations, which gives two interfaces, and a normal pressure is applied to the Z direction, the equation becomes

$$\gamma = \frac{1}{2} \int_{-1/2H_z}^{1/2H_z} [P_{zz} - 1/2(P_{xx} + P_{yy})] dz \quad \text{Equation 5}$$

where H_z is the box height/length in the Z direction, P_{zz} is the component of the pressure tensor in the Z direction, P_{xx} and P_{yy} are pressure tensor components in the tangential directions. In our simulations, the pressure tensor is measured every 1 Å distance along the z direction, these pressure tensors were reported to log files every 100 step (1fs/step) for analysis.

3.2.2. Surfactant Molecules Investigated in the MD Simulation Studies

We included in our simulation work three non-ionic surfactants, all having the ethylene oxide (EO) as the head group, with alkyl- (CH), propylene oxide- (PO) and poly(lactic acid)- (LA) based surfactant tail groups. The CH tail groups are representative of the Brij surfactant class ($CH_3(CH_2)_{12}(OCH_2CH_2)_4OH$ or EO_4-CH_4 , where CH_4 contains the same number of heavy atoms along the back-bone chain as PO_4 and LA_4 . Because HFO-1234ze is hydrophobic, CH tails are expected to have poor solvation in HFO-1234ze, and thus serve as the negative control. PO ($H(OCH(CH_3)CH_2)_4(OCH_2CH_2)_4OH$ or EO_4-PO_4) and LA ($H(OCH(CH_3)C(=O))_4(OCH_2CH_2)_3OH$ or EO_4-LA_4) are moieties that find wide applicability in the pharmaceutical and medical industry, including their use in FDA-approved formulations.[214] Because of their local dipoles that arise due to the presence of oxygen atoms, they are expected to interact more favorably with the propellant. The LA repeat unit is also expected to be more polar than PO , and those three tail groups help us to systematically investigate the effect of interaction strength between HFO-1234ze and the surfactant tail groups on their structure and interfacial

activity at the HFO-1234ze|H₂O interface. In the studies related to the surfactant balance, a series of EO_8-PO_m surfactants, with $m = 2$ to 12, were investigated. These surfactant class was chose as they turned out to be the most interfacially active as discussed below. The homopolymers EO_8 and PO_8 were also studied.

3.2.3. *In situ* (high-pressure) Tensiometry

3.2.3.1. Materials

A series of Pluronic surfactants ($EO_nPO_mEO_n$) were kindly provided by BASF. The homopolymers poly(ethylene oxide) 3,400Mw (PEG3400) was purchased from Acros Organics. All of the surfactants were used as received. Their commercial names and corresponding structures are shown in **Table 9**. Deionized water (NANOpure, Barnstead), with a resistivity of 17.6 M Ω .cm⁻¹ and surface tension of 72 mN.m⁻¹ at 298 K, was used in all experiments. Commercial grade HFO-1234ze was a gift from Honeywell (Hanover, Germany). Basic alumina (99%) was purchased from Fisher Scientific and was used as received.

Table 9 Commercial name, molecular weight (MW), molecular structure, wt.%EO and experimental tension of the various surfactants studied in this work at the HFO-1234ze|H₂O interface.

Surfactant	MW	Structure	EO (wt.%)	γ (mN.m ⁻¹)
Pluronic L62	2,500	EO ₆ PO ₃₄ EO ₆	20	3.0±0.2 ₄
Pluronic P84	4,200	EO ₁₉ PO ₄₃ EO ₁₉	40	1.2±0.0 ₂
Pluronic P85	4,600	EO ₂₆ PO ₄₀ EO ₂₆	50	1.4±0.0 ₁
Pluronic F87	7,700	EO ₆₁ PO ₄₀ EO ₆₁	70	4.0±0.1 ₃
Pluronic F88	11,400	EO ₁₀₄ PO ₄₀ EO ₁₀₄	80	8.1±0.0 ₃
PEG 3400	3,400	EO ₇₉	100	17.2±0.10

3.2.3.2. Purification of HFO-1234ze

The purification of the commercial HFO-1234ze sample was done under pressure, using a similar procedure as described before.[206] Briefly, the commercial sample was loaded into a variable-volume high-pressure cell, which was filled with basic alumina (25 vol.%). The contents in the cell were thoroughly mixed for 5 h using a magnetic stirrer. The alumina was then allowed to settle for 45-60 min. Treated HFO-1234ze was transferred to another pressure cell for the interfacial tension measurements.

3.2.3.3. Interfacial Tension Measurements

The γ measurements were performed in a high-pressure pendant drop tensiometer similar to that described in the literature.[174] The apparatus, schematically shown in **Figure 16**, consists of a variable-volume high pressure cell (MEASURING CELL) equipped with a front window and two side windows, which allows the visualization of the system under pressure and extraction of the droplet profiles with the help of the light source and a digital camera. The temperature (T) was monitored inside the cell, close to the droplet, and controlled with a heating tape wrapped around the cell and a temperature controller (Cole Parmer, EW-89000-10) to ± 0.2 K. The pressure (P) was also monitored in the front part of the pressure cell with a pressure transducer (Sensotec FP2000) to ± 0.07 MPa. The binary HFO-1234ze|H₂O interfacial tension (γ_0) and that of the surfactant modified interface (γ) were determined using the pendant drop technique. Briefly, a pendant drop of propellant was formed at the tip of a capillary connected to a six-port injection valve (Valco Instruments). For the γ measurements, the cell was initially filled with water - with or without surfactant. Drops of HFO-1234ze was injected into the system and allowed to equilibrate until the saturation pressure of the system was reached. Several drops were generated and their equilibrium tension was measured. Equilibrium was assumed to be reached when the

variation in γ became less than the maximum expected experimental error and consistent with time.[215] Every condition was repeated at least three times.

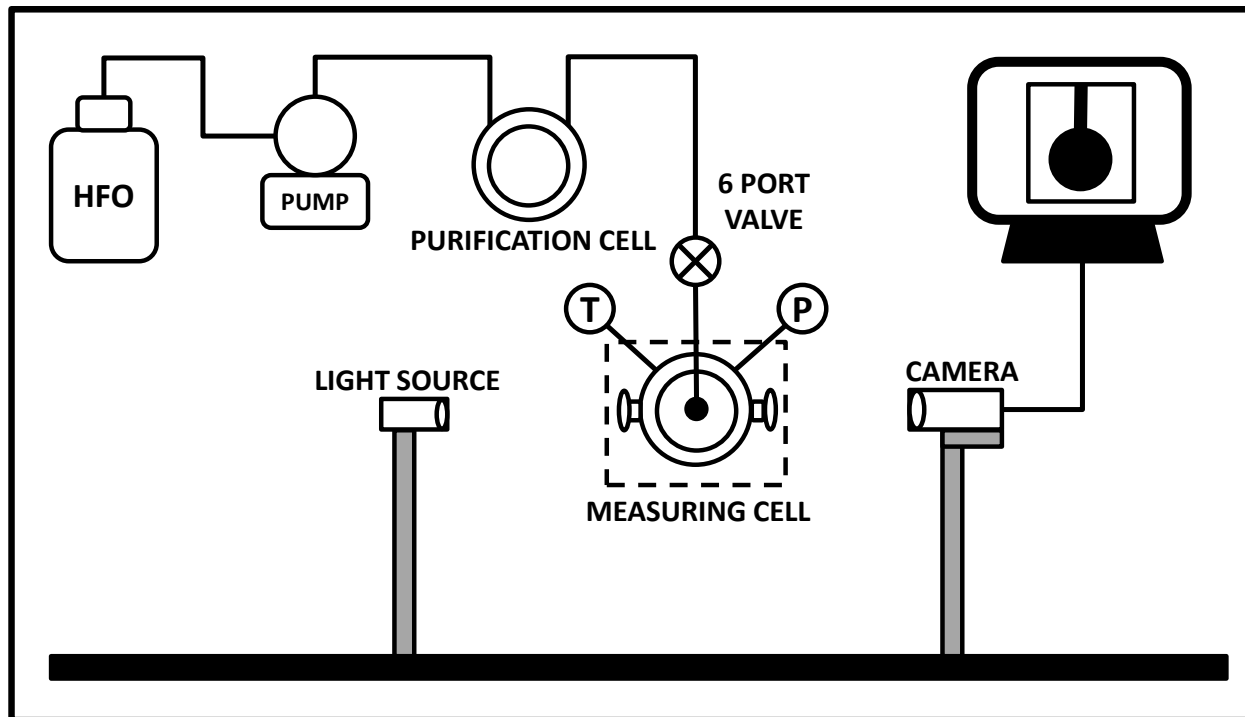


Figure 16 Schematic diagram of the high-pressure tensiometer. HFO = HFO-1234ze tank with dip tube. PUMP = ISCO computer controlled pump for pressurizing the system. PURIFICATION CELL = cell for contact between HFO-1234ze and alumina for purification of the propellant. MEASURING CELL = cell where the pendant drop of propellant is formed in bulk water with or without surfactant. T = temperature controller. P = pressure sensor. CAMERA & LIGHT SOURCE = used to digitize the image on the computer where the droplet profile is extracted from.

3.3. Results and Discussions.

3.3.1. Surface Tension of HFO-1234ze and the Effect of Temperature.

The force field (FF) used was first validated by comparing surface tension of HFO-1234ze (σ_{HFO}) with experimental measurements from the literature. The σ_{HFO} was evaluated at 3 different temperatures: 270K, 298K, and 330K. The MD simulation results are summarized in **Table 10**, along with the experimental literature values.

Table 10 Computer simulation results for the surface tension of HFO-1234ze as a function of temperature (T). Experimental results from the literature are also shown.

Surface Tension (mN.m ⁻¹)		
HFO-1234ze		
T (K)	This work	Exptl.*
270	13.8±1.1	13.3
298	10.3±1.9	9.0
330	5.2±1.9	4.9

* Higashi et al.[144]

The results range from 13.3-4.9 mN.m⁻¹ as the temperature increases from 270K to 330K, with a σ_{HFO} of 9.0 mN.m⁻¹ at 298K. The calculated MD results show excellent agreement with the experimental values, and are also capable of quantitatively predict the effect of T on the surface tension, thus demonstrating the strength of this FF.

The surface tension of HFO-1234ze ($\sigma_{\text{HFO}}^{\text{@298}} = 9.0 \text{ mN/m}$) is quite similar to that observed for HFAs at 298k - 8.11 mN.m⁻¹ for HFA-134a and 10.24 mN.m⁻¹ for HFA-227.[140, 216] In applications where fluorocarbon propellants are used to generate aerosols, the similarity of their surface tension will lead to easier transition from HFAs to HFOs. For example, pressurized inhalers depend on an appropriate aerodynamic particle size distribution for efficient delivery,[217, 218] and surface tension is the dominating factor of droplet formation,[219, 220] which eventually determines the aerosol particle size.

3.3.2. The Binary HFO-1234ze|H₂O Interface: Interfacial Tension and Microstructure

Having validated the model for the calculation of the surface tension of HFO-1234ze, the next step was to determine the tension of the binary HFO-1234ze|H₂O interface. Both the calculated interfacial tension from MD simulations (γ_0) and experimental interfacial tension values (γ_0^{EXP}) of the bare interface are shown in **Table 11**.

Table 11 Computer simulation results for the interfacial tension (γ) of the bare and surfactant-modified HFO-1234ze|H₂O interface. Conditions were 298K, 1.01 MPa, and surfactant density (at interface) of 75 Å²/molecule. The difference between the HFO-1234ze|H₂O binary interfacial tension (γ_0) and that of the surfactant-modified interface is also shown ($\Delta\gamma = \gamma_0 - \gamma$) – this is equal to the surface pressure (Π). The experimental value for the interfacial tension of the HFO-1234ze|H₂O binary interface (γ_0^{EXP}) determined in this work is also shown. The subscripts indicate the number of repeat units in the head (*EO*) and tail (*CH*, *PO*, and *LA*) groups.

	H ₂ O		<i>EO₄-CH₄</i> (mN/m)		<i>EO₄-PO₄</i> (mN/m)		<i>EO₄-LA₄</i> (mN/m)	
	γ_0^{EXP}	γ_0	γ	$\Delta\gamma$	γ	$\Delta\gamma$	γ	$\Delta\gamma$
HFO-1234ze	41.9	40.9	23.3	17.6	12.3	28.7	16.9	24.0

The calculated interfacial tension of the bare interface at 298K was determined to be 40.9±0.9mN.m⁻¹. This value is in quantitative agreement with the experimental value we determined using high-pressure pendant drop tensiometry of 41.9±0.2mN.m⁻¹. The interfacial tension of the HFO-1234ze|H₂O interface is seen to be significantly higher than that of the HFA-134a|H₂O, reported to be 33.5mN.m⁻¹, [174] and that for HFA-227|H₂O, which has been reported to be between 34mN.m⁻¹ to 35mN.m⁻¹. The relative larger value of the interfacial tension HFO-1234ze compared to HFAs cannot be rationalized based on the polarity of the propellants alone. The dipole moment of HFA-134a is 2.058D, and it is more polar than HFO-1234ze (1.443D). A lower tension for HFA-134a is thus expected. However, the same rationale cannot be applied when comparing the tension for HFO-1234ze to that of HFA-227. The dipole moment for HFA-227 0.94D, which is much lower than that for HFO-1234ze, but its interfacial tension against water is still smaller than that for HFO-1234ze. Some of the more hydrophobic nature of HFO-1234ze may be attributed to its C=C. The higher tension of the HFO-1234ze|H₂O interface is expected to serve as a stronger driving force for surfactant adsorption.

To a large extent, the region closest to interface (a few molecular diameter's thick), where the tangential stresses are pronounced, and the system is attempting to minimize unfavorable contacts,

gives rise to the system interfacial energy/tension (γ).[221] One way to probe the microstructure in the vicinity of the interfacial region is to determine its Z -density profile, which is shown in **Figure 17**.

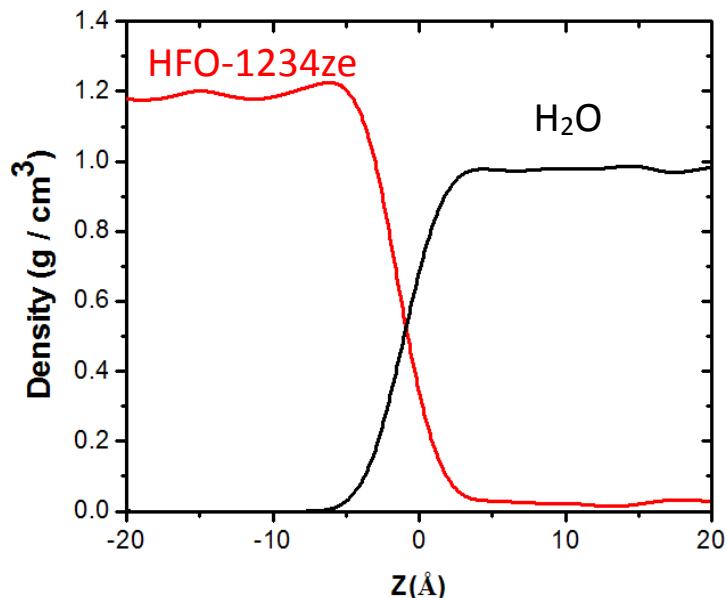


Figure 17 Z -density profile for the HFO-1234ze|H₂O interface at 298K and 1.01MPa.

It can be seen from Z -density profile that, away from the interface, the density (ρ) of both phases oscillates around the correct experimental value.[24] It is also important to note that a stable interface is formed. These results further indicate the appropriateness of the models for HFO-1234ze and water. The interfacial width can be defined as the distance through which both phases have lower than 90% of their bulk density – this is also referred to as the 10-90 density-defined interfacial width. According to this, the 10-90 interfacial width of bare HFO-1234ze|H₂O is 5.6 Å, which is comparable to that of HFA-134a|H₂O interface (ca. 5).[206]

3.3.3. The Surfactant-modified HFO-1234ze|H₂O Interface: Microstructure, Interfacial Tension, and Surfactant Balance.

3.3.3.1. Effect of the Surfactant Tail Chemistry.

The effect of the surfactant tail chemistry on the tension of the HFO-1234ze|H₂O interface was determined at 298K, 1.01MPa and at 75Å²/surfactant coverage. A summary of the interfacial tension (γ) results as a function of tail chemistry from the MD simulations is shown in **Table 11**. The difference between the HFO-1234ze|H₂O binary interfacial tension (γ_0) and that of the surfactant-modified interface, which is equal to the surface pressure (γ), is also shown in **Table 11**.

The results show that all surfactants are interfacially active in the sense that they reduce the interfacial tension of the binary system. The non-ionic surfactant with the *PO* tail group (*EO₄-PO₄*) is seen to induce the largest interfacial tension reduction – $\Delta\gamma = 28.7 \text{ mN.m}^{-1}$. The surfactant with the *CH* tail group (*EO₄-CH₄*), our negative control, is the least interfacially active, with a $\Delta\gamma$ of only 17.6 mN.m⁻¹. These results correlate well with the ability of HFO to solvate these moieties. Using *ab initio* calculations, we have determined the pair interaction energy (E_b^{st}) between HFO and these tail chemistries, which directly relates to the strength of interaction between HFO and the fragments, and thus the ability of HFO to solvated those groups. We observed that while the E_b^{st} between HFO and CH tail group was ca. -9 kJ.mol⁻¹, that for LA was more than double at -19 kJ.mol⁻¹. When comparing the tension reduction between the *PO*- and *LA*- based surfactants, we see that the *PO*-based surfactant is more interfacially active at the HFO-1234ze|H₂O interface, while the calculated binding energies are nearly the same at -19 kJ.mol⁻¹. The higher active of the *PO*-based surfactants can come from a more appropriate surfactant balance or structural differences, as will be discussed in more detail below.

3.3.3.2. Microstructure of the HFO-1234ze|H₂O Interface in the presence of surfactant.

As discussed earlier, there is a strong relationship between the microstructure of the interfacial region and the interfacial tension. The *Z*-density profile of all species, including HFO-1234ze,

H₂O, and the surfactants' head and tail groups were determined at 298K, 1.01MPa and 75Å²/surfactant, and are shown in **Figure 18** as a function of surfactant tail chemistry.

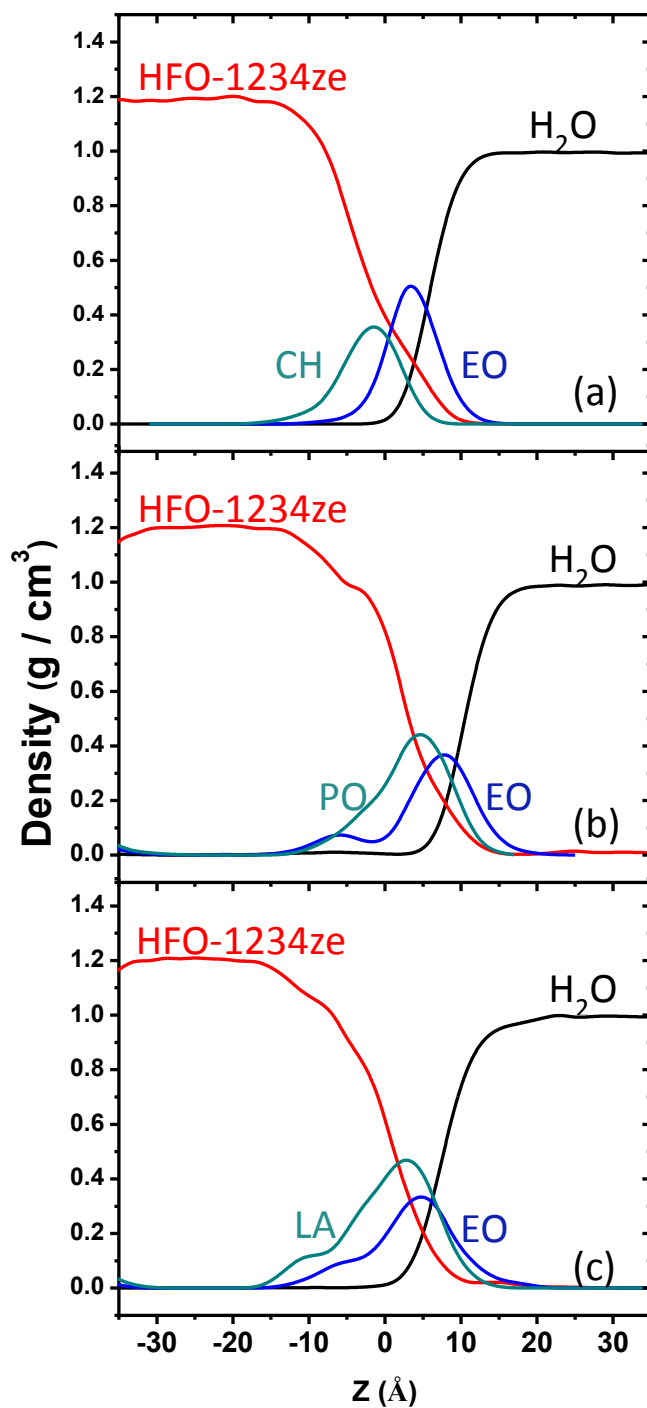


Figure 18 Z-density profile for the HFO-1234ze|H₂O interface modified with (a) EO₄-CH₄ surfactant; (b) EO₄-PO₄ surfactant; (c) EO₄-LA₄ surfactant, at 298K, 1.01MPa and 75 Å²/molecule.

We can observe that the *EO* head group, for all three surfactants systems, has considerable overlap with both phases. This interesting behavior is observed because the *EO* group in the surfactant is not only hydrophilic, but is also HFO-philic. As we have pointed out before, our *ab initio* calculations showed that ether groups are well solvated by HFO. In this case, *EO* does not have the same traditional behavior as head-group (hydrophilic) as it is also HFO-philic, and thus the balance of the surfactant is more nuanced than compared to traditional interfaces.

As for the tail groups, we can observe that while the *CH* moiety has very little overlap with H_2O , both *PO* and *LA* tails have considerably more overlap with H_2O . The tail group position in the *Z*-density profile depends on their hydrophilicity and HFO-philicity. *CH* seems to largely overlap with HFO-1234ze, but it is the least capable of reducing the γ of the interface. The HFO-1234ze| H_2O system is different from the water-organic system in that a hydrophobic group is not necessarily fluoroolefin-philic, and hydrophilic is not necessarily fluoroolefin-phobic (as discussed earlier). In this case, we have previously shown that *CH* is not well solvated by HFO. The overlap of the *CH* moiety with HFO-1234ze is largely driven by its hydrophobicity (and not because it is HFO-philic). Thus, in spite of its overlap with the HFO phase, it does not help much in reducing interfacial tension, which is achieved upon minimizing the less favorable contacts between H_2O and HFO-1234ze.

We can also observe that the interface is broadened in the presence of surfactants. The 10-90 density profile defined interface width increased from 5.6 Å for bare HFO-1234ze| H_2O interface to 19.5 for CH_4 - EO_4 , 22.7 Å for PO_4 - EO_4 , and 23.3 Å for LO_4 - EO_4 . The broadening of the interface indicates a reduction in the unfavorable contacts between HFO-1234ze and H_2O , and as a consequence, a reduction in interfacial tension.[222] For binary systems, the interfacial tension arises from the fact that molecular interactions in the bulk cannot be completely satisfied (loss of

enthalpy) as the interface is approached; i.e., the inevitable contacts between dissimilar molecules at the interface are not as favorable as those with the like molecules in bulk.[179, 223] Because surfactants have head and tail groups that can interact favorably with H₂O and HFO-1234ze, respectively, they will (i) create an exclude volume area/ barrier that will naturally displace HFO-1234ze and H₂O from the interface (bulkier head and tail groups will occupy more space), and in doing so, they will decrease those less favorable contacts; and (ii) the surfactant will provide (more) favorable interaction sites between HFO-1234ze and the tail fragment when compared to HFO-1234ze and water contacts that existed before the addition of surfactant; and also more favorable contacts between H₂O and the head-group - compared to water and HFO-1234ze. Effectively, the surfactant creates two other interfacial regions, which have an overall lower total interfacial energy when compared to the original HFO-1234ze-water interface.

We can see from the RDF profiles shown in **Figure 19** that the contacts between HFO-1234ze and H₂O are greatly reduced in the presence of surfactants, when compared to the bare interface.

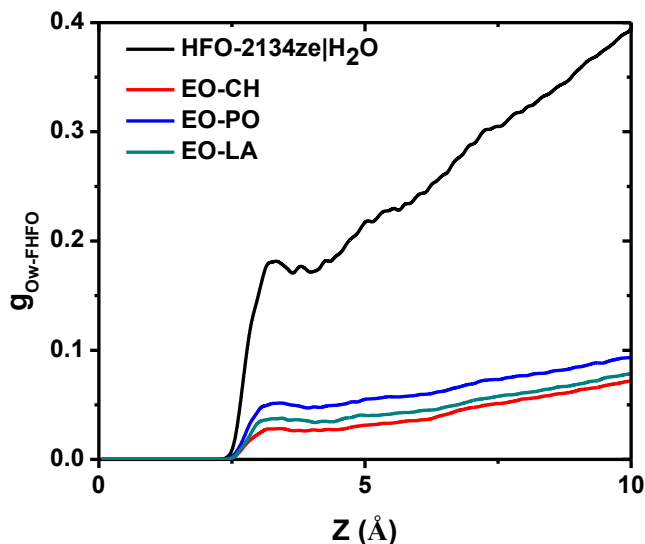


Figure 19 RDF of oxygen (*O*) atoms from H₂O to fluorine (*F*) atoms from HFO-1234ze. Conditions are 298K, 1.01MPa and 75 Å²/molecule.

We can observe that, in spite of the fact that the *CH*-based surfactant provided the least reduction in interfacial tension, it is the one most capable of decreasing the contacts between HFO-1234ze and H₂O. The solvation profiles of the tail groups, to be discussed next, will help explain this apparent discrepancy. We then turn our attention to the second attribute of the surfactant layer, which is to provide favorable contact points to water and HFO through the head and tail groups. We focus here on understanding the effect of solvation of the tail groups by HFO-1234ze - shown in **Figure 20**, as the solvation of *EO* by water has been addressed in the literature.[224]

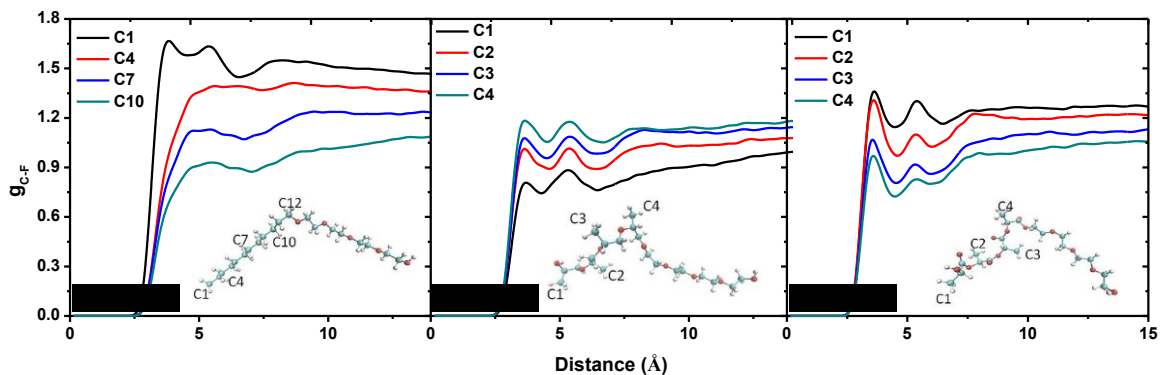


Figure 20 Radial distribution function (RDF) of fluorine atoms (F) from HFO-1234ze and the backbone carbon (C) atoms of the tail group of (a) EO_4-CH_4 ; (b) EO_4-PO_4 ; (c) EO_4-LA_4 surfactants. $C1$ = carbon atom furthest from the EO head-group; $C4$ or $C10$ = carbon atoms closest to the EO head-group. Conditions are 298K, 1.01MPa and $75 \text{ \AA}^2/\text{molecule}$.

These RDF profiles show that the CH tail group (**Figure 20a**) is indeed poorly solvated by HFO-1234ze. A solvation shell of HFO-1234ze around the C atoms of the tail group is poorly defined, except for the C atom furthest from the tethering point to the surfactant head-group ($C1$), which is simply pushed towards the outer surfactant layer due to the hydrophobic nature of the surfactant, as discussed earlier. In contrast, we can see that a first and second solvation shell is observed for both the PO and LA tail groups (**Figure 20b** and **20c**), and for all C atoms along those backbones. One interesting fact to observe from **Figure 20b** is that the tail end ($C1$) is the least solvated C by HFO-1234ze in the PO tail group. This is related to the fact that the terminus of the PO tail is OH , and thus it will tend to point towards the water-bulk layer.

3.3.3. Surfactant Balance at the HFO-1234ze|H₂O Interface

In the process of rationally designing surfactants for HFO-1234ze|H₂O interface, the first step in our study was focused on discriminating the most appropriate surfactant tail group chemistry, which was determined to be the ether-based moiety – PO . The next step in the optimization consists in finding the optimum balance in the head/tail group for the best surfactant studied; i.e., the EO/PO ratio. For this study, we investigated a surfactant series with the following structure –

EO_8-PO_m , where m varies from 2 to 12, with the homopolymers of EO_8 and PO_8 . This is equivalent of varying the $EO\%$ from 0 to 100. The MD simulation results of the effect of the EO wt% at the HFO-1234ze|H₂O interface at 298K, 1.01MPa, and $75\text{\AA}^2/\text{molecule}$ are summarized in **Figure 21**.

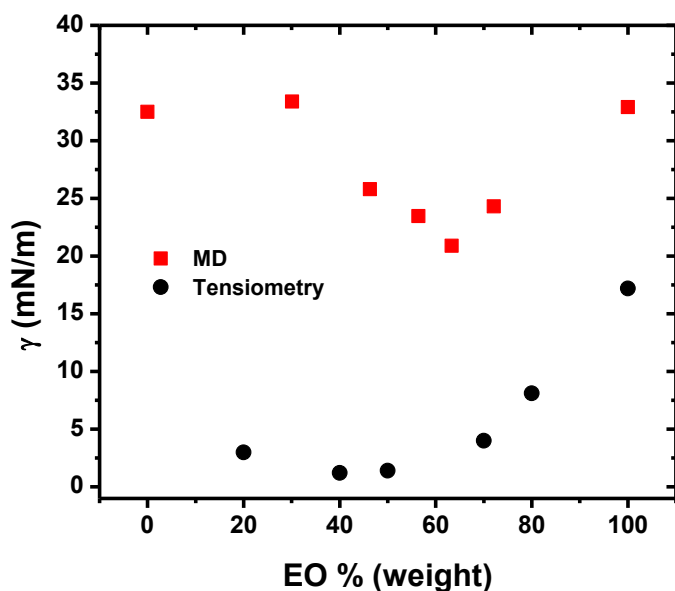


Figure 21 Interfacial tension (γ) of the surfactant-modified HFO-1234ze|H₂O interface a function of EO % (weight) of the surfactant. MD simulations (EO_8PO_m , with $m = 2$ to 12, and the homopolymers EO_8 and PO_8) and experimental measurements ($EO_nPO_mEO_n$, Mw from 2,500 to 11,400) at 298K and saturation pressure of the propellant (1.034MPa). Simulations at $75\text{\AA}^2/\text{molecule}$.

It can be observed that the homopolymers (EO_8 and PO_8) have substantial activity at the HFO-1234ze|H₂O interface, with a decrease in the tension of the binary system of more than $8\text{mN}\cdot\text{m}^{-1}$. We can also observe that a minimum in tension is found during the scan in EO wt.%. As the wt.% EO increases (from the PO homopolymer), the tension of the interface decreases because the surfactant partitions more towards the interface. At the minimum in tension, the surfactant is said to be at the balanced point. This is called the hydrophilic-to-HFO-philic balance (HFB), and is located at ca. 62 EO wt.% for this surfactant class. As more EO is added, the surfactant starts partitioning more to the other side (aqueous) of the interface, and the tension starts increasing again.

Such fundamental understanding of the surfactant at the interface is relevant as it can directly guide the identification of effective surface active agents, and also because it is directly related to the ability to form and stabilize dispersions of water and HFO, and can also be used to determine the preferred curvature of emulsions and microemulsions formed with such non-miscible solvents. This knowledge is of industrial relevance when preparing medical foams and other medical sprays with HFOs.[140, 225]

The interfacial tension of the HFO1234-ze|H₂O interface was also determined experimentally. A series of $EO_nPO_mEO_n$ block copolymer surfactants, having a similar number of PO units were employed. Their structures are presented in **Table 11**. The tension of the homopolymer PEG340 was also evaluated. All the measurements were performed at 298K, saturation pressure (1.034MPa) of the propellant, and 1mM surfactant solution. All surfactants were solubilized in the aqueous phase. The results are summarized in **Table 11**, and plotted as a function of *wt.% EO* in **Figure 21**, together with the MD results.

The homopolymer (EO_{79}) showed a high interfacial activity, with a tension reduction close to $24.7\text{mN}\cdot\text{m}^{-1}$. This result is similar to that observed in the MD results, but more pronounced due to the higher MW of the EO used in the experimental work. This is a result from the fact that EO is highly hydrophilic and simultaneously HFO-philic. This behavior is very different from what is expected on traditional interfaces as discussed earlier, where the second phase is usually an alkyl-based hydrophobic solvent, and where interactions with EO would arise simply from dispersive forces. In HFO propellants, local dipole interactions are not only possible, but potentially very strong, as we have shown in our *ab initio* calculations. Because of this unique interaction between EO and water and at the same time HFO, the V-shaped curve traditionally observed when the tension is scanned as a function of the % hydrophile is somewhat shallow in

this case. The HFB for the experimental system with the *PO*-based copolymers is less well-defined because of the fact that there is less control in the surfactant architecture than those surfactants set up in the MD simulations. However, the HFB can be identified to be between 40 and 50 *wt.% EO*, the two lowest values in the tension vs. *wt.% EO* curve.; i.e., at the HFB is ca. 45*wt.% EO*, where the γ is close to 1.2 mN.m⁻¹. This minimum in tension represents a reduction of ca. 40mN.m⁻¹ when compared with the binary system. The discrepancy in HFB between experimental and computational results can be largely attributed to differences in structure and size of the copolymer surfactants. These results suggest that such surfactant class could not only aid in the formation of emulsion in HFO-1234ze-water systems, but possibly to form reverse aggregates, which may have special relevance in the development of medical sprays.

3.4. Conclusions

In this work we used a combined computational and experimental approach to rationally design surfactants for the HFO-1234ze|H₂O interface. A recently developed 12-6LJ FF for HFO-1234ze[226] was shown to quantitatively predict the experimental surface tension of HFO-1234ze as a function of temperature, thus establishing the relevance of the model to interfacial systems. MD results for the tension of HFO-1234ze|SPC/E H₂O interface (40.9mN.m⁻¹) was shown to be also in quantitative agreement with the experimental value obtained in this work (41.9mN.m⁻¹) using a high-pressure pendant drop tensiometer. MD simulations were then used to understand the behavior of non-ionic (*EO*-based) surfactants with tail chemistries of systematically varying polarity: *CH* (*EO-CH*); *PO* (*EO-PO*) and *LA* (*EO-LA*). The interfacial tension and structural information from MD simulations of the surfactant-modified interface provided a microscopic view to understand the surfactant effect, and to screen the most appropriate tail chemistry. The *EO-PO* surfactant was found to be the most active at the HFO-1234ze|H₂O interface, with an

interfacial tension reduction of 28.7 mN.m^{-1} . Once the best chemistry was identified, MD simulations were used to determine the optimum surfactant balance; i.e. the ratio of the *EO* head-group to *PO* tail-group that would reduce the tension of the interface the most, which is defined as the hydrophilic-to-HFO-philic balance (HFB). The HFB was determined to be located at ca. $62 \text{ wt.}\%$ *EO*. The trend in tension vs. $\text{wt.}\% \text{EO}$ from the MD results are in good agreement with the experimental values found for the tri-block *EO-PO-EO*, with the observed differences being attributed to the difference in structure of the two surfactant classes and in the MW. The experimental HFB for *EO-PO-EO* was found to be at ca. $45 \text{ wt.}\% \text{EO}$. The low tension values obtained for the surfactants close to the optimum balance suggest that they are capable of forming emulsions and potentially microemulsions of systems involving HFO-1234ze and water. The relevance of this work stems from the fact that this is the first time that the properties of the bare and surfactant modified HFO-1234ze|H₂O interface has been reported – either experimental or computational results. In summary, the results suggest HFO-1234ze may be a suitable alternative to HFAs in the formation of aerosols containing dispersions of water and HFO-1234ze for medical applications

CHAPTER 4

PEGYLATED, NH₂-TERMINATED PAMAM DENDRIMERS: A MICROSCOPIC VIEW FROM ATOMISTIC COMPUTER SIMULATION

4.1. Introduction

Dendrimers are well defined, highly branched, nanostructured polymers comprised of dendritic arms branching out from a common core.[227] Their unique structure, which is characterized by high size uniformity, low polydispersity, and a large number of surface groups that can be easily modified, make them very attractive for a variety of biomedical applications, including *in vivo* and *in vitro* diagnostics,[228] and drug and gene delivery.[229] PAMAM dendrimers, with their low cytotoxicity and biocompatibility, are one of the most studied dendrimer nanocarriers (DNCs) in drug delivery applications.[230] The conjugation of ligands onto the surface of nanocarriers has been extensively employed to enhance their efficacy.[231] Of special interest is poly(ethylene glycol) (PEG). PEG can help protect the payload, improve biocompatibility of the carrier, decrease the rate of elimination from systemic circulation, and can also serve as flexible linkers between DNCs and targeting moieties that can be used to promote tissue, cellular and subcellular targeting.[232, 233]

The potential behavior and applicability of dendrimers and their conjugates as drug carrying molecules are greatly impacted by their microstructure and surface properties, as they dictate how these nanocarriers will interact with the physiological environment, and their eventual fate, as well as the fate of the therapeutic cargo associated with them.[234-238] Understanding their microstructure is, therefore, of great relevance. Experimental diffraction techniques such as small-angle neutron scattering (SANS) and small-angle X-ray scattering (SAXS) are best suited among all experimental techniques to probe the structure of DNCs.[239] A number SANS and SAXS

studies have helped elucidate the effect of important variables such as the generation, surface functionalization and pH on the microstructure of PAMAM dendrimers.[240-244] However, SANS and SAXS alone cannot easily provide direct and/or model-free atomic level information of key aspects of these carriers and their conjugates, such as the position of functional surface groups and the interaction of ligands with the dendrimer surface.[245-247]

Computational studies, therefore, fill an important gap in this area, as they have the potential to provide atomic level information on the microstructure of DNCs, and the impact of relevant variables such as the effects of generation, pH, surface chemistry and the presence of ligands.[248, 249] Initial computational studies have focused on systems in vacuum that do not resemble the physiological environment.[250] Several united-atom models of PAMAM dendrimers have been also proposed.[251-254] While those models have certain limitations on what can be extracted with regards to the dendrimer microstructure, they serve an important purpose, which is to allow for the extension of dendrimer studies to more complex systems, such as understanding the interactions between DNCs and lipid membranes.[255, 256] With enhanced computational power, more recent computational work on PAMAM dendrimers have addressed their structure at the atomic level,[257-261] albeit to a limited extent. Moreover, up to now, there has been no report on fully atomistic models for PEGylated PAMAM dendrimers, and very little work has been published on the microstructure of such conjugates from an experimental perspective.[262] This is a strong limitation as PEG is highly used ligand as discussed above.

In order to address the challenges and opportunities discussed above, the objective of this work was to study the microstructure of PEGylated, amine(NH_2)-terminated PAMAM dendrimers using fully atomistic and solvated models. We first investigated the microstructures of NH_2 -terminated PAMAM as a function of their generation (GXNH_2 , where X is the generation) from $X = 2$ through

5. We then investigated the effect of PEGylation density (no, low, medium and high density), and the molecular weight of PEG ($M_w = 500$ or 1000) conjugated onto the PAMAM dendrimers ($GXNH_2-NPEG500$ or $GXNH_2-NPEG1000$, where N is the number of PEGs). We report the results in terms of experimentally accessible variables, such as radius of gyration (R_g), and compare those with available experimental and computational information. We also take an in depth look at the microstructure of the dendrimers using a number of tools such as the radial atom distribution (RAD) and radial distribution functions (RDF). These tools allow us to determine important microstructural information such as the position and solvation of the terminal surface groups, and the structure of the PEG-layer. We discuss our results from a drug-delivery perspective; i.e., how the accessed microstructure information may impact the dendrimer conjugate as a drug carrier system.

4.2. Methods and Models

All simulations in our study were performed remotely on Ranger, from the Texas Advanced Computing Center,[263] using NAMD 2.8 for the Molecular Dynamics (MD) simulations and VMD 2.9 for visualization.[264, 265] The all-atom (AA) force field (FF) for the GXNH₂ dendrimers was developed from a combination of the CHARMM 35 FF and *ab initio* calculations performed in our laboratories. Bond distance, bond angle, dihedral and vdW potential parameters were from CHARMM 35 FF.[266, 267] *Ab initio* calculations were used to adjust the charge distribution within amidoamine monomers. Gaussian 09 was used at the MP2 level of theory and 6-31g(d) basis set for structural optimization, and charge distributions were obtained from CHELPG analysis.[268] Charge distribution of the residues were adjusted so as to achieve the correct overall charge of the fully protonated dendrimer, while maintaining those charges as close as possible to those from the original CHARMM FF. Terminal (primary) amines are fully protonated, which corresponds to the experimental condition of G_xNH₂ at physiological pH.[269] The FF for PEG is a revised and well-tested CHARMM FF for ethers (C35r).[270] The TIP3PM water model was employed in this work. From now on, however, we use the notation TIP3P for simplicity. The TIP3P FF has been shown to give reasonable structural and energetic results for pure water and is also optimized for CHARMM FF, which we used to derive our FF for the GXNH₂ dendrimers.[271] Details on all FF parameters can be found in *Supplemental Information*.

All simulations were performed in the isobaric-isothermal (NPT) ensemble, at 298K and 1 atm. These conditions were maintained with the Langevin thermostat and Langevin piston method.[272, 273] A 1 fs step length was used to conserve energy. A cut off of 12Å was applied for both VDW and electrostatic interactions. VDW interactions were smoothly shifted to zero from 10-12Å, and the real part of the electrostatic interactions were smoothly shifted to zero from 0-12Å. Particle

Mesh Ewald (PME) was used to compensate for the long-range electrostatic interactions.[210] Periodic boundary conditions (PBC) were used in all directions. The solvation boxes were carefully built such that GXNH₂ dendrimers or the PEGylated GXNH₂ dendrimers did not see their own PBC copy, which mimics the desired infinite dilute solution of the dendrimers. The initial coordinates of the dendrimers were generated using GaussView 5.0.[274] A 20 ps minimization was performed to remove bad contacts in vacuum, and then the solvation (water) box was added to the system. Equal number of Cl⁻ ions to the number of protonated primary amines in the dendrimers were added to the solvation box in order to neutralize the system. The solvated systems were minimized again for 20 ps to remove bad contacts, and then MD simulations were carried out to equilibrate the solvated structures. The simulations were run for 27ns. Statistics were taken from the last 2 ns of the runs, when the solvated structures had been equilibrated.

4.3. Results and discussions

4.3.1. Effect of generation on the size and shape of GXNH₂ dendrimers.

In order to understand the effect of dendrimer generation (X in GXNH₂), PEGylation density (N in GXNH₂-NPEG), and molecular weight (Mw) of the conjugated PEG (500 or 1000 Mw) onto the dendrimer microstructure, we first characterized the nanocarriers with respect to their radius of gyration (R_g). R_g was chosen as the first benchmark as it can be directly compared to experimental results. Moreover, knowledge of the size and shape of the dendrimers is of great relevance and key properties that determine their potential applicability, as is the case in the selection of dendrimers as nanocarriers for drug delivery applications[237, 275].

The R_g for a dendrimer with N atoms is given by

$$R_g^2 = \frac{1}{M} \sum_{k=1}^N [m_k (r_k - r_{mean})^2] \quad \text{Equation 6}$$

where r_{mean} is the center of the dendrimer, $(r_k - r_{mean})$ is the distance of the k^{th} atom from the center, m_k is the mass of the k^{th} atom, and M is the total mass of the dendrimer. The evolution of R_g for $G_X\text{NH}_2$ as a function of generation (X) is shown in **Figure 22**.

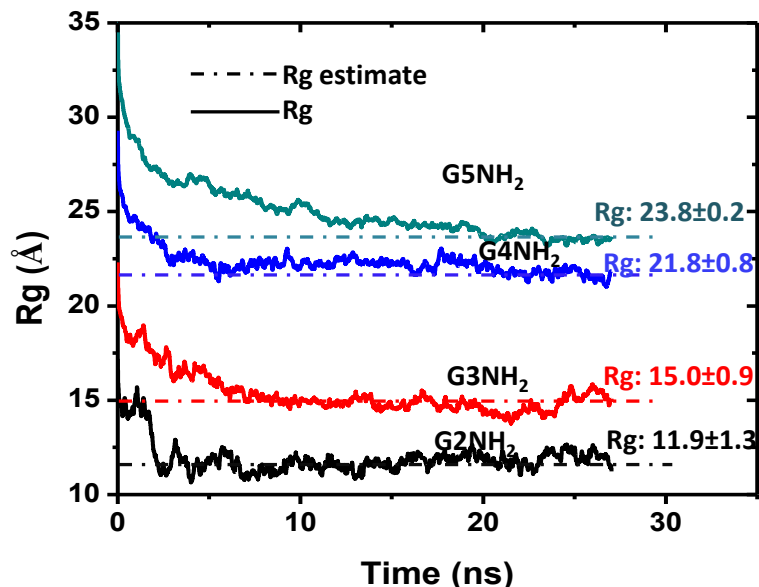


Figure 22 Time course of the radius of gyration (R_g) of the NH_2 -terminated PAMAM dendrimers generation 2-5 – $G_X\text{NH}_2$ - where X denotes the generation. Average and deviation of the molecular dynamics (MD) simulations were calculated from the last 2 ns, using block sizes of 0.1 ns. NPT ensemble - 298K and 1 atm.

These results are summarized in **Table 12**, and compared with the available computational results, and the range of experimental values reported from SANS and SAXS.

Table 12 Radius of gyration (R_g) as a function of the generation of the NH_2 -terminated PAMAM dendrimers ($G_X\text{NH}_2$). Literature results (experimental range and computational) are also shown for comparison.

Radius of gyration (R_g) (Å)

<i>Generat ion</i>	SANS ^a	SAXS ^b	United atom model ^c	All atom model ^d	This study
G2NH₂				14.5	11.9±0. 9
G3NH₂	16.2	14.7- 16.5	13.1	10.4-19.7	15.0±1. 3
G4NH₂	18.0- 21.6	17.1- 18.6	21.7-23.2	16.7-26.7	21.8±1. 1
G5NH₂	22.9- 25.9	21.9- 25.3	25.1-26.7	20.7-32.8	23.8±1. 9

^a Range of values reported from small angle neutral scattering (SANS) experiments.[242, 243, 276]

^b Range of values reported from small angle X-ray scattering (SAXS) experiments.[257, 277]

^c [278, 279]

^d [248, 280] Only models using explicit water are included here for comparison.

The values determined for R_g in this work are seen to be in excellent agreement with the experimental results. All values fall within the range reported for SANS/SAXS. These results suggest that the proposed FF is adequate to represent the microstructure of the dendrimer nanocarriers. It is worth noticing that while it may be relatively simple to fit the FF parameters to reproduce a single condition (generation), the fact that the selected FF is capable of reproducing the experimental R_g for a range of generations further indicates the strength of the model. The results are also in agreement with previous computational results for those dendrimers whose generations have been studied.[42, 46, 252, 256, 281-290]

The equilibrium behavior of the dendrimers was determined via the autocorrelation function of the R_g (C_{Rg}) - cross-correlation of time course of R_g with itself. The C_{Rg} curves are shown in **Figure 2**.

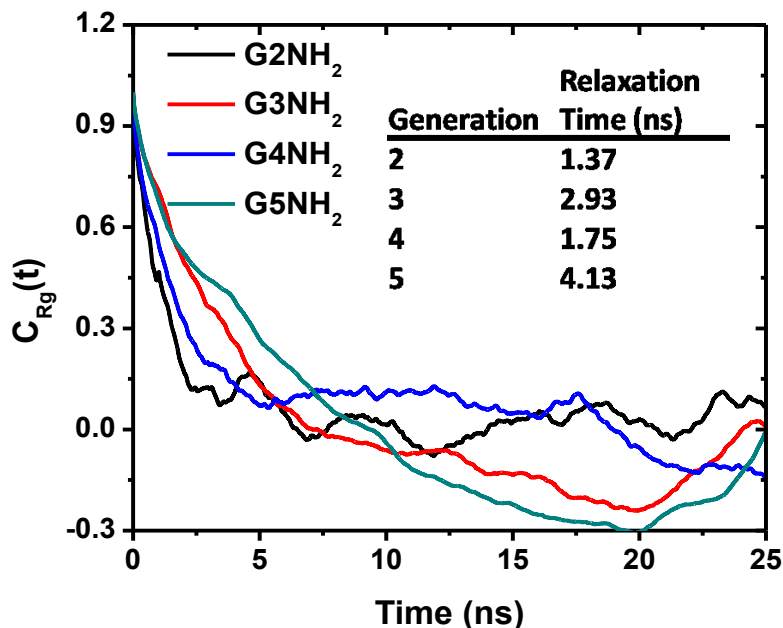


Figure 23 Autocorrelation function of the radius of gyration (R_g) as a function of time ($C_{R_g}(t)$) for NH_2 -terminated PAMAM dendrimers generation 2-5 - GXNH_2 , where X denotes the generation. Relaxation times, calculated as $C_{R_g}(t) = 1/e$, and are shown as an inset table.

The results show that after about 10 ns of equilibration, the autocorrelation functions for G2NH_2 through G5NH_2 fluctuate around 0, indicating that their overall structure is well equilibrated. Relaxation times, defined as the time when $C_{R_g}(t) = 1/e$, were also determined. These results are included as an inset table in **Figure 23**. Relaxation time is the characteristic time scale of a process, and in this case is related to the relaxation behavior of the solvated polymer - based on which R_g is calculated. It is worth noticing that the results show a decrease in relaxation time when going from G3NH_2 to G4NH_2 - 2.93ns compared to 1.75ns; i.e., the relaxation time decreased with an increase in molar mass of the polymer, contrary to the scaling law from polymer theory which states that:[291]

$$\eta_0 = aM_w^z$$

where η_0 is the zero shear viscosity, a is a pre-factor, M_w is the molecular weight of the polymer, and z is the scaling factor, which is ca. 3.3-3.5 for monodispersed linear flexible polymers. The larger the η_0 , the longer the time required for the polymer to assume different conformations. According to this theory, η_0 should thus increase with an increase in the M_w of the polymer. Consequently, the relaxation time should also increase with an increase in M_w , to a degree that will depend on the polymer structure and solvent conditions. The reverse trend observed for G3NH₂ and G4NH₂ seen here is attributed to the unique characteristics of these hyperbranched polymers. PAMAM dendrimers are macromolecules with many degrees of freedom, and are thus capable of undergoing changes in conformation without changing their size - which is characterized by R_g . For example, it was observed from SANs experiment that the R_g of G4NH₂ remains nearly invariant even with significant changes in its radial density profile are induced as the protonation level of the dendrimer changes.[292]

Further examination of the screenshots of equilibrium configurations of the dendrimers also helps to explain the relaxation times discussed above. The conformations shown in **Figure 24** reveal that G4NH₂ does not assume a densely packed structure like G2NH₂ or G3NH₂, but instead it assumes an “open” structure, which is segmented into several relatively independent subunits.

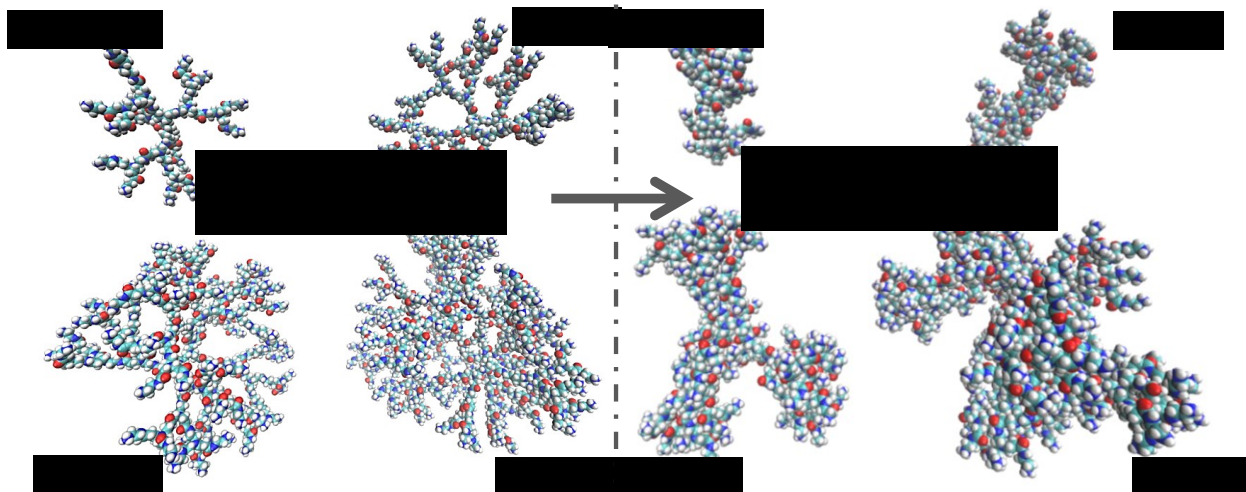


Figure 24 Snapshots of equilibrium conformations of the NH_2 -terminated PAMAM dendrimers generation 2-5 – GXNH_2 , where X denotes the generation. Atoms represented as VDW spheres. Snapshots of starting configurations are those taken after 20 ps of initial minimization. Equilibrium configurations are snapshots taken after 27 ns. Solvated (water) systems at 298K and 1 atm. Water and Cl^- ions were removed from the snapshots to improve visualization of dendrimers.

The relaxation time for G3NH_2 is thus dependent on the molecule as a whole, while that for G4NH_2 is dependent on its subunits, which have a smaller molar mass than the G3NH_2 , thus leading to shorter relaxation times. G5NH_2 also assumes a segmented structure, but the relaxation time did not decrease relative to G3NH_2 because the subunits for G5NH_2 have larger M_w than G3NH_2 itself.

Our observations agree with description of dendrimer microstructures obtained from SAXS, in which the scattering curve suggests that lower generation PAMAM dendrimers do not assume a hard sphere shape, and as generation grows from G4NH_2 to G8NH_2 , PAMAM dendrimers will eventually evolve from star- to sphere-like structures.[277] These observations have important implications when considering the use of such nanocarriers as drug delivery systems. The fact that these higher generation dendrimers (G4NH_2 and G5NH_2) present “open” structures with compact subunits indicate the potential of the carriers to transport therapeutics that interact with the carrier

surface through physical forces (dispersion/H-bonding/electrostatic), but less so as “encapsulated” within (expected) “cavities”. [293-295]

The “segmented open” structure of G4NH₂ and G5NH₂ discussed here, will also serve to reconsider the way we interpret related experimental observations. For example, in earlier SANS experiments, the calculation of water penetration into G4NH₂-G6NH₂ PAMAM dendrimers was attempted using “appropriate molecular boundary radius”, which already assumed a simplified compact structure. [296] However, considering a “segmented open” structure of G4NH₂ and G5NH₂ PAMAM dendrimers as shown here, different interpretation of the experimental results are expected. Further discussions will be carried out later in this manuscript regarding the concept of “segmented open” structure, and details about how this different understanding in microstructure can lead to different interpretations of experimental observations.

In order to better understand the microstructure of the nanocarriers, we analyzed their radial atom distribution (RAD) profiles, which represent the number of atoms at a distance r from a carbon atom at the center of the dendrimer core. These profiles are similar to the radial density profiles used to resolve the debate between “dense-core” vs. “dense-shell” models proposed for the dendrimers. [297] However, RADs, are easier to interpret due to the much less overlap between the profiles. RADs for the different dendrimer generations are shown in **Figure 25**.

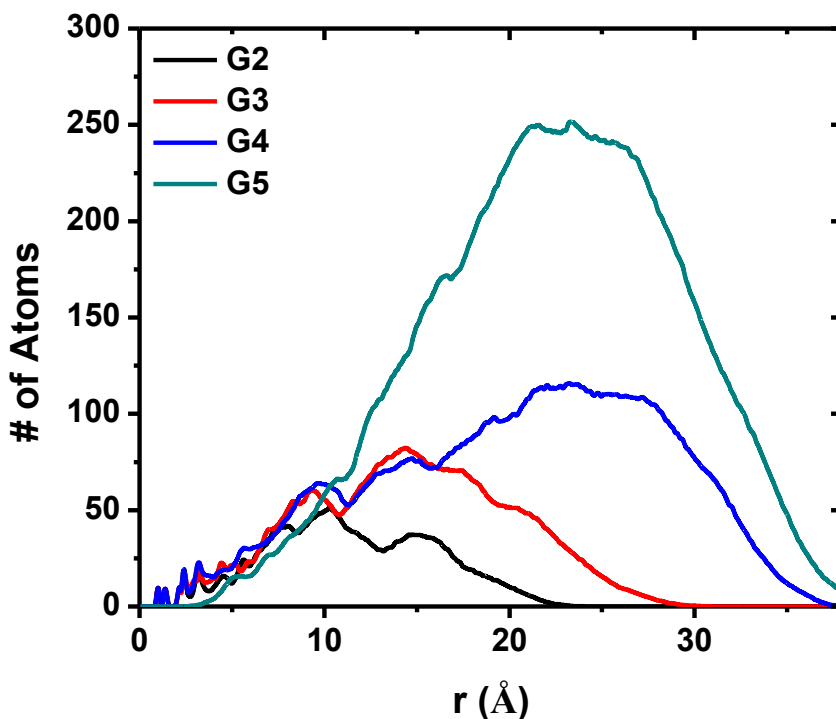


Figure 25 Radial atom distribution (RAD) of the NH_2 -terminated PAMAM dendrimers as a function of their generation - GXNH_2 , where X is the generation. The RAD is the number of atoms at a distance (r) from a carbon atom at the center of the dendrimer core.

We can see from **Figure 25** that as the generation increases, more atoms are present in a specific layer, thus resulting in a higher peak, and more extended distributions, as expected. We also notice that for the region where $r < 10 \text{ \AA}$, G2NH_2 - G5NH_2 have very similar atoms distributions, which indicates that, at least for the generations considered in our study, the core of all the dendrimers remains structurally similar. It is also interesting to observe that the peak for G5NH_2 is observed to be at almost the same position as for G4NH_2 . There are two competing factors leading to a more collapsed structure of G5NH_2 . As the generation goes up, the number of protonated primary amines increases, and so does the repulsion between the terminal groups that oppose the collapsing forces generated by dispersive interactions within atoms in the core. However, as the generation increases, so does the overall size of the dendrimers, and the distance

between primary amines increases, thus resulting in less repulsion, and facilitating the collapse. The second reason for the collapse is related to the fact that as generation of the dendrimers increases, the number of atoms (N_a) increases with generation (X) as $N_a \sim 2^{X+2}$. To maintain a densely packed structure, the space those monomers need to fill (V) scales with X as $V \sim X^3$, so that to a certain generation, in our case $X=4$, the number of monomers cannot fill up the increase in space, resulting in (i) the peak of RAD to be shifted to the left (or less to the right), and (ii) the dendrimer assuming a more “opened” structure.

4.3.2. Distribution and solvation of primary and branching amines

4.3.2.1. Branching amines. In dendrimer theory, the dendrimers’ structural behavior mostly depend on spacer length and distribution of branching points.[259] The behavior of branching amines in terms of their separation distance and solvation are thus key properties to understand dendrimer microstructure. We used G4NH₂ as an example to study the behavior of the branching amines. In our system, the spacer length can be characterized by the distance between two neighbor branching amines (N_i-N_j). Radial distribution function (RDF) of branching amines to branching amines of different generations ($g_{N_i-N_j}$) for G4NH₂ are shown in **Figure 26**. N_4 represents the primary amines and N_0 represents branching amines closest to the core of G4 PAMAM dendrimer.

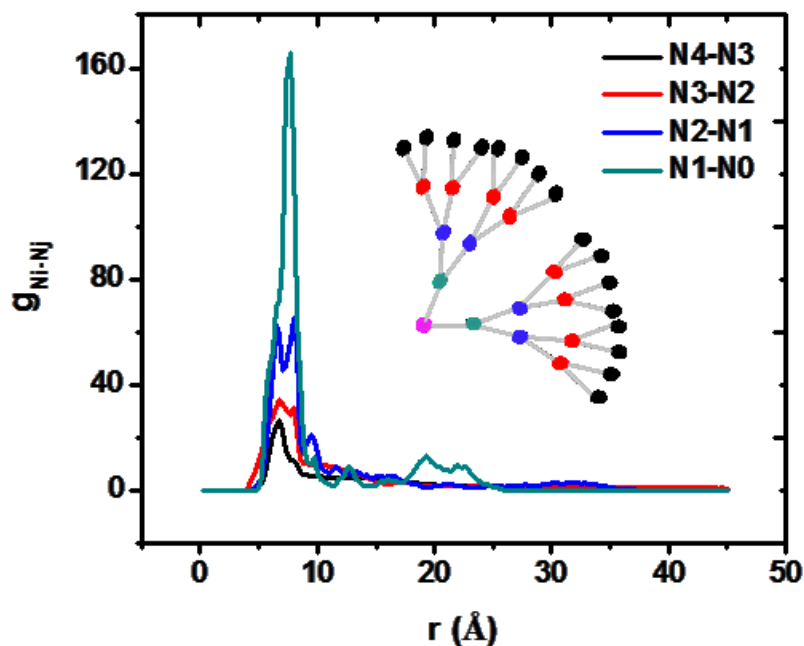


Figure 26 Radial pair distribution function ($g_{N_i-N_j}$) of branching amines (N_i) to different generation branching amines (N_j) for the G4NH₂ dendrimer. N_4 represents the primary amines and N_0 represents the branching amines closest to the core.

The peak position shows the separation distance between two generation branching amines, which corresponds to the spacer length. All peaks appear between 7-8 Å which means the amidoamine monomer (spacer) is quite rigid on itself. The inner most monomer (spacer), N_1-N_0 , shows the sharpest peak, which means all the inner most monomers (spacers) are very close in term of length. From N_1-N_0 to N_4-N_3 the peak slightly shifts to the left. This is a result from the fact that the outermost monomer (spacer) has a much lower density, and it is thus easier for the N_4-N_3 monomer to assume a more relaxed conformation compared to others.

The solvation behavior of primary amines and branching amines is a very important consideration in developing strategies for the use of GXNH₂ dendrimers as drug carriers, because therapeutic molecules are either conjugated to the GXNH₂ dendrimers' primary amines[298] or complexed/encapsulated with/to dendrimers through non-bonded interactions formed between the

therapeutics and both the primary and branching amines.[299] Solvation behavior of primary amines and branching amines will tell to what extent those amines have access to solvent environment, usually aqueous, and consequently, the ability to perform chemistry with those functionalizable groups and to efficiently load therapeutics onto the nanocarriers. In **Figure 27** we show the solvation profiles for different generation branching amines (N_i) of G_4NH_2 – the radial distribution profiles between branching amines N_i and oxygen from water (O_w), where N_4 represents the primary amines and N_0 the branching amines closest to the core.

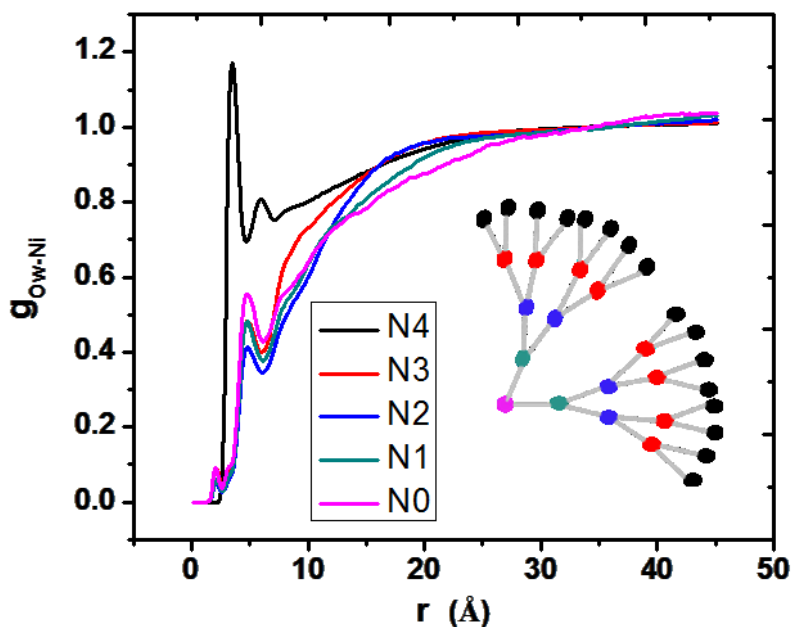


Figure 27 Radial pair distribution function (solvation profiles) between the oxygen of H_2O (O_w) and the branching amines of G_4NH_2 (N_i) ($g_{O_w-N_i}$). N_4 represents the primary amines, and N_0 represents the branching amines closest to the core.

Because the bond length between $N-C$ is longer than that of $C-H$, the first solvation peak position is slightly different for branching amines compared to primary amines, which is reflected on the profiles shown in **Figure 27**. As expected, we observe that the primary amines (N_4) have

the highest first solvation peak. Less expected is the fact that the inner most branching amines (N_0) have a higher first solvation peak than middle branching amines (N_1, N_2, N_3). This observation is in agreement with the results discussed in terms of **Figure 1**. G_4NH_2 assumes an “open” structure with the core (N_0) having good accessibility to water, while middle branching amines that are confined in each subunit by hydrophobic interactions, thus have the least water accessibility. Given this microscopic picture, one can conclude that the loading of therapeutics onto G_4NH_2 via hydrophobic interactions is most likely to happen first through interactions with the inner most branching amines, and then be possibly trapped within the “opening area” between two subunits.

4.3.2.2. Primary amines. The surface chemistry of nanocarriers is of great relevance in drug delivery applications as those characteristics will greatly influence the interactions between the carrier and the physiological environment, and thus dictates the fate of the carrier and consequently of the cargo associated with the carrier. In the case of G_4NH_2 dendrimers, the position and solvation of their primary amines is of even greater relevance, as those are the functionalizable surface groups where drugs [300], imaging agents[301] and other ligands[302] may be conjugated. Of course, such chemistry (conjugation) cannot be achieved or it will be greatly hindered if the primary amines are not available at the exterior surface of the dendrimers. Because of its relevance, there has been great interest in understanding the location of those terminal groups, through both experimental investigations[303] and also computer simulations.[42, 281] We thus provide a detailed analysis with regards to the position and solvation of the terminal NH_2 groups for the dendrimers G_2NH_2 - G_5NH_2 . In **Figure 28 (a)** snapshots of the equilibrium configurations of the G_4NH_2 dendrimers are shown. All primary amines are labeled as yellow VDW spheres, while and all inner branching amines are labeled as blue VDW spheres. All other atoms and bonds are represented by colored lines.

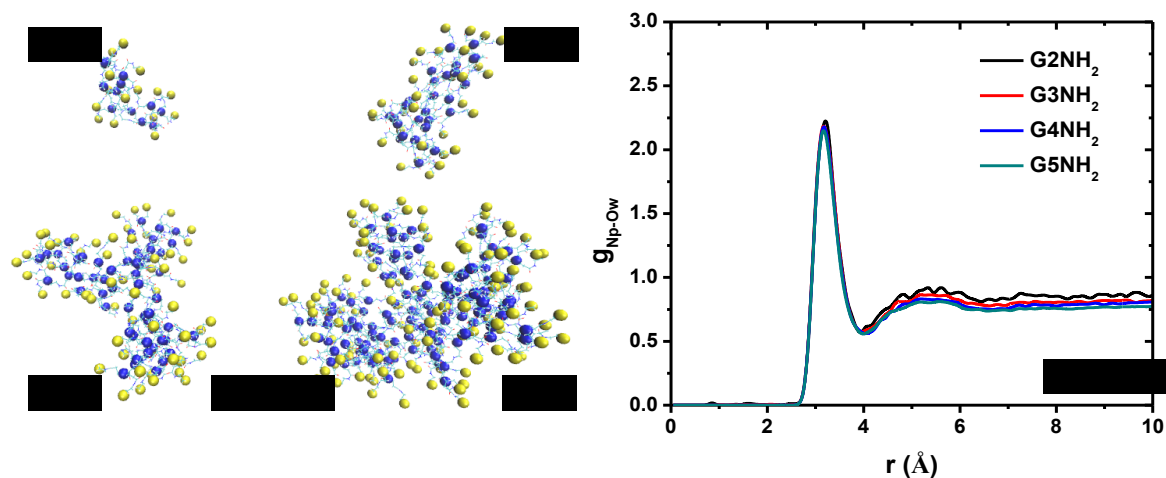


Figure 28 (a) Screen shots of G_XNH_2 dendrimers after equilibration. All primary amines are labeled as yellow VDW spheres, and all inner branching amines are labeled as blue VDW spheres. All other atoms and bonds are represented by colored lines. (b) Radial pair distribution functions of the primary amines of G2-G5NH₂ (N_p) to the oxygen of H₂O (O_w) ($g_{N_p-O_w}$).

Through this simple (qualitative) representation, it can be inferred that all primary amines reside in the outer shell of G2NH₂-G5NH₂ dendrimers. In order to provide a quantitative assessment to this observation, we also studied the primary amines' solvation profiles for G2NH₂-G5NH₂. Those results are shown in **Figure 28 (b)**. The first solvation peaks of the primary amines are seen to remain virtually the same for all dendrimers, independent of their generation - G2NH₂-G5NH₂. This demonstrates that they are equally accessible to water, and thus quantitatively establishes that all primary amines reside in the outer shell or surface of the dendrimers. These results help address a long standing debate in the dendrimer literature on whether primary amines “back-fold” into the dendrimer structure or remain on their surface.[304]

While most studies agree that for lower generation G_XNH_2 dendrimers, including G2NH₂ and G3NH₂, primary amines reside in the outer shell or surface of the dendrimers,[42, 305] some studies have suggested that the terminal amine-groups of higher generations G_XNH_2 “back-fold”

into the dendrimer structure.[240, 241, 304] The fact that our results show that the RDF profiles of primary amines to *O* from water for G4NH₂ and G5NH₂ are very close to those for G2NH₂ and G3NH₂, strongly suggest that those higher generation dendrimers do not “back-fold”. This conclusion also makes thermodynamic sense as a very unfavorable enthalpic penalty would be expected for a fully protonated primary amine to insert itself within the internal of dendrimers which are highly hydrophobic. This observation does not conflict with some experimental studies that shows primary amines or terminal monomers can be found quite close to core of dendrimers – which could be thought of as “back-folding”. [240, 259, 306] The key to understand these experiments is to realize that G4NH₂ and G5NH₂ assume a “segmented open” structure, with the presence of subunits. Regions close to the core of the dendrimer are thus accessible to primary amines without the need to back-fold into the dendrimer structure.

4.3.3. Effect of PEGylation on PAMAM dendrimer microstructure

There are several advantages in PEGylating dendrimer nanocarriers. They help improve biocompatibility,[44, 290, 307] enhance aqueous solubility, which is especially relevant to achieve high density of conjugation of hydrophobic therapeutics,[308] increase plasma circulation time,[309] and are also used as flexible linkers for the attachment of ligands for cellular[310] and organelle targeting.[311] In this work, we systematically investigated the effect of PEGylation density and PEG Mw on the microstructure of G3NH₂ dendrimer.

4.3.3.1. Effect of PEGylation density on the microstructure of G3NH₂

The R_g of G3NH₂ was determined at different densities of PEG 500 Mw. The effect of PEG density was studied both on size of the core of the conjugate (G3NH₂ alone) and onto the overall size of the conjugate (G3NH₂-NPEG500). The results are shown in **Figure 29**.

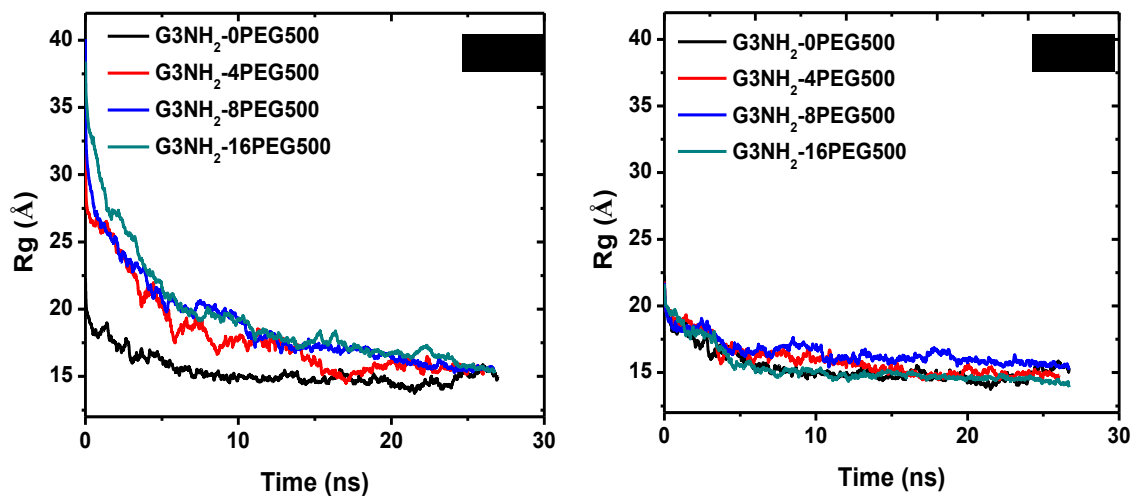


Figure 29 Evolution of the radius of gyration (R_g) of PEGylated G3NH₂ conjugates as a function of graft density of PEG 500 Mw – G3NH₂-XPEG500, where X is the number of conjugated PEG 500 Mw. (a) R_g of the whole conjugate – including PEG. (b) R_g of the dendrimer core only.

As we increase the density of PEG500 (N) on G3NH₂-NPEG500, we observe that the R_g of the PAMAM-PEG conjugation increased, but only slightly so - **Figure 29 (a)**. This suggests low Mw PEG grafting on PAMAM dendrimers will have only small effects on overall size of DNC conjugate, in agreement with the literature.[290] R_g of the dendrimer part of the conjugate alone, however, did not show a monotonic increase with increasing PEG density - **Figure 29 (b)**. For the core of the conjugate (G3NH₂ part only), as the PEG 500 density increases from no PEG500 to 8 PEG500, the R_g of the core increased, indicating that the PAMAM part is being swollen. As there should not be any crowding effect at this low grafting density, the swelling is attributed mostly to the fact that PEG is well solvated by water, and this solvation provides an outward force pull on the PAMAM core, which results in the swelling of the core. However, as the PEG 500 density increases from 8 to 16 PEG500, the R_g of the core decreased. While the same type of forces that promote the outward pulling of the core still exist as the density increases from 8 to 16 PEG500, other forces counterbalance this outward pull. For every PEG chain tethered onto the

primary amines of the PAMAM dendrimers, there also will be the neutralization of a +1 charged site from the protonated primary amines. These protonated primary amines (before addition of PEG) act to oppose the collapse of the dendrimers, as discussed earlier. At some point, in the case of for G3NH₂ as the PEG 500 density increases from 1/4 to 1/2 grafting density, the surface charges are reduced to a critical point in which their density is not able to sustain the attractive interactions of the PAMAM core. The core thus collapses because of lack of electrostatic repulsion between primary surface amines.

To investigate the changes induced by PEGylation density onto the dendrimer microstructure in more detail, we determined their RAD profiles. The RAD profiles in **Figure 30 (a)** show that as the PEG density at the surface increases, the RADs of G3NH₂-NPEG500 show a wider distribution. G3NH₂-16PEG500 has a thick layer, of almost 1 nm of PEG, which surrounds the dendrimer. This “coat” is expected to have a significant impact on its interaction with the physiological environment, and may also affect the release of therapeutic molecules (especially hydrophobic) that may be directly conjugated onto the dendrimer surface, as they will need to diffuse through this extra barrier. **Figure 30 (b)** shows the RADs of the PAMAM core only. The two competing effects of PEG solvation and electrostatic repulsion by the primary charged amines discussed above are clearly observed in **Figure 30 (b)**. By increasing the PEG density on G3NH₂ from 8 to 16, the RHS of the RAD curve is further pulled/shifted outward compared to the other dendrimers, which corresponds to a stronger pull out force induced by a larger number of PEG chains. However, the LHS of the RAD curve is shifted to the left, which corresponds to a collapse induced by the reduction of the electrostatic repulsions from primary amines that are no longer charged. The RAD profiles show that the two effects compete with each other for all PEG densities. For G3NH₂-16PEG500, the competition results in shrinkage of PAMAM part.

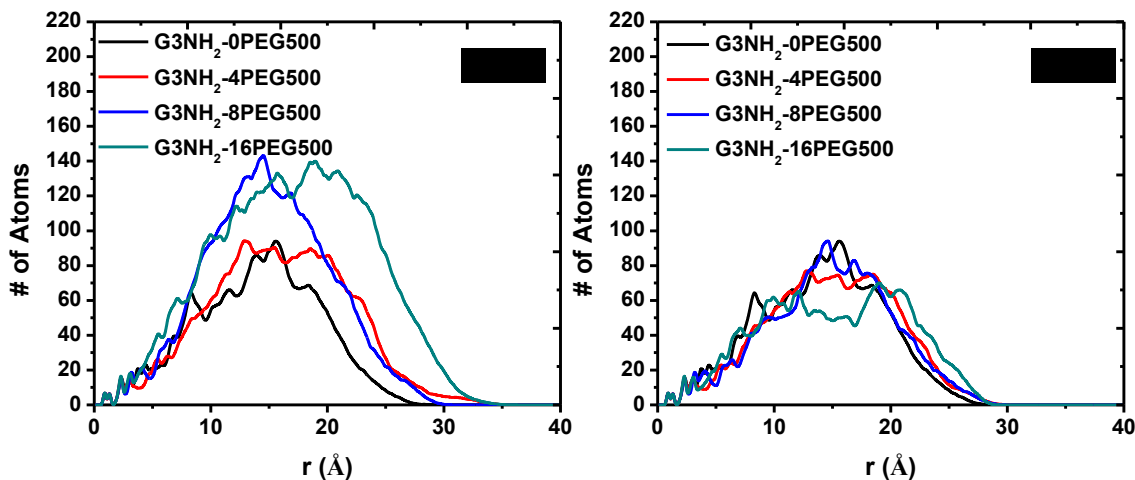


Figure 30 Radial atom distribution (RAD) of PEGylated G3NH₂ conjugates (G3NH₂-NPEG500) as a function of number of PEG 500 Mw grafts (N). (a) RAD of the whole conjugate – including PEG. (b) RAD of the dendrimer core only.

We also examined the primary amines' solvation profile for the G3NH₂ dendrimers PEGylated with different densities of PEG 500 Mw. The results are shown in **Figure 31 (a)**. The solvation peaks of the primary amines of PEGylated G3NH₂ are seen to be smaller than that of G3NH₂ with no PEG500, and the peaks decrease as the PEGylation density increases. PEGylation impacts solvation of primary amines in two ways: (i) in a direct way, the conjugation of PEG500 converts primary amines to secondary amines (amines with 2 organic substituents), and (ii) in an indirect way, there is a steric blocking of water from the remaining primary amines due to interaction between *O* of PEG and the primary amines themselves, as will be discussed in more detail later. The picture is very different, however, for inner branching amines (N_i), whose profiles are shown in **Figure 31 (b)**. PEGylation is seen to significantly reduce the height of the first and second solvation peaks, which may be attributed, at least in part, to a collapse of the dendrimer core as PEGylation increases.

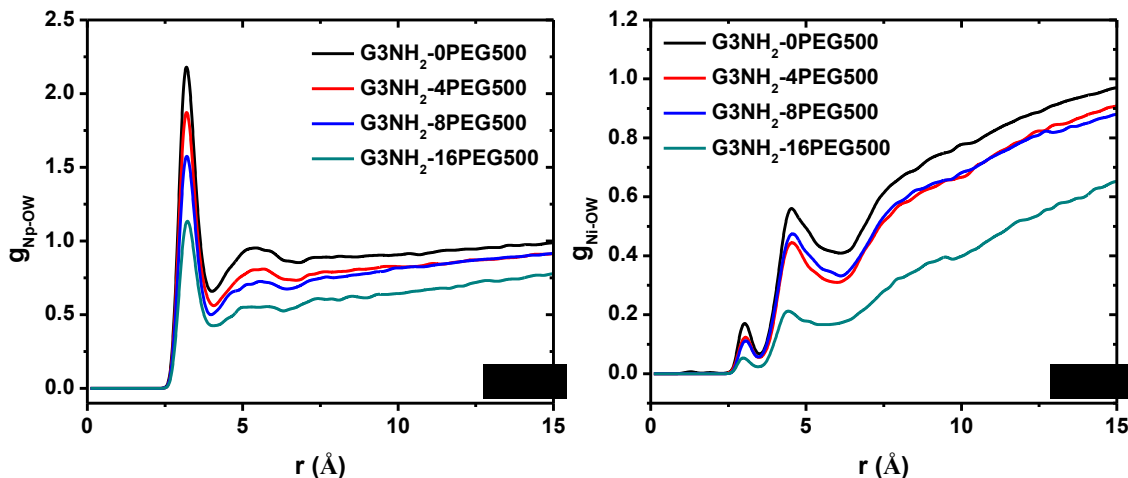


Figure 31 Radial pair distribution function of H₂O oxygen (O_w) to (a) primary amines (N_p) ($g_{N_p-O_w}$) and (b) inner amines (N_i) ($g_{N_i-O_w}$) of PEGylated G3NH₂ conjugates as a function of graft density of PEG 500 Mw – G3NH₂-NPEG500, where N is the number of conjugated PEG 500 Mw.

Understanding the solvation behavior of the primary amines of PEGylated dendrimers is of relevance as any impact on their solvation (the ones not covalently modified) will in turn affect their interaction with the physiological environment, as for example non-specific interactions with proteins, tissues and cell walls. The presence of this thick and strongly interacting PEG layer is expected to impact the zeta potential of the carriers above and beyond that which should be observed by the simple removal of the primary amine charges that happen upon conjugation of the PEG grafts. This impact is expected due to the electrostatic screening of the unmodified primary amines by the PEG layer.

4.3.3.2. Effect of PEG molecular weight on microstructure of G3NH₂

Besides PEG density, PEG molecular weight is another major factor that can be utilized to change the microstructure of drug nanocarriers, and thus to optimize their efficiency.[288] Here we investigate the effect of PEG Mw on the microstructure of G3NH₂ by comparing three systems: G3NH₂ with no PEG; G3NH₂-8PEG500 and G3NH₂-8PEG1000. The R_g 's for the conjugates are

shown in **Figure 32 (a)** (of whole conjugate). The R_g for the dendrimer part of the conjugate are shown in **Figure 32 (b)** (core only).

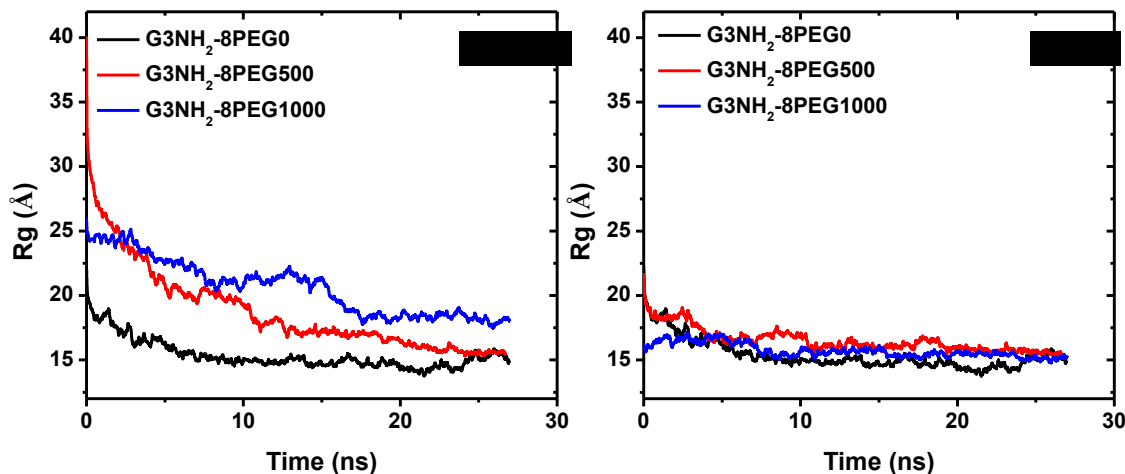


Figure 32 Evolution of the radius of gyration (R_g) of $G3NH_2$ conjugates as a function of PEG length – PEG 500 Mw and PEG 1000 Mw. (a) R_g of the whole conjugate – including PEG. (b) R_g of the dendrimer core only.

The R_g increased from $G3NH_2$ -8PEG500 to $G3NH_2$ -8PEG 1000, as expected. The increase of R_g from 8 PEG500 to 8 PEG1000 is larger than the increase in R_g from 8 PEG500 to 16 PEG 500. Considering the total molecular weight of 16 PEG500 is same as 8 PEG1000, this means PEG length has a larger effect on the size of PAMAM dendrimer than number of PEGs conjugated. The larger effect of PEG length can be attributed again to the competition between the two effects of PEG on dendrimers. The outward pulling force from 8PEG1000 is same as from 16PEG500, but with fewer PEG chains, $G3NH_2$ -8PEG1000 has more unmodified primary amines which provides for a stronger repulsion coming from the dendrimer core and more pronounced increase in R_g compared to $G3NH_2$ -16PEG500. Another reason for 8PEG1000's bigger impact on overall size of DNCs could be the degree of interactions between primary amines and PEG chain, which will be discussed later. In **Figure 32 (b)** we report the R_g of PAMAM part of the PAMAM-PEG

conjugates. The impact of PEG length on the size of the PAMAM core is not significant. Combined, these results suggest that the solvation and crowding effect of larger Mw PEGs are very significant in the overall dendrimer conjugate size.

Radial atom distributions (RAD) were again used to probe further into the dendrimer microstructure. The RADs for PEGylated G3NH₂ as a function of PEG size are shown in **Figure 12**. In **Figure 33 (a)** we show the RAD of the conjugates. NH₂-8PEG1000 have ~1nm thick layer compared to G3NH₂, which is similar to that of 16PEG500, but with less interactions with primary amines, and assuming a more extended conformation as a result (**Figure 34**). As for the impact of the PEG length on the size of the core, the RADs shown in **Figure 33 (b)** indicate that the LHS of the RAD plot for G3NH₂-8PEG1000 did not shift as much to the left as that for G3NH₂-16PEG500, which comes from the difference in their number of unmodified primary amines. This is relevant, as the number of functional groups accessible for conjugation of the therapeutic cargo can be maximized that way – by having fewer PEGs of larger Mw.

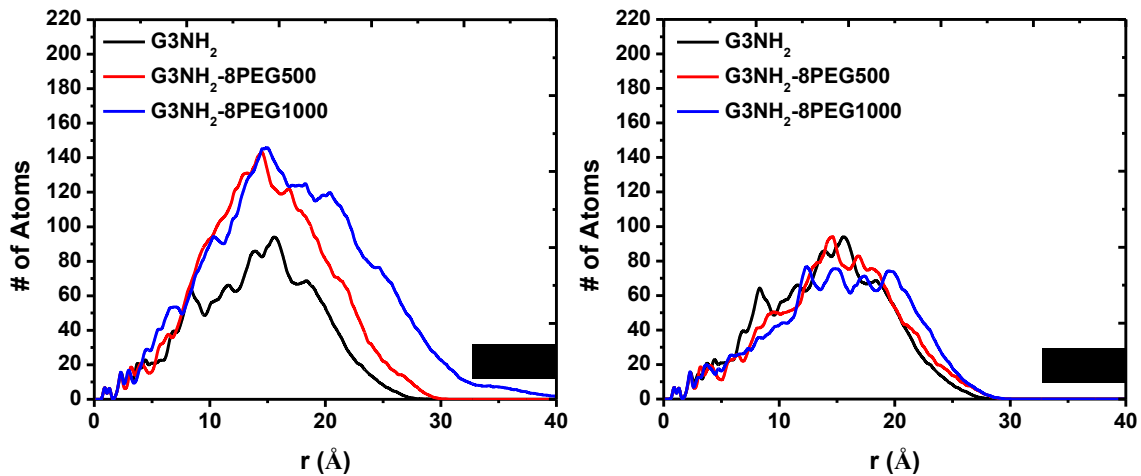


Figure 33 Radial atom distribution (RAD) of PEGylated G3NH₂ conjugates as a function of the PEG length. (a) RAD of the whole conjugated – including PEG. (b) RAD of the dendrimer core only.

4.3.3.3. Effect of PEG density and molecular weight combined on the microstructure of G3NH₂

To determine the effect of both PEG density and Mw combined on the microstructure of G3NH₂, we first examined their equilibrium structures visually as shown in **Figure 34**.

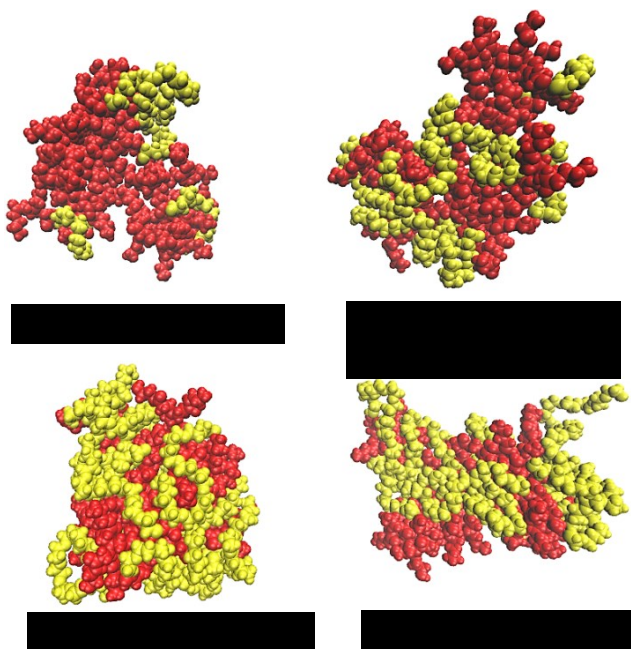


Figure 34 Screenshots of the equilibrium configurations of PEGylated G3NH₂ conjugates as a function of PEG density (N in G3NH₂-NPEG) and PEG length (500 or 1000Mw). Dendrimer atoms represented in red and PEG atoms in yellow VDW spheres.

Those snapshots indicate that the PEG chains grafted onto the dendrimers are flexible enough and interact strongly enough with the protonated primary amine surface groups of the dendrimers, so as to fold in close contact with the surface (strong adsorption). Such information has not been available until now as atomic level information is not easily accessible experimentally, and no fully atomistic simulations of PEGylated dendrimers have been carried out in the past.[312, 313] We also studied the radial pair functions between primary amines (N_p) of dendrimers and the Oxygen in PEG (O_{PEG}) to better understand this interaction. The results are shown in **Figure 35**.

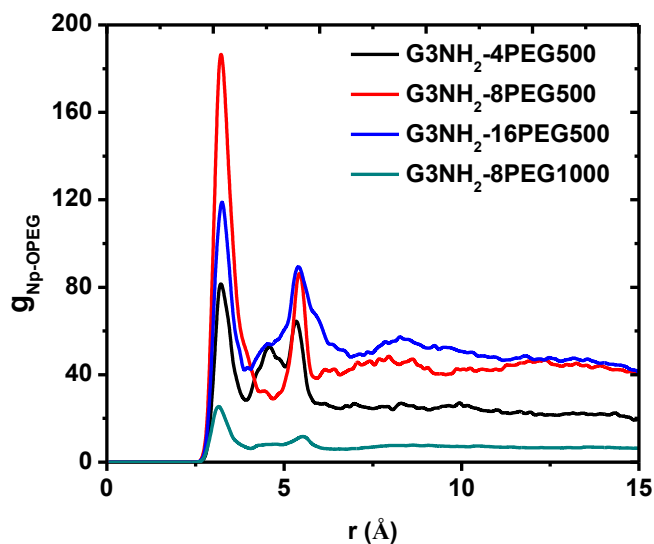


Figure 35 Radial pair distribution function between the oxygen from PEG (O_{PEG}) and primary amines (N_p) (g_{N_p-OPEG}) of dendrimers with generation 2-5 - G_XNH_2 , where X represents the generation.

All PAMAM-PEG conjugates show strong interactions between primary amines of dendrimers and Oxygen from PEG, albeit to different extent. The first peak is at 3.2 Å, which is close to typical hydrogen bond distance of 3 Å. This makes sense because all unmodified primary amines are positively charged (+1e) and Oxygen atoms from PEG have a negative partial charge that is strong enough to form hydrogen bonds with those primary amines.[314] Because we have seen from **Figure 31 (a)** that up to 16 PEG, G_3NH_2 will not significantly block water from solvating primary amines, we can safely say that while Oxygen atoms from PEG interact strongly with primary amines, this has a relatively small impact on the primary amines' accessibility to small molecules like water.

In **Figure 34**, $G_3NH_2-8PEG1000$ is seen to have some PEG chains stretched out to water, indicating less interaction with primary amines – compare to $G_3NH_2-16PEG500$, for example, which has the same number of total repeat units. From **Figure 35** it can be observed that G_3NH_2-

8PEG1000 also shows the smallest peak in RDF between N_p and O_{PEG} . These results indicate, therefore, that as PEG Mw increases, the fraction of the PEG chain that will be strongly interacting with the surface of dendrimer will decrease, and the fraction of PEG that will assume a more extended conformation will increase. Nonetheless, it can be seen from **Figure 34** that quite a significant amount of the surface is still “covered” by PEG repeat units that interact with the primary amines. It is expected that the PEGylation will impact the zeta potential of this carriers through the strong interaction between ether oxygen in PEG and terminal NH_2 groups that have not been modified. Some experimental studies support that view; decrease in zeta potential is greater than expected simply due to substitution of terminal amines by PEG;[315] while other studies have suggested a more direct correlation between degree of PEGylation and zeta potential.[316]

This effect of PEG Mw on the PEG layer microstructure may have great implications on the development of active targeting nanocarriers. First, targeting moieties located at the end of flexible PEG chains will have a better chance to interact with their receptors in cases when PEG is extended out into the bulk aqueous environment compared to those systems where PEG populates the vicinity of the dendrimer surface, which will decrease the opportunity for those targeting moieties to interact with their receptors. Secondly, the presence of a PEG layer on the surface may also act as a diffuse barrier for the release of therapeutics into the bulk phase after the labile bond connecting the dendrimer and the therapeutic is cleaved.

4.4. Conclusions

In this work we investigated the microstructure of PEGylated, amine-terminated PAMAM dendrimers using molecular dynamics (MD) simulations with fully atomistic models. We show that the proposed force field (FF) for the PAMAM dendrimers is capable of correctly capturing

available SAXS and SANS experimental information on their size – R_g . We also show that G4NH₂ and G5NH₂ have a “segmented opened” structure that allows for the primary amines to locate close to the dendrimer core, without “back-folding”. We provide here an alternative view to the concept of back-folding in protonated PAMAM dendrimers. Our results point to a thermodynamically favorable structure where primary amines may reside close to the core, and are yet on the dendrimer’s surface, a configuration that can be assumed in such segmented open structures observed here. These results can be reconciled with experimental SANS/SAXS studies and yet represent a thermodynamically favorable conformation. Primary amines for G2NH₂-G5NH₂ are shown to reside in outer shells, and their solvation peaks remain the same. PEGylation was found to influence the microstructures in many ways, including an increase in the overall size of the DNCs, while not affecting much the solvation of unmodified terminal (primary) amines. PEG at low densities are shown to form a thick layer that closely interacts with the surface of the dendrimer, providing a “barrier” that may impact the release profile of conjugated/adsorbed therapeutics, and how these nanocarriers interact with the physiological environment. The microstructure of PEG can be dramatically altered by modifying the number of grafts while keeping the overall number of PEG units constant. Grafting of 8PEG1000 to G3NH₂ produces a coat that partially extends out into the aqueous phase, while 16PEG500 grafts are more collapsed onto the surface of the dendrimer. This will have great implications on the use of PEG as a flexible linker to targeting moieties. The understanding of such microscopic structural information of PAMAM dendrimers has great implications in terms of the design of such carriers for drug and gene delivery and imaging applications.

CHAPTER 5

THE CHEMISTRY OF THE TERMINAL SURFACE GROUPS OF PAMAM DENDRIMERS DETERMINE THE MICROSTRUCTURE OF THE GRAFTED PEG LAYER

5.1. Introduction

Dendrimers are synthetic hyperbranched polymers, characterized by high size uniformity, low polydispersity, and the presence of multifunctional surface groups that are readily modifiable.[317-319] These characteristics make dendrimers very attractive for a variety of potential biomedical applications, including as nanocarriers for drug and gene delivery, and as imaging agents.[317, 320-322] Poly(amido amine) (PAMAM) dendrimers are one of the most studied dendrimer nanocarriers (DNCs). PAMAM dendrimers contain an alkyl-diamine core and tertiary amine branching points.[298] Because of their structure, PAMAM dendrimers contain a large number of surface groups per molecular volume.[323] Their surface groups can be neutral (e.g. hydroxyl –OH),[324] cationic (e.g. amine-terminated –NH₂) or anionic (e.g. carboxyl –COOH),[317, 325, 326] and the number of surface groups and overall size (molar mass) can be precisely controlled by varying their generation (G).

There are several strategies for loading the therapeutic cargo onto PAMAM DNCs. Biomacromolecules such as DNA and RNA,[327] as well as small molecules can be complexed with DNCs via electrostatic interactions.[328, 329] The therapeutic cargo can also be ‘encapsulated’ in the DNCs through hydrophobic interactions. Finally, drug molecules can be conjugated to DNCs through the formation of labile covalent bonds, for improved spacial and temporal drug release resolution.[330-332] Besides the loading of the therapeutic cargo, there are many advantages in modifying the DNCs with ligands in order to improve their interaction with

the physiological environment, and thus improve the pharmacokinetic profile of the therapeutics.[333] For example, arginine can be conjugated to PAMAM dendrimer to achieve enhanced gene transfections efficiency,[322] triphenylphosphonium can be conjugated to PAMAM dendrimer to target mitochondria,[302] folate can be conjugated to PAMAM dendrimer to target tumor cells that over express folate receptors.[334] PEG is a particularly popular ligand that is widely used to impart special characteristics to DNCs. PEG can help protect payload, improve biocompatibility of the carrier, decrease the rate of elimination form systemic circulation, modulate the transport across cellular barriers and also serve as a flexible linker between dendrimer and targeting moieties that can be used to better present ligands and promote targeting.[335-338]

The microstructure of the DNCs is crucial to their functions. They impact on the loading/encapsulation/conjugation (chemistry) of the therapeutic cargo, and how the DNCs interact with the physiological environment, and thus with their effectiveness as drug delivery carriers.[339] The chemistry of the surface terminal groups of DNCs in turn are expected to impact the structure of the DNCs as they are not only directly exposed and thus solvated by the physiological aqueous environment surrounding the carrier, but also control the balance of hydrophobic forces of the core (that tend to collapse the dendrimer structure) to repulsive (solvation, electrostatic repulsion or steric) forces of the terminal surface groups. The structure of DNCs can be to some extent assessed through small angle neutron scattering (SANS)[242, 340] or small angle x-ray scattering (SAXS).[277] However, there are certain limitations as to the extent of the microstructure that can be probed with those experimental techniques, and computational studies such as molecular dynamics (MD) simulations can provide atomistic-level information of the carriers, and thus serve as complementary tool to understand the microstructure of DNCs.

In light of the opportunities for PAMAM dendrimers discussed above, and the relevance of their structure in biomedical applications, in this work we probe the effect of the chemistry of the terminal surface groups of PAMAM dendrimers on their microstructure using MD simulations. We study three dendrimers with the same generation but varying the chemistry of the surface group: G3OH, G3NH₃⁺, and G2.5COO⁻. We also study the effect of conjugating PEG of 1000 Mw (PEG1000) onto the dendrimer surface, on the microstructure of the nanocarriers. We report results in terms of experimentally accessible variables, such as radius of gyration (R_g), and compare those with available experimental and computational information. We also discuss the microstructure of the solvent environment around the dendrimers, so as to understand the accessibility of primary functional groups to water molecules, or interactions between dendrimer terminal groups and PEG chain. Results are discussed from a drug / gene delivery perspective, that is, how the accessed microstructure information may impact the dendrimer as drug delivery carriers.

5.2. Methods and Models

All molecular dynamics (MD) simulations in our study were performed remotely on Kraken using NAMD 2.8.[264] The systems were visualized using VMD2.9.[265] The all-atom (AA) force field (FF) for the PAMAM dendrimers were developed from a combination of CHARMM 35 FF,[341, 342] and *ab initio* calculations performed in our laboratories. Bond distance, bond angle, dihedral, and van der Waals (vdW) potential parameters were from CHARMM 35 FF, while *ab initio* calculations were used to adjust the charge distribution within amido amine monomers. The terminal amines and carboxyl groups of dendrimers studied in this work are fully ionized to NH_3^+ and COO^- , thus representing physiological conditions.[343-345] Gaussian 09 was used at the MP2 level of theory and 6-31g(d) basis set for structural optimization of amido amine monomers.[164] We optimized for a fragment larger than a single amido amine monomer in the *ab initio* study to ensure that every atom in a single amido amine monomers is in a bonding environment that is similar to being in a dendrimer. Charge distributions were obtained from the CHELPG analysis.[346] Charge distribution of the residues were adjusted to achieve the realistic overall charge of the dendrimers in physiological condition, while maintaining those charges as close as possible to the original CHARMM 35 FF. The CHARMM 35 FF (C35r) was used for PEG.[347] The CHARMM TIP3PM FF was used as the water model for it has been shown to give reasonable structural and energetic results for pure water,[271] and is optimized for the CHARMM FF being used to treat the PAMAM dendrimers and PEG. We use the notation TIP3P (instead of TIP3PM) for now on for simplicity. 32 Cl^- ion were added to the solvation box in the system containing the amine-terminated dendrimers in order to neutralize the 32 NH_3^+ groups present at physiological pH. Similarly, 32 Na^+ ions were added to the solvation box in order to neutralize the 32 COO^- groups present in the carboxyl terminated dendrimers at physiological

conditions. Because G3OH is neutral at physiological pH, 16 Cl^- and 16 Na^+ were added to solvation box in order to achieve similar ionic strength to $G3NH_3^+$ and $G2.5COO^-$. The FF for ions (Na^+ and Cl^-) are from CHARMM 35. Further detail of the FF for G3OH and G3COOH can be found in supplemental information. The FF for NH_2 -terminated PAMAM dendriemr has been published by our group recently and is not repeated here.[348]

All simulations were performed in the isobaric-isothermal (NPT) ensemble at 298 K and 1 atm. Langevin thermostat and Langevin piston were used to maintain the desired temperature and pressure.[349] A 1 fs step length was used to conserve energy. A cutoff of 12 Å was applied for both vdW and electrostatic interactions. The vdW interactions were smoothly shifted to 0 from 10 to 12 Å, and the real part of electrostatic interactions was smoothly shifted to 0 from 0 to 12 Å. Particle mesh Ewardl (PME) was used to compensate for long-range electrostatic interactions. Periodic boundary conditions (PBC) were used in all directions.[350] The solvation boxes were carefully built such that PAMAM dendrimers or PEGylated PAMAM dendrimers did not see their own PBC copy, thus mimicking the desired infinite dilute solution of the dendrimers. The initial coordinates of the dendrimers were generated using GaussView 5.0.[351] A 20 ps minimization was performed to eliminate bad contacts in vacuum, and then the solvation (water) box was added to the system to equilibrate the solvated structures. The simulations were run for 27 ns. Statistics were taken from the last 2 ns of the runs.

5.3. Results and discussions

5.3.1. *Effect of terminal chemistry on size and shape of generation 3 PAMAM dendrimers*

5.3.1.1. *. Effect of terminal groups chemistry on the size of PAMAM dendrimers.* In order to understand the effect of the chemistry of the terminal surface groups of the PAMAM dendrimers

on their size, we determine the radius of gyration (R_g) of the G2.5COO⁻ and G3OH nanocarriers. The results for G3NH₃⁺ have been reported in our previous work.[348] R_g can be used to quantify the size of non-spherical objects, and it is also a relevant quantity to ascertaining the appropriateness of the all atom (AA) FFs proposed in this work as it can be directly compared to experiments such as small angle neutron scattering (SANS) and small angle x-ray scattering (SAXS) when available, or to previous simulation works.[242, 243, 248, 257, 340] Moreover, knowledge of the size of the dendrimers is of great importance as it is one of the key properties that determines their potential applicability, as is the case in the selection of dendrimers as nanocarriers for drug delivery applications.

The R_g for a dendrimer with N atoms is given by

$$R_g^2 = \frac{1}{M} \sum_{k=1}^N [m_k (r_k - r_{mean})^2] \quad \text{Equation 7}$$

where r_{mean} denotes the center of the dendrimer, $(r_k - r_{mean})$ denotes the distance of the k th atom from the center, m_k denotes the mass of the dendrimer. The evolution of R_g for the G3 PAMAM dendrimers as a function of the chemistry of the terminal surface groups are shown in **Figure 36**.

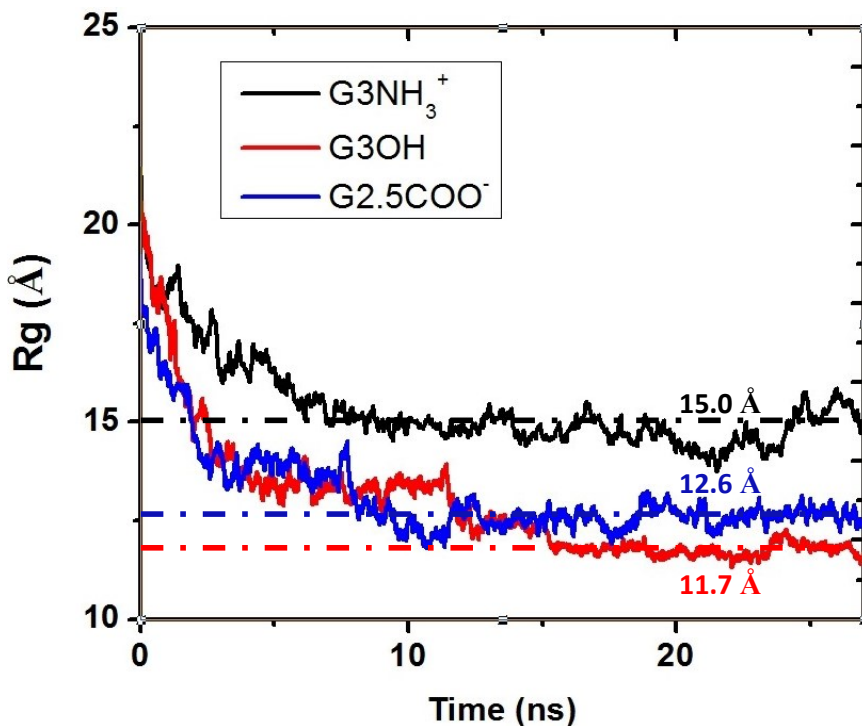


Figure 36. Time course of the radius of gyration (R_g) of generation 3 PAMAM dendrimers as a function of the chemistry of the terminal surface group. Average R_g 's were calculated from the last 10 ns of equilibration. NPT ensemble - 298K and 1 atm

R_g of $G3NH_3^+$ reported in our MD simulation not only is about average of those reported from all-atom model molecular dynamics simulations (10.4-19.7Å), but is also in close agreement with those reported from SANS and SAXS (14.7-16.5Å). While there is no experimental SANS or SAXS R_g results for $G3OH$ or $G2.5COO^-$, the close agreement between the experimental results and computational R_g values observed for $G3NH_3^+$, whose FF was the same except for terminal monomers, suggesting the appropriateness of the FF. It can be seen from **Figure 36** that the R_g for $G2.5COO^-$ is the smallest, as expected, due to its half generation. $G3OH$ has an $R_g = 12.6\text{Å}$, which is larger than that for $C2.5COO^-$ ($R_g = 11.7\text{Å}$), but significantly smaller than the R_g of 15.0Å found for $G3NH_3^+$ that has a similar MW. Because of the absence of surface charges that should balance the cohesive forces of the surface groups on the center of the dendrimer, $G3OH$ is significantly more collapsed than $G3NH_3^+$. [348]

5.3.1.2. *Effect of terminal groups chemistry on the shape of PAMAM dendrimers.* Screen shots of the equilibrium configurations of the different dendrimer structures are shown in **Figure 37**.

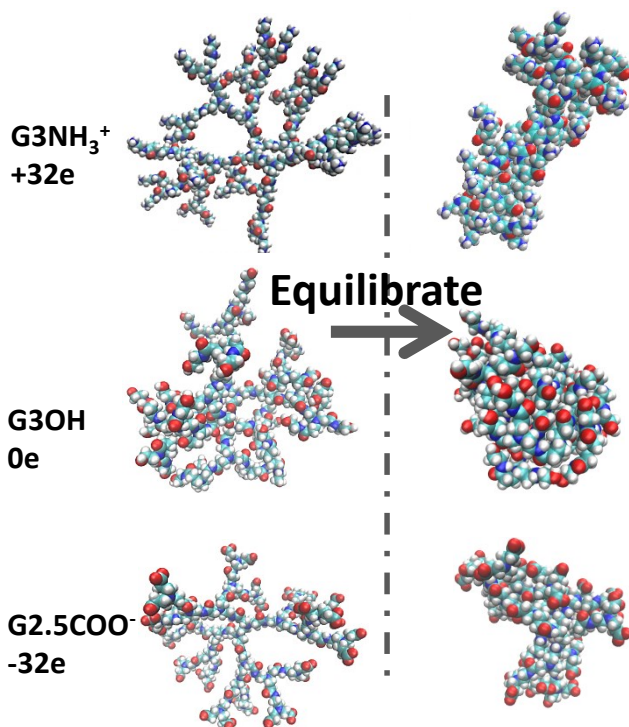


Figure 37. Snapshots of equilibrium conformations of generation 3 PAMAM dendrimer as a function of the chemistry of the terminal surface group. Atoms represented as VDW spheres. Snapshots of starting configurations are those taken after 20 ps of initial minimization. Equilibrium configurations are snapshots taken after 27 ns simulation time. Solvated (water) systems at 298K and 1 atm. Water and Cl⁻ / Na⁺ ions were removed from the snapshots to improve visualization of the dendrimers.

Further examination of the screenshots indicates that G3NH₃⁺ and G2.5COO⁻ assume a less dense packed structure when compared with G3OH. Again, this comes from the fact that G3NH₃⁺ and G2.5COO⁻ have charged terminal groups, giving rise to electrostatic repulsive forces that are able to prevent the core from collapsing, and consequently from assuming a more dense packed structure. Another effect of the charged terminal groups on the shape of the dendrimers is that, in an effort to enlarge average distances between charged terminal groups, the charged dendrimers

will try to maximize surface areas, and assume a non-globular structure, which has been described in the literature as “open” structures.[348]

The conformation of the PAMAM dendrimers is of great relevance with respect to their drug and gene carrier ability. During drug conjugation (via covalent bond) and complexation (via electrostatic forces) to load drug / gene onto dendrimer nanocarriers, it is most likely for the drug / gene to be trapped into “opening” of $G3NH_3^+$ and $G3COO^-$. Because by doing this, drug / gene will create the most contacts with surface groups of dendrimers, which maximize the electrostatic interactions or the chance to form covalent bonds. In terms of using dendrimers as drug carriers upon complex formations with therapeutic molecules, the “open” structure observed for $G3NH_3^+$ and $G2.5COO^-$ suggest that the use of the term “encapsulation” is somewhat misleading as no true “cavity” is present. The concept of an opening vs. cavity has been also discussed in the light of experimental SANS results.[348]

5.3.2. *Different terminal groups will lead to different microstructure of PEGylated DNCs*

5.3.2.1. *The chemistry of terminal surface groups greatly affects their location.* The surface chemistry of the PAMAM dendrimers is of relevance in drug delivery applications, as those characteristics will greatly influence how the nanocarriers interact with the physiological environment, and thus dictates various aspects of the efficacy and efficiency of dendrimer nanocarriers. The location of the terminal groups also impacts the ability to transform those surface groups, which is necessary in order to conjugate the therapeutic cargo and other ligands.

There has been a great deal of interest in understanding the location of terminal groups of PAMAM dendrimers.[276, 352, 353] While earlier reports suggested that the terminal amines of PAMAM would fold back into the core of the dendrimer,[276, 354, 355] our recent studies indicate

that there is no “back-folding” observed for NH₂-terminated PAMAM from G2-G5.[348] These studies were reconciled with experimental SANS and SAXS results that show terminal amine groups close to the core,[340] by demonstrating that the dendrimers have opened structures where ionized groups can remain close to the core and yet be fully solvated by the aqueous environment.

Here we discuss the effect of the chemistry of the terminal surface-groups on their position. In **Figure 38**, equilibrium conformation of all the three dendrimers are shown. The terminal surface groups (*N* for NH₃⁺, *O* for OH, ether *O* for COO⁻) are labeled as yellow vdW spheres and inner branching amines are labeled as blue vdW spheres. All other atoms and bonds are represented by colored lines.

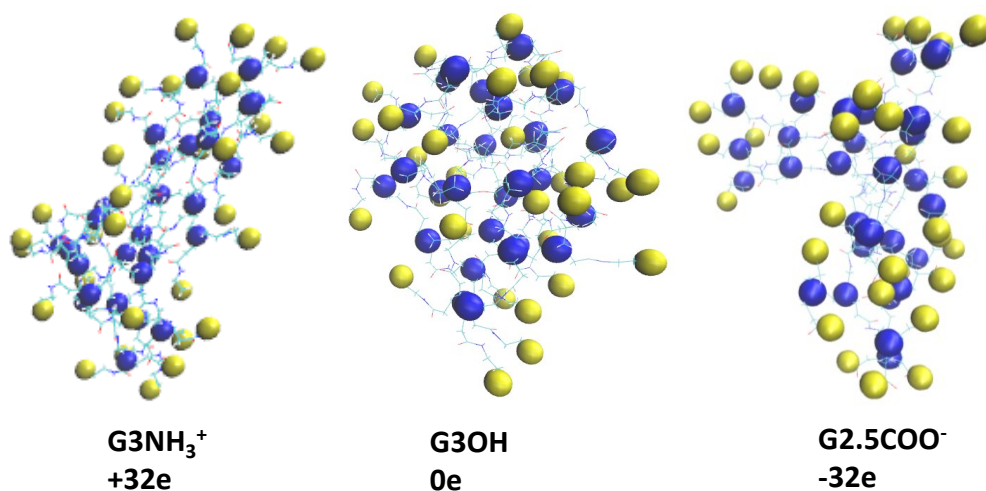


Figure 38. Snapshots of equilibrium conformations of generation 3 PAMAM dendrimer as a function of the chemistry of the terminal surface group after 27ns simulation time. Heavy atoms from terminal groups of PAMAM dendrimer are shown in yellow VDW spheres, branching amine atoms are shown in blue VDW spheres.

Through this qualitative representation, it can be seen that no “back-folding” is seen for G3NH₃⁺ or G2.5COO⁻, while for G3OH, some of the terminal groups do seem to insert themselves into the inner structures of the dendrimer. A study of the solvation profile of terminal groups can quantify the effect of terminal groups’ back-folding of G3OH.

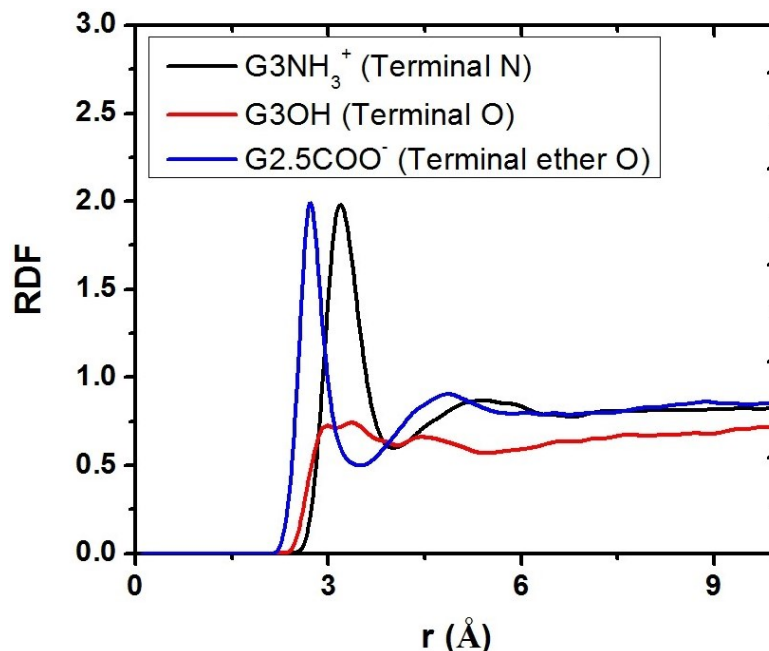


Figure 39. RDF of heavy atoms of terminal groups (terminal N for G3NH₃⁺, terminal O for G3OH, terminal ether O for G2.5COO⁻) to O atom of H₂O.

We have discussed in earlier publications that, there is no back-folding of terminal primary amines for G2NH₃⁺-G5NH₃⁺. And this conclusion is based on the fact that terminal primary amines of G2NH₃⁺-G5NH₃⁺ all have clear water solvation single peak. It can be seen from **Figure 39** that, G3NH₃⁺ and G2.5COO⁻ both have clear water solvation single peak, suggesting there is no back-folding of terminal groups of G2.5COO⁻. Which is reasonable as it will be thermodynamically unfavorable for charged terminal groups to insert themselves into PAMAM dendriemr core which is hydrophobic. While for G3OH, there is not a sharp and clear first solvation peak. Instead, the first peak split into two neighboring bumps. Two bumps means not all terminal groups are in identical solvation environment, and the only logical explanation is that there is back-folding of terminal groups for G3OH.

Given that the inner branching monomers of all three PAMAM dendrimers are identical, the difference between locations of terminal groups can only be attributed to the difference of terminal chemistry. In the absence of electrostatic repelling forces, G3OH collapses into a “globular”

structure, which has minimum surface area for that fixed volume. This leads to the back-folding of some of the terminal groups. Because the terminal group of G3OH (OH) is not charged at physiological pH, it is thermodynamically more acceptable that they are inserted into the hydrophobic core of the PAMAM dendrimer.

5.3.3. Effect of PEGylation on microstructures of PAMAM dendrimers with different terminal chemistry

In order to better discuss the effect of PEGylation, we focus on two issues that are 1) PAMAM dendrimer terminal chemistry's effect on PEG layer and 2) PEG chain's effect on microstructures of PAMAM dendrimer. DNC will be used to refer to PEGylated PAMAM dendrimers (including PEG part), while $G3NH_3^+$, G3OH, $G2.5COO^-$ will be used to refer to un-pegylated PAMAM dendrimers, PAMAM dendrimer core will be used to refer to dendrimer part of the pegylated PAMAM dendrimers.

5.3.3.1. PAMAM dendrimer terminal chemistry's effect on PEG layer

There are several benefits in PEGylation of dendrimers. PEG can increase solubility of the DNC, modulate release profile, reduce cytotoxicity of DNC and serve as flexible linker to better present targeting ligands to their receptors. All those benefits PEG has to offer are associated with PEG layer's microstructure – they are dependent on the right amount of PEG layer formation, right density of PEG attached, and right length of conjugated PEG chain.

In this study, PEGylation is seen to have significantly different microstructures based on different terminal chemistry. As we can see from **Figure 40** that for $G3NH_2$, PEG seem to be quite collapsed and tend to insert themselves into dendrimer opening. For G3OH, PEG chains are quite extended while for $G3COOH$, PEG chain is even more extended.

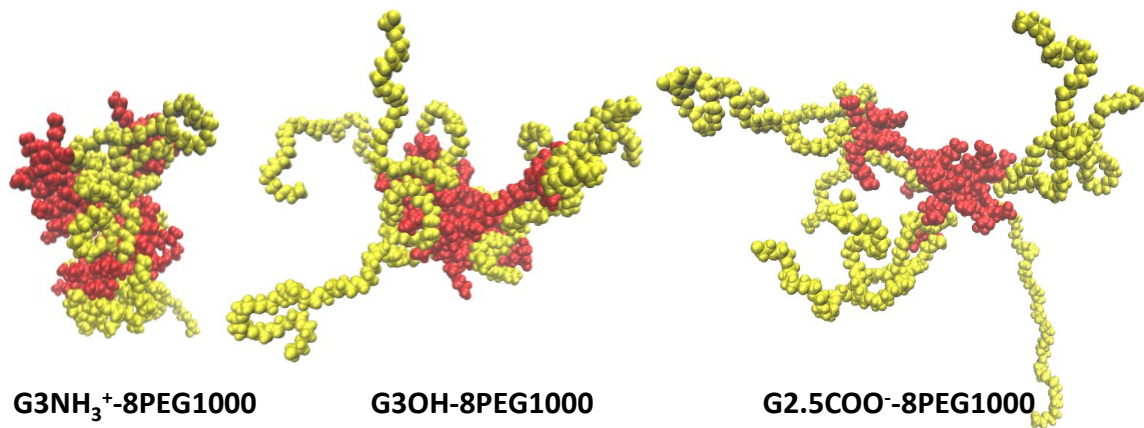


Figure 40. Snapshots of the equilibrium configurations of PEGylated G3 PAMAM dendrimers as a function of the chemistry of the terminal surface group. All dendrimers at a constant grafting density of 8 PEG, Mw. 1000. Dendrimer atoms represented in red and PEG atoms in yellow VDW spheres. Equilibrium configurations are snapshots taken after 27 ns simulation time. Solvated (water) systems at 298K and 1 atm. Water and Cl^- / Na^+ ions were removed from the snapshots to improve visualization of the dendrimers.

Terminal groups' effect on PEG microstructure is not discussed before, but it was reported previously that for G2-G5 NH₂ terminated PAMAM dendrimers, conjugated PEG chain all adhere to the surface or opening of the dendrimers.[348] The collapsed PEG microstructures have great implications in the development of active targeting nanocarriers. First, targeting ligands located in the end of flexible PEG chains most likely will be buried in PEG chains within dendrimer opening, which will have much less chance to interact with their receptors compared to those with PEG extended to bulk physiological environment, and thus the DNCs' function of targeting is compromised. Also, the presence of a PEG layer adheres to the surface / opening of dendrimers will create a diffuse barrier for the release of payload inside DNCs, thus modulating the release profile of the DNC. G3NH₂ is thus expected to have a significant different behavior upon PEGylation concerning ease of conjugation, solubility enhancement upon PEGylation, release profile and toxicity profile when compared with G3OH and G3COOH.

While **Figure 40** depicts qualitatively the microstructures of PEG that are conjugated to PAMAM dendrimers, MD study also enable us to use more atomic scale tools to study quantitatively the interactions between terminal groups of PAMAM dendrimer and PEG chain.

Figure 41 shows the integrated radial distribution function (RDF) between heavy atoms of terminal groups of PAMAM dendrimers to the heavy atoms of PEG chain (O).

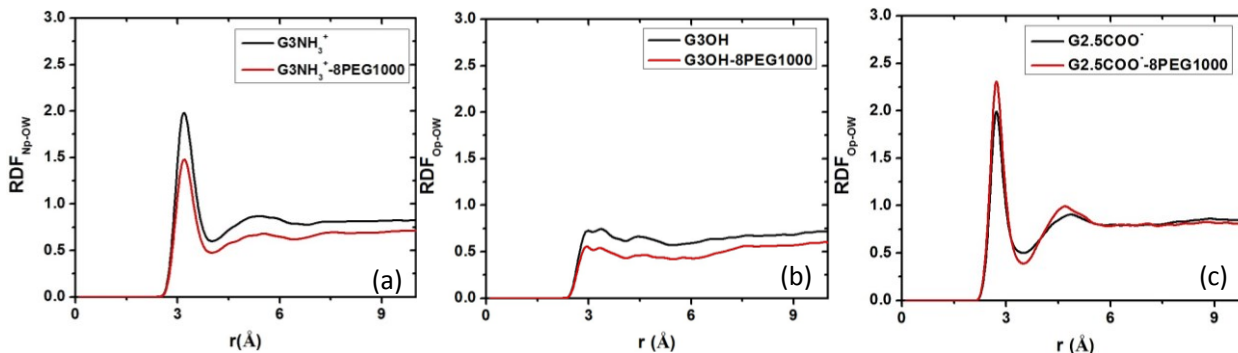


Figure 41. Solvation profile of primary functional of G3 PAMAM dendrimers by water. Solvation profile before and after PEGylation. (a) NH_3^+ terminated (N atom), (b) OH terminated (O atom), (c) COO^- terminated (ether O atom).

It can be seen from **Figure 41** that, in each layer of a certain distance to heavy atoms from terminal group of PAMAM dendrimers - N atoms from terminal groups of G3NH_2 has most O from PEG, which means G3NH_2 terminal groups interact the most with PEG chain, while G3COOH terminal groups interact the least with PEG chain. It was proposed before that the collapse of PEG chain for PEGylated NH_2 terminated PAMAM dendrimer is caused by electrostatic interactions between positively charged NH_2 groups from PAMAM dendrimers and negatively charged O atom from PEG chain. Terminal chemistry of PAMAM dendrimers' effect on PEG microstructure observed in this study confirmed again that positively charged terminal groups (NH_3^+) will interact strongly with PEG chain. Although PEG is neutral in physiological pH, but the O atom in PEG chain carry a negative partial charge that is known to be enough for strong electrostatic interactions like hydrogen bond.[356]

It is clear from **Figure 41** that PEG interacts strongly with positively charged NH_3^+ terminal group when compared with OH terminal group, and the electrostatic interactions forces will have significant effect on PEG's microstructures (more collapsed) as shown in **Figure 40**. While it is also observed from Figure 5 that negatively charged COO^- terminal group interact less with PEG chain when compared with OH terminal group, no significant effect on PEG's microstructures can be seen from **Figure 40**. The effect of the difference between COO^- and OH seen in **Figure 41** will be seen on microstructures of PAMAM dendrimers (sec. 3.3.2).

5.3.3.2. Effect of PEGylation on PAMMA dendrimers' microstructure

Terminal group chemistry of PAMAM dendrimers will affect microstructures of PEG, and PEG will also affect microstructures of PAMAM dendrimers to which it is conjugated in multiple ways. By conjugating a PEG chain onto one terminal group of charged PAMAM dendrimers (G3NH_3^+ , G2.5COO^-), the charge associated with that terminal group will be eliminated in this process. Less charge leads to less electrostatic repelling forces, which will affect size and shape of PAMAM dendrimer.

PAMAM dendrimers' structure can be seen as a hydrophobic core shelled by hydrophilic terminal monomers. The hydrophilic shell becomes more hydrophilic upon PEGylation, which will serve to stretch the inner hydrophobic core more toward water. Upon PEGylation, terminal groups will no longer reside in the outer shell of dendrimers. This could have a few effects on DNC's functions. One of the major effects is that PEG layer will change the way terminal groups are presented to physiological environment.

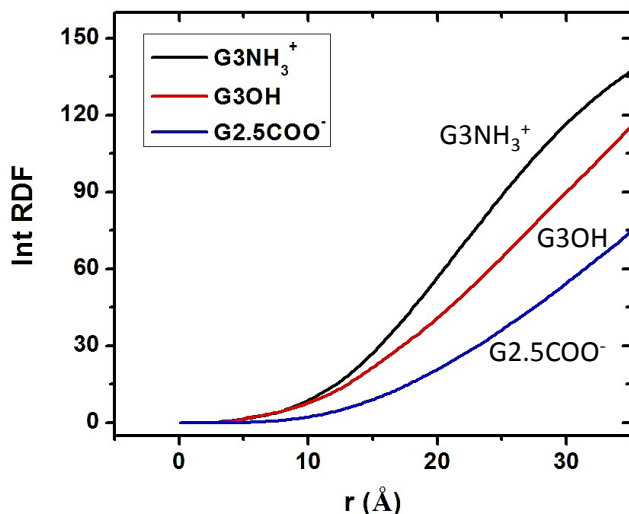


Figure 42. Integral of the radial pair distribution function (RDF) of the terminal heavy atoms (N for NH_3^+ , O for OH, O for COO^-) of G3 PAMAM dendrimers to oxygen (O) atoms of the PEG chain.




As can be seen from **Figure 42**, PEGylation will change water accessibility of terminal group for all three dendrimers. It is not surprising to see that for G3NH_3^+ and G3OH, PEGylation cut down the water accessibility of terminal groups. By surrounding PAMAM dendrimers they conjugated to, PEG will limit to some extent water accessibility naturally.

But for G2.5COO^- , water accessibility of terminal groups is found to be slightly increased after PEGylation as shown in **Figure 42**. This is related to the change in microstructures of G2.5COO^- after PEGylation. Because G2.5COO^- has the least interaction with PEG chain, one effect is that PEG chain is stretched into water rather than closely surrounding G2.5COO^- , so G2.5COO^- is minimally shielded by the existence of the PEG layer. Another effect is that G2.5COO^- is stretched by PEG chain to a “star” shaped conformation. During this microstructure transformation, terminal groups’ local environment is changed from being presented next to a surface to being presented as the end of a branch of the “star”. Geometrically being in the end of a branch of the “star” will have more accessibility to water.

The start shape of PEGylated G2.5COO⁻ will also have profound effect on DNCs' efficacy and efficiency in drug delivery. G2.5COO⁻-8PEG1000 thus can benefit the most from PEG's solvation enhancement, while still present modifiable terminal groups quite well when compared to G3NG₃⁺. This could make a huge difference when it comes to certain applications where payload needs to be conjugated to PAMAM dendrimer terminal groups after PEGylation. For example, in order to conjugate both payload and PEG onto terminal groups of PAMAM dendrimers, it is desirable to have PEG first conjugated just to minimize the exposure of the payload to reactions. Also for some payload which carries charge, it is hard for chemical reactions to happen because electrostatic forces will either be attractive and help to form strong complex or to repel. So it is also important that PEG be conjugated first so to decrease zeta potential of PAMAM dendrimers.

The interactions between PEG and dendrimers are also reflected by size. Dendrimer terminal chemistry's effect on microstructures of PEG chain can be seen from R_g of PEGylated PAMAM dendrimers. PEG chains' effect on PAMAM dendrimers' microstructure can be seen from R_g of the dendrimer part of PEGylated PAMAM dendrimers. R_g calculated from different part of DNCs are demonstrated and summarized in **Table 1**.

Table 13 Radius of gyration (R_g) of equilibrated DNCs. For PEGylated PAMAM dendrimers, R_g of the whole molecule as well as R_g of the dendrimer part of the molecule (PEG chain excluded) were calculated and compared.

	$R_g(\text{Å})$	$G3NH_3^+$	$G3OH$	$G3COO^-$
	Dendrimer without pEGylation	15.0±0.9	12.6±0.8	11.7±0.8
	PEGylated dendrimer	17.3±0.2	22.2±0.6	29.5±1.1
	Dendrimer part of pEGylated dendrimer	15.3±0.2	13.9±0.5	14.0±0.6

It is not surprising to see that PEGylated G3 PAMAM dendrimers are bigger than un-PEGylated G3 PAMAM dendrimers. Different terminal chemistry will affect microstructures of PEG layer, and this can also be reflected by their R_g increase upon PEGylation. For $G3NH_3^+$, R_g increases only 2.28 Å (from 15.0 Å to 17.28 Å) upon PEGylation. While for $G3COO^-$, R_g increases 17.77 Å upon PEGylation (from 11.7 Å to 29.5 Å) (**Table 13**).

PEG will have three major effect on size of dendrimer part of the conjugate. PEG is well solvated by water, and this solvation provides an outward force pull on the dendrimer part, which results in the swelling of the dendrimer part inside. Also for charged PAMAM dendrimers like $G3NH_3^+$ and $G2.5COO^-$, every PEG chain conjugated will neutralize 1 charged site from the terminal groups and decrease electrostatic forces, which results in the shrinking of the dendrimer part inside. The third effect is that PEG interacts with PAMAM dendrimers, and PEG layer's

microstructure will greatly change the way how its solvation force can serve to pull the dendrimer core outward.

We can see from **Table 1** that dendrimer part of $G3NH_3^+-8PEG1000$ (15.3Å) does not show much difference in size from $G3NH_3^+$ (15.0Å), which means the swelling effect from solvation force provided by PEG is similar in magnitude to the shrinking effect from less electrostatic force by conjugation of PEG. The dendrimer part of $G2.5COO^-8PEG1000$ (14.0) is significantly bigger than the size of $G3COO^-$ (11.7). Although the neutralization of charged terminal groups and the length and number of PEG chain is the same for both $G3NH_3^+-8PEG1000$ and $G3COO^-8PEG1000$, PEG's microstructure is quite different.

The difference can be attributed to different microstructures of PEG layer for $G3NH_3^+$ and $G2.5COO^-$. As mentioned above, PEG conjugated onto $G3NH_3^+$ has the most collapsed microstructure which contributes to least increase in R_g upon PEGylation, and PEG conjugated onto $G2.5COO^-$ has the least collapsed microstructure. The less collapsed PEG microstructure contribute to the much bigger outward pulling force for dendrimer part of $G3COO^-8PEG1000$, thus contribute to the biggest increase in R_g upon PEGylation.

5.4. Conclusions

In this work, we investigated the microstructures of generation 3(or 2.5) PAMAM dendrimers of different terminal chemistry, and how PEG affect their microstructures differently. Due to surface charge at physiological condition, $G3NH_3^+$ and $G3COO^-$ assume a less dense packed, "open" microstructure. With no surface charge at physiological condition, $G3OH$ has a more densely packed microstructure. The difference in microstructure can be reflected on the solvation profile of heavy atoms from terminal groups of PAMAM dendrimers, which is critical for PAMAM dendrimers' biomedical applications. O atom in PEG chain has negative partial charges

that are capable of strong electrostatic interactions. And as a consequence, PEG conjugated to positively charged $G3NH_3^+$ has the most collapsed microstructures while PEG conjugated to negatively charged $G3COO^-$ has the least collapsed microstructures. Terminal groups chemistry will affect PEG layers' microstructures, and PEG layers' microstructures also will affect PAMAM dendrimers to which it is conjugated. PEGylation can change the way terminal groups' water accessibility, and thus PAMAM dendrimers' behavior in biomedical applications. PEG can serve to swell the dendrimer part by solvation force pulling outward, and to shrink the dendrimer part by decrease electrostatic forces. $G3NH_3^+-8PEG1000$ has the least increase in R_g of dendrimer part compared with $G3NH_3^+$ because the more collapsed PEG chain provide less solvation force pulling outward. $G3COO^-$ has the most increase in R_g of dendrimer part when compared with $G3COO^-$ because it has the least collapsed PEG chain, thus the most solvation forced pulling outside from PEG chain.

CONCLUSIONS

In Chapter one we studied the solvation of relevant tail fragments in HFO-1234ze using *ab initio* calculations. The chemistries investigated are representative of additives of interest to the various industries where HFOs may find use as working fluids. The tail fragments were selected to allow us to systematically probe the effect of both polarity and structure (degree of branching) on their solvation by HFOs. Binding energies between the HFO-1234ze solvent (*s*) and the tail fragment (*t*) (E_b^{st}) indicate that the more polar ether- (*EO* and *PO*) and ester-based fragments (*GA*, *LA* and *TMGA*) are well-solvated by HFO-1234ze with E_b^{st} 's of ca. -20 kJ.mol⁻¹. The non-polar alkane-based fragments (*C5* and *ISO*) are not solvated to the same extent, with E_b^{st} 's of ca. -9 kJ.mol⁻¹. However, polarity alone cannot be used to predict or discriminate which of the polar groups are best solvated. The self-interaction between the tail fragments (E_b^{tt}) is used to determine a quantity termed the Enhancement Factor (E_{enh}), which is defined as the ratio between E_b^{st} / E_b^{tt} . Based on this definition, the E_{enh} is expected to be a better predictor of the solvation of a particular fragment compared to E_b^{st} alone, and can be used to further discriminate the effect of fragment chemistry/structure on their solvation. Because the interaction between *GA-GA* is much stronger than that between *EO-EO*, the E_{enh} for the *EO* is much greater – the largest from all investigated fragment at $E_{enh} = 1.30$. This quantity, E_{enh} , thus allow us to further discriminate solvation in HFO. Different from polarity, the branching of the tail chemistry is seen to have little effect on E_b^{st} . However, at high enough branching densities, it can significantly impact tail-tail interaction. While E_b^{tt} for *GA-GA* (no CH₃ pendant group) is > -25 kJ.mol⁻¹, that for *TMGA-TMGA* (two CH₃ pendant groups) is ca. -15 kJ.mol⁻¹. Branching can serve to reverse the trend in E_{enh} . While for *GA* (no branching) and *LA* (one methyl pendant group) E_{enh} is less than one; that for *TMGA* (two methyl pendant groups) E_{enh} is greater than one (1.27), and very close to that for *EO*. These results suggest that the structure of the tail fragment will also have a significant impact in its solvation,

along with the polarity. We also determined that the solvation in HFO-1234ze is similar to that of a working fluid currently being used in the industry, the HFA-134a. In summary, the results shown here provide information that can be utilized to further evaluate the potential of this new generation of greener working fluids, the HFOs, in replacing the HFAs.

In Chapter 2 we used a combined computational and experimental approach to rationally design surfactants for the HFO-1234ze|H₂O interface. A recently developed 12-6LJ FF for HFO-1234ze was shown to quantitatively predict the experimental surface tension of HFO-1234ze as a function of temperature, thus establishing the relevance of the model to interfacial systems. MD results for the tension of HFO-1234ze|SPC/E H₂O interface ($40.9\text{mN}\cdot\text{m}^{-1}$) was shown to be also in quantitative agreement with the experimental value obtained in this work ($41.9\text{mN}\cdot\text{m}^{-1}$) using a high-pressure pendant drop tensiometer. MD simulations were then used to understand the behavior of non-ionic (*EO*-based) surfactants with tail chemistries of systematically varying polarity: *CH* (*EO-CH*); *PO* (*EO-PO*) and *LA* (*EO-LA*). The interfacial tension and structural information from MD simulations of the surfactant-modified interface provided a microscopic view to understand the surfactant effect, and to screen the most appropriate tail chemistry. The *EO-PO* surfactant was found to be the most active at the HFO-1234ze|H₂O interface, with an interfacial tension reduction of $28.7\text{mN}\cdot\text{m}^{-1}$. Once the best chemistry was identified, MD simulations were used to determine the optimum surfactant balance; i.e. the ratio of the *EO* head-group to *PO* tail-group that would reduce the tension of the interface the most, which is defined as the hydrophilic-to-HFO-philic balance (HFB). The HFB was determined to be located at ca. $62\text{wt}\% \text{EO}$. The trend in tension vs. $\text{wt}\% \text{EO}$ from the MD results are in good agreement with the experimental values found for the tri-block *EO-PO-EO*, with the observed differences being attributed to the difference in structure of the two surfactant classes and in the MW. The experimental HFB for *EO-PO-EO* was

found to be at ca. 45 wt.%EO. The low tension values obtained for the surfactants close to the optimum balance suggest that they are capable of forming emulsions and potentially microemulsions of systems involving HFO-1234ze and water. The relevance of this work stems from the fact that this is the first time that the properties of the bare and surfactant modified HFO-1234ze|H₂O interface has been reported – either experimental or computational results. In summary, the results suggest HFO-1234ze may be a suitable alternative to HFAs in the formation of aerosols containing dispersions of water and HFO-1234ze for medical applications.

In Chapter 3 we investigated the microstructure of PEGylated, amine-terminated PAMAM dendrimers using molecular dynamics (MD) simulations with fully atomistic models. We show that the proposed force field (FF) for the PAMAM dendrimers is capable of correctly capturing available SAXS and SANS experimental information on their size – R_g . We also show that G4NH₂ and G5NH₂ have a “segmented opened” structure that allows for the primary amines to locate close to the dendrimer core, without “back-folding”. We provide here an alternative view to the concept of back-folding in protonated PAMAM dendrimers. Our results point to a thermodynamically favorable structure where primary amines may reside close to the core, and are yet on the dendrimer’s surface, a configuration that can be assumed in such segmented open structures observed here. These results can be reconciled with experimental SANS/SAXS studies and yet represent a thermodynamically favorable conformation. Primary amines for G2NH₂-G5NH₂ are shown to reside in outer shells, and their solvation peaks remain the same. PEGylation was found to influence the microstructures in many ways, including an increase in the overall size of the DNCs, while not affecting much the solvation of unmodified terminal (primary) amines. PEG at low densities are shown to form a thick layer that closely interacts with the surface of the dendrimer, providing a “barrier” that may impact the release profile of conjugated/adsorbed therapeutics, and

how these nanocarriers interact with the physiological environment. The microstructure of PEG can be dramatically altered by modifying the number of grafts while keeping the overall number of PEG units constant. Grafting of 8PEG1000 to G3NH₂ produces a coat that partially extends out into the aqueous phase, while 16PEG500 grafts are more collapsed onto the surface of the dendrimer. This will have great implications on the use of PEG as a flexible linker to targeting moieties. The understanding of such microscopic structural information of PAMAM dendrimers has great implications in terms of the design of such carriers for drug and gene delivery and imaging applications.

In Chapter 4, we investigated the microstructures of generation 3(or 2.5) PAMAM dendrimers of different terminal chemistry, and how PEG affect their microstructures differently. Due to surface charge at physiological condition, G3NH₃⁺ and G3COO⁻ assume a less dense packed, “open” microstructure. With no surface charge at physiological condition, G3OH has a more densely packed microstructure. The difference in microstructure can be reflected on the solvation profile of heavy atoms from terminal groups of PAMAM dendrimers, which is critical for PAMAM dendrimers’ biomedical applications. O atom in PEG chain has negative partial charges that are capable of strong electrostatic interactions. And as a consequence, PEG conjugated to positively charged G3NH₃⁺ has the most collapsed microstructures while PEG conjugated to negatively charged G3COO⁻ has the least collapsed microstructures. Terminal groups chemistry will affect PEG layers’ microstructures, and PEG layers’ microstructures also will affect PAMAM dendrimers to which it is conjugated. PEGylation can change the way terminal groups’ water accessibility, and thus PAMAM dendrimers’ behavior in biomedical applications. PEG can serve to swell the dendrimer part by solvation force pulling outward, and to shrink the dendrimer part by decrease electrostatic forces. G3NH₃⁺-8PEG1000 has the least increase in R_g of dendrimer

part compared with $G3NH_3^+$ because the more collapsed PEG chain provide less solvation force pulling outward. $G3COO^-$ has the most increase in R_g of dendrimer part when compared with $G3COO^-$ because it has the least collapsed PEG chain, thus the most solvation forced pulling outside from PEG chain.

We have Chapter 1 and Chapter 2 dedicated to systemically screening and optimization of biocompatible moieties for the steric stabilization of suspension formulations in HFO-based propellants (Aim #1), by utilizing ab initio calculations, molecular dynamics simulations and high pressure tensiometry. We have Chapter 3 and Chapter 4 dedicated to design PAMAM functional dendrimer nanocarriers for the delivery of therapeutics to and through the lungs (Aim #2), by studying their microstructures using molecular dynamics simulation. Those results and discussions all contribute to the development of pressurized metered dose inhalers (pMDIs).

APPENDIX A: SUPPLEMENTAL INFORMATION FOR CHAPTER 2

Table S1: Partial charge distribution of the HFA-134a and ester-based tail fragment pairs. Partial charges are obtained at the MP2 level of theory and aug-cc-pVDZ basis set, from geometries optimized at MP2/6-31g+(d,p). Change in atom charge (Δ) is relative to the charge of the propellant or tail when not interacting. Bold atoms are involved in “strong interactions”, in which O··H or F··H distances $< 3 \text{ \AA}$. Atom numbers correspond to those shown in **Figure 9**. Tail fragments are: glycolic acid (*GA*), lactic acid (*LA*), and tetramethyl glycolic acid (*TMGA*).

HFA-134a-GA			HFA-134a-LA			HFA-134a-TMGA		
	charge	Δ		charge	Δ		charge	Δ
H₁	0.103	-0.007	H₁	0.089	-0.021	H₁	0.095	-0.015
C ₂	0.057	0.039	C ₂	0.08	0.062	C ₂	0.063	0.045
C ₃	0.497	-0.037	C ₃	0.492	-0.042	C ₃	0.543	0.009
H ₄	0.098	-0.012	H ₄	0.094	-0.016	H ₄	0.095	-0.015
F₅	-0.215	-0.008	F₅	-0.218	-0.011	F₅	-0.22	-0.013
F₆	-0.19	0.025	F ₆	-0.2	0.015	F₆	-0.211	0.004
F₇	-0.162	0.014	F₇	-0.139	0.037	F₇	-0.17	0.006
F ₈	-0.188	-0.012	F ₈	-0.192	-0.016	F ₈	-0.198	-0.022
C ₉	0.146	0.04	C ₉	0.094	0.014	C ₉	-0.025	0.03
H₁₀	0.019	-0.02	H ₁₀	0.04	-0.008	H₁₀	0.066	-0.015
H ₁₁	0.064	0.01	H ₁₁	0.069	0.011	H ₁₁	0.087	-0.005
H ₁₂	0.026	-0.013	H₁₂	0.031	-0.011	H ₁₂	0.069	-0.012
C ₁₃	0.773	0.019	C ₁₃	0.625	-0.093	C ₁₃	0.599	-0.032
C ₁₄	-0.157	-0.045	C ₁₄	0.217	0.099	C ₁₄	0.359	0.034
H ₁₅	0.046	0.008	H ₁₅	-0.037	-0.02	C ₁₅	-0.311	0.03
H₁₆	0.056	0.018	C ₁₆	-0.161	0.085	H ₁₆	0.057	-0.016
C ₁₇	0.014	0.047	H ₁₇	0.049	-0.027	H ₁₇	0.067	-0.011
H ₁₈	0.021	-0.008	H₁₈	0.029	-0.027	H₁₈	0.072	-0.001
H₁₉	-0.007	-0.016	H ₁₉	0.028	-0.019	O ₁₉	-0.324	0.005
H ₂₀	-0.001	-0.01	O ₂₀	-0.403	0.03	O₂₀	-0.521	-0.002
O ₂₁	-0.465	-0.008	O₂₁	-0.505	0.021	C ₂₁	-0.245	-0.024
O₂₂	-0.537	-0.013	C ₂₂	-0.268	-0.132	H ₂₂	0.032	0
			H ₂₃	0.047	0.023	H ₂₃	0.064	0.004
			H₂₄	0.065	0.032	H ₂₄	0.045	0.006
			H ₂₅	0.073	0.025	C ₂₅	-0.195	0.026
						H ₂₆	0.028	-0.004
						H ₂₇	0.049	-0.011
						H₂₈	0.029	-0.01

Table S2: Partial charge distribution of the HFA-227 and ester-based tail fragment pairs. Partial charges are obtained at the MP2 level of theory and aug-cc-pVDZ basis set, from geometries optimized at MP2/6-31g+(d,p). Change in atom charge (Δ) is relative to the charge of the propellant or tail when not interacting. Bold atoms are involved in “strong interactions”, in which O··H or F··H distances $< 3 \text{ \AA}$. Atom numbers correspond to those shown in **Figure 10**. Tail fragments are: glycolic acid (*GA*), lactic acid (*LA*), and tetramethyl glycolic acid (*TMGA*).

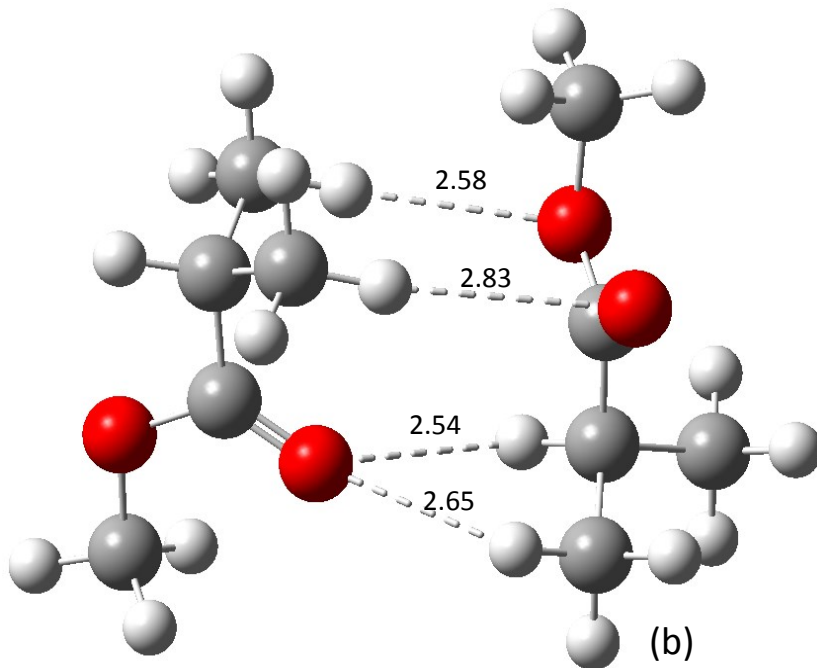
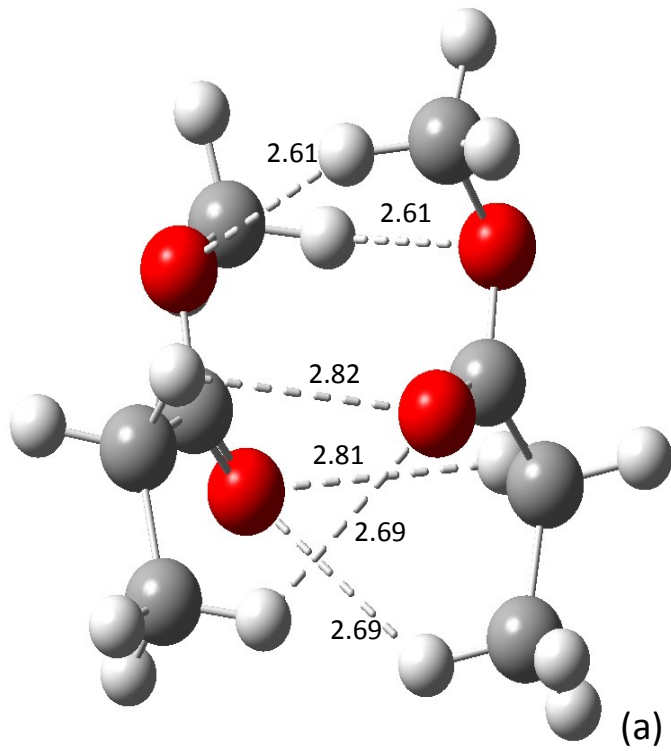
HFA227-GA			HFA227-LA			HFA227-TMGA		
	charge	Δ		charge	Δ		charge	Δ
H1	0.18	-0.008	H1	0.16	-0.028	H1	0.176	-0.012
C2	-0.077	0.054	C2	0.015	0.146	C2	-0.019	0.112
C3	0.566	0.025	C3	0.51	-0.031	C3	0.51	-0.031
F4	-0.179	-0.011	F4	-0.155	0.013	F4	-0.157	0.011
F5	-0.192	-0.012	F5	-0.168	0.012	F5	-0.179	0.001
F6	-0.169	-0.018	F6	-0.176	-0.025	F6	-0.167	-0.016
C7	0.502	-0.039	C7	0.579	0.038	C7	0.59	0.049
F8	-0.159	-0.018	F8	-0.194	-0.053	F8	-0.188	-0.047
F9	-0.154	-0.003	F9	-0.173	-0.022	F9	-0.177	-0.026
F10	-0.155	0.025	F10	-0.215	-0.035	F10	-0.211	-0.031
F11	-0.162	0.006	F11	-0.186	-0.018	F11	-0.186	-0.018
C12	-0.002	0.031	C12	-0.219	0.027	C12	-0.291	0.05
H13	-0.003	-0.012	H13	0.045	-0.002	H13	0.06	-0.013
H14	0.027	-0.002	H14	0.045	-0.011	H14	0.059	-0.014
H15	0	-0.009	H15	0.066	-0.01	H15	0.072	-0.006
C16	-0.127	-0.015	C16	0.151	0.033	C16	0.0317	-0.2933
H17	0.049	0.011	H17	-0.021	-0.004	C17	0.626	-0.005
H18	0.043	0.005	C18	0.651	-0.067	C18	-0.05	0.016
C19	0.767	0.013	C19	0.08	0	H19	0.088	0.007
C20	0.164	0.058	H20	0.052	0.004	H20	0.095	0.003
H21	0.029	-0.01	H21	0.071	0.003	H21	0.078	-0.003
H22	0.062	-0.002	H22	0.044	0.002	O22	-0.322	0.007
H23	0.011	-0.028	O23	-0.391	0.042	O23	-0.544	-0.025
O24	-0.469	-0.012	O24	-0.544	-0.018	C24	-0.262	-0.041
O25	-0.543	-0.019	C25	-0.147	-0.012	H25	0.076	0.016
			H26	0.052	0.004	H26	0.046	0.014
			H27	0.025	0.001	H27	0.047	0.008
			H28	0.026	-0.007	C28	-0.242	-0.021
						H29	0.066	0.006
						H30	0.051	0.012
						H31	0.041	0.009

Table S3(a). Partial charge distribution of the HFO-1234ze and tail fragment pairs. Partial charges are obtained at the MP2 level of theory and aug-cc-pVDZ basis set, from geometries optimized at MP2/6-31g+(d,p). Change in atom charge (Δ) is relative to the charge of the propellant or tail when not interacting. Bold atoms are involved in “strong interactions”, in which O··H or F··H distances $< 3 \text{ \AA}$. Atom numbers correspond to those shown in **Figure 9**. Tail fragments are: pentane (*C5*), iso-hexane (*ISO*), ethylene oxide (*EO*), propylene oxide (*PO*).

	HFO-1234ze-ISO		HFO-1234ze-EO		HFO-1234ze-PO			
	charge	Δ	charge	Δ	charge	Δ		
H1	0.207	-0.026	H1	0.188	-0.045	H1	0.279	0.046
H2	0.103	-0.018	H2	0.143	0.022	H2	0.106	-0.015
C3	0.22	0.002	C3	0.129	-0.089	C3	0.204	-0.014
C4	-0.348	0.041	C4	-0.212	0.177	C4	-0.364	0.025
C5	0.601	-0.035	C5	0.446	-0.19	C5	0.544	-0.092
F6	-0.216	-0.003	F6	-0.205	0.008	F6	-0.193	0.02
F7	-0.204	0.004	F7	-0.147	0.061	F7	-0.194	0.014
F8	-0.185	0.023	F8	-0.147	0.061	F8	-0.195	0.013
F9	-0.183	-0.003	F9	-0.178	0.002	F9	-0.176	0.004
C10	-0.299	0.03	C10	-0.108	0.086	C10	-0.327	-0.007
H11	0.063	-0.009	H11	0.033	0	H11	0.074	0.008
H12	0.052	-0.008	H12	0.015	-0.043	H12	0.091	0.014
H13	0.049	-0.013	H13	0.039	-0.019	H13	0.082	-0.002
C14	0.372	-0.026	C14	0.221	-0.157	C14	0.48	-0.048
H15	-0.066	0	C15	-0.008	0.037	H15	-0.034	0.016
C16	0.162	-0.058	C16	-0.002	0.043	C16	0.363	-0.021
H17	-0.034	0.019	C17	0.219	-0.159	H17	-0.036	-0.005
H18	-0.013	0.024	H18	-0.004	0.041	H18	-0.024	0.024
C19	-0.196	-0.028	H19	-0.009	0.036	C19	-0.215	-0.005
H20	0.049	0.016	C20	-0.086	0.108	H20	0.045	-0.009
H21	0.037	0.009	H21	0.009	-0.049	H21	0.046	0.016
H22	0.043	0.015	H22	0.028	-0.005	H22	0.067	0.013
C23	-0.229	0.069	H23	0.033	-0.025	O23	-0.524	0.001
H24	0.026	-0.04	O24	-0.398	0.089	C24	-0.277	0.065
H25	0.05	0.007				H25	0.052	-0.046
H26	0.045	-0.014				H26	0.064	0.003
C27	-0.175	-0.029				H27	0.06	-0.008
H28	0.032	0.019						
H29	0.039	0.022						

Table S3(b). Partial charge distribution of the HFO-1234ze and ester-based tail fragment pairs. Partial charges are obtained at the MP2 level of theory and aug-cc-pVDZ basis set, from geometries optimized at MP2/6-31g+(d,p). Change in atom charge (Δ) is relative to the charge of the propellant or tail when not interacting. Bold atoms are involved in “strong interactions”, in which O··H or F··H distances $< 3 \text{ \AA}$. Atom numbers correspond to those shown in **Figure 11**. Tail fragments are: glycolic acid (*GA*), lactic acid (*LA*), and tetramethyl glycolic acid (*TMGA*).

	HFO-1234ze-GA		HFO-1234ze-LA		HFO-1234ze-TMGA			
	charge	Δ	charge	Δ	charge	Δ		
H1	0.213	-0.02	H1	0.222	-0.011	H1	0.23	-0.003
H2	0.134	0.013	H2	0.125	0.004	H2	0.125	0.004
C3	0.162	-0.056	C3	0.183	-0.035	C3	0.183	-0.035
C4	-0.26	0.129	C4	-0.304	0.085	C4	-0.316	0.073
C5	0.455	-0.181	C5	0.545	-0.091	C5	0.546	-0.09
F6	-0.194	0.019	F6	-0.213	0	F6	-0.206	0.007
F7	-0.158	0.05	F7	-0.194	0.014	F7	-0.193	0.015
F8	-0.155	0.053	F8	-0.163	0.045	F8	-0.181	0.027
F9	-0.181	-0.001	F9	-0.182	-0.002	F9	-0.183	-0.003
C10	0.017	0.05	C10	-0.235	0.01	C10	-0.204	0.137
H11	-0.02	-0.029	H11	0.042	-0.005	H11	0.039	-0.034
H12	-0.006	-0.015	H12	0.051	-0.005	H12	0.02	-0.053
H13	0.021	-0.008	H13	0.068	-0.008	H13	0.051	-0.027
C14	-0.115	-0.003	C14	0.185	0.067	C14	0.288	-0.037
H15	0.034	-0.004	H15	-0.037	-0.02	C15	0.678	0.047
H16	0.045	0.007	C16	0.671	-0.047	C16	-0.023	0.043
C17	0.761	0.007	C17	0.091	0.011	H17	0.075	-0.006
C18	0.203	0.098	H18	0.041	-0.007	H18	0.086	-0.006
H19	0.014	-0.025	H19	0.057	-0.011	H19	0.067	-0.014
H20	0.051	-0.013	H20	0.045	0.003	O20	-0.346	-0.017
H21	-0.009	-0.048	O21	-0.416	0.017	O21	-0.549	-0.03
O22	-0.474	-0.017	O22	-0.534	-0.008	C22	-0.272	-0.051
O23	-0.538	-0.014	C23	-0.135	0.001	H23	0.049	0.017
			H24	0.025	0.001	H24	0.051	0.012
			H25	0.005	-0.028	H25	0.075	0.015
			H26	0.047	-0.001	C26	-0.263	-0.042
						H27	0.072	0.012
						H28	0.053	0.014
						H29	0.048	0.016



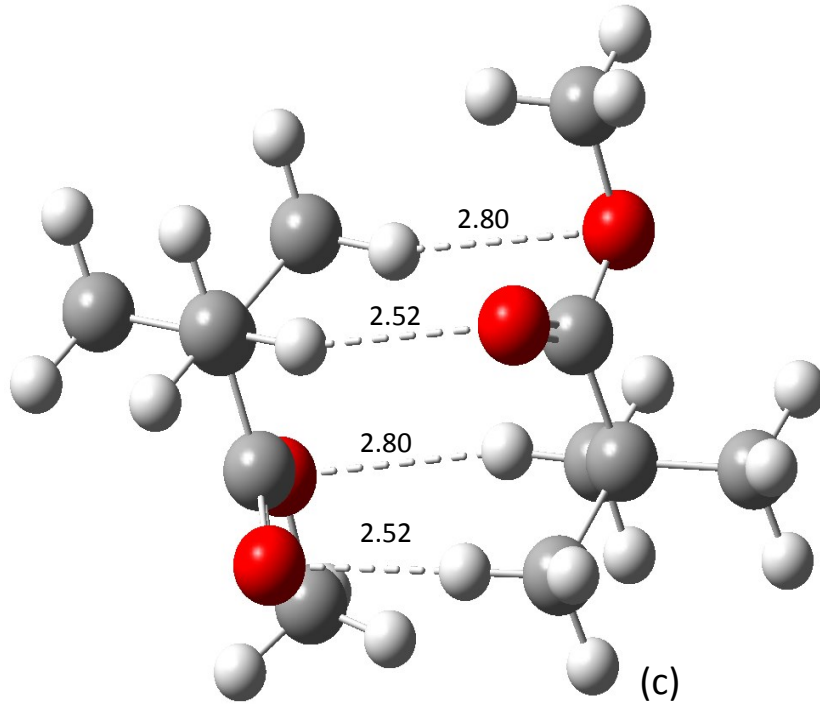


Figure S1. Optimized geometries of the self-interacting tail-tail fragments at the MP2/6-31g+(d,p) level of theory and basis set. Tail fragments are: (a) glycolic acid (*GA*), (b) lactic acid (*LA*) and (c) tetramethyl glycolic acid (*TMGA*), which are all representatives of the ester chemistries, but with increasing degree of branching. Dashed lines and numbers in parenthesis represent the “strong interaction” sites and the number of “strong interactions”, respectively. “Strong interaction” is defined as those between O··H, and with a separation distance $< 3\text{Å}$. [31]

APPENDIX B: SUPPLEMENTAL INFORMATION FOR CHAPTER 3

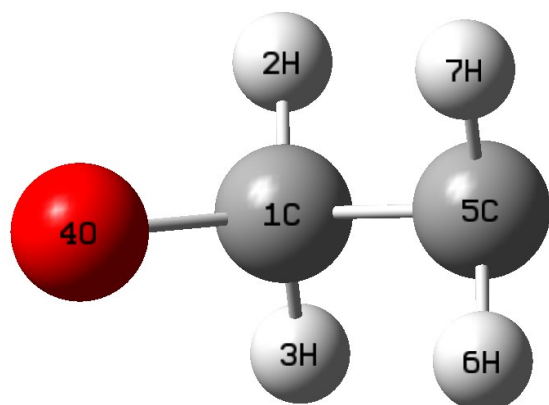


Table S2. Atom type and charges for PEG chain, which is the repeating unit of PEG head chain.

Atom #	Atom type	Charge (e)
1	CLP	-0.01
2	HLP	0.09
3	HLP	0.09
4	OLP	-0.34
5	CLP	-0.01
6	HLP	0.09
7	HLP	0.09

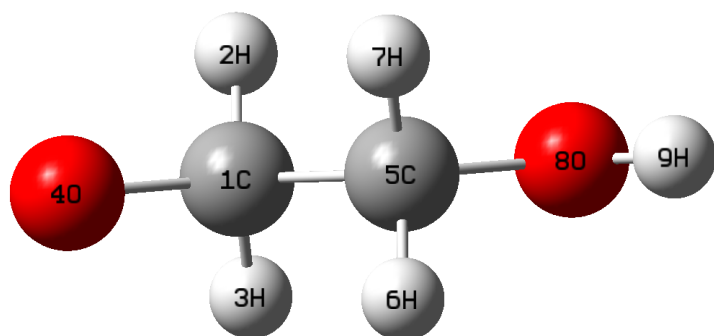


Table S3. Atom type and charges for PEG chain, which is the terminal unit of PEG head chain.

Atom #	Atom type	Charge (e)
1	CLP	-0.01
2	HLP	0.09
3	HLP	0.09
4	OLP	-0.34
5	CLP	0.10
6	HLP	0.15
7	HLP	0.15
8	OLP	-0.65
9	HLP	0.42

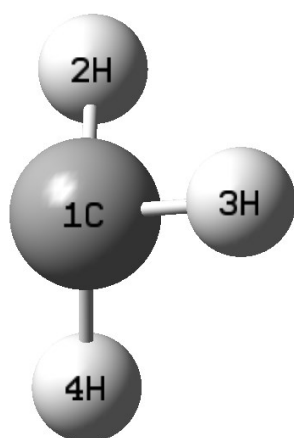


Table S3. Atom type and charges for residue CH₃, which is the terminal unit of CH tail chain.

Atom #	Atom type	Charge (e)
1	CL1	-0.27
2	HL1	0.09
3	HL1	0.09
4	HL1	0.09

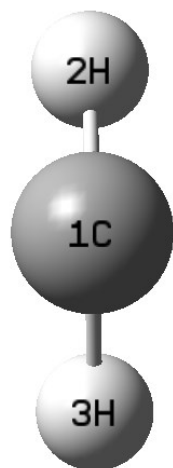


Table S4. Atom type and charges for residue CH₂, which is the repeating unit of CH tail chain.

Atom #	Atom type	Charge (e)
1	CL2	-0.18
2	HL1	0.09
3	HL1	0.09

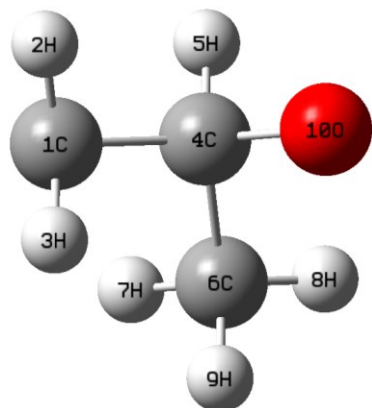


Table S5. Atom type and charges for PO chain, which is the repeating unit of PO tail chain.

Atom #	Atom type	Charge (e)
1	CPO	-0.1633
2	HPO	0.0957
3	HPO	0.0957
4	CPO	0.4264
5	HPO	-0.0132
6	CPO	-0.5319
7	HPO	0.1400
8	HPO	0.1400
9	HPO	0.1400
10	OPO	-0.3303

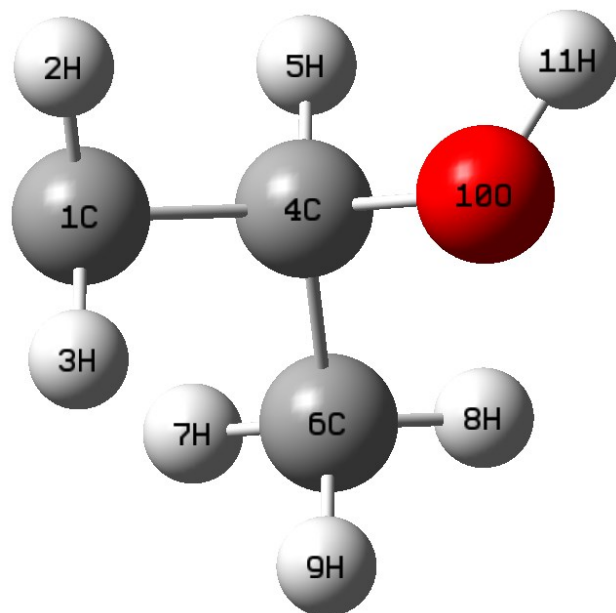


Table S6. Atom type and charges for PO chain, which is the terminal unit of PO tail chain.

Atom #	Atom type	Charge (e)
1	CPO	-0.1633
2	HPO	0.0957
3	HPO	0.0957
4	CPO	0.4264
5	HPO	-0.0132
6	CPO	-0.5319
7	HPO	0.1360
8	HPO	0.1360
9	HPO	0.1360
10	OPO	-0.6500
11	HPO	0.3350

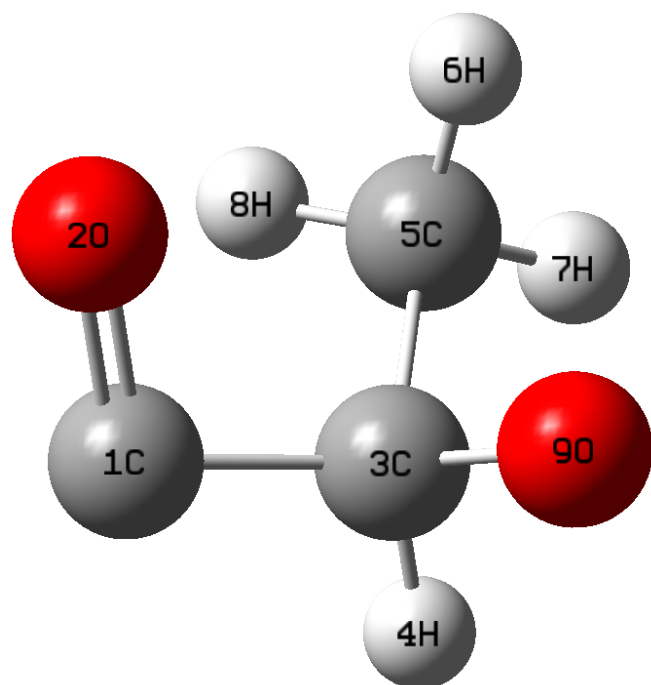


Table S7. Atom type and charges for LA chain, which is the repeating unit of LA tail chain.

Atom #	Atom type	Charge (e)
1	CA3	0.6200
2	OA1	-0.5200
3	CA2	0.1100
4	HA1	0.1300
5	CA1	-0.2700
6	HA1	0.0900
7	HA1	0.0900
8	HA1	0.0900
9	OA2	-0.3400

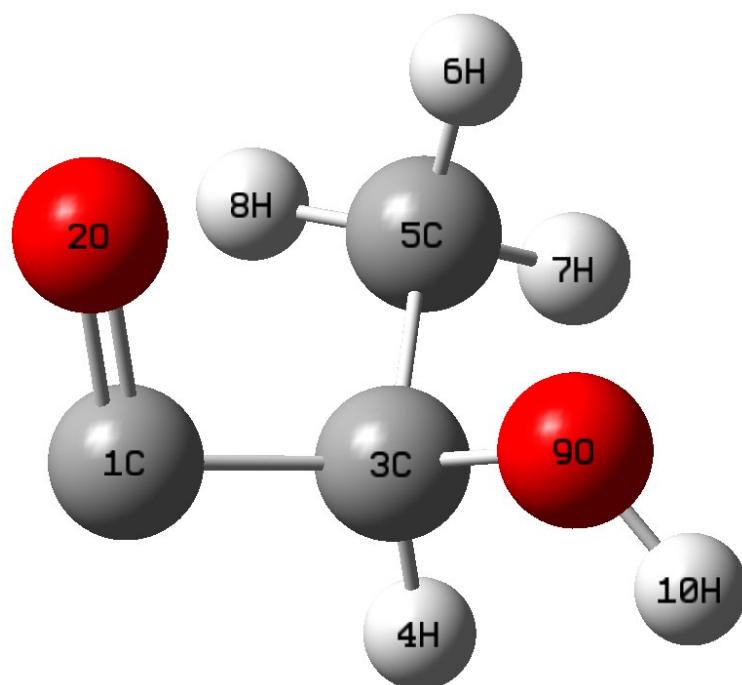


Table S8. Atom type and charges for LA chain, which is the terminal unit of LA tail chain.

Atom #	Atom type	Charge (e)
1	CA3	0.6200
2	OA1	-0.5200
3	CA2	0.1100
4	HA1	0.1300
5	CA1	-0.2700
6	HA1	0.0900
7	HA1	0.0900
8	HA1	0.0900
9	OA2	-0.4300
10	HA1	-0.0900

Table S9. Force field parameters used. All potential energies below are based on kcal/mol

$$U_{LJ} = -\varepsilon \left[\left(\frac{R_{min}}{r_{ij}} \right)^{12} - 2 \left(\frac{R_{min}}{r_{ij}} \right)^6 \right]$$

Atom	ε	$R_{min}/2$ (Å)
Cl	-0.09339870	2.020428
F1	-0.04868656	1.638792
H1	-0.01987206	1.403075
OT	-0.15535373	1.776854
HT	-0.00000000	0.000000
CM	-0.09799235	1.908185
CT	-0.07430927	1.908185
FM	-0.05644599	1.627570
FT	-0.05644599	1.650019
HM	-0.01570268	1.487262
HC	-0.01570268	1.038277
CL2	-0.05600000	2.010000
CL1	-0.07800000	2.010000
HL1	-0.03500000	1.340000
Clp	-0.05500000	2.175000
Olp	-0.10000000	1.650000
Hlp	-0.02200000	1.320000
CPO	-0.05600000	2.010000
HPO	-0.02200000	1.320000
OPO	-0.10000000	1.650000
CA1	-0.07800000	2.040000
CA2	-0.05600000	2.010000
CA3	-0.07000000	2.000000
OA1	-0.12000000	1.700000
OA2	-0.15210000	1.770000
HA1	-0.02200000	1.320000

$$U_{bond} = k(r_{ij} - r_0)^2$$

Atom		k	r_0 (Å)
Cl	H1	500.0	1.0900
Cl	Cl	500.0	1.5290
Cl	F1	500.0	1.3600
OT	HT	450.0	1.0000
HT	HT	500.0	1.5139
CM	CM	676.8	1.331
CM	CT	317.6	1.511
CT	FT	369.2	1.353
CM	HM	388.9	1.086
CM	FM	445.7	1.330
CM	HC	388.9	1.086
Clp	Hlp	317.13	1.100
Clp	Clp	222.50	1.530

Clp Olp	360.00	1.415
Cl2 Olp	360.00	1.415
HLP OLP	450.00	0.957
CL1 HL1	309.00	1.111
CL1 CL2	222.50	1.528
CL2 HL1	322.00	1.111
CL2 CL2	222.50	1.530
CPO HPO	327.5	1.090
CPO CPO	309.0	1.520
CPO OPO	369.5	1.400
CPO OLP	369.5	1.400
OPO HPO	450.0	0.957
CA3 OLP	150.0	1.334
CA1 HA1	322.0	1.111
CA1 CA2	222.5	1.530
CA2 HA1	309.0	1.111
CA2 CA3	200.0	1.522
CA2 OA2	150.0	1.334
CA3 OA1	750.0	1.220
CA3 OA2	150.0	1.334
HA1 OA2	450.0	0.957

$$U_{angle} = k_{\theta}(\theta - \theta_0)^2$$

Atoms	k_{θ}	θ_0
Cl Cl Hl	37.51	110.70
Cl Cl Fl	50.01	109.50
Hl Cl Hl	33.00	107.80
Hl Cl Fl	40.01	107.00
Fl Cl Fl	77.02	109.10
HT OT HT	90.00	109.47
HM CM CM	36.35	120.60
FT CT FT	87.86	107.50
CM CT FT	74.85	111.30
HM CM CT	32.33	115.10
HM CM HM	29.31	118.70
CM CM FM	50.52	122.60
FM CM FM	85.38	112.60
FM CM CT	76.38	112.50
CM CM CT	50.12	124.10
CM CM HC	36.35	120.60
CT CM HC	32.33	115.10
FM CM HM	30.00	113.00
CLp CLp Hlp	34.50	110.00
Hlp CLp OLP	60.00	109.50
Hlp Clp Hlp	35.50	109.00
CLp CLp OLP	45.00	111.50
Cl2 Olp Clp	95.00	123.00
Clp Olp Clp	95.00	123.00
HLP OLP CLP	57.5	106.00

HL1	CL1	HL1	35.0	109.00
CL2	CL1	HL1	34.50	110.00
CL1	CL2	H11	34.50	110.00
CL1	CL2	CL2	58.35	113.60
HL1	CL2	HL1	35.00	109.00
CL2	CL2	HL1	26.50	110.10
CL2	CL2	CL2	58.35	113.60
CL2	CL2	OLP	35.00	111.50
HL1	CL2	OLP	50.00	109.50
HPO	CPO	HPO	38.50	108.30
CPO	CPO	HPO	42.9	109.48
CPO	CPO	CPO	54.00	111.33
CPO	OPO	CPO	74.5	109.23
OPO	CPO	HPO	56.0	110.07
OPO	CPO	CPO	59.5	108.86
HPO	CPO	OLp	56.0	110.07
CPO	CPO	OLP	59.5	108.86
CPO	OPO	HPO	57.5	106.00
CLP	OLP	CPO	74.5	109.23
CPO	CPO	HPO	42.9	109.49
CA1	CA2	HA1	33.0	109.50
CA1	CA2	CA3	54.0	111.33
CA1	CA2	OA2	55.0	109.00
HA1	CA1	HA1	35.0	109.00
CA2	CA1	HA1	33.0	109.50
CA2	CA3	OA1	70.0	125.00
CA2	CA3	OA2	55.0	109.00
CA2	OA2	CA3	40.0	109.60
CA3	CA2	HA1	33.0	109.50
HA1	CA2	OA2	60.0	109.00
CA3	CA2	OA2	75.0	110.00
OA1	CA3	OA2	90.0	125.90
CA3	OLp	CLp	74.5	109.20
CA2	CA3	OLp	45.0	111.50
OA1	CA3	OLp	30.0	110.00
CA2	OA2	HA1	57.5	106.00

$$U_{Dihedral} = k(1 + \cos(n\varphi + \emptyset))$$

Atoms	k	n	\emptyset
F1 C1 C1 F1	0.01127	0	0
F1 C1 C1 F1	0.00389	1	0
F1 C1 C1 F1	-0.04865	2	180
F1 C1 C1 F1	2.12491	3	0
F1 C1 C1 H1	-0.02911	0	0
F1 C1 C1 H1	0.00316	1	0
F1 C1 C1 H1	0.01978	2	180
F1 C1 C1 H1	2.11393	3	0
HM CM CT FT	0.17806	3	0
FM CM CT FT	0.24964	3	0

CM	CM	CT	FT	0.14223	3	180
HM	CM	CM	CT	6.65392	2	180
HM	CM	CM	FM	6.65392	2	180
HM	CM	CM	HC	6.65392	2	180
HC	CM	CM	FM	6.65392	2	180
HC	CM	CT	FT	0.17806	3	0
CT	CM	CM	FM	6.65392	2	180
HLp	CLp	CLp	HLp	1.20000	2	180
HLp	CLp	CLp	OLp	0.00000	1	0
OLp	CLp	CLp	OLp	0.59000	1	180
OLp	CLp	CLp	OLp	1.1600	2	0
HLp	CLp	OLp	CLp	0.2000	3	0
CLp	CLp	OLp	CLp	0.4000	1	0
CLp	CLp	OLp	CLp	0.4900	3	0
CLp	CLp	OLp	CL2	0.4000	1	0
HLp	CLp	OLp	CL2	0.2000	3	0
CLP	OLP	CL2	CL2	0.5700	1	0
CLP	OLP	CL2	HL1	0.2840	3	0
CLP	CLP	OLP	HLP	1.3300	1	0
CLP	CLP	OLP	HLP	0.1800	2	0
CLP	CLP	OLP	HLP	0.3200	3	0
HLP	CLP	OLP	HLP	1.8000	2	180
HL1	CL1	CL2	HL1	0.1600	3	0
HL1	CL1	CL2	CL2	0.2000	3	0
CL1	CL2	CL2	HL1	0.2000	3	0
CL1	CL2	CL2	CL2	0.1510	2	0
CL1	CL2	CL2	CL2	0.0813	3	180
CL1	CL2	CL2	CL2	0.1082	4	0
CL1	CL2	CL2	CL2	0.2039	5	0
HL1	CL2	CL2	HL1	0.1900	3	0
HL1	CL2	CL2	CL2	0.2000	3	0
CL2	CL2	CL2	CL2	0.0645	2	0
CL2	CL2	CL2	CL2	0.1498	3	180
CL2	CL2	CL2	CL2	0.0946	4	0
CL2	CL2	CL2	CL2	0.1125	5	0
CL2	CL2	CL2	OLP	0.3900	2	0
HL1	CL2	CL2	OLP	0.1600	3	0
HPO	CPO	CPO	OPO	-0.1700	3	180
HPO	CPO	CPO	CPO	-0.1400	3	180
HPO	CPO	CPO	HPO	-0.1400	3	180
CPO	OPO	CPO	HPO	-0.4050	3	180
OPO	CPO	CPO	OPO	-0.1450	1	180
OPO	CPO	CPO	OPO	-0.1220	2	180
OPO	CPO	CPO	OPO	-0.1700	3	180
!CPO	CPO	OPO	CPO	1.5045	1	180
!CPO	CPO	OPO	CPO	0.510	2	180
CPO	CPO	OPO	CPO	0.4000	1	0
CPO	CPO	OPO	CPO	0.4900	3	0
CPO	CPO	OPO	CPO	0.2500	3	180
OLP	CPO	CPO	HPO	0.0000	0	0
OLP	CPO	CPO	CPO	0.0000	0	0
OLP	CPO	CPO	OPO	0.0000	0	0
HPO	CPO	OLP	CLP	0.0000	0	0
CPO	CPO	OLP	CLP	0.0000	0	0

OPO CPO CPO CPO	0.9850	1	180
OPO CPO CPO CPO	0.0150	2	180
CPO CPO OPO HPO	0.0000	0	0
HPO CPO OPO HPO	0.0000	0	0
CLP CLP OLP CPO	0.4000	1	0
CLP CLP OLP CPO	0.4900	3	0
HLP CLP OLP CPO	0.2000	3	0
CA1 CA2 CA3 OA1	0.0500	6	180
CA1 CA2 CA3 OA2	0.0500	6	180
CA1 CA2 OA2 CA3	0.7000	1	180
HA1 CA1 CA2 HA1	0.1600	3	0
HA1 CA1 CA2 CA3	0.1600	3	0
HA1 CA1 CA2 OA2	0.1600	3	0
CA2 CA3 OA2 CA2	0.0000	3	0
HA1 CA2 CA3 OA1	0.0500	6	180
HA1 CA2 CA3 OA2	0.0500	6	180
HA1 CA2 OA2 CA3	0.0000	3	0
CA3 CA2 OA2 CA3	0.0000	3	0
OA1 CA3 OA2 CA2	0.9650	1	180
OA2 CA2 CA3 OA1	0.0500	6	180
OA2 CA2 CA3 OA2	0.0500	6	180
CLp CLp OLp CA3	0.0000	3	0
HLp CLp OLp CA3	0.0000	3	0
CLp OLp CA3 CA2	0.0000	3	0
CLp OLp CA3 OA1	0.0000	3	0
OA2 CA2 CA3 OLp	0.0500	6	180
CA1 CA2 CA3 OLp	0.0500	6	180
HA1 CA2 CA3 OLp	0.0500	6	180
CA1 CA2 OA2 HA1	0.0000	3	0
HA1 CA2 OA2 HA1	0.0000	3	0
CA3 CA2 OA2 HA1	0.0000	3	0

APPENDIX C: SUPPLEMENTAL INFORMATION FOR CHAPTER 4

Force Field Development.

We have considered many different approaches when developing the charge distribution for the proposed force field (FF), including the one mentioned by reviewer – charge neutrality for the internal residues. However, we decided to take a different approach; one in which not only the overall charge of the dendrimer is considered, but also one that conforms as close as possible to the CHARMM FF – the potential of that approach is clear in terms of the ability to extend the FF to other more complex simulation environments. We found out that indeed, when charges were taken either from the CHARMM FF or from our own *ab initio* calculations, they do not support neutrality of the internal residues. Therefore, we decided not to artificially force neutrality of the residues. For that reason we kept the charges as close as possible to the original CHARMM FF, with minimal modifications supported by our *ab initio* work, so as to conform to the restriction/to provide an overall charge that corresponds to the fully protonated dendrimer - condition of interest here, as the dendrimers are fully protonated under physiological conditions. For G3NH2 PAMAM dendrimer, there is, therefore, 1 core unit (-0.6e each), 28 branching monomers (-0.15e each), and 32 terminal units (+1.15 each). This could be easily extended to dendrimers under different conditions/different degrees of protonation by adjusting the charge of the terminal units.

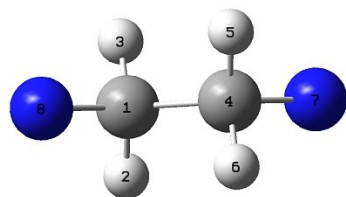


Figure S1. Structure of residue AMC, the core of PAMAM dendrimer. Color code: N in blue, C in grey, H in white. All atoms are numbered the same as in table S1.

Table S14 Atom type and charges for residue AMC

Atom #	Atom type	Charge (e)
1	CL1	-0.35
2	HL1	0.25
3	HL1	0.25
4	CL1	-0.35
5	HL1	0.25
6	HL1	0.25
7	NL2	-0.45
8	NL2	-0.45

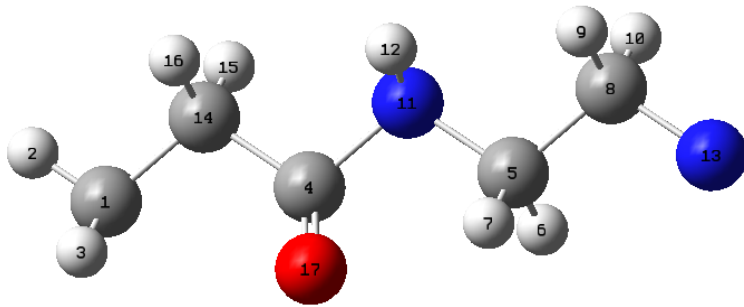


Figure S2. Structure of residue AMT, the monomer (repeating unit) of PAMAM dendrimer. Color code: N in blue, C in grey, O in red, H in white. All atoms are numbered the same as in table S2.

Table S15 Atom type and charge for residue AMT (monomer).

Atom #	Atom type	Charge (e)
1	CL1	-0.35
2	HL1	0.25
3	HL1	0.25
4	CL2	0.50
5	CL1	-0.04
6	HL1	0.10
7	HL1	0.10
8	CL1	-0.35
9	HL1	0.25
10	HL1	0.25
11	NL1	-0.47
12	HL1	0.31
13	NL2	-0.45
14	CL1	-0.18
15	HL1	0.09
16	HL1	0.09
17	OL1	-0.50

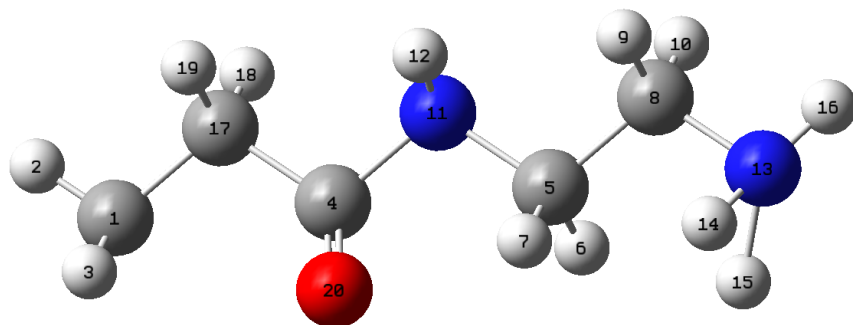


Figure S3. Structure of residue AMH, the terminal monomer (surface group) of PAMAM dendrimer. Color code: N in blue, C in grey, O in red, H in white. All atoms are numbered the same as in table S3.

Table S16 Atom type and charge for residue AMH (monomer at surface). When it is grafted with PEG, #15 and #16 will not be part of the chain, and #13 will have -0.41e.

Atom #	Atom type	Charge (e)
1	CL1	-0.35
2	HL1	0.25
3	HL1	0.25
4	CL2	0.51
5	CL1	-0.04
6	HL1	0.10
7	HL1	0.10
8	CL1	0.13
9	HL1	0.09
10	HL1	0.09
11	NL1	-0.47
12	HL2	0.31
13	NL2	-0.30
14	HL1	0.33
15	HL1	0.33
16	HL1	0.33
17	CL1	-0.18
18	HL1	0.09
19	HL1	0.09
20	OL1	-0.51

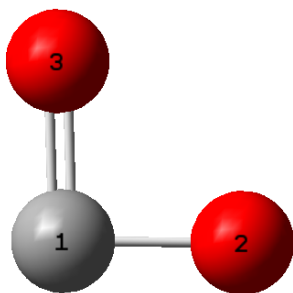


Figure S4. Structure of residue LIK, the linker between the PEG and PAMAM dendrimer. Color code: C in grey, O in red. 1 is connected to dendrimer (N) while 2 is connected to PEG (C). All atoms are numbered the same as in table S4.

Table S4 Atom type and charge for residue LIK (linker).

Atom #	Atom type	Charge (e)
1	CL1	0.63
2	OL1	-0.34
3	OL1	-0.52

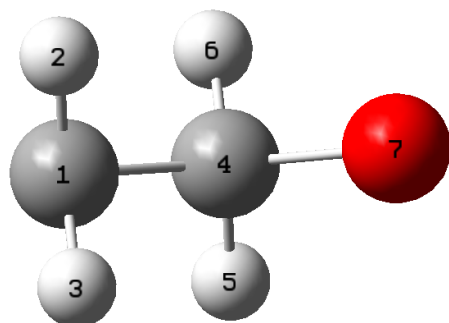


Figure S5. Structure of residue PEG, the monomer for PEG chain. Color code: C in grey, O in red, H in white. All atoms are numbered the same as in table S5.

Table S4 Atom type and charge for residue LIK (linker).

Atom #	Atom type	Charge (e)
1	CLP	-0.01
2	HLP	0.09
3	HLP	0.09
4	CLP	-0.01
5	HLP	0.09
6	HLP	0.09
7	OLP	-0.34

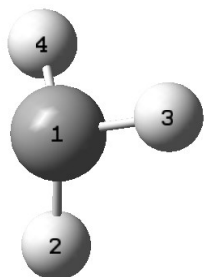


Figure S6. Structure of residue MET, at the end of PEG chain. Color code: C in grey, H in white. All atoms are numbered the same as in table S6.

Table S6 Atom type and charge for residue LIK (linker).

Atom #	Atom type	Charge (e)
1	CLP	-0.27
2	HLP	0.09
3	HLP	0.09
4	HLP	0.09

Table S7. Force field parameters employed in this study.

All potential energies below are based on kcal/mol

$$U_{LJ} = -\varepsilon \left[\left(\frac{R_{min}}{r_{ij}} \right)^{12} - 2 \left(\frac{R_{min}}{r_{ij}} \right)^6 \right]$$

Atom	ε	$R_{min}/2$ (Å)
C11	-0.06800	2.000
C12	-0.11000	2.000
N11	-0.35000	1.850
N12	-0.20000	1.850
H11	-0.02200	1.320
H12	-0.03000	1.403
O11	-0.24000	1.950
Clp	-0.05500	2.175
Olp	-0.10000	1.650
Hlp	-0.02200	1.320

$$U_{bond} = k(r_{ij} - r_0)^2$$

Atom		k	r_0 (Å)
C11	H11	317.13	1.100
C11	C11	222.00	1.530
C11	N12	320.00	1.430
C11	C12	365.00	1.502
C12	O11	650.00	1.230
C12	C11	365.00	1.502
N11	H12	480.00	1.000
C11	N11	320.00	1.430
N11	C12	430.00	1.360
H11	N12	480.00	1.000
Clp	Olp	360.00	1.415
O11	P	237.00	1.580
Clp	Hlp	317.13	1.100
Clp	Clp	222.50	1.530
C11	O11	650.00	1.230
C11	Olp	650.00	1.320
Clp	O11	650.00	1.320

$$U_{angle} = k_{\theta}(\theta - \theta_0)^2$$

Atoms	k_{θ}	θ_0
C11 C11 H11	50.00	120.0
H11 C11 H11	35.50	109.0
H11 C11 C12	50.00	120.0

H11	C11	N11	51.50	109.5
H11	C11	N12	51.50	109.5
O11	C12	N11	80.00	122.5
O11	C12	C11	80.00	121.0
N11	C11	C11	80.00	116.5
N11	C12	C11	80.00	116.5
N12	C11	C11	80.00	116.5
C11	N11	H12	34.00	123.0
C11	N11	C12	50.00	120.0
C11	C11	C12	40.00	120.0
C12	N11	H12	50.00	111.0
H11	N12	C11	34.00	123.0
H11	N12	H11	23.00	120.0
C11	N12	C11	50.00	120.0
C11	C11	O11	80.00	121.0
C11	O11	C11	40.00	109.0
H11	C11	O11	50.00	122.0
O11	C11	O11	50.00	123.0
N12	C11	O11	80.00	122.5
Hlp	Clp	Hlp	35.50	109.0
CLp	CLp	HLp	34.50	110.0
HLp	CLp	OLp	60.00	109.5
CLp	CLp	OLp	45.00	111.5
CL1	OLp	CLp	95.00	109.7
HLp	CLp	OL1	60.00	109.5
CLp	CLp	OL1	45.00	110.0
CL1	OL1	CLp	95.00	109.7
HL1	CL1	OLp	60.00	109.5
Olp	Clp	Olp	50.00	123.0
Clp	Olp	Clp	95.00	123.0

$$U_{Dihedral} = k(1 + \cos(n\varphi + \emptyset))$$

Atoms	k	n	\emptyset
N12 C11 C11 N12	0.6000	1	0
N12 C11 C11 H11	0.0000	1	0
N12 C11 C11 C12	0.0000	1	0
N12 C11 C11 N11	0.6000	1	0
N11 C12 C11 C11	0.0000	1	0
N11 C12 C11 H11	0.0000	1	0
N11 C11 C11 H11	0.0000	1	0
O11 C12 C11 C11	1.4000	1	0
O11 C12 C11 H11	0.0000	1	0
O11 C12 N11 H12	2.5000	2	180
O11 C12 N11 C11	2.5000	2	180
H11 C11 C11 H11	1.4000	2	180
H11 C11 C11 C12	0.0500	3	180
H11 C11 N11 C11	0.0000	1	0

H11	C11	N11	H12	2.5000	2	180
H12	N11	C11	C11	2.5000	2	180
C11	C11	N11	C12	0.2000	2	180
C11	N12	C11	C11	0.2000	1	180
H11	N11	C11	C11	2.5000	2	180
H11	N12	C11	H11	1.4000	2	180
C11	N12	C11	H11	0.0000	1	0
C11	C12	N11	H12	2.5000	2	180
C11	C12	N11	C11	0.2000	1	180
C12	N11	C11	H11	0.0000	1	0
C11	C11	N12	H11	2.5000	2	180
CL1	NL2	CL1	OL1	0.0000	2	180
HL1	NL2	CL1	OL1	2.5000	2	180
HLp	CLp	CLp	HLp	1.2000	2	180
HLp	CLp	CLp	OLp	0.0000	1	0
OLp	CLp	CLp	OLp	0.5900	1	180
OLp	CLp	CLp	OLp	1.1600	2	0
HLp	CLp	OLp	CLp	0.2000	3	0
CLp	CLp	OLp	CLp	0.4000	1	0
CLp	CLp	OLp	CLp	0.4900	3	0
CLp	CLp	OLp	CL1	0.5700	1	0
HLp	CLp	OLp	CL1	0.2840	3	0
CLp	OLp	CL1	HL1	0.2000	3	0
OL1	CLp	CLp	HLp	0.0000	3	180
OL1	CLp	CLp	OLp	0.0000	1	0
OL1	CLp	CLp	OLp	0.0900	3	0
HLp	CLp	OL1	CL1	0.2840	3	0
CLp	CLp	OL1	CL1	0.4000	1	0
CLp	CLp	OL1	CL1	0.4900	3	0
NL2	CL1	OL1	CLp	0.0000	1	0
OL1	CL1	OL1	CLp	0.0000	1	0
Olp	Clp	Olp	Clp	0.0000	1	0

Table S8. Radius of gyration (R_g) as a function PEG chain length and number of grafts.

	G3NH ₂	G3NH ₂ - 4PEG500	G3NH ₂ - 8PEG500	G3NH ₂ - 16PEG500	G3NH ₂ - 8PEG1000
R_g (Å)	15.0	15.6	16.2	16.9	18.1
$R_{g\text{-core}}$ (Å)	15.0	15.1	16.3	14.1	15.5

APPENDIX D: SUPPLEMENTAL INFORMATION FOR CHAPTER 5

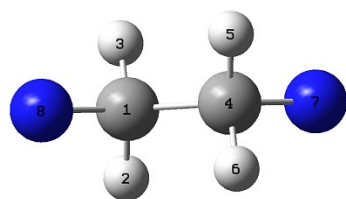


Figure S1. Structure of residue AMC, the core of PAMAM dendrimer ($G3NH_3^+$, $G3OH$, $G2.5COO^-$). Color code: N in blue, C in grey, H in white. All atoms are numbered the same as in table S1.

Table S17 Atom type and charges for residue AMC

Atom #	Atom type	Charge (e)
1	CL1	-0.35
2	HL1	0.25
3	HL1	0.25
4	CL1	-0.35
5	HL1	0.25
6	HL1	0.25
7	NL2	-0.45
8	NL2	-0.45

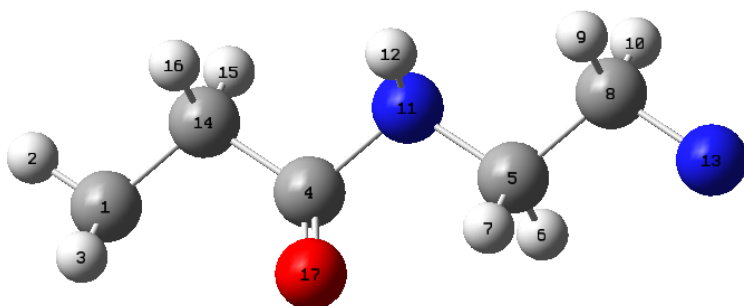


Figure S2. Structure of residue AMT, the monomer (repeating unit) of PAMAM dendrimer ($G3NH_3^+$, $G3OH$, $G2.5COO^-$). Color code: N in blue, C in grey, O in red, H in white. All atoms are numbered the same as in table S2.

Table S18 Atom type and charge for residue AMT (monomer).

Atom #	Atom type	Charge (e)
1	CL1	-0.35
2	HL1	0.25
3	HL1	0.25
4	CL2	0.50
5	CL1	-0.04
6	HL1	0.10
7	HL1	0.10
8	CL1	-0.35
9	HL1	0.25
10	HL1	0.25
11	NL1	-0.47
12	HL1	0.31
13	NL2	-0.45
14	CL1	-0.18
15	HL1	0.09
16	HL1	0.09
17	OL1	-0.50

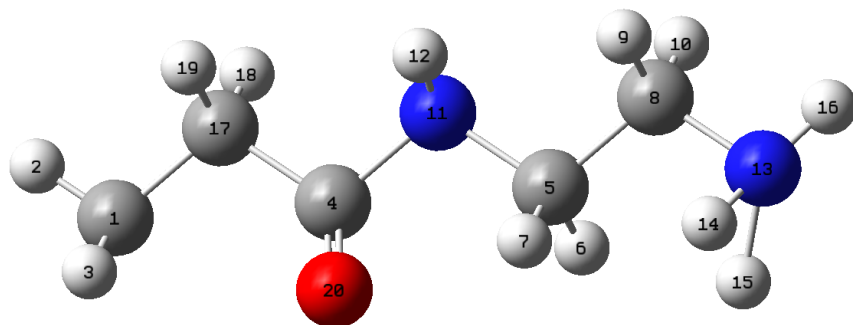


Figure S3. Structure of residue AMH, the terminal monomer (surface group) of G3NH₃⁺ PAMAM dendrimer. Color code: N in blue, C in grey, O in red, H in white. All atoms are numbered the same as in table S3.

Table S19 Atom type and charge for residue AMH (monomer at surface). When it is grafted with PEG, #15 and #16 will not be part of the chain, and #13 will have -0.41e.

Atom #	Atom type	Charge (e)
1	CL1	-0.35
2	HL1	0.25
3	HL1	0.25
4	CL2	0.51
5	CL1	-0.04
6	HL1	0.10
7	HL1	0.10
8	CL1	0.13
9	HL1	0.09
10	HL1	0.09
11	NL1	-0.47
12	HL2	0.31
13	NL2	-0.30
14	HL1	0.33
15	HL1	0.33
16	HL1	0.33
17	CL1	-0.18
18	HL1	0.09
19	HL1	0.09
20	OL1	-0.51

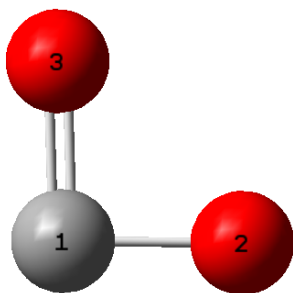


Figure S4. Structure of residue LIK, the linker between the PEG and $G3NH_3^+$ PAMAM dendrimer. Color code: C in grey, O in red. 1 is connected to dendrimer (N) while 2 is connected to PEG (C). All atoms are numbered the same as in table S4.

Table S4 Atom type and charge for residue LIK (linker).

Atom #	Atom type	Charge (e)
1	CL1	0.63
2	OL1	-0.34
3	OL1	-0.52

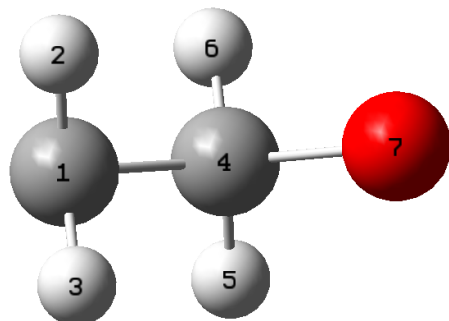


Figure S5. Structure of residue PEG, the monomer for PEG chain. Color code: C in grey, O in red, H in white. All atoms are numbered the same as in table S5.

Table S4 Atom type and charge for residue PEG.

Atom #	Atom type	Charge (e)
1	CLP	-0.01
2	HLP	0.09
3	HLP	0.09
4	CLP	-0.01
5	HLP	0.09
6	HLP	0.09
7	OLP	-0.34

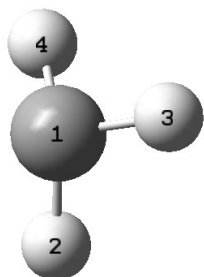


Figure S6. Structure of residue MET, at the end of PEG chain. Color code: C in grey, H in white. All atoms are numbered the same as in table S6.

Table S6 Atom type and charge for residue MET.

Atom #	Atom type	Charge (e)
1	CLP	-0.27
2	HLP	0.09
3	HLP	0.09
4	HLP	0.09

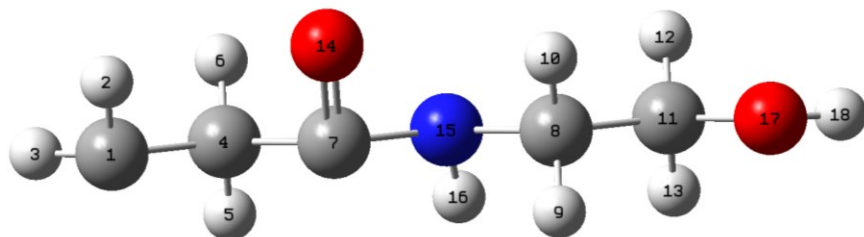


Figure S7. Structure of residue AMX, the terminal monomer (surface group) of G3OH PAMAM dendrimer. Color code: N in blue, C in grey, O in red, H in white. All atoms are numbered the same as in table S7.

Table S7 Atom type and charge for residue AMX (monomer at surface) of G3OH PAMAM dendrimer. When it is grafted with PEG, #17 and #18 will not be part of the chain.

Atom #	Atom type	Charge (e)
1	CL1	-0.35
2	HL1	0.25
3	HL1	0.25
4	CL1	-0.18
5	HL1	0.09
6	HL1	0.09
7	CL2	0.51
8	CL1	-0.04
9	HL1	0.10
10	HL1	0.10
11	CL1	0.05
12	HL1	0.09
13	HL1	0.09
14	OL1	-0.51
15	NL1	-0.47
16	HL2	0.31
17	OL2	-0.65
18	HL1	0.42

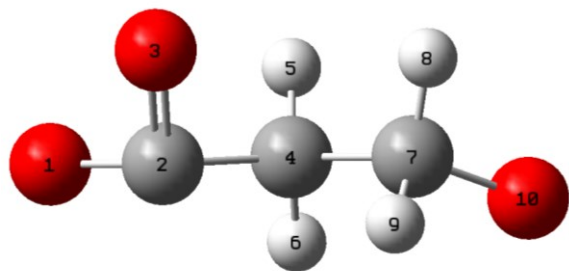


Figure S8. Structure of residue LIN, the linker between G3OH PAMAM dendrimer and PEG chain. Color code: N in blue, C in grey, O in red, H in white. All atoms are numbered the same as in table S8.

Table S8 Atom type and charge for residue LIN.

Atom #	Atom type	Charge (e)
1	OL1	-0.34
2	CL1	0.63
3	OL1	-0.52
4	CL1	-0.08
5	HL1	0.09
6	HL1	0.09
7	CL1	-0.08
8	HL1	0.09
9	HL1	0.09
10	OL1	-0.10

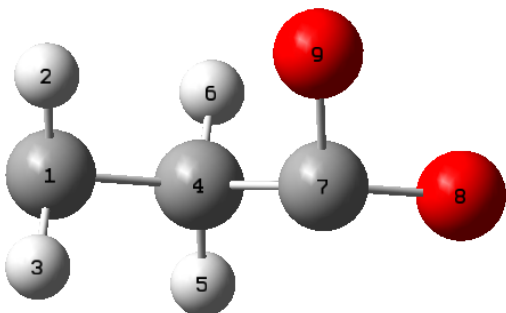


Figure S10. Structure of residue AMY, the terminal monomer (surface group) of G2.5COO⁻ PAMAM dendrimer. Color code: N in blue, C in grey, O in red, H in white. All atoms are numbered the same as in table S10.

Table S10 Atom type and charge for residue AMY.

Atom #	Atom type	Charge (e)
1	CL1	-0.35
2	HL1	0.25
3	HL1	0.25
4	CL1	-0.18
5	HL1	0.09
6	HL1	0.09
7	CL2	0.34
8	OL1	-0.67
9	OL3	-0.67

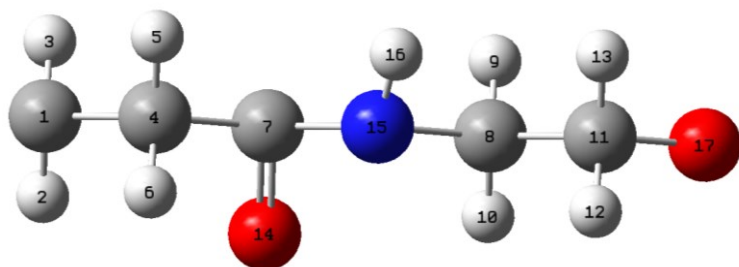


Figure S9. Structure of residue LYN, the linker between G2.5COO⁻ PAMAM dendrimer and PEG chain. Color code: N in blue, C in grey, O in red, H in white. All atoms are numbered the same as in table S9.

Table S9 Atom type and charge for residue LYN.

Atom #	Atom type	Charge (e)
1	CL1	-0.35
2	HL1	0.25
3	HL1	0.25
4	CL1	-0.28
5	HL1	0.09
6	HL1	0.09
7	CL2	0.51
8	CL1	0.08
9	HL1	0.09
10	HL1	0.09
11	CL1	-0.01
12	HL1	0.09
13	HL1	0.09
14	OL1	-0.51
15	NL1	-0.47
16	HL2	0.31
17	OL2	-0.17

Table S11. Force field parameters employed in this study.

All potential energies below are based on kcal/mol

$$U_{LJ} = -\varepsilon \left[\left(\frac{R_{min}}{r_{ij}} \right)^{12} - 2 \left(\frac{R_{min}}{r_{ij}} \right)^6 \right]$$

Atom	ε	$R_{min}/2$ (Å)
C11	-0.06800	2.000
C12	-0.11000	2.000
N11	-0.35000	1.850
N12	-0.20000	1.850
H11	-0.02200	1.320
H12	-0.03000	1.403
O11	-0.24000	1.950
Clp	-0.05500	2.175
Olp	-0.10000	1.650
Hlp	-0.02200	1.320

$$U_{bond} = k(r_{ij} - r_0)^2$$

Atom		k	r_0 (Å)
C11	H11	317.13	1.100
C11	C11	222.00	1.530
C11	N12	320.00	1.430
C11	C12	365.00	1.502
C12	O11	650.00	1.230
C12	C11	365.00	1.502
N11	H12	480.00	1.000
C11	N11	320.00	1.430
N11	C12	430.00	1.360
H11	N12	480.00	1.000
Clp	Olp	360.00	1.415
O11	P	237.00	1.580
Clp	Hlp	317.13	1.100
Clp	Clp	222.50	1.530
C11	O11	650.00	1.230
C11	Olp	650.00	1.320
Clp	O11	650.00	1.320

$$U_{angle} = k_{\theta}(\theta - \theta_0)^2$$

Atoms	k_{θ}	θ_0
C11 C11 H11	50.00	120.0

H11	C11	H11	35.50	109.0
H11	C11	C12	50.00	120.0
H11	C11	N11	51.50	109.5
H11	C11	N12	51.50	109.5
O11	C12	N11	80.00	122.5
O11	C12	C11	80.00	121.0
N11	C11	C11	80.00	116.5
N11	C12	C11	80.00	116.5
N12	C11	C11	80.00	116.5
C11	N11	H12	34.00	123.0
C11	N11	C12	50.00	120.0
C11	C11	C12	40.00	120.0
C12	N11	H12	50.00	111.0
H11	N12	C11	34.00	123.0
H11	N12	H11	23.00	120.0
C11	N12	C11	50.00	120.0
C11	C11	O11	80.00	121.0
C11	O11	C11	40.00	109.0
H11	C11	O11	50.00	122.0
O11	C11	O11	50.00	123.0
N12	C11	O11	80.00	122.5
H1p	C1p	H1p	35.50	109.0
CLp	CLp	HLp	34.50	110.0
HLp	CLp	OLp	60.00	109.5
CLp	CLp	OLp	45.00	111.5
CL1	OLp	CLp	95.00	109.7
HLp	CLp	OL1	60.00	109.5
CLp	CLp	OL1	45.00	110.0
CL1	OL1	CLp	95.00	109.7
HL1	CL1	OLp	60.00	109.5
Olp	C1p	Olp	50.00	123.0
Clp	Olp	Clp	95.00	123.0

$$U_{Dihedral} = k(1 + \cos(n\varphi + \phi))$$

Atoms	k	n	ϕ
N12 C11 C11 N12	0.6000	1	0
N12 C11 C11 H11	0.0000	1	0
N12 C11 C11 C12	0.0000	1	0
N12 C11 C11 N11	0.6000	1	0
N11 C12 C11 C11	0.0000	1	0
N11 C12 C11 H11	0.0000	1	0
N11 C11 C11 H11	0.0000	1	0
O11 C12 C11 C11	1.4000	1	0
O11 C12 C11 H11	0.0000	1	0
O11 C12 N11 H12	2.5000	2	180
O11 C12 N11 C11	2.5000	2	180
H11 C11 C11 H11	1.4000	2	180

H11	C11	C11	C12	0.0500	3	180
H11	C11	N11	C11	0.0000	1	0
H11	C11	N11	H12	2.5000	2	180
H12	N11	C11	C11	2.5000	2	180
C11	C11	N11	C12	0.2000	2	180
C11	N12	C11	C11	0.2000	1	180
H11	N11	C11	C11	2.5000	2	180
H11	N12	C11	H11	1.4000	2	180
C11	N12	C11	H11	0.0000	1	0
C11	C12	N11	H12	2.5000	2	180
C11	C12	N11	C11	0.2000	1	180
C12	N11	C11	H11	0.0000	1	0
C11	C11	N12	H11	2.5000	2	180
CL1	NL2	CL1	OL1	0.0000	2	180
HL1	NL2	CL1	OL1	2.5000	2	180
HLp	CLp	CLp	HLp	1.2000	2	180
HLp	CLp	CLp	OLp	0.0000	1	0
OLp	CLp	CLp	OLp	0.5900	1	180
OLp	CLp	CLp	OLp	1.1600	2	0
HLp	CLp	OLp	CLp	0.2000	3	0
CLp	CLp	OLp	CLp	0.4000	1	0
CLp	CLp	OLp	CLp	0.4900	3	0
CLp	CLp	OLp	CL1	0.5700	1	0
HLp	CLp	OLp	CL1	0.2840	3	0
CLp	OLp	CL1	HL1	0.2000	3	0
OL1	CLp	CLp	HLp	0.0000	3	180
OL1	CLp	CLp	OLp	0.0000	1	0
OL1	CLp	CLp	OLp	0.0900	3	0
HLp	CLp	OL1	CL1	0.2840	3	0
CLp	CLp	OL1	CL1	0.4000	1	0
CLp	CLp	OL1	CL1	0.4900	3	0
NL2	CL1	OL1	CLp	0.0000	1	0
OL1	CL1	OL1	CLp	0.0000	1	0
Olp	Clp	Olp	Clp	0.0000	1	0

REFERENCES

1. Saah, M., et al., *Design, synthesis, and pharmacokinetic evaluation of a chemical delivery system for drug targeting to lung tissue*. J Pharm Sci, 1996. **85**(5): p. 496-504.
2. Meisner, D., J. Pringle, and M. Mezei, *Liposomal pulmonary drug delivery. I. In vivo disposition of atropine base in solution and liposomal form following endotracheal instillation to the rabbit lung*. J Microencapsul, 1989. **6**(3): p. 379-87.
3. Karathanasis, E., R. Bhavane, and A.V. Annapragada, *Glucose-sensing pulmonary delivery of human insulin to the systemic circulation of rats*. Int J Nanomedicine, 2007. **2**(3): p. 501-13.
4. Patil, J.S. and S. Sarasija, *Pulmonary drug delivery strategies: A concise, systematic review*. Lung India, 2012. **29**(1): p. 44-9.
5. Islam, N. and M.J. Cleary, *Developing an efficient and reliable dry powder inhaler for pulmonary drug delivery--a review for multidisciplinary researchers*. Med Eng Phys, 2012. **34**(4): p. 409-27.
6. Rogueda, P.G. and D. Traini, *The nanoscale in pulmonary delivery. Part 1: deposition, fate, toxicology and effects*. Expert Opin Drug Deliv, 2007. **4**(6): p. 595-606.
7. Johnson, M.A., et al., *Delivery of albuterol and ipratropium bromide from two nebulizer systems in chronic stable asthma. Efficacy and pulmonary deposition*. Chest, 1989. **96**(1): p. 6-10.
8. Peters, J., et al., *The clinical effectiveness and cost-effectiveness of inhaler devices used in the routine management of chronic asthma in older children: a systematic review and economic evaluation*. Health Technol Assess, 2002. **6**(5): p. 1-167.
9. Amirav, I. and M.T. Newhouse, *Metered-dose inhaler accessory devices in acute asthma: efficacy and comparison with nebulizers: a literature review*. Arch Pediatr Adolesc Med, 1997. **151**(9): p. 876-82.

10. Braunstein, G. and R. Sharma, *The pressurized metered dose inhaler (pMDI) remains the most commonly prescribed device for the delivery of inhaled asthma medications*. *Respir Med*, 2000. **94** **Suppl B**: p. S1-2.
11. Borgstrom, L., et al., *Variability in lung deposition of inhaled drug, within and between asthmatic patients, with a pMDI and a dry powder inhaler, Turbuhaler*. *Int J Pharm*, 2000. **193**(2): p. 227-30.
12. De Backer, W., et al., *Lung deposition of BDP/formoterol HFA pMDI in healthy volunteers, asthmatic, and COPD patients*. *J Aerosol Med Pulm Drug Deliv*, 2010. **23**(3): p. 137-48.
13. Qian, F., et al., *Pulmonary delivery of a GLP-1 receptor agonist, BMS-686117*. *Int J Pharm*, 2009. **366**(1-2): p. 218-20.
14. Zheng, Y., et al., *Pulmonary delivery of a dopamine D-1 agonist, ABT-431, in dogs and humans*. *Int J Pharm*, 1999. **191**(2): p. 131-40.
15. Tripathi, S.K., et al., *Linear polyethylenimine-graft-chitosan copolymers as efficient DNA/siRNA delivery vectors in vitro and in vivo*. *Nanomedicine*, 2012. **8**(3): p. 337-45.
16. Malmo, J., et al., *siRNA delivery with chitosan nanoparticles: Molecular properties favoring efficient gene silencing*. *J Control Release*, 2012. **158**(2): p. 261-8.
17. Wu, L., M. Al-Haydari, and S.R.P. da Rocha, *Novel propellant-driven inhalation formulations: engineering polar drug particles with surface-trapped hydrofluoroalkane-philes*. *European Journal of Pharmaceutical Sciences*, 2008. **33**(2): p. 146-158.
18. Hatch, T.F., *Distribution and deposition of inhaled particles in respiratory tract*. *Bacteriological Reviews*, 1961. **25**(3): p. 237.
19. Wu, L., et al., *Core-shell particles for the dispersion of small polar drugs and biomolecules in hydrofluoroalkane propellants*. *Pharm Res*, 2008. **25**(2): p. 289-301.
20. Wu, L. and S. da Rocha, *Nanoparticle-stabilized Colloids in Compressible Hydrofluoroalkanes*. *Langmuir*, 2011.

21. Galka, M.D., J.M. Lownsbury, and P. Blowers, *Greenhouse gas emissions for refrigerant choices in room air conditioner units*. Environ Sci Technol, 2012. **46**(23): p. 12977-85.
22. Skarmoutsos, I. and P.A. Hunt, *Structural and dynamic properties of the new alternative refrigerant 2,3,3,3-tetrafluoro-1-propene (HFO-1234yf) in the liquid state*. J Phys Chem B, 2010. **114**(51): p. 17120-7.
23. Levi, C., J.M. Martin, and I. Bar, *Fundamental vibrational frequencies and dominant resonances in methylamine isotopologues by ab initio and density functional theory methods*. J Comput Chem, 2008. **29**(8): p. 1268-76.
24. Higashi, Y., K. Tanaka, and T. Ichikawa, *Critical parameters and saturated densities in the critical region for trans-1, 3, 3, 3-tetrafluoropropene (HFO-1234ze (E))*. Journal of Chemical & Engineering Data, 2009. **55**(4): p. 1594-1597.
25. Bharatwaj, B.S., L. Wu, and S.R.P. Da Rocha, *Novel Propellant-Driven Formulations For The Pulmonary Delivery Of Biomolecules: Particle Engineering, Aerosol Characteristics And In Vitro Toxicity*. The 2007 Annual Meeting, 2007.
26. Kaur, G., et al., *Advances in Pulmonary Delivery of Nanoparticles*. Artif Cells Blood Substit Immobil Biotechnol, 2011.
27. White, S., et al., *EXUBERA®: pharmaceutical development of a novel product for pulmonary delivery of insulin*. Diabetes technology & therapeutics, 2005. **7**(6): p. 896-906.
28. Murata, M., et al., *Pulmonary delivery of elcatonin using surface-modified liposomes to improve systemic absorption: Polyvinyl alcohol with a hydrophobic anchor and chitosan oligosaccharide as effective surface modifiers*. Eur J Pharm Biopharm, 2011.
29. Vujanic, A., et al., *Long-term antibody and immune memory response induced by pulmonary delivery of the influenza iscomatrix vaccine*. Clin Vaccine Immunol, 2012. **19**(1): p. 79-83.

30. Dempsey, O.J., et al., *Evaluation of the effect of a large volume spacer on the systemic bioactivity of fluticasone propionate metered-dose inhaler*. CHEST Journal, 1999. **116**(4): p. 935-940.
31. Lam, J.K.-W., W. Liang, and H.-K. Chan, *Pulmonary delivery of therapeutic siRNA*. Adv Drug Deliv Rev, 2012. **64**(1): p. 1-15.
32. Nielsen, E.J., et al., *Pulmonary gene silencing in transgenic EGFP mice using aerosolised chitosan/siRNA nanoparticles*. Pharm Res, 2010. **27**(12): p. 2520-2527.
33. Gary, D.J., N. Puri, and Y.-Y. Won, *Polymer-based siRNA delivery: perspectives on the fundamental and phenomenological distinctions from polymer-based DNA delivery*. Journal of Controlled Release, 2007. **121**(1): p. 64-73.
34. Duxbury, M.S., S.W. Ashley, and E.E. Whang, *RNA interference: a mammalian SID-1 homologue enhances siRNA uptake and gene silencing efficacy in human cells*. Biochem Biophys Res Commun, 2005. **331**(2): p. 459-463.
35. Meade, B.R. and S.F. Dowdy, *Exogenous siRNA delivery using peptide transduction domains/cell penetrating peptides*. Adv Drug Deliv Rev, 2007. **59**(2): p. 134-140.
36. Howard, K.A., et al., *RNA interference in vitro and in vivo using a chitosan/siRNA nanoparticle system*. Molecular Therapy, 2006. **14**(4): p. 476-484.
37. Patil, M.L., M. Zhang, and T. Minko, *Multifunctional Triblock Nanocarrier (PAMAM-PEG-PLL) for the Efficient Intracellular siRNA Delivery and Gene Silencing*. ACS Nano, 2011. **5**(3): p. 1877-1887.
38. Xue, H.Y. and H.L. Wong, *Solid lipid-PEI hybrid nanocarrier: an integrated approach to provide extended, targeted, and safer siRNA therapy of prostate cancer in an all-in-one manner*. ACS Nano, 2011. **5**(9): p. 7034-47.
39. Pierrat, P., et al., *A cationic phospholipid-detergent conjugate as a new efficient carrier for siRNA delivery*. Chemistry, 2012. **18**(13): p. 3835-9.

40. Tenchov, B., et al., *Highly efficient cationic ethylphosphatidylcholine siRNA carrier for GFP suppression in modified breast cancer cells*. *Anticancer Res*, 2012. **32**(7): p. 2563-6.
41. Won, Y.W., et al., *Poly(oligo-D-arginine) with internal disulfide linkages as a cytoplasm-sensitive carrier for siRNA delivery*. *Mol Ther*, 2011. **19**(2): p. 372-80.
42. Maiti, P.K., T. Cagin, and a.e. al., *Structure of PAMAM Dendrimers: Generation 1 through 11*. *Macromolecules*, 2004. **37**: p. 6236-6254.
43. Kazzouli, S.E., S. Mignani, and a.e. al., *Dendrimer therapeutics: covalent and ionic attachments*. *New J Chem*, 2012. **36**: p. 227-240.
44. Luo, D., K. Haverstick, and a.e. al., *Poly(ethylene glycol)-Conjugated PAMAM Dendrimer for Biocompatible High-Efficiency DNA Delivery*. *Macromolecules*, 2002. **35**: p. 3456-3462.
45. Pavan, G.M., P. Posocco, and a.e. al., *PAMAM Dendrimer for siRNA Delivery: Computational and Experimental Insights*. *Chemistry-A European Journal*, 2010. **16**: p. 7781-7795.
46. Lin, S.-T., P.K. Maiti, and W.A.G. III, *Dynamics and Thermodynamics of Water in PAMAM Dendrimers at Subnanosecond Time Scales*. *Journal of Physical Chemistry B*, 2005. **109**: p. 8663-8672.
47. Arima, H., et al., *Folate-PEG-appended dendrimer conjugate with alpha-cyclodextrin as a novel cancer cell-selective siRNA delivery carrier*. *Mol Pharm*, 2012. **9**(9): p. 2591-604.
48. Tang, Y., et al., *Efficient in vitro siRNA delivery and intramuscular gene silencing using PEG-modified PAMAM dendrimers*. *Mol Pharm*, 2012. **9**(6): p. 1812-21.
49. Arima, H., K. Motoyama, and T. Higashi, *Potential Use of Polyamidoamine Dendrimer Conjugates with Cyclodextrins as Novel Carriers for siRNA*. *Pharmaceuticals*, 2012. **5**: p. 61-78.
50. Wu, L. and S.R.P. da Rocha, *Biocompatible and biodegradable copolymer stabilizers for hydrofluoroalkane dispersions: a colloidal probe microscopy investigation*. *Langmuir*, 2007. **23**(24): p. 12104-12110.

51. National Heart Lung and Blood Institute. *National Heart Lung and Blood Institute Factbook*. 2010 [cited 2011; Available from: http://www.nhlbi.nih.gov/about/factbook/FactBook_2010.pdf.
52. National Cancer Institute. *Lung Cancer*. 2011; Available from: <http://www.cancer.gov/cancertopics/types/lung>.
53. World Health Organization. *Chronic Obstructive Pulmonary Disorders - Fact sheet* 2011; Available from: <http://www.who.int/mediacentre/factsheets/fs315/en/index.html>.
54. American Lung Association, *State of lung diseases in diverse communities*. 2010, American Lung Association: Washington, DC. p. 1-101.
55. da Rocha, S.R.P., B. Bharatwaj, and S. Saiprasad, *Science and Technology of Pressurized Metered-Dose Inhalers*, in *Controlled Pulmonary Drug Delivery*, H.D.C. Smyth and A.J. Hickey, Editors. 2011. p. 165-201.
56. Smyth, H.D.C., *The influence of formulation variables on the performance of alternative propellant-driven metered dose inhalers*. *Adv Drug Deliv Rev*, 2003. **55**(7): p. 807-828.
57. Vervaet, C. and P.R. Byron, *Drug-surfactant-propellant interactions in HFA-formulations*. *Int J Pharm*, 1999. **186**(1): p. 13-30.
58. Williams III, R.O. and J. Liu, *Formulation of a protein with propellant HFA 134a for aerosol delivery*. *Eur J Pharm Sci*, 1999. **7**(2): p. 137-144.
59. Marijani, R., et al., *Evaluation of metered dose inhaler (MDI) formulations of ciclosporin*. *J Pharm Pharmacol*, 2007. **59**(1): p. 15-21.
60. Young, P.M., et al., *The influence of micronised particulates on the aerosolisation properties of pressurised metered dose inhalers*. *Journal of Aerosol Science*, 2009. **40**(4): p. 324-337.
61. O'Donnell, K.P. and R.O. Williams III, *Pulmonary dispersion formulations: The impact of dispersed powder properties on pressurized metered dose inhaler stability*. *Drug Dev Ind Pharm*, 2013(00): p. 1-12.

62. Gao, Y., et al. *Comparison of the thermodynamic performance of direct expansion ground source heat pump using hydrofluoroolefins (HFOs) based on theoretical analysis*. in *Power and Energy Engineering Conference (APPEEC)*. 2012. Asia-Pacific: IEEE.
63. Schmidt, T., et al., *Biotransformation of 2,3,3,3-tetrafluoropropene (HFO-1234yf) in male, pregnant and non-pregnant female rabbits after single high dose inhalation exposure*. *Toxicology and Applied Pharmacology*, 2012. **263**(1): p. 32-38.
64. Rusch, G.M., *Organic chlorofluoro hydrocarbons*. *Patty's Toxicology*, 2012.
65. Koyama, S., N. Takata, and S. Fukuda, *Drop-in experiments on heat pump cycle using HFO-1234ze (E) and its mixtures with HFC-32*, in *International Refrigeration and Air Conditioning Conference at Purdue*. 2010: Purdue University. p. 1-7.
66. Bogdan, M., J. Ling, and D. Williams, *Next generation (LGWP) of blowing agents for spray foam applications*, in *Proceedings of CPI*. 2009, Honeywell Solstice™ Blowing Agent.
67. Tasinato, N., et al., *Anharmonic force field and vibrational dynamics of CH₂F₂ up to 5000 cm⁻¹ studied by Fourier Transform Infrared spectroscopy and state-of-the-art ab initio calculations*. *The Journal of Chemical Physics*, 2012. **136**(214302): p. 1-17.
68. Aphalo, P.J., et al., *Reviewers of the 2010 UNEP environmental effects assessment report*. United Nations Environment Programme, 2010: p. 233.
69. Conti, D.S., et al., *Solvation in hydrofluoroalkanes: How can ethanol help?* *Journal of Pharmacy and Pharmacology*, 2011. **64**(9): p. 1236-1244.
70. Zhang, X., et al., *Experimental study on cryogenic moisture uptake in polyurethane foam insulation material*. *Cryogenics*, 2012. **52**(12): p. 810-815.
71. Noakes, T., *Medical aerosol propellants*. *Journal of Fluorine Chemistry*, 2002. **118**(1): p. 35-45.
72. Zhao, Y., S.A. Jones, and M.B. Brown, *Dynamic foams in topical drug delivery*. *Journal of Pharmacy and Pharmacology*, 2010. **62**(6): p. 678-684.

73. Febriyenti, F., A.M. Noor, and S.B.B. Baie, *Physical evaluations of Haruan spray for wound dressing and wound healing*. International Journal of Drug Delivery, 2011. **3**(1): p. 115-124.
74. Meltzer, E.O., et al., *Safety and efficacy of once-daily treatment with beclomethasone dipropionate nasal aerosol in subjects with perennial allergic rhinitis*. Allergy and Asthma Proceedings, 2012. **33**(3): p. 249-257.
75. Djupesland, P., *Nasal drug delivery devices: Characteristics and performance in a clinical perspective - a review*. Drug Delivery and Translational Research, 2013. **3**(1): p. 42-62.
76. Bell, J. and S. Newman, *The rejuvenated pressurised metered dose inhaler*. Expert Opin Drug Deliv, 2007. **4**(3): p. 215-234.
77. Cheng, Y., et al., *Respiratory deposition patterns of salbutamol pMDI with CFC and HFA-134a formulations in a human airway replica*. Journal of aerosol medicine, 2001. **14**(2): p. 255-266.
78. Klomfar, J., M. Součková, and J. Pátek, *Liquid-phase p-p-T data for 2,3,3,3-tetrafluoroprop-1-ene (R-1234yf) and 1,1,2,3,3,3-hexafluoroprop-1-ene (R-1216) at temperatures from (208 to 353) K under pressures up to 40 MPa*. Journal of Chemical & Engineering Data, 2012. **57**(11): p. 3283-3289.
79. Padilla, M., R. Revellin, and J. Bonjour, *Two-phase flow of HFO-1234yf, R-134a and R-410A in sudden contractions: Visualization, pressure drop measurements and new prediction method*. Experimental Thermal and Fluid Science, 2013.
80. Honeywell International Inc. *Honeywell Low Global Warming Technologies - Applications*. 2004-2013 2-18-2013]; Available from: <http://www51.honeywell.com/sm/lgwp-uk/applications.html>.
81. Paulechka, E., et al., *A systematic approach for development of an OPLS-like force field and its application to hydrofluorocarbons*. The Journal of Physical Chemistry B, 2012. **116**(49): p. 14389-14397.

82. Di Nicola, G., F. Polonara, and G. Santori, *Saturated pressure measurements of 2,3,3,3-tetrafluoroprop-1-ene (HFO-1234yf)*. Journal of Chemical & Engineering Data, 2009. **55**(1): p. 201-204.
83. Lindley, A.A. and T.J. Noakes, *Consideration of Hydrofluoroolefins (HFOs) as potential candidate medical propellants*. 2010, Mexichem Fluor.
84. Csonka, S., I. Weymann, and G. Zarand, *An electrically controlled quantum dot based spin current injector*. Nanoscale, 2012. **4**(12): p. 3635-9.
85. Morris-Cohen, A.J., et al., *Controlling the rate of electron transfer between a quantum dot and a tri-ruthenium molecular cluster by tuning the chemistry of the interface*. Phys Chem Chem Phys, 2012. **14**(40): p. 13794-801.
86. Nagy, A., et al., *Comprehensive analysis of the effects of CdSe quantum dot size, surface charge, and functionalization on primary human lung cells*. ACS Nano, 2012. **6**(6): p. 4748-62.
87. Esposito, M., et al., *Stochastically driven single-level quantum dot: a nanoscale finite-time thermodynamic machine and its various operational modes*. Phys Rev E Stat Nonlin Soft Matter Phys, 2012. **85**(3 Pt 1): p. 031117.
88. Quinones, G.A., et al., *Ultrasensitive detection of cellular protein interactions using bioluminescence resonance energy transfer quantum dot-based nanoprobe*. J Cell Biochem, 2012. **113**(7): p. 2397-405.
89. Ikpi, M.E., et al., *Fabrication of a self-aligned cross-wire quantum-dot chain light emitting diode by molecular beam epitaxial regrowth*. Nanotechnology, 2012. **23**(22): p. 225304.
90. Wang, J., et al., *Quantum dot-based near-infrared electrochemiluminescent immunosensor with gold nanoparticle-graphene nanosheet hybrids and silica nanospheres double-assisted signal amplification*. Anal Chem, 2012. **84**(11): p. 4893-9.

91. Hughes, B.K., et al., *Control of PbSe quantum dot surface chemistry and photophysics using an alkylselenide ligand*. ACS Nano, 2012. **6**(6): p. 5498-506.
92. Mendoza, M. and S. Ujevic, *Magneto-conductance fingerprints of purely quantum states in the open quantum dot limit*. J Phys Condens Matter, 2012. **24**(23): p. 235302.
93. Foell, C.A., et al., *Saturation behaviour of colloidal PbSe quantum dot exciton emission coupled into silicon photonic circuits*. Opt Express, 2012. **20**(10): p. 10453-69.
94. Ling, H.S., et al., *Voltage-tunable dual-band quantum dot infrared photodetectors for temperature sensing*. Opt Express, 2012. **20**(10): p. 10484-9.
95. Aouadi, M., et al., *Orally delivered siRNA targeting macrophage Map4k4 suppresses systemic inflammation*. Nature, 2009. **458**(7242): p. 1180-1184.
96. Lai, S.K., Y.-Y. Wang, and J. Hanes, *Mucus-penetrating nanoparticles for drug and gene delivery to mucosal tissues*. Adv Drug Deliv Rev, 2009. **61**(2): p. 158-171.
97. Stone, R., *NIH to review gene therapy program*. Science, 1995. **268**(5211): p. 627.
98. Cohen-Haguenauer, O., *A review of current basic approaches to gene therapy*. Nouv Rev Fr Hematol, 1994. **36 Suppl 1**: p. S3-9.
99. Merkel, O.M., et al., *Stability of siRNA polyplexes from poly (ethylenimine) and poly (ethylenimine)-g-poly (ethylene glycol) under in vivo conditions: effects on pharmacokinetics and biodistribution measured by Fluorescence Fluctuation Spectroscopy and Single Photon Emission Computed Tomography (SPECT) imaging*. Journal of Controlled Release, 2009. **138**(2): p. 148-159.
100. Woo, S.L., *Introductory remarks to the review series on gene therapy*. Trends Genet, 1994. **10**(4): p. 111-2.
101. Jenks, S., *Gene therapy review finds few complications*. J Natl Cancer Inst, 1993. **85**(15): p. 1188-90.

102. Gershon, D., *Gene therapy panel. NIH merger to shorten review.* Nature, 1992. **355**(6362): p. 664.
103. Palca, J., *Changes ahead for gene therapy review process?* Science, 1991. **253**(5020): p. 624-5.
104. Gonzalez-Carmona, M.A., et al., *Inhibition of hepatitis C virus RNA translation by antisense bile acid conjugated phosphorothioate modified oligodeoxynucleotides (ODN).* Antiviral Res, 2013. **97**(1): p. 49-59.
105. Onizuka, K., et al., *Site-specific modification of RNA by functionality-transfer ODN probes.* Nucleic Acids Symp Ser (Oxf), 2009(53): p. 67-8.
106. Cao, Q., et al., *Combination of integrin siRNA and irradiation for breast cancer therapy.* Biochem Biophys Res Commun, 2006. **351**(3): p. 726-32.
107. Storvold, G.L., et al., *siRNA: a potential tool for future breast cancer therapy?* Crit Rev Oncog, 2006. **12**(1-2): p. 127-50.
108. Devi, G.R., *siRNA-based approaches in cancer therapy.* Cancer Gene Ther, 2006. **13**(9): p. 819-29.
109. Duxbury, M.S., et al., *Systemic siRNA-mediated gene silencing: a new approach to targeted therapy of cancer.* Ann Surg, 2004. **240**(4): p. 667-74; discussion 675-6.
110. Rojanarata, T., et al., *Chitosan-thiamine pyrophosphate as a novel carrier for siRNA delivery.* Pharm Res, 2008. **25**(12): p. 2807-14.
111. Buyens, K., et al., *A fast and sensitive method for measuring the integrity of siRNA-carrier complexes in full human serum.* J Control Release, 2008. **126**(1): p. 67-76.
112. Wang, X.L., et al., *A multifunctional and reversibly polymerizable carrier for efficient siRNA delivery.* Biomaterials, 2008. **29**(1): p. 15-22.
113. Sato, A., et al., *Polymer brush-stabilized polyplex for a siRNA carrier with long circulatory half-life.* J Control Release, 2007. **122**(3): p. 209-16.

114. Matsui, K., et al., *RNAi gene silencing using cerasome as a viral-size siRNA-carrier free from fusion and cross-linking*. *Bioorg Med Chem Lett*, 2007. **17**(14): p. 3935-8.
115. Nguyen, J., et al., *Fast degrading polyesters as siRNA nano-carriers for pulmonary gene therapy*. *Journal of Controlled Release*, 2008. **132**(3): p. 243-251.
116. Nielsen, E.J., et al., *Pulmonary gene silencing in transgenic EGFP mice using aerosolised chitosan/siRNA nanoparticles*. *Pharm Res*, 2010. **27**(12): p. 2520-7.
117. Liao, Z.X., et al., *Enhancement of efficiencies of the cellular uptake and gene silencing of chitosan/siRNA complexes via the inclusion of a negatively charged poly(gamma-glutamic acid)*. *Biomaterials*, 2010. **31**(33): p. 8780-8.
118. Convertine, A.J., et al., *pH-Responsive Polymeric Micelle Carriers for siRNA Drugs*. *Biomacromolecules*, 2010.
119. Biswal, B.K., N.B. Debata, and R.S. Verma, *Development of a targeted siRNA delivery system using FOL-PEG-PEI conjugate*. *Mol Biol Rep*, 2010. **37**(6): p. 2919-26.
120. Chen, M., et al., *Chitosan/siRNA nanoparticles encapsulated in PLGA nanofibers for siRNA delivery*. *ACS Nano*, 2012. **6**(6): p. 4835-44.
121. Umeda, Y., et al., *PEG-attached PAMAM dendrimers encapsulating gold nanoparticles: growing gold nanoparticles in the dendrimers for improvement of their photothermal properties*. *Bioconjug Chem*, 2010. **21**(8): p. 1559-64.
122. Zhao, Y., et al., *Synthesis and grafting of folate-PEG-PAMAM conjugates onto quantum dots for selective targeting of folate-receptor-positive tumor cells*. *J Colloid Interface Sci*, 2010. **350**(1): p. 44-50.
123. Qi, R., et al., *PEG-conjugated PAMAM dendrimers mediate efficient intramuscular gene expression*. *AAPS J*, 2009. **11**(3): p. 395-405.

124. Singh, P., et al., *Folate and folate-PEG-PAMAM dendrimers: synthesis, characterization, and targeted anticancer drug delivery potential in tumor bearing mice*. *Bioconjug Chem*, 2008. **19**(11): p. 2239-52.
125. Kim, T.I., et al., *PAMAM-PEG-PAMAM: novel triblock copolymer as a biocompatible and efficient gene delivery carrier*. *Biomacromolecules*, 2004. **5**(6): p. 2487-92.
126. Mittnacht, U., et al., *Chitosan/siRNA nanoparticles biofunctionalize nerve implants and enable neurite outgrowth*. *Nano Lett*, 2010. **10**(10): p. 3933-9.
127. Johansson, M.P., V.R. Kaila, and D. Sundholm, *Ab initio, density functional theory, and semi-empirical calculations*. *Methods Mol Biol*, 2013. **924**: p. 3-27.
128. Bar, J., R.S. Herbst, and A. Onn, *Targeted drug delivery strategies to treat lung metastasis*. *Expert Opin Drug Deliv*, 2009. **6**(10): p. 1003-16.
129. Li, L., et al., *Quantum Dot - Aluminum phthalocyanine Conjugates perform photodynamic reactions to kill cancer cells via fluorescence resonance energy transfer (FRET)*. *Nanoscale Res Lett*, 2012. **7**(1): p. 386.
130. Kang, H., et al., *Multimodal optical studies of single and clustered colloidal quantum dots for the long-term optical property evaluation of quantum dot-based molecular imaging phantoms*. *Biomed Opt Express*, 2012. **3**(6): p. 1312-25.
131. Moussa, I. and I. Parikh, *Dry aerosol suspension of phospholipid-stabilized drug microparticles in a hydrofluoroalkane propellant*. 2000, Google Patents.
132. Arnaud, D. and J.C. Tanguy, *Azeotropic mixture with 1, 1, 1-trifluoroethane and propane a low boiling point and its applications as a refrigerant fluid, as an aerosol propellant, or as a blowing agent for plastic foams*. 1992, Google Patents.
133. Gurge, R., J. Hirsh, and M. Trumbore, *Topical pharmaceutical foam composition*. 2006, Google Patents.

134. Bredeson, E.S. and V.L. Valoppi, *Integral skin foams employing pentafluoropropane blowing agents*. 1999, Google Patents.
135. Protocol, M., *Montreal protocol on substances that deplete the ozone layer*. Washington, DC: US Government Printing Office, 1987. **26**.
136. Protocol, K., *Framework Convention on Climate Change*. 2010.
137. Tsai, W.-T., *An overview of environmental hazards and exposure risk of hydrofluorocarbons (HFCs)*. Chemosphere, 2005. **61**(11): p. 1539-1547.
138. Barclay, T. *CFCs: The Way Ahead for Refrigerants and Sterilisation Mixtures*. in *The Changing Scene of Health Care and Technology: Proceedings of the 11th International Congress of Hospital Engineering, June 1990, London, UK*. 1990. Taylor & Francis.
139. Kontny, M., et al., *Issues surrounding MDI formulation development with non-CFC propellants*. Journal of Aerosol Medicine, 1991. **4**(3): p. 181-187.
140. Vervaet, C. and P.R. Byron, *Drug-surfactant-propellant interactions in HFA-formulations*. International journal of pharmaceutics, 1999. **186**(1): p. 13-30.
141. Yoganathan, D. and W.N. Rom, *Medical aspects of global warming*. American journal of industrial medicine, 2001. **40**(2): p. 199-210.
142. Leach, C.L., *The CFC to HFA transition and its impact on pulmonary drug development*. Respiratory care, 2005. **50**(9): p. 1201-1208.
143. Dolovich, M., *New delivery systems and propellants*. Canadian respiratory journal: journal of the Canadian Thoracic Society, 1998. **6**(3): p. 290-295.
144. Higashi, Y. *Thermophysical properties of HFO-1234yf and HFO-1234ze (E)*. in *International Symposium on Next-generation Air Conditioning and Refrigeration Technology*. 2010.
145. Zyhowski, G. and A. Brown, *Low Global Warming Fluids for Replacement of HFC-245fa and HFC-134a in ORC Applications*. 2011, Honeywell.

146. Pham, H.T., R.R. Singh, and D.P. Wilson, *Pentafluoropropene-based compositions*. 2005, Google Patents.
147. Yana Motta, S.F., E.D. Vera Bercerra, and M.W. Spatz, *Analysis of LGWP alternatives for small refrigeration (plugin) applications*. 2010.
148. Kondo, S., K. Takizawa, and K. Tokuhashi, *Effects of temperature and humidity on the flammability limits of several 2L refrigerants*. *Journal of Fluorine Chemistry*, 2012. **144**: p. 130-136.
149. Schuster, P., et al., *Biotransformation of *trans*-1, 1, 1, 3-tetrafluoropropene (HFO-1234ze)*. *Toxicology and applied pharmacology*, 2009. **239**(3): p. 215-223.
150. Rusch, G.M., et al., *The acute, genetic, developmental and inhalation toxicology of trans-1, 3, 3, 3-tetrafluoropropene (HFO-1234ze)*. *Drug and chemical toxicology*, 2013. **36**(2): p. 170-180.
151. Calm, J.M. and D.A. Didion, *Trade-offs in refrigerant selections: past, present, and future*. *International Journal of Refrigeration*, 1998. **21**(4): p. 308-321.
152. COULOMB, D., *Refrigeration: The challenges associated with sustainable development*. *Interlinked Challenges, Interlinked Solutions: Ozone Protection and Climate Change*, 2006: p. 12.
153. Powell, R.L., *CFC phase-out: have we met the challenge?* *Journal of Fluorine Chemistry*, 2002. **114**(2): p. 237-250.
154. Saidur, R., et al., *A review on the performance of nanoparticles suspended with refrigerants and lubricating oils in refrigeration systems*. *Renewable and Sustainable Energy Reviews*, 2011. **15**(1): p. 310-323.
155. Wu, L., M. Al-Haydari, and S.R. da Rocha, *Novel propellant-driven inhalation formulations: engineering polar drug particles with surface-trapped hydrofluoroalkane-philic*. *European Journal of Pharmaceutical Sciences*, 2008. **33**(2): p. 146-158.
156. Peguin, R.P., L. Wu, and S.R. da Rocha, *The ester group: How hydrofluoroalkane-philic is it?* *Langmuir*, 2007. **23**(16): p. 8291-8294.

157. Tanaka, K., G. Takahashi, and Y. Higashi, *Measurements of the isobaric specific heat capacities for trans-1, 3, 3, 3-tetrafluoropropene (HFO-1234ze (E)) in the liquid phase*. Journal of Chemical & Engineering Data, 2010. **55**(6): p. 2267-2270.
158. Tanaka, K., G. Takahashi, and Y. Higashi, *Measurements of the vapor pressures and $p \rho T$ properties for trans-1, 3, 3, 3-tetrafluoropropene (HFO-1234ze (E))*. Journal of Chemical & Engineering Data, 2010. **55**(6): p. 2169-2172.
159. Koban, M. *HFO-1234yf low GWP refrigerant LCCP analysis*. in *SAE World Congress*. 2009.
160. Honeywell, *New low global warming potential aerosol propellant*. www.honeywell.com, 2011.
161. Latajka, Z., et al., *Ab initio study of interactions between methanol and nitrogen or carbon monoxide*. Journal of Molecular Structure, 1989. **194**: p. 45-60.
162. Peguin, R. and S.d. Rocha, *Solvent-solute interactions in hydrofluoroalkane propellant*. Journal of physical chemistry
2008.
163. Islam, A., B. Chowdhry, and M. Snowden, *Heteroaggregation in colloidal dispersions*. Advances in colloid and interface science, 1995. **62**(2): p. 109-136.
164. Frisch, M., et al., *Gaussian 09, Revision A. 02*, Gaussian. Inc., Wallingford, CT, 2009. **200**.
165. Ayala, P.Y. and G.E. Scuseria, *Linear scaling second-order Moller–Plesset theory in the atomic orbital basis for large molecular systems*. The Journal of chemical physics, 1999. **110**(8): p. 3660-3671.
166. Gutowski, M., et al., *The basis set superposition error in correlated electronic structure calculations*. Chemical physics letters, 1986. **124**(4): p. 370-375.
167. Gutowski, M. and G. Chal, *Critical evaluation of some computational approaches to the problem of basis set superposition error*. The Journal of chemical physics, 1993. **98**(7): p. 5540-5554.

168. Singh, U.C. and P.A. Kollman, *An approach to computing electrostatic charges for molecules*. Journal of Computational Chemistry, 1984. **5**(2): p. 129-145.
169. Wu, L., R.P. Peguin, and S.R. da Rocha, *Understanding solvation in hydrofluoroalkanes: ab initio calculations and chemical force microscopy*. The Journal of Physical Chemistry B, 2007. **111**(28): p. 8096-8104.
170. Kudin, K.N., R. Car, and R. Resta, *Longitudinal polarizability of long polymeric chains: Quasi-one-dimensional electrostatics as the origin of slow convergence*. The Journal of chemical physics, 2005. **122**(13): p. 134907.
171. Baldrick, P., *Pharmaceutical excipient development: the need for preclinical guidance*. Regulatory Toxicology and Pharmacology, 2000. **32**(2): p. 210-218.
172. Redenti, E., L. Szente, and J. Szejtli, *Drug/cyclodextrin/hydroxy acid multicomponent systems. Properties and pharmaceutical applications*. Journal of pharmaceutical sciences, 2000. **89**(1): p. 1-8.
173. Peguin, R.P. and S.R. da Rocha, *Solvent– solute interactions in hydrofluoroalkane propellants*. The Journal of Physical Chemistry B, 2008. **112**(27): p. 8084-8094.
174. Selvam, P., et al., *Surfactant design for the 1, 1, 1, 2-tetrafluoroethane-water interface: ab initio calculations and in situ high-pressure tensiometry*. Langmuir, 2006. **22**(21): p. 8675-8683.
175. Wu, L., et al., *Molecular scale behavior in alternative propellant-based inhaler formulations*. LUNG BIOLOGY IN HEALTH AND DISEASE, 2007. **221**: p. 373.
176. Desiraju, G.R., *The CH... O hydrogen bond: structural implications and supramolecular design*. Accounts of Chemical Research, 1996. **29**(9): p. 441-449.
177. Desiraju, G.R., *Hydrogen bridges in crystal engineering: interactions without borders*. Accounts of chemical research, 2002. **35**(7): p. 565-573.

178. Studart, A.R., E. Amstad, and L.J. Gauckler, *Colloidal stabilization of nanoparticles in concentrated suspensions*. Langmuir, 2007. **23**(3): p. 1081-1090.
179. Rosen, M.J. and J.T. Kunjappu, *Surfactants and interfacial phenomena*. 2012: John Wiley & Sons.
180. Agency, U.E.P., *TRANSITIONING TO LOW-GWP ALTERNATIVES IN MVACs*. EPA, 2010.
181. Minor, B. and M. Spatz, *HFO-1234yf low GWP refrigerant update*. 2008.
182. Committee, E., *Regulation (EC) No 842: 2006 of the European parliament and of the council of 17 May 2006 on certain fluorinated greenhouse gaser*. Official Journal of the European Union, 2006. **161**: p. 1-8.
183. Fontelles, J.B. and H. Winkler, *Directive 2006/40/ec of the european parliament and of the council*. Official Journal of the European Union, 2006. **161**: p. 12-18.
184. EPA, *Protection of Stratospheric Ozone: New Substitute in the Motor Vehicle Air Conditioning Sector Under the Significant New Alternatives Policy (SNAP) Program Federal Register*, 2009. **74**(200).
185. Pearson, A., *THE INSTITUTE OF REFRIGERATION*. Proc. Inst. R, 2013. **2012**(13): p. 7-1.
186. Spatz, M. and B. Minor. *HFO-1234yf, a low GWP refrigerant for MAC*. in *VDA Alternative Refrigerant Winter Meeting, Saalfelden, Austria*. 2008.
187. Labelle, C.B. and K.K. Gleason, *Environmental, Safety and Health Issues Associated With Low Dielectric Constant Films Grown By Chemical Vapor Deposition*. Environmental Issues in the Electronics/semiconductor Industries and: Electrochemical/photochemical Methods for Pollution Abatement, 1998. **98**(5): p. 27.
188. Muijser, H., *TNO Report. Sub-chronic (13-week) Inhalation Toxicity Study with HFO-1234ze in Rates Rusch, G.(2004)*. Trans HFO-1234: An acute (4-hour) Inhalation Toxicity Screening Study with a Micronucleus Assay in the Mouse and Rat Via Nose-Only Exposure, 2008.

189. Cripps, A., et al., *Pharmaceutical transition to non-CFC pressurized metered dose inhalers*. Respiratory medicine, 2000. **94**: p. S3-S9.
190. McDonald, K.J. and G.P. Martin, *Transition to CFC-free metered dose inhalers—into the new millennium*. International Journal of Pharmaceutics, 2000. **201**(1): p. 89-107.
191. Singh, R.R. and H.T. Pham, *Azeotrope-like compositions of tetrafluoropropene and trifluoroiodomethane*. 2006, Google Patents.
192. Singh, R.R. and G. Knopeck, *AEROSOL COMPOSITIONS CONTAINING FLUORINE SUBSTITUTED OLEFINS AND METHODS AND SYSTEMS USING SAME*. 2007, Google Patents.
193. Bowman, J.M., D.J. Williams, and R.R. Singh, *Foaming Agents, Foamable Compositions, Foams and Articles Containing Fluorine Substituted Olefins, and Methods of Making Same*. 2007, Google Patents.
194. *Compositions containing fluorine substituted olefins*. 2011, EP Patent 2,277,969.
195. Hart, J.W. and T.C. Rolfson, *Aerosol package containing a foam-forming emulsion and propellant system*. 1976, Google Patents.
196. Raabe, G. and E.J. Maginn, *A Force Field for 3, 3, 3-fluoro-1-propenes, including HFO-1234yf*. The Journal of Physical Chemistry B, 2010. **114**(31): p. 10133-10142.
197. Song, Y.Z., et al., *Experimental and density functional theory and ab initio Hartree-Fock study on the vibrational spectra of 2-(4-fluorobenzylideneamino)-3-(4-hydroxyphenyl) propanoic acid*. Spectrochim Acta A Mol Biomol Spectrosc, 2008. **69**(2): p. 682-7.
198. Coe, J.D., B.G. Levine, and T.J. Martinez, *Ab initio molecular dynamics of excited-state intramolecular proton transfer using multireference perturbation theory*. J Phys Chem A, 2007. **111**(44): p. 11302-10.

199. Volk, D.E., et al., *Ab initio base-pairing energies of an oxidized thymine product, 5-formyluracil, with standard DNA bases at the BSSE-free DFT and MP2 theory levels*. *Org Biomol Chem*, 2007. **5**(10): p. 1554-8.
200. Frisch, M., et al., *Gaussian 03, revision C. 02*. 2008.
201. Raabe, G., *Molecular modeling of fluoropropene refrigerants*. *The Journal of Physical Chemistry B*, 2012. **116**(19): p. 5744-5751.
202. Patel, S. and C.L. Brooks, *CHARMM fluctuating charge force field for proteins: I parameterization and application to bulk organic liquid simulations*. *Journal of Computational Chemistry*, 2004. **25**(1): p. 1-16.
203. Smith, G.D., O. Borodin, and D. Bedrov, *Quantum Chemistry Based Force Field for Simulations of Poly (propylene oxide) and Its Oligomers*. *The Journal of Physical Chemistry A*, 1998. **102**(50): p. 10318-10323.
204. Kafka, G.R., S.L. Masters, and D.W. Rankin, *Structure enhancement methodology using theory and experiment: gas-phase molecular structures using a dynamic interaction between electron diffraction, molecular mechanics, and ab initio data*. *J Phys Chem A*, 2007. **111**(26): p. 5913-20.
205. da Rocha, S.R. and K.P. Johnston, *Interfacial thermodynamics of surfactants at the CO₂-water interface*. *Langmuir*, 2000. **16**(8): p. 3690-3695.
206. Peguin, R.P., P. Selvam, and S.R. da Rocha, *Microscopic and thermodynamic properties of the HFA134a-water interface: atomistic computer simulations and tensiometry under pressure*. *Langmuir*, 2006. **22**(21): p. 8826-8830.
207. Stone, M.T., et al., *Molecular differences between hydrocarbon and fluorocarbon Surfactants at the CO₂/water interface*. *The Journal of Physical Chemistry B*, 2003. **107**(37): p. 10185-10192.
208. Adelman, S., *Generalized Langevin Equations and Many - Body Problems in Chemical Dynamics*. *Advances in Chemical Physics*, Volume 44, 1980: p. 143-253.

209. de Leeuw, S.W., J.W. Perram, and E.R. Smith, *Simulation of electrostatic systems in periodic boundary conditions. I. Lattice sums and dielectric constants*. Proceedings of the Royal Society of London. A. Mathematical and Physical Sciences, 1980. **373**(1752): p. 27-56.
210. Darden, T., D. York, and L. Pedersen, *Particle mesh Ewald: An $N \cdot \log(N)$ method for Ewald sums in large systems*. J Chem Phys, 1993. **98**: p. 10089.
211. Alejandre, J., D.J. Tildesley, and G.A. Chapela, *Molecular dynamics simulation of the orthobaric densities and surface tension of water*. J Chem Phys, 1995. **102**: p. 4574.
212. Dang, L.X. and T.-M. Chang, *Molecular dynamics study of water clusters, liquid, and liquid–vapor interface of water with many-body potentials*. J Chem Phys, 1997. **106**: p. 8149.
213. van Buuren, A.R., S.J. Marrink, and H.J. Berendsen, *A molecular dynamics study of the decane/water interface*. The Journal of Physical Chemistry, 1993. **97**(36): p. 9206-9212.
214. Kohn, J., W.J. Welsh, and D. Knight, *A new approach to the rationale discovery of polymeric biomaterials*. Biomaterials, 2007. **28**(29): p. 4171-4177.
215. Peguin, R.P.S., P. Selvam, and S.R.P. da Rocha, *Microscopic and Thermodynamic Properties of the HFA134a–Water Interface: Atomistic Computer Simulations and Tensiometry under Pressure*. Langmuir, 2006. **22**(21): p. 8826-8830.
216. Rogueda, P.G., *HPFP, a model propellant for pMDIs*. Drug development and industrial pharmacy, 2003. **29**(1): p. 39-49.
217. Mitchell, J.P., et al., *Aerodynamic particle size analysis of aerosols from pressurized metered-dose inhalers: comparison of Andersen 8-stage cascade impactor, next generation pharmaceutical impactor, and model 3321 aerodynamic particle sizer aerosol spectrometer*. AAPS PharmSciTech, 2003. **4**(4): p. 425-433.
218. Kim, C., D. Trujillo, and M. Sackner, *Size aspects of metered-dose inhaler aerosols*. The American review of respiratory disease, 1985. **132**(1): p. 137-142.

219. Shulman, M.L., et al., *Dissolution behavior and surface tension effects of organic compounds in nucleating cloud droplets*. Geophysical Research Letters, 1996. **23**(3): p. 277-280.
220. Tolman, R.C., *The effect of droplet size on surface tension*. The journal of chemical physics, 2004. **17**(3): p. 333-337.
221. da Rocha, S.R., et al., *Molecular structure of the water-supercritical CO₂ interface*. The Journal of Physical Chemistry B, 2001. **105**(48): p. 12092-12104.
222. Van Vlimmeren, B., et al., *Simulation of 3D mesoscale structure formation in concentrated aqueous solution of the triblock polymer surfactants (ethylene oxide)₁₃ (propylene oxide)₃₀ (ethylene oxide)₁₃ and (propylene oxide)₁₉ (ethylene oxide)₃₃ (propylene oxide)₁₉. Application of dynamic mean-field density functional theory*. Macromolecules, 1999. **32**(3): p. 646-656.
223. Fowkes, F.M., *Dispersion force contributions to surface and interfacial tensions, contact angles, and heats of immersion*. Adv. Chem. Ser, 1964. **43**(1): p. 99-111.
224. Ma, T.Y., et al., *PEG 400, a hydrophilic molecular probe for measuring intestinal permeability*. Gastroenterology, 1990. **98**(1): p. 39-46.
225. Liao, Y.-H., et al., *The effects of polyvinyl alcohol on the in vitro stability and delivery of spray-dried protein particles from surfactant-free HFA 134a-based pressurised metered dose inhalers*. International journal of pharmaceutics, 2005. **304**(1): p. 29-39.
226. Raabe, G. and E.J. Maginn, *Molecular Modeling of the Vapor– Liquid Equilibrium Properties of the Alternative Refrigerant 2, 3, 3, 3-Tetrafluoro-1-propene (HFO-1234yf)*. The Journal of Physical Chemistry Letters, 2009. **1**(1): p. 93-96.
227. Kono, K., *Dendrimer-based bionanomaterials produced by surface modification, assembly and hybrid formation*. Polymer journal, 2012. **44**(6): p. 531-540.
228. Peng, C., et al., *PEGylated dendrimer-entrapped gold nanoparticles for *in vivo* blood pool and tumor imaging by computed tomography*. Biomaterials, 2012. **33**(4): p. 1107-1119.

229. Arima, H., et al., *Potential use of folate-polyethylene glycol (PEG)-appended dendrimer (G3) conjugate with α -cyclodextrin as DNA carriers to tumor cells*. *Cancer Gene Ther*, 2012. **19**(5): p. 358-366.
230. Svenson, S. and D.A. Tomalia, *Dendrimers in biomedical applications—reflections on the field*. *Adv Drug Deliv Rev*, 2012.
231. Huang, B., et al., *The facile synthesis of multifunctional PAMAM dendrimer conjugates through copper-free click chemistry*. *Bioorg Med Chem Lett*, 2012. **22**(9): p. 3152-3156.
232. Arima, H., et al., *Folate-PEG-appended dendrimer conjugate with α -cyclodextrin as a novel cancer cell-selective siRNA delivery carrier*. *Mol Pharm*, 2012. **9**(9): p. 2591-2604.
233. Tang, Y., et al., *Efficient in vitro siRNA delivery and intramuscular gene silencing using PEG-modified PAMAM dendrimers*. *Mol Pharm*, 2012. **9**(6): p. 1812-1821.
234. Ciolkowski, M., et al., *The influence of PAMAM dendrimers surface groups on their interaction with porcine pepsin*. *Biochimica et Biophysica Acta (BBA)-Proteins and Proteomics*, 2013.
235. Thiagarajan, G., K. Greish, and H. Ghandehari, *Charge affects the oral toxicity of poly (amido amine) dendrimers*. *European Journal of Pharmaceutics and Biopharmaceutics*, 2013.
236. Janaszewska, A., et al., *Modified PAMAM dendrimer with 4-carbomethoxypyrrolidone surface groups reveals negligible toxicity against three rodent cell-lines*. *Nanomedicine: Nanotechnology, Biology and Medicine*, 2013.
237. Jones, C.F., et al., *Cationic PAMAM dendrimers disrupt key platelet functions*. *Mol Pharm*, 2012. **9**(6): p. 1599-1611.
238. Paul, A., et al., *PAMAM Dendrimer-Baculovirus Nanocomplex for Microencapsulated Adipose Stem Cell-Gene Therapy: In Vitro and in Vivo Functional Assessment*. *Mol Pharm*, 2012. **9**(9): p. 2479-2488.

239. Ballauff, M., *SAXS and SANS studies of polymer colloids*. Current opinion in colloid & interface science, 2001. **6**(2): p. 132-139.
240. Liu, Y., et al., *PAMAM dendrimers undergo pH responsive conformational changes without swelling*. J Am Chem Soc, 2009. **131**(8): p. 2798-2799.
241. Porcar, L., et al., *Structural investigation of PAMAM dendrimers in aqueous solutions using small-angle neutron scattering: effect of generation*. J. Phys. Chem. B, 2008. **112**(47): p. 14772-14778.
242. Topp, A., et al., *Effect of solvent quality on the molecular dimensions of PAMAM dendrimers*. Macromolecules, 1999. **32**(21): p. 7232-7237.
243. Amis, E., A. Topp, and B. Bauer. *SANS study of labeled PAMAM dendrimer*. in *ABSTRACTS OF PAPERS OF THE AMERICAN CHEMICAL SOCIETY*. 1997. AMER CHEMICAL SOC 1155 16TH ST, NW, WASHINGTON, DC 20036.
244. Prosa, T.J., et al., *A SAXS study of the internal structure of dendritic polymer systems*. Journal of Polymer Science Part B: Polymer Physics, 1997. **35**(17): p. 2913-2924.
245. Caminade, A.-M., R. Laurent, and J.-P. Majoral, *Characterization of dendrimers*. Adv Drug Deliv Rev, 2005. **57**(15): p. 2130-2146.
246. Beck Tan, N., et al., *A small angle scattering study of dendrimer–copper sulfide nanocomposites*. Polymer, 1999. **40**(10): p. 2537-2545.
247. Funayama, K. and T. Imae, *Structural analysis of spherical water-soluble dendrimer by SANS*. Journal of Physics and Chemistry of Solids, 1999. **60**(8): p. 1355-1357.
248. Han, M., P. Chen, and X. Yang, *Molecular dynamics simulation of PAMAM dendrimer in aqueous solution*. Polymer, 2005. **46**(10): p. 3481-3488.
249. Ouyang, D., et al., *The effect of pH on PAMAM dendrimer–siRNA complexation—Endosomal considerations as determined by molecular dynamics simulation*. Biophys Chem, 2011. **158**(2): p. 126-133.

250. Maiti, P.K., et al., *Structure of PAMAM dendrimers: Generations 1 through 11*. *Macromolecules*, 2004. **37**(16): p. 6236-6254.
251. Marrink, S.J., A.H.d. Vries, and A.E. Mark, *Coarse Grained Model for Semiquantitative Lipid Simulations*. *Journal of Physical Chemistry B*, 2004. **108**: p. 750-760.
252. Lee, H. and R.G. Larson, *Molecular dynamics simulations of PAMAM dendrimer-induced pore formation in DPPC bilayers with a coarse-grained model*. *J Phys Chem B*, 2006. **110**(37): p. 18204-11.
253. Marrink, S.J., H.J. Risselada, and a.e. al., *The MARTINI Force Field: Coarse Grained Model for Biomolecular Simulations*. *Journal of Physical Chemistry B*, 2007. **111**: p. 7812-7824.
254. Monticelli, L., S.K. Kandasamy, and a.e. al., *The MARTINI Coarse-Grained Force Field: Extension to Proteins*. *Journal of Chemical Theory and Computation*, 2008. **4**: p. 819-834.
255. Lee, H. and R.G. Larson, *Lipid bilayer curvature and pore formation induced by charged linear polymers and dendrimers: the effect of molecular shape*. *The Journal of Physical Chemistry B*, 2008. **112**(39): p. 12279-12285.
256. Lee, H. and R.G. Larson, *Membrane pore formation induced by acetylated and polyethylene glycol-conjugated polyamidoamine dendrimers*. *The Journal of Physical Chemistry C*, 2011. **115**(13): p. 5316-5322.
257. Maiti, P.K., et al., *Effect of solvent and pH on the structure of PAMAM dendrimers*. *Macromolecules*, 2005. **38**(3): p. 979-991.
258. Maiti, P.K. and B. Bagchi, *Structure and dynamics of DNA-dendrimer complexation: role of counterions, water, and base pair sequence*. *Nano Lett*, 2006. **6**(11): p. 2478-2485.
259. Ballauff, M. and C.N. Likos, *Dendrimers in solution: insight from theory and simulation*. *Angewandte Chemie International Edition*, 2004. **43**(23): p. 2998-3020.

260. Han, M., P. Chen, and X. Yang, *Molecular dynamics simulation of PAMAM dendrimer in aqueous solution*. *Polymer*, 2005. **46**: p. 3481-3488.
261. Maingi, V., et al., *Dendrimer building toolkit: Model building and characterization of various dendrimer architectures*. *Journal of computational chemistry*, 2012. **33**(25): p. 1997-2011.
262. Hedden, R.C. and B.J. Bauer, *Structure and dimensions of PAMAM/PEG dendrimer-star polymers*. *Macromolecules*, 2003. **36**(6): p. 1829-1835.
263. Kim, B.-D. and J.E. Cazes, *Performance and scalability study of sun constellation cluster'ranger'using application-based benchmarks*. *Proc. TeraGrid*, 2008. **2008**.
264. Phillips, J.C., et al., *Scalable molecular dynamics with NAMD*. *Journal of computational chemistry*, 2005. **26**(16): p. 1781-1802.
265. Humphrey, W., A. Dalke, and K. Schulten, *VMD: visual molecular dynamics*. *Journal of molecular graphics*, 1996. **14**(1): p. 33-38.
266. Foloppe, N. and A.D. MacKerell Jr, *All - atom empirical force field for nucleic acids: I. Parameter optimization based on small molecule and condensed phase macromolecular target data*. *Journal of computational chemistry*, 2000. **21**(2): p. 86-104.
267. MacKerell, A.D. and N.K. Banavali, *All - atom empirical force field for nucleic acids: II. Application to molecular dynamics simulations of DNA and RNA in solution*. *Journal of computational chemistry*, 2000. **21**(2): p. 105-120.
268. Frisch, M., et al., *Gaussian 09; Gaussian. Inc., Wallingford, CT, 2009*.
269. Cakara, D., J. Kleimann, and M. Borkovec, *Microscopic protonation equilibria of poly (amidoamine) dendrimers from macroscopic titrations*. *Macromolecules*, 2003. **36**(11): p. 4201-4207.
270. Lee, H., et al., *Molecular dynamics studies of polyethylene oxide and polyethylene glycol: Hydrodynamic radius and shape anisotropy*. *Biophys J*, 2008. **95**(4): p. 1590-1599.

271. Mark, P. and L. Nilsson, *Structure and dynamics of the TIP3P, SPC, and SPC/E water models at 298 K*. The Journal of Physical Chemistry A, 2001. **105**(43): p. 9954-9960.
272. Feller, S.E., et al., *Constant-pressure molecular-dynamics simulation-the Langevin piston method*. Journal of Chemical Physics, 1995. **103**(11): p. 4613-4621.
273. Izaguirre, J.A., et al., *Langevin stabilization of molecular dynamics*. J Chem Phys, 2001. **114**: p. 2090.
274. Dennington, R., T. Keith, and J. Millam, *Gaussview*. Gaussview, 2009. **Version 5**.
275. Albertazzi, L., et al., *In vivo distribution and toxicity of PAMAM dendrimers in the central nervous system depend on their surface chemistry*. Mol Pharm, 2012. **10**(1): p. 249-260.
276. Maiti, P.K. and W.A. Goddard, *Solvent quality changes the structure of G8 PAMAM dendrimer, a disagreement with some experimental interpretations*. The Journal of Physical Chemistry B, 2006. **110**(51): p. 25628-25632.
277. Prosa, T.J., B.J. Bauer, and E.J. Amis, *From stars to spheres: A SAXS analysis of dilute dendrimer solutions*. Macromolecules, 2001. **34**(14): p. 4897-4906.
278. Lee, H. and R.G. Larson, *Molecular dynamics simulations of PAMAM dendrimer-induced pore formation in DPPC bilayers with a coarse-grained model*. The Journal of Physical Chemistry B, 2006. **110**(37): p. 18204-18211.
279. Lee, H. and R.G. Larson, *Coarse-grained molecular dynamics studies of the concentration and size dependence of fifth-and seventh-generation PAMAM dendrimers on pore formation in DMPC bilayer*. The Journal of Physical Chemistry B, 2008. **112**(26): p. 7778-7784.
280. Lee, I., et al., *Structural molecular dynamics studies on polyamidoamine dendrimers for a therapeutic application: effects of pH and generation*. Macromolecules, 2002. **35**(11): p. 4510-4520.

281. Maiti, P.K., T. Cagin, and a.e. al., *Effect of Solvent and pH on the Structure of PAMAM Dendrimers*. *Macromolecules*, 2005. **38**: p. 979-991.
282. Maiti, P.K. and B. Bagchi, *Structure and Dynamics of DNA-Dendrimer Complexation: Role of Counterions, Water, and Base Pair Sequence*. *Nano Lett*, 2006. **6**: p. 2478-2485.
283. Maiti, P.K. and W.A. Goddard, *Solvent Quality Changes the Structure of G8 PAMAM Dendrimer, a Disagreement with Some Experimental Interpretations*. *Journal of Physical Chemistry B*, 2006. **110**: p. 25628-25632.
284. Maiti, P.K. and R. Messina, *Counterion Distribution and Zeta-Potential in PAMAM Dendrimer*. *Macromolecules*, 2008. **41**: p. 5002-5006.
285. Maiti, P.K. and B. Bagchi, *Diffusion of flexible, charged, nanoscopic molecules in solution: Size and pH dependence for PAMAM dendrimer*. *The Journal of Chemical Physics*, 2009. **131**: p. 214901.
286. Maiti, P.K., Y. Li, and a.e. al., *Structure of polyamidoamide dendrimers up to limiting generations: A mesoscale description*. *The Journal of Chemical Physics*, 2009. **130**: p. 144902.
287. Lee, H., J.R. Baker, Jr., and R.G. Larson, *Molecular dynamics studies of the size, shape, and internal structure of 0% and 90% acetylated fifth-generation polyamidoamine dendrimers in water and methanol*. *J Phys Chem B*, 2006. **110**(9): p. 4014-9.
288. Lee, H. and R.G. Larson, *Molecular dynamics study of the structure and interparticle interactions of polyethylene glycol-conjugated PAMAM dendrimers*. *J Phys Chem B*, 2009. **113**(40): p. 13202-7.
289. Lee, H. and R.G. Larson, *Multiscale modeling of dendrimers and their interactions with bilayers and polyelectrolytes*. *Molecules*, 2009. **14**(1): p. 423-38.
290. Lee, H. and R.G. Larson, *Effects of PEGylation on the Size and Internal Structure of Dendrimers: Self-Penetration of Long PEG Chains into the Dendrimer Core*. *Macromolecules*, 2011. **44**: p. 2291-2298.
291. Rubinstein, M. and R.H. Colby, *Polymer physics*. 2003: OUP Oxford.

292. Porcar, L., et al., *Intramolecular structural change of PAMAM dendrimers in aqueous solutions revealed by small-angle neutron scattering*. The Journal of Physical Chemistry B, 2010. **114**(5): p. 1751-1756.
293. Lin, S.-T., P.K. Maiti, and W.A. Goddard III, *Dynamics and thermodynamics of water in PAMAM dendrimers at subnanosecond time scales*. The Journal of Physical Chemistry B, 2005. **109**(18): p. 8663-8672.
294. Hong, Y.-R. and C.B. Gorman, *Attenuating electron-transfer rates via dendrimer encapsulation: The case of metal tris (bipyridine) core dendrimers*. Langmuir, 2006. **22**(25): p. 10506-10509.
295. Mondal, S. and P. Basu, *Dendrimer Encapsulation of [MoVOS₄] Cores: Implications for the DMSO Reductase Family of Enzymes*. Inorg Chem, 2001. **40**(2): p. 192-193.
296. Li, T., et al., *Assess the intramolecular cavity of a PAMAM dendrimer in aqueous solution by small-angle neutron scattering*. Macromolecules, 2008. **41**(22): p. 8916-8920.
297. Ma, Y.-q., *Theoretical and computational studies of dendrimers as delivery vectors*. Chem Soc Rev, 2013. **42**(2): p. 705-727.
298. Majoros, I.J., et al., *PAMAM dendrimer-based multifunctional conjugate for cancer therapy: synthesis, characterization, and functionality*. Biomacromolecules, 2006. **7**(2): p. 572-579.
299. Dufès, C., I.F. Uchegbu, and A.G. Schätzlein, *Dendrimers in gene delivery*. Adv Drug Deliv Rev, 2005. **57**(15): p. 2177-2202.
300. Gillies, E.R. and J.M. Frechet, *Dendrimers and dendritic polymers in drug delivery*. Drug Discov Today, 2005. **10**(1): p. 35-43.
301. Wiener, E., et al., *Dendrimer - based metal chelates: A new class of magnetic resonance imaging contrast agents*. Magnetic resonance in medicine, 1994. **31**(1): p. 1-8.
302. Biswas, S., et al., *Surface conjugation of triphenylphosphonium to target poly (amidoamine) dendrimers to mitochondria*. Biomaterials, 2012. **33**(18): p. 4773-4782.

303. Rosenfeldt, S., et al., *Distribution of end groups within a dendritic structure: A SANS study including contrast variation*. *Macromolecules*, 2002. **35**(21): p. 8098-8105.
304. Maiti, P.K., et al., *Effect of solvent and pH on the structure of PAMAM dendrimers*. *Macromolecules*, 2005. **38**(3): p. 979-991.
305. Wooley, K.L., et al., *Shapes of Dendrimers from Rotational-Echo Double-Resonance NMR*. *Journal of American Chemistry Society*, 1997. **119**: p. 53-58.
306. Porcar, L., et al., *Structural investigation of PAMAM dendrimers in aqueous solutions using small-angle neutron scattering: effect of generation*. *The Journal of Physical Chemistry B*, 2008. **112**(47): p. 14772-14778.
307. Hedden, R.C. and B.J. Bauer, *Structure and Dimensions of PAMAM/PEG Dendrimer-Star Polymers*. *Macromolecules*, 2003. **36**: p. 1829-1835.
308. Kichler, A., et al., *Intranasal gene delivery with a polyethylenimine-PEG conjugate*. *Journal of Controlled Release*, 2002. **81**(3): p. 379-388.
309. Harris, J.M. and R.B. Chess, *Effect of pegylation on pharmaceuticals*. *Nature Reviews Drug Discovery*, 2003. **2**(3): p. 214-221.
310. Singh, P., et al., *Folate and Folate-PEG-PAMAM Dendrimers: Synthesis, Characterization, and Targeted Anticancer Drug Delivery Potential in Tumor Bearing Mice*. *Bioconjug Chem*, 2008. **19**(11): p. 2239-2252.
311. Breunig, M., S. Bauer, and A. Göpferich, *Polymers and nanoparticles: intelligent tools for intracellular targeting?* *European Journal of Pharmaceutics and Biopharmaceutics*, 2008. **68**(1): p. 112-128.
312. Lee, H. and R.G. Larson, *Effects of PEGylation on the size and internal structure of dendrimers: Self-penetration of long PEG chains into the dendrimer core*. *Macromolecules*, 2011. **44**(7): p. 2291-2298.

313. Rathgeber, S., et al., *Dynamics of star-burst dendrimers in solution in relation to their structural properties*. J Chem Phys, 2002. **117**: p. 4047.
314. Osada, Y. and M. Sato, *Thermal equilibrium of the intermacromolecular complexes of polycarboxylic acids realized by cooperative hydrogen bonding*. Journal of Polymer Science: Polymer Letters Edition, 1976. **14**(3): p. 129-134.
315. He, H., et al., *PEGylated Poly (amidoamine) dendrimer-based dual-targeting carrier for treating brain tumors*. Biomaterials, 2011. **32**(2): p. 478-487.
316. Zhu, S., et al., *Partly PEGylated polyamidoamine dendrimer for tumor-selective targeting of doxorubicin: the effects of PEGylation degree and drug conjugation style*. Biomaterials, 2010. **31**(6): p. 1360-1371.
317. Esfand, R. and D.A. Tomalia, *Poly (amidoamine)(PAMAM) dendrimers: from biomimicry to drug delivery and biomedical applications*. Drug discovery today, 2001. **6**(8): p. 427-436.
318. Boas, U. and P.M. Heegaard, *Dendrimers in drug research*. Chemical Society Reviews, 2004. **33**(1): p. 43-63.
319. Tomalia, D., et al., *A new class of polymers: starburst-dendritic macromolecules*. Polymer Journal, 1985. **17**(1): p. 117-132.
320. Cloninger, M.J., *Biological applications of dendrimers*. Current opinion in chemical biology, 2002. **6**(6): p. 742-748.
321. Venditto, V.J., C.A.S. Regino, and M.W. Brechbiel, *PAMAM dendrimer based macromolecules as improved contrast agents*. Molecular pharmaceutics, 2005. **2**(4): p. 302-311.
322. Choi, J.S., et al., *Enhanced transfection efficiency of PAMAM dendrimer by surface modification with L-arginine*. Journal of controlled release, 2004. **99**(3): p. 445-456.
323. Jevprasesphant, R., et al., *The influence of surface modification on the cytotoxicity of PAMAM dendrimers*. International Journal of Pharmaceutics, 2003. **252**(1): p. 263-266.

324. Lee, J.H., et al., *Polyplexes assembled with internally quaternized PAMAM-OH dendrimer and plasmid DNA have a neutral surface and gene delivery potency*. *Bioconjugate chemistry*, 2003. **14**(6): p. 1214-1221.
325. Klajnert, B. and M. Bryszewska, *Fluorescence studies on PAMAM dendrimers interactions with bovine serum albumin*. *Bioelectrochemistry*, 2002. **55**(1): p. 33-35.
326. Scott, R.W., O.M. Wilson, and R.M. Crooks, *Synthesis, characterization, and applications of dendrimer-encapsulated nanoparticles*. *The Journal of Physical Chemistry B*, 2005. **109**(2): p. 692-704.
327. Zhou, J., et al., *PAMAM dendrimers for efficient siRNA delivery and potent gene silencing*. *Chemical communications*, 2006(22): p. 2362-2364.
328. Papagiannaros, A., et al., *Doxorubicin–PAMAM dendrimer complex attached to liposomes: cytotoxic studies against human cancer cell lines*. *International journal of pharmaceutics*, 2005. **302**(1): p. 29-38.
329. Kleinman, M.H., et al., *Effect of protonation and PAMAM dendrimer size on the complexation and dynamic mobility of 2-naphthol*. *The Journal of Physical Chemistry B*, 2000. **104**(48): p. 11472-11479.
330. Zhu, S., et al., *PEGylated PAMAM dendrimer-doxorubicin conjugates: in vitro evaluation and in vivo tumor accumulation*. *Pharmaceutical research*, 2010. **27**(1): p. 161-174.
331. Lee, C.C., et al., *Designing dendrimers for biological applications*. *Nature biotechnology*, 2005. **23**(12): p. 1517-1526.
332. Najlah, M., et al., *Synthesis, characterization and stability of dendrimer prodrugs*. *International journal of pharmaceutics*, 2006. **308**(1): p. 175-182.
333. áBaker Jr, J.R., *Tumor angiogenic vasculature targeting with PAMAM dendrimer–RGD conjugates*. *Chemical communications*, 2005(46): p. 5739-5741.

334. Quintana, A., et al., *Design and function of a dendrimer-based therapeutic nanodevice targeted to tumor cells through the folate receptor*. *Pharmaceutical research*, 2002. **19**(9): p. 1310-1316.
335. Luo, D., et al., *Poly (ethylene glycol)-conjugated PAMAM dendrimer for biocompatible, high-efficiency DNA delivery*. *Macromolecules*, 2002. **35**(9): p. 3456-3462.
336. Kojima, C., et al., *Synthesis of polyamidoamine dendrimers having poly (ethylene glycol) grafts and their ability to encapsulate anticancer drugs*. *Bioconjugate chemistry*, 2000. **11**(6): p. 910-917.
337. Kim, T.-i., et al., *PAMAM-PEG-PAMAM: novel triblock copolymer as a biocompatible and efficient gene delivery carrier*. *Biomacromolecules*, 2004. **5**(6): p. 2487-2492.
338. Kojima, C., et al., *Influence of dendrimer generation and polyethylene glycol length on the biodistribution of PEGylated dendrimers*. *International journal of pharmaceutics*, 2010. **383**(1): p. 293-296.
339. Kim, S.H. and J.A. Katzenellenbogen, *Hormone-PAMAM dendrimer conjugates: Polymer dynamics and tether structure affect ligand access to receptors*. *Angewandte Chemie International Edition*, 2006. **45**(43): p. 7243-7248.
340. Liu, Y., et al., *PAMAM dendrimers undergo pH responsive conformational changes without swelling*. *Journal of the American Chemical Society*, 2009. **131**(8): p. 2798-2799.
341. MacKerell, A.D., N. Banavali, and N. Foloppe, *Development and current status of the CHARMM force field for nucleic acids*. *Biopolymers*, 2000. **56**(4): p. 257-265.
342. Vanommeslaeghe, K., et al., *CHARMM general force field: A force field for drug - like molecules compatible with the CHARMM all - atom additive biological force fields*. *Journal of computational chemistry*, 2010. **31**(4): p. 671-690.
343. van/Hest, J., et al., *Acid-functionalized amphiphiles, derived from polystyrene-poly (propylene imine) dendrimers, with a pH-dependent aggregation*. *Macromolecules*, 1995. **28**(19): p. 6689-6691.

344. Kitchens, K.M., M.E. El-Sayed, and H. Ghandehari, *Transepithelial and endothelial transport of poly (amidoamine) dendrimers*. *Advanced drug delivery reviews*, 2005. **57**(15): p. 2163-2176.
345. Kitchens, K.M., et al., *Transport of poly (amidoamine) dendrimers across Caco-2 cell monolayers: influence of size, charge and fluorescent labeling*. *Pharmaceutical research*, 2006. **23**(12): p. 2818-2826.
346. Cramer, C.J., *Essentials of computational chemistry: theories and models*. 2013: John Wiley & Sons.
347. Lee, H., et al., *Molecular dynamics studies of polyethylene oxide and polyethylene glycol: hydrodynamic radius and shape anisotropy*. *Biophysical journal*, 2008. **95**(4): p. 1590-1599.
348. Yang, L. and S.R. da Rocha, *PEGylated, NH₂-terminated PAMAM Dendrimers: A Microscopic View from Atomistic Computer Simulations*. *Molecular pharmaceutics*, 2014.
349. Eskici, G. and P. Axelsen, *Molecular Modeling and Simulations of Reverse Micelles*. *Biophysical Journal*, 2014. **106**(2): p. 291a.
350. Chen, S., M. Wang, and Z. Xia, *Multiscale Fluid Mechanics and Modeling*. *Procedia IUTAM*, 2014. **10**: p. 100-114.
351. Dennington, R., T. Keith, and J. Millam, *GaussView, Version 5,*. Semichem Inc. Shawnee Mission KS, 2009.
352. Lyulin, S.V., et al., *Effect of solvent quality and electrostatic interactions on size and structure of dendrimers. Brownian dynamics simulation and mean-field theory*. *Macromolecules*, 2004. **37**(8): p. 3049-3063.
353. Topp, A., et al., *Probing the location of the terminal groups of dendrimers in dilute solution*. *Macromolecules*, 1999. **32**(21): p. 7226-7231.
354. Fréchet, J.M., *Dendrimers and supramolecular chemistry*. *Proceedings of the National Academy of Sciences*, 2002. **99**(8): p. 4782-4787.

355. Boas, U., J.B. Christensen, and P.M. Heegaard, *Dendrimers: design, synthesis and chemical properties*. Journal of Materials Chemistry, 2006. **16**(38): p. 3785-3798.
356. Zhang, M., T. Desai, and M. Ferrari, *Proteins and cells on PEG immobilized silicon surfaces*. Biomaterials, 1998. **19**(10): p. 953-960.

ABSTRACT**DESIGN OF FUNCTIONAL DENDRIMER NANOCARRIERS AND FORMULATIONS IN PROPELLANT-BASED INHALERS FOR PULMONARY DRUG DELIVERY**

by

LIN YANG**August 2014****Advisor:** Sandro R.P. da Rocha**Major:** Materials Science and Engineering**Degree:** Doctor of Philosophy

This Dissertation focuses on addressing two of the major challenges in developing pressurized metered dose inhalers for pulmonary drug / gene delivery to and through the lungs. First challenge is to design biocompatible moieties for the steric stabilization of suspension formulations in HFO-based propellants. Using a combination of tools including ab initio calculation, molecular dynamics simulation and high pressure tensiometry, potential fluorocarbon-philic moieties were systematically screened. Surfactants with those chemistries as tail fragments were studied at the HFO|H₂O interface for their ability to lower the interfacial tension at HFO|H₂O interface. Selected surfactants were further optimized for surfactant balance by altering the head to tail ratio.

The second challenge is to design PAMAM functional dendrimer nanocarriers for the delivery of therapeutics to and through the lungs. Using molecular dynamics simulations, we investigate the microstructures of PAMAM dendrimers as a function of generation, PEGylation

density, PEGylation PEG length, dendrimer terminal chemistry. Our discussion is focused on how the differences in microstructures of PAMAM dendrimers will affect the function, efficacy and efficiency of PAMAM dendrimer as drug / gene nanocarriers.

AUTOBIOGRAPHICAL STATEMENT

EDUCATION

- Ph.D., Materials Science and Engineering, Wayne State University, 2014
- B.E., Polymer Materials and Engineering, Donghua University, China, 2009

PUBLICATIONS:

1. **Yang, L.** and da Rocha, S. R. P. “*PEGylated, NH₂-terminated PAMAM dendrimers: A Microscopic View From Atomistic Computer Simulation*” *Molecular Pharmaceutics*, 2014, 11(5), 1459-1470.
2. **Yang, L.** and da Rocha, S. R. P. “*The Impact of the Chemistry of the Terminal Surface Groups of PAMAM Dendrimers on the Conformation of the Grafted PEG Layer*” Manuscript submitted to *Molecular Pharmaceutics*.
3. **Yang, L.** and da Rocha, S. R. P. “*Designing Hydrofluoro-alkane (HFA) and Hydrofluoroolefin(HFO) – Philic Moieties for Medical Aerosols*”. Manuscript to be submitted.
4. **Yang, L.** and da Rocha, S. R. P. “*Rational Surfactant Design for Hydrofluoroolefin (HFO): A Combination of Molecular Dynamics and Experimental Approach*”. To be submitted.
5. Conti, D. S.; Grashik, J.; **Yang, L.**; Wu, L.; da Rocha, S. R. P. “*Solvation in Hydrofluoroalkanes: How can Ethanol Help?*”. *Journal of Pharmacy and Pharmacology*. 2012, 64, p.1236-1244.